To the Graduate Council:

I am submitting herewith a dissertation written by Kathleen Sue Giesfeldt entitled "Approaches to Uniform-Morphology: Polymer-Based SERS Substrates." I have examined the final electronic copy of this dissertation for form and content and recommend that it be accepted in partial fulfillment of the requirements for the degree of Doctor of Philosophy, with a major in Chemistry.

Michael J. Sepaniak
Major Professor

We have read this dissertation
and recommend its acceptance:

Charles Feigerle

Youngmi Lee

Kimberly Gwinn

Accepted for the Council:

Anne Mayhew
Vice Chancellor and
Dean of Graduate Studies

(Original signatures are on file with official student records.)

APPROACHES TO UNIFORM-MORPHOLOGY: POLYMER-BASED SERS SUBSTRATES

A Dissertation
Presented for the
Doctor of Philosophy
Degree
The University of Tennessee, Knoxville

Kathleen Sue Giesfeldt
May 2005

DEDICATION

This dissertation is dedicated to my father,
Merle M. Giesfeldt
For his insistence that science and math are the
foundations of knowledge

And

Memphis B. Giesfeldt
My faithful companion, solace, and inspiration

ACKNOWLEDGEMENTS

> In all sciences the student is discovering that nature, as he calls it, is always working, in wholes and in every detail, after the laws of the human mind. Every creation, in parts or in particles, is on the method and by the means which our mind approves as soon as it is thoroughly acquainted with the facts; hence the delight. No matter how far or how high science explores, it adopts the method of the universe as fast as it appears; and this discloses that the mind as it opens, the mind as it shall be, comprehends and works thus ; that is to say, the Intellect builds the universe and is the key to all it contains. . . I believe in the existence of the material world as the expression of the spiritual or the real, and in the impenetrable mystery which hides (and hides through absolute transparency) the mental nature, I await the insight which our advancing knowledge of material laws shall furnish. Ralph Waldo Emerson, "The Conscious Order"
>
> I would like to thank Dr. Sepaniak, for taking in a former art conservator and turning her into a chemist. My thanks to all the Sepaniak group members past, present, in particular, I am indebted to Marco de Jesús for his patience, humor, mechanical abilities, and insightfulness; you are a friend, collaborator, and mentor. I have felt honored to be a part of the extraordinary collaborative team: Marco, Maggie Connatser, and Pampa Dutta. I have greatly appreciated the discussions, debates, and problem-solving sessions. I thank the Sepaniak group members for their assistance and camaraderie during the maintenance of the physical vapor deposition instrument and the LabRam, especially during those times when it seemed that all hope was lost. I would also like to acknowledge Tim Free for his amazing mechanical prowess and input. In addition, my gratitude goes out to Drs. Feigerle and Turner and to Richard Stein, of Cooke Vacuum Systems, Inc, I learned much during my consultations with them on vacuum systems.
>
> I would like to acknowledge all my friends and family who have supported, nurtured, encouraged, listened to me and helped me maintain my sense of humor throughout this odyssey. Above all, I wish to express my gratitude to:
> Both of my parents for their constant encouragement of my interest in science.
> Peter Haendler, for his love and fanatical support of the "BuckeyBoom" project. May this be the beginning of a long and prosperous partnership.
> Ina St. George, A true friend and conservation colleague who always keeps me tied to my art conservation roots.
> Sharon Giesfeldt and Elizabeth Becker, my sisters, co-conspirators, instigators, and two of the most amazing women I know and love. Thanks for listening and just being there when I needed you.
> David Giesfeldt, brother and friend. Your presents of homemade food made graduate school bearable.
> J. Matthew Farmer, friend, and fellow chemist. Thank you for your chemical and spiritual guidance.

Abstract

Polymer-nano-metallic-particle composites have demonstrated technological potential due to their unique optical and electrical properties. We report on composites prepared via physical vapor deposition of silver and gold onto pliable polydimethlysiloxane (PDMS) polymer. Rapid metal diffusion and nano-metallic-particle formation in a phase-separated surface layer of the PDMS creates unique sub-surface-based composites that vary in properties based on rate of deposition and average metal thickness. In addition, nano-metallic-particle spacing can be altered with fair reproducibility and reversibility by physically manipulating the composite. A practical technological characteristic of these composite materials arises from their potential to be molded into functional devices.

Surface enhanced Raman scattering (SERS) substrate selectivity and the analytical figures of merit, such as reproducibility and dynamic range have limited the general acceptance of the technique for routine analytical applications. Herein, we explore the potential approaches to fabricate polymer-based substrates with uniform morphology by electron beam lithography, imprinting, and casting. The objective is to produce a homogeneous analyte environments that will address the issues associated with the figures of merit.

The optical properties of the materials are studied by visible wavelength optical extinction spectrometry and SERS. DC conductivity measurements were made during depositions to study percolation conditions for the materials. Depth-profiling was performed by X-Ray Photoelectron Spectrometry.

Table of Contents

Page

Part 1. Introduction to Raman Spectroscopy: History, Theory,and Instrumentation…….…….. 1

History of Raman Spectroscopy……. 2

Mechanism of Raman Scattering…… 4

The Raman Cross-section……... 6

Wave Model of Raman Spectrometry……... 10

Raman Instrumentation……. 16

Sources…….. 18

Transducers……...…… 19

Wavelength Selectors…… 22

Raman Spectrometer Systems……... 26

References……. 37

Part 2. Surface Enhanced Raman Scattering (SERS): History, Theory, and Substrates…….…….. 39

History……..…… 40

SERS Theories…….. 45

Electromagnetic Theory…… 45

Chemical Enhancement Theory…… 54

Substrates…….. 57

Statement of the Problem……. 65

References…… 68

Part 3. Discontinuous Metal Films for SERS Substrates: Theory, Preparation, and Characterization…….…… 89

Introduction……... 90

Physical Vapor Deposition Theory…….. 91

Thermal Evaporation Sources…….……. 94

Thin Film Theory……. 96

Considerations for Solid Supports……... 99

Characterization of Thin Films……..…… 102

References…….…….. 116

Part 4. Studies of the Optical Properties of Metal-Pliable Polymer Composite Materials……..…… 120

Introduction…….……...…… 121

Experimental……... 123

Results and Discussion…….. 127

Thickness and Deposition Rate Studies…….… 127

Optimization of Particle Proximity…… 136

References……... 142

Part 5. Gold-Polymer Nanocomposites: Studies of their Optical Properties and Their Potential as SERS Substrates……..……. 145

Introduction……. 146

Experimental……... 150

Results and Discussion……... 152

Studies of Nanocomposite Properties Related to Metal Thickness and Deposition Rate……... 153

Translation Rate/ STT……. 160

Selectivity……... 165

The Effect of pH and Anions on Analyte Absorption and SERS Activity……. 167

References……... 176

Part 6. Preliminary Investigations of Polymer-Based SERS Substrates with Uniform Morphology……. 180

Introduction…… 181

Experimental…….. 184

Nanowell Cross-gratings and Nanoparticle Arrays…… 189

Nanowell Cross-Gratings……... 191

Nanoparticle Arrays via EBL……. 198

Imprinting and Casting…….. 202

References……. 206

Vita……..209

List of Tables

Table		Page
1.1	Typical values for spectroscopic cross-sections with incident radiation……..	7
1.2	Common lasers for Raman Spectroscopy……..	18
2.1	Comparison of SERS substrates……..…….……...	58
3.1	Characterization Techniques…….…….……...…….	104
4.1.	The 1050 cm^{-1} band areas (arbitrary units) of *p*-ATP for a substrate cycled between stretches……...…… .	141
5.1	pH of NaX solutions……...……	175

List of Figures

Figure **Page**

1.1 Comparison of energy levels for infrared (IR) and for conventional Raman spectroscopy……..... 4

1.2 Comparison of Rhodamine 6-G spectra by several analytical spectroscopic techniques. A) UV-Vis, B) Structure of Rhodamine 6G, C) Fluorescence, and D) Raman spectroscopy……..……...……. 8

1.3 Energy levels for conventional Raman, pre-resonance Raman, discrete resonance Raman, continuum Raman, and fluorescence processes……...…....… 9

1.4. Comparison of Stokes and Anti-Stokes for para-aminothiophenol (pATP) on Ag-PDMS SERS substrate……...…...… 15

1.5 Diagram of Raman instrument with 90^0 collection geometry…… 17

1.6 Illustration of triple monochromator configurations…… 27

1.7 Optical diagram of an FT-Raman spectrometer..…….. 30

1.8 Schematic of confocal Raman microscope……..……. 34

1.9 Example of Raman mapping of silver-coated nanogratings and pATP….…… 36

2.1 Illustration of the unique morphologies and compositions of colloids that have been produced…… 43

2.2 Illustration of the charges and electromagnetic field of surface plasmons propagating in the *x* direction on a surface……... 46

2.3 Illustration of the electromagnetic enhancement of a "hot spot" or "lightening rod" effect between adclusters……... 47

2.4 Charge Transfer Model is based on an overlap of the HOMO and LUMO of the electron wavefronts for both the adsorbate and metal……55

2.5 Schemes for etching, imprinting, and lift-off methods for substrate preparation via electron beam lithography on Si wafers…….. 64

3.1 Basic physical vapor deposition system with its component parts……... 91

3.2 Comparison of evaporation (A) and effusion (B) processes during physical vapor deposition……..…… 93

3.3 Common thermal sources for evaporation and effusion used for physical vapor deposition of materials……. 95

3.4 The cluster aggregation on the surface of a solid support…… 96

3.5 Theoretical thin film growth patterns……... 97

3.6 Observed formation of a thin metal film by physical vapor deposition……... 98

3.7 A) Example of inherent roughness of Ag-coated PDMS, B) Example of inhomogeneity of nanoparticle size and shape due to the vapor deposited metal film (both samples: ~20 nm Ag, 1Å/s)…… 101

4.1 The XPS depth profiles of 20 nm Ag on PDMS showing area percent for two Ag lines……..…… 128

4.2 DC conductivity curves obtained during deposition at 0.2 and 1.0 Å/s……. 130

4.3 Scanning electron micrographs of Ag-PDMS surface at 90,000 fold magnification for deposition rates of 1.0 Å/s (left) and 0.2 Å/s (right)…….. 131

4.4 Optical extinction curves for 15 nm average Ag thickness Ag-PDMS substrates at the two different deposition rates (left)…….. 132

4.5 Band areas (left) of 1 x 10^{-5} M *p*-ATP on Ag-PMDS at deposition rate of 1.0 Å/s (blue bar for 0.2 Å/s)…….. 133

4.6 Spectra (A) of 1x 10^{-5} M *p*-ATP on Ag-PDMS (black line) and Ag-Glass (red). Spectra (B) of 1 x 10^{-4}M *p*-ABA on Ag-PDMS (black line) and Ag-Glass (red)…….. 135

4.7 A: image of the macro-simulation. B-D: graphically enhanced images as PDMS is allowed to relax from the original ~ 150% stretched state (B, ~147%; C, ~134%; D, ~125%; E, ~119%)……... 137

4.8 Optical extinction curves of Ag-PDMS substrate with excitation beam polarization parallel (left) and perpendicular (right) to direction of stretch…….. 139

4.9 SERS band profiles of 1 x 10^{-5} M *p*-ATP with excitation beam polarization parallel (left) and perpendicular (right) of pre-stretched

Ag-PDMS substrate (15 nm Ag, 1.0 Å/s)……... 140

5.1 The XPS depth profiles of 30 nm Au on PDMS showing atomic percent for two Au lines…….. 154

5.2 DC conductivity curves obtained during the deposition of Au at 0.2 and 1.0 Å/s……. 156

5.3 Scanning electron micrographs of 30 nm Au-PDMS surface at 100,000 fold magnification for deposition rates of 0.2 Å/s (left) and 1.0 Å/s (right)……... 157

5.4 Optical extinction curves for Au-PDMS obtained at a deposition rate of 1.0 Å/s for six different average thicknesses of Au (left)……... 158

5.5 Spectrum (inset) is of 1 x 10^{-4} M 1,2-PDA (conditions: 5 second acquisition time; mean of 21 spectra; 2800 rpm; background and baseline corrected; excitation of 4.5 mW at 633 nm; 25 nm average Au thickness deposited at 1.0 Å/s)…… 159

5.6 Comparison of optimized Au SERS substrates (glass and PDMS substrates) under STT conditions to illustrate improved SERS signal intensity and functional group affinity……. 161

5.7 A study of the long-term viability of the Au-PDMS substrates…….. 162

5.8 Temporal study of the effect of 8.9 mW of laser irradiation on substrate and analyte under stationary and STT-SERS conditions…… 163

5.9 Calibration plots for 1,2-PDA with Au (top) and Ag (bottom) nanocomposites substrates……. 166

5.10 Comparison of selectivities of Ag-PDMS (upper) and Au-PDMS (lower) for a series of naphthalene derivatives that show the affinity of Au-PDMS for amine and nitro functionalities…….. 168

5.11 A) The SERS intensity as a function of pH. A 5.97 x 10^{-4}M solution of n phenyl-1,2 diphenylene diamine (pK_a=4.45) was analyzed under STT conditions (2800 rpm and incident laser power of 4.5 mW)…….. 171

5.12 Comparison of band areas on Au-Glass (782 cm^{-1}, 7 nm, 0.5 Å/s, stationary conditions (N=21)) and Au-PDMS (777 cm^{-1}, 25 nm, 1.0 Å/s, STT-SERS conditions (N=21))……. 173

6.1 1) A 1 μm area of the AutoCad patterns to show a comparison of the four nanowell cross-gratings……..……..... 185

6.2. Illustration of the theorized nano-titer well function (left) and what the empirical data suggests (right)…… 192

6.3 SEM micrographs illustrating the effect of metal film thickness on the inherent roughness of the Ag film…….…….…….193

6.4 Comparison of Ag film thickness and SERS spectral band areas……..…… 195

6.5 Comparison of white light illumination of Ag-coated nanowell cross-gratings. ……..... 196

6.6 Effect of source laser on the generation of surface plasmons and SERS intensity with 20 nm Au-coated NCGs and 1 x 10^{-4}M 1,2 PDA…...…… 197

6.7. Micrographs and white-light illumination images of 10 nm Ag coated nanoparticle cross-gratings……...…….. 200

6.8 10 nm Ag-coated set of nanoparticle cross-gratings that were vapor-treated with p-ATP. ……..… 201

6.9 Process of imprinting and casting nanostructured polymer substrates…...…… 203

Nomenclature

Part 1 Symbols:

α	polarizability (deformability of the electron cloud of the molecule due to the electric field)
α_0	equilibrium polarizability
$\frac{\delta\alpha}{\delta Q}$	rate of change of the polarizability with respect to Q_{equil}
c	speed of light (2.997 924 58 x 10^8 m/s)
cm^{-1}	wavenumber
d	distance between analyte and surface of the metal nanoparticle
E	electric field of the incident radiation (laser beam)
E_{appl}	applied electric field
E_{eff}	effective electric field inside the particle
E_{dipole}	EM field of the dipole
E_{inc}	irradiance of the incident photon (W m^{-2})
E_{metal}	effective field induced by the metal nanoparticle
E_0	maximum amplitude of the incident electromagnetic field
E_{out}	EM field peripheral to the spheroid
E_{scatt}	energy of scattered photons,
ΔE_{vib}	difference in energy for a given vibrational mode
$\varepsilon(\omega)$	dielectric function of the conductor (metal surface)
ε_0	dielectric of the ambient surroundings (air, water, solution)

γ	lightening rod factor
h	Planck's constant (6.626 068 76 x 10^{-34} J·s)
I	intensity
k	Boltzman's constant (1.380 650 3 x 10^{-23} J/K)
k^2_{ll}	parallel momentum of SP μ = induced dipole moment
μm	micrometer (micron)
nm	nanometer
ν	frequency (vibration or radiation)
ν_{inc}	frequency of the incident radiation
P_{scatt}	rate of scattering from a molecule
Q	normal coordinate
Q_{equil}	normal coordinate at equilibrium
Q_0	maximum value for Q, the maximum internuclear distance
r	radius of the metal nanoparticle
Re	equilibrium bond length
R(ω)	average enhancement
σ_{scatt}	scattering cross-section (m^2)
T	temperature (in Kelvin)
t	time (general)
ω	frequency of the SP

General Terms:

AFM	atomic force mircroscopy
AOTF	acoustic-optic tuning filters
ASR	Atomic-scale roughness
CCD	charge-coupled device
CT	charge transfer
DUV	deep ultraviolet
EBL	electron beam lithography
EM	electromagnetic
EMF	Electromagnetic field
EUV	Extreme ultraviolet
FT-IR	Fourier-transform infrared spectroscopy
FT-Raman	Fourier-transform Raman spectroscopy
FWHM	Full width at half maximum
Ge	Germanium
HF	Holographic filters
HNF	Holographic notch filters
HOMO	Highest occupied molecular orbital
IR	Infrared
LCTF	Liquid-crystal tuning filters
LN	Liquid nitrogen
LSP	Localized surface plasmons

LUMO	Lowest unoccupied molecular orbital
NIR	Near infrared
NSL	Nanosphere lithography
PDA	Photo diode arrays
PLM	Polarized light microscopy
PMT	Photomulitplier tubes
PVD	Physical, or thermal, vapor deposition
Q.E.	quantum efficiency
RBS	Rutherford back-scattering spectroscopy
RIE	Reactive ion etching
RR	Resonance Raman
RSD	Relative standard deviations
SANS	Small-angle neutron scattering
SEM	Scanning electron microscopy
SERS	Surface enhanced Raman scattering
SM	Single molecule
SP	Surface plasmon
STEM	Scanning transmission electron microscopy
SThM	Scanning thermal microscopy
STT	Sample translation technique
TCR	Temperature coefficient of resistivity
TEM	Transmission electron microscopy
UV	Ultraviolet

UV-Vis	Ultraviolet and visible light spectroscopy
XPS	X-ray photoelectron spectroscopy
XRD	X-ray Crystal Diffraction

Concentration Terms:

M	Molar (mole/liter)
%	percent
ppm	parts per million
ppb	parts-per-billion

Chemicals and Reagents:

1,2-PDA	n phenyl-1,2 diphenylene diamine
MA	methacrylate
PABA	para aminobenzoic acid
p-ATP	para aminothiolphenol
PDMS	polydimethylsiloxane
PMMA	polymethyl methacrylate

Part 1

Introduction to Raman Spectroscopy: History, Theory, and Instrumentation

History of Raman Spectroscopy

Electromagnetic radiation can be absorbed, transmitted, or scattered when it encounters a particle or molecule. For both the Tyndall and Rayleigh scattering phenomena, the energy of the scattered photon is the same as the incident photon; the difference between the two is due to the interaction of the photon with either a particle or a molecule, respectively. A change in the energy of a photon when it interacts with a molecule was first predicted in Germany by Smekal in 1923.[1-3] During a trip to the Mediterranean Sea, C. V. Raman was fascinated by the interplay of light on the surface of the water. This inspired the formulation of a series of experiments that confirmed this change in energy first predicted by Smekal. The paper published in Nature in 1928 by C. V. Raman and Krishan outlined the process whereby a sample is irradiated with a monochromatic beam that produces a "secondary radiation", which is the result of the inelastic collisions with a small fraction of the molecules in the sample and matrix.[4-6] He was awarded the Nobel Prize in physics in 1931 for his experimental exploration of the phenomenon.

This technique became the dominant vibrational spectroscopy until the late 1940's with the advent of commercially available infrared (IR) spectrometers. Raman spectroscopy could be used to study gases, liquids, including aqueous solutions, and solids; however it was limited by its instrumentation. Raman spectroscopy has vacillated between state-of-the-art and a nearly dying technique that has evolved by reinventing itself over the last century with improved instrumentation and the development of alternate methods to improve the efficiency of Raman scattering and its collection. An

understanding of where the field began, in terms of instrumentation and theory, elucidates the development and attraction of many pre-eminent scientists to the sub-field of surface enhanced Raman scattering (SERS).

Raman spectroscopy requires a narrow bandwidth source, which was provided initially by mercury arc lamps and glass filters. It was not until the 1960's that Raman spectroscopy began to reaffirm its applicability for analytical chemistry with the introduction of lasers, double monochromators, and electronic detectors.[7, 8] These components revived the method to a certain extent, but it was still considered a time- and labor-consuming technique, nearly 12 hours to collect a full spectrum. Laser line filters, charge-coupled devices as detectors, better data-processing instrumentation, Fourier-Transform Raman, and the discovery of surface enhanced Raman scattering (SERS) further revitalized the field during the 1980's. Up until the late 1980's, the technique had been viewed as a purely academic and research-oriented tool; with these improvements to the instrumentation, new applications were developed that directly competed with IR. A few of these applications were, but not limited to, gemology, environmental science, catalysts, in vitro biological studies, and polymer science industrial process and control engineering for semiconductors, carbon-based materials (single and multi-walled nanotubes, fullerenes, as well as, graphite and diamond films), glasses, and pigments, quality control for pharmaceuticals and personal care products. Further developments in the 1990's improved the ruggedness and compactness of the instruments that moved them from strictly a bench-top instrument to field-ready for space exploration, art conservation and archeology, forensics, and Homeland Security applications. Confocal Raman microprobes and microscopy improved the sensitivity of the technique to very weak

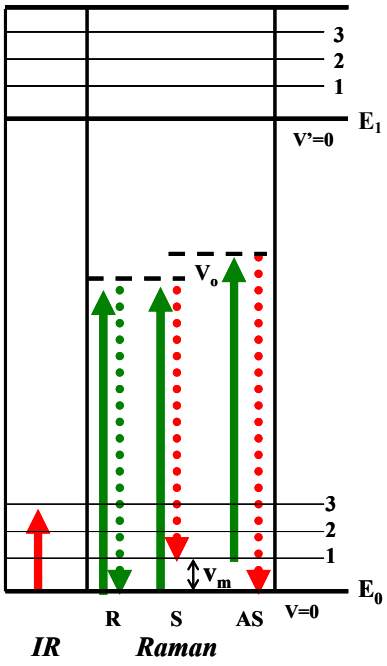


Figure 1.1. Comparison of energy levels for infrared (IR) and for conventional Raman spectroscopy. (Rayleigh (R), Stokes (S), Anti-Stokes (AS))

signals that previously were difficult or impossible to detect and permitted the probing and mapping of surfaces and surface chemistries without interferences from the bulk phases.

Mechanism of Raman Scattering

Infrared (IR) spectroscopy is a one photon event whereby the incident photon is absorbed by the molecule (Figure 1.1). The IR sources are blackbody radiators that consist of heated inert materials and produce a continuum of radiation. Examples of IR sources are Nernst Glower, globars, nichrome wires, and tungsten filaments. IR is considered to be a true absorption process whereby energy is conserved and the resulting state is a discrete state. This can occur when a molecule vibrates or rotates, a permanent

or transitory change in the dipole moment will be established. The charge distribution can be altered by the oscillating EMF of the incident radiation. This process is most efficient if the frequency of the incident radiation matches an energy level of a specific vibrational quantum state. This process can modify the amplitude of a specific vibrational or rotational mode via the absorption of the radiation.

Unlike IR, Raman is a two-photon event that employs high intensity monochromatic radiation that is generally not at a wavelength that could induce an electronic transition (Figure 1.1). For Raman, the absorption of energy from the incident photon is not a process where energy is conserved; it is considered a "virtual absorption". This results in potentially an infinite number of virtual states that do not have well-defined energy values and correspond to the energy of the molecule during the irradiation, but are not dependent upon the wavelength of the incident radiation.

The incident radiation can momentarily give rise to a distortion of the electron cloud around the bond of a molecule. Thus, a temporary change in the dipole moment is induced which polarizes the molecule. When the molecule relaxes it will emit a photon. The phenomenon can be described by the formula, $E_{scatt} = h\nu \pm \Delta E_{vib}$. Where E_{scatt} is the energy of scattered photons, h is Planck's constant, ν is the frequency of the photon, and ΔE_{vib} is the difference in energy for a given vibrational mode. The energy of the scattered photon, per the mathematical description above, can be have an increase or decrease in energy from that of the incident radiation due to inelastic collisions. When the energy is shifted to longer wavelengths, lower energy, it produces Stokes line. Conversely, scattered photons with shorter more energetic wavelength are known as

Anti-Stokes. Elastically scattered radiation, Rayleigh scattering, is the most intense and has no change in energy

The Raman Cross-section

Raman scattering is a very inefficient process that has limited the technique in comparison to other spectroscopic techniques such as absorbance (IR) and fluorescence. One means to compare these techniques is through a common measurement of the efficiency and sensitivity.[9] A cross-section (σ) is an estimate of the probability of the rate of incident photons interacting with a molecule to the rate of the scattering in area which is described by the equation:

$$P_{scatt} = \sigma_{scatt} E_{inc} \qquad \text{Eqn. 1.1}$$

Where:

P_{scatt} = the rate of scattering from a molecule

σ_{scatt} = scattering cross-section (m^2)

E_{inc} = irradiance of the incident photon ($W\ m^{-2}$)

The cross-section is a property of individual molecules and is independent of the irradiance of the incident photon. A comparison with other spectroscopic techniques (Table 1.1) shows how the low efficiency of Raman leads to low analytical sensitivity and the interference by both Rayleigh scattering and fluorescence.

Table 1.1 Typical values for spectroscopic cross-sections with incident radiation

Process	Radiation Type	σ (cm^2)
Absorption	UV IR	10^{-18} 10^{-20}
Fluorescence[1]		10^{-19}
Rayleigh Scattering		10^{-26}
Raman Scattering		10^{-29}
Pre-Resonance Raman Scattering		$\sim 10^{-27}$
Resonance Raman Scattering[2]		10^{-23}

[1] The fluorescence cross-section is highly dependent upon the environment in which the analyte resides. This may induce quenching of the analyte signal.
[2] Specific vibrational modes of the analyte are excited during the Resonance Raman, which alters the cross-section.

Although Raman and fluorescence are considered two-photon events, the actual processes lead to a considerable difference in the cross-sections. The cross-section of fluorescence is approximately ten orders of magnitude greater than that of Raman scattering. Despite the larger cross-sections for both fluorescence and UV-Vis spectrometry, the spectra that are generated are very information poor and generally cannot be used for qualitative spectral identification (Figure 1.2)

For conventional Raman scattering, the cross-section is approximately ten orders of magnitude lower than that of IR. However, IR contends with insensitive detectors, weak sources, stray light, and it is not applicable for aqueous solutions. Advances in instrumentation and numerous variations on conventional Raman spectroscopy, such as

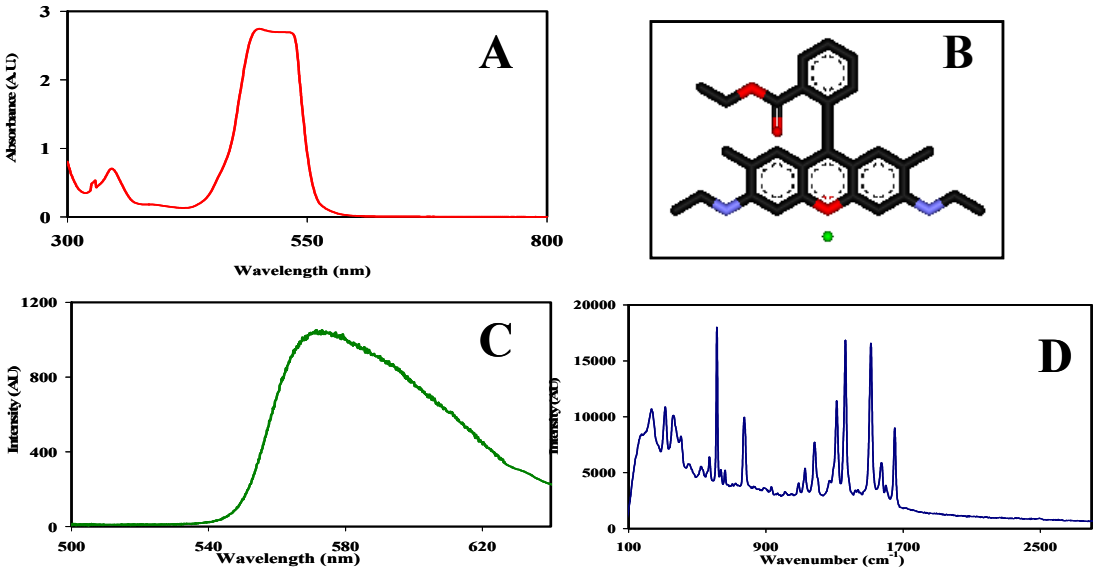


Figure 1.2. Comparison of Rhodamine 6-G spectra by several analytical spectroscopic techniques. A) UV-Vis, B) Structure of Rhodamine 6G, C) Fluorescence, and D) Raman spectroscopy.

pre-resonance, resonance Raman, and continuum Raman, as well as the evolution of surface enhanced Raman scattering (SERS) have made it possible to achieve low detection limits while maintaining the structurally rich information that is shown in Figure 1.2 C.

Figure 1.3 illustrates the processes of the aforementioned Raman techniques. For pre-resonance Raman, the incident radiation frequency approaches that of an electronic transition of the molecule, which results in an enhancement of the Raman intensities associated with that specific electronic transition. For discrete Resonance Raman (DRR) spectroscopy, the frequency of the laser beam is tuned to coincide with an electronic transition (resonance) specific to an individual chromophore or chemical moiety of interest. DRR can enhance intensities up to 10^2-10^6 of these particular spectral bands and often overwhelms Raman signals from all of the other transitions. The time scales for

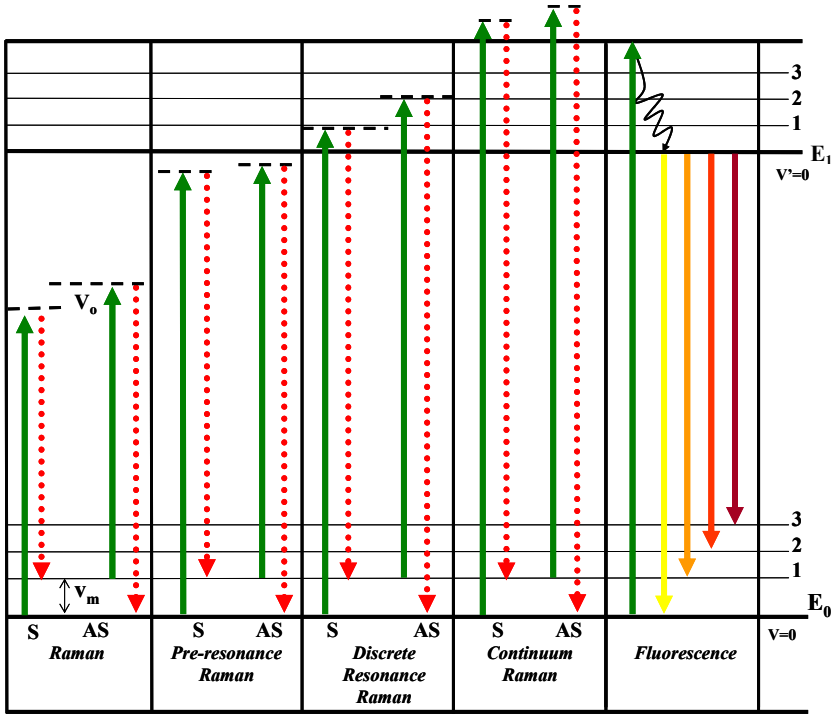


Figure 1.3 Energy levels for conventional Raman, pre-resonance Raman, discrete resonance Raman, continuum Raman, and fluorescence processes. (Stokes (S) and Anti-Stokes (AS)).

discrete Resonance Raman and fluorescence are approximately 10^{-14}s and 10^{-8} s, respectively. Thus, the rejection or reduction of the fluorescence, often at the expense of the signal intensity, is achieved either by charge-coupled device (CCD) with nearly femtosecond gating or a tunable lasers with either UV or NIR wavelengths. Pre-resonance and discrete resonance Raman permit the detection of analytes at nearly nanomolar concentrations and are particularly useful when studying the metal-ligand chromophores in biological molecules. When the incident photon energy is greater or equal to the dissociative continuum of the analyte, the process is known as continuum resonance Raman scattering. As with the discrete Resonance

Raman method, the enhancement of Raman intensities for discrete spectral bands can be orders of magnitude greater than conventional Raman scattering.

Wave Model of Raman Spectrometry

The phenomenon of Raman scattering can be described by a wave model that is an extension of a quantum mechanical model.[10] In this model, the Raman-active vibrational modes are associated with a change in the polarizability of the molecule. The incident photon inelastically collides with molecule, energy is transferred between photon and molecule, and the incident photon is scattered such that there is a change in the energy of the photon per the equation, ($E_{scatt} = h\nu \pm \Delta E_{vib}$). The incident photon has an associated electromagnetic field (EMF), such that the oppositely directed forces of the EMF are experienced by electrons and protons of the molecule. Therefore, the electrons and protons are displaced away from each other, which briefly polarizes the molecule, and a transitory dipole moment is induced. This process can be described by:

$$\mu = \alpha\ E \qquad \text{Eqn. 1.2}$$

where:

μ = induced dipole moment

E= electric field of the incident radiation (laser beam)

α = polarizability (deformability of the electron cloud of the molecule due to the electric field)

Polarizability can be described as a tensor with two Cartesian components (the incident and scattered photons) connected by a single quantum mechanical event. The EMF of the incident radiation oscillates over time according to the equation

$$E = E_0 \cos(2\pi \upsilon_{inc} t) \qquad \text{Eqn. 1.3}$$

Such that:

E_0 is the maximum amplitude of the incident electromagnetic field

ν_{inc} = frequency of the incident radiation

t = time

Since the molecular vibration is slower than that of the incident radiation's EMF oscillation, the amplitude of the induced dipole moment (μ) becomes a modulated wave that matches the frequency of the external field given by combining equations 1.2 and 1.3.

$$\mu = \alpha E_0 \cos(2\pi \nu_{inc} t) \qquad \text{Eqn. 1.4}$$

Equation 1.4 provides the estimate of the overall deformation of the molecule with the incident EMF. Therefore, polarizability (α) and the amplitude of the incident EMF can be represented as harmonic functions and μ is comprised of several frequency components.

Polarizability (α) does not have a constant value. Certain vibrational and rotational modes will vary with and by α. The geometry of the molecule and, subsequently, the electron cloud can be compressed and extended during the vibrations, which, in turn, alters the polarizability. This is most easily visualized with diatomic molecules where the internuclear distance varies with the vibrational movement. Overall

polarizability (α) is a system of coefficients that establishes a direct relationship between the induced dipole moment and the electric field. For small displacements, a Taylor series can be used to expand the polarizability equation.

$$\alpha = \alpha_0 + \frac{\delta\alpha}{\delta Q} Q + K \qquad \text{Eqn. 1.5}$$

Where:

α_0 = equilibrium polarizability

Q = a normal coordinate

$\frac{\delta\alpha}{\delta Q}$ = the rate of change of the polarizability with respect to Q_{equil}

K= integer

Higher orders in the Taylor series are negligible in the harmonic approximation and are ignored (experimentally, only the first two terms have a strong impact on the results). The Taylor expansion expresses the effect on the molecule's vibrations during an induced dipole due to the electric field (E_0). The coordinate Q, for a diatomic molecule would be the difference between the equilibrium internuclear distance and the internuclear separation. The normal coordinate Q will vary periodically as given by

$$Q = Q_0 \cos(2\pi\nu_{Q\nu} t) \qquad \text{Eqn. 1.6}$$

Q_0 is a constant and is the maximum value for Q, the maximum internuclear distance. The frequency of the normal coordinate vibration is given by $\nu_{Q\nu}$. Substituting equation 1.6 into 1.5 gives

$$\alpha = \alpha_0 + \frac{\delta\alpha}{\delta Q} Q_0 \cos(2\pi\nu_{Q\nu} t) + K \qquad \text{Eqn. 1.7}$$

By substituting equation 1.7 into equation 1.4, an expression of the induced dipole moment (μ) is derived.

$$\mu = \alpha E_0 \cos(2\pi v_{inc} t) + \frac{\delta\alpha}{\delta Q} Q_0 E_0 (\cos(2\pi v_{Qv} t))(\cos(2\pi v_{inc} t)) \quad \text{Eqn. 1.8}$$

Applying the trigonometric half-angle angle identity ($\cos x \cos y = \frac{1}{2}[\cos(x+y) + \cos(x-y)]$) to equation 1.8 results in

$$\mu = \alpha E_0 \cos(2\pi v_{inc} t) + \frac{\delta\alpha}{\delta Q}\frac{Q_0 E_0}{2}\cos[2\pi(v_{inc} - v_{Qv})t] + \frac{\delta\alpha}{\delta Q}\frac{Q_0 E_0}{2}\cos[2\pi(v_{inc} + v_{Qv})t] \quad \text{Eqn. 1.9}$$

Equation 1.9 describes Rayleigh scattering with the first term, which is at the same frequency as the incident radiation (ν_{inc}). The second and third terms describe the Stokes ($\nu_{inc} - \nu_{Qv}$) and Anti-Stokes ($\nu_{inc} + \nu_{Qv}$) frequencies, respectively. The vibrational frequency of the bond modulates that of incident radiation with respect to internuclear distance and polarizability. When the classical quantum mechanics results for Raman transitions are $\Delta\upsilon = \pm 1$, there is a net change in the dipole moment and the polarizability. When $\delta\alpha/\delta Q=0$, there is no net change in the polarizability of the molecule and thus, the induced dipole is zero, which results only in Rayleigh scattering. The intensity of the scattered radiation is proportional to the ν^4 and E_0^2 . According to classical theory, the oscillating dipole will emit radiation in all directions at the same frequency of that of the dipole moment and incident radiation. The intensity of all the emitted radiation will be proportional to the square of μ ($I \propto \mu^2 = \alpha^2 E_0^2$**),** such that the Rayleigh scattering

intensity is proportional to α^2 and Raman scattering intensity to $(\delta\alpha/\delta Q)^2$. However, this equation predicts that the Anti-Stokes scattering would have a greater intensity than the Stokes-shifted scattering. This simplified equation does not take into account the Boltzman distribution, which is a statistical description that the greatest population of the molecules is in the ground state.

$$\frac{Anti-StokesIntensities}{StokesIntensities} = \frac{(\upsilon_{inc}+\upsilon_{Qv})^4}{(\upsilon_{inc}-\upsilon_{Qv})^4}\ e^{-\left(h\upsilon_{Qv}/kT\right)} \qquad \text{Eqn. 1.10}$$

Such that:

h = Planck's constant

k = Boltzman's constant

T = temperature (in Kelvin)

The correct ratio of intensities includes the exponential term from the Boltzman quantum mechanical arguments, such the theory then agrees with empirical results. Equation 1.10 accounts for the differences in the intensities of the Stokes and Anti-Stokes Raman bands in the spectrum of Figure 1.4. It is interesting to note that for Surface Enhanced Raman Scattering (SERS), that the intensities of the Anti-Stokes bands can be enhanced through a population pumping effect due to the EMF generated by the incident laser and the rough metal substrates.

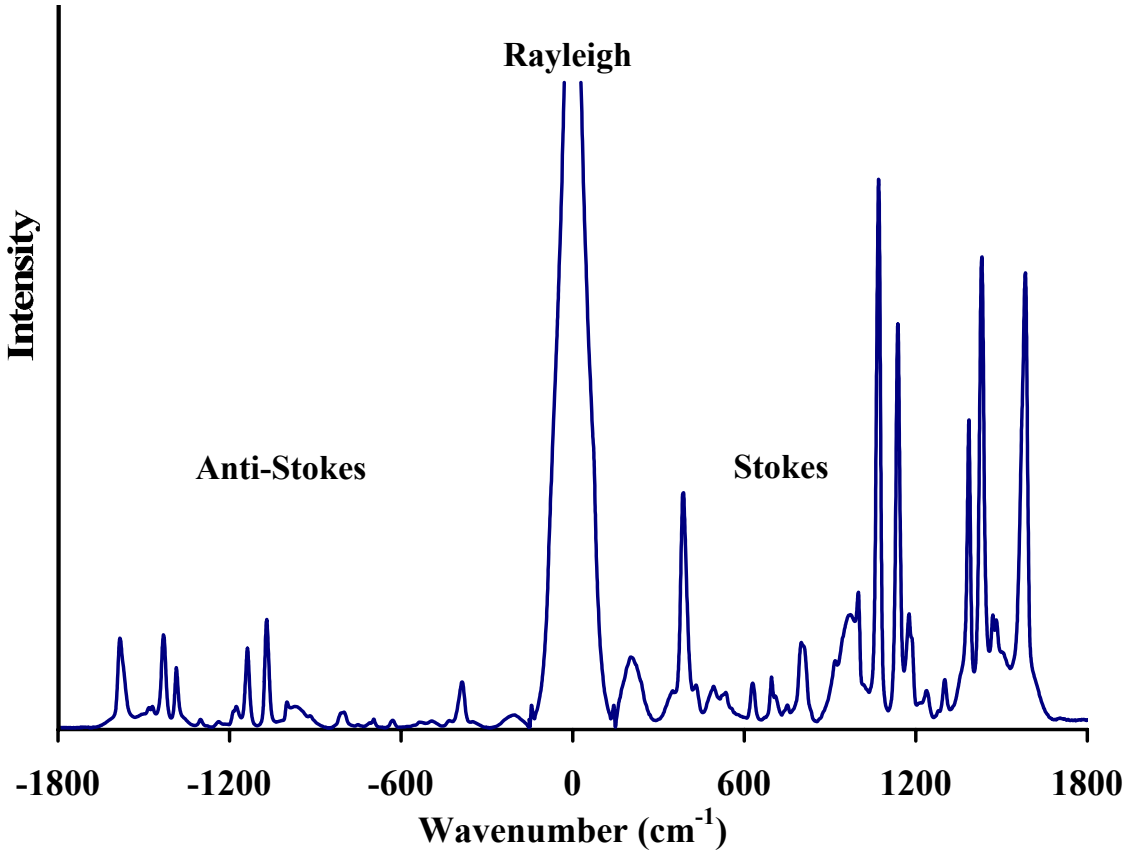


Figure 1.4. Comparison of Stokes and Anti-Stokes for para-aminothiophenol (pATP) on Ag-PDMS SERS substrate.

Raman Instrumentation

Certain limitations have plagued Raman spectroscopy over the last half century, such as detection limits and low sensitivity. These issues have been addressed by improvements in its instrumentation.[8, 10-18] Figure 1.5 illustrates the basic components of a Raman instrument: an intense source of radiation at specific wavelength, a sample illumination and collection system, a spectrometer/ wavelength selector, and an appropriate transducer and computer processing system per the application. Due to the weakness of the Raman scattered intensity, each the performance characteristics of each component must be chosen based on their inherent sensitivity and length of time for the collection of a full spectrum. From sources to transducers, Raman systems have been transformed by the emergent technology from other fields. The development of superior dispersive elements, holographic notch filters, and confocal microscopy have improved the sensitivity and through-put of the instrument. The progression from bench-top to field-ready instruments continues to rely on improvements in ruggedness and reliability, miniaturization of electronic components, and stable, efficient, and intense sources.

Sample preparation for Raman is considered much simpler than IR. Small micrometer-sized pieces of solid materials and films of liquids and solids can be directly probed without prior preparation. Glass and quartz cells can be used for gaseous and liquids samples, including aqueous solutions. However, the surfaces of these cells need to be free of dust particles to prevent spectrum from being masked the Tyndall effect,. Fiber optic probes can be used for direct remote sensing, including vertical surfaces. With the appropriate hot or cold stage apparati, the organization (and reorganization) of crystal lattice structures can be interrogated.

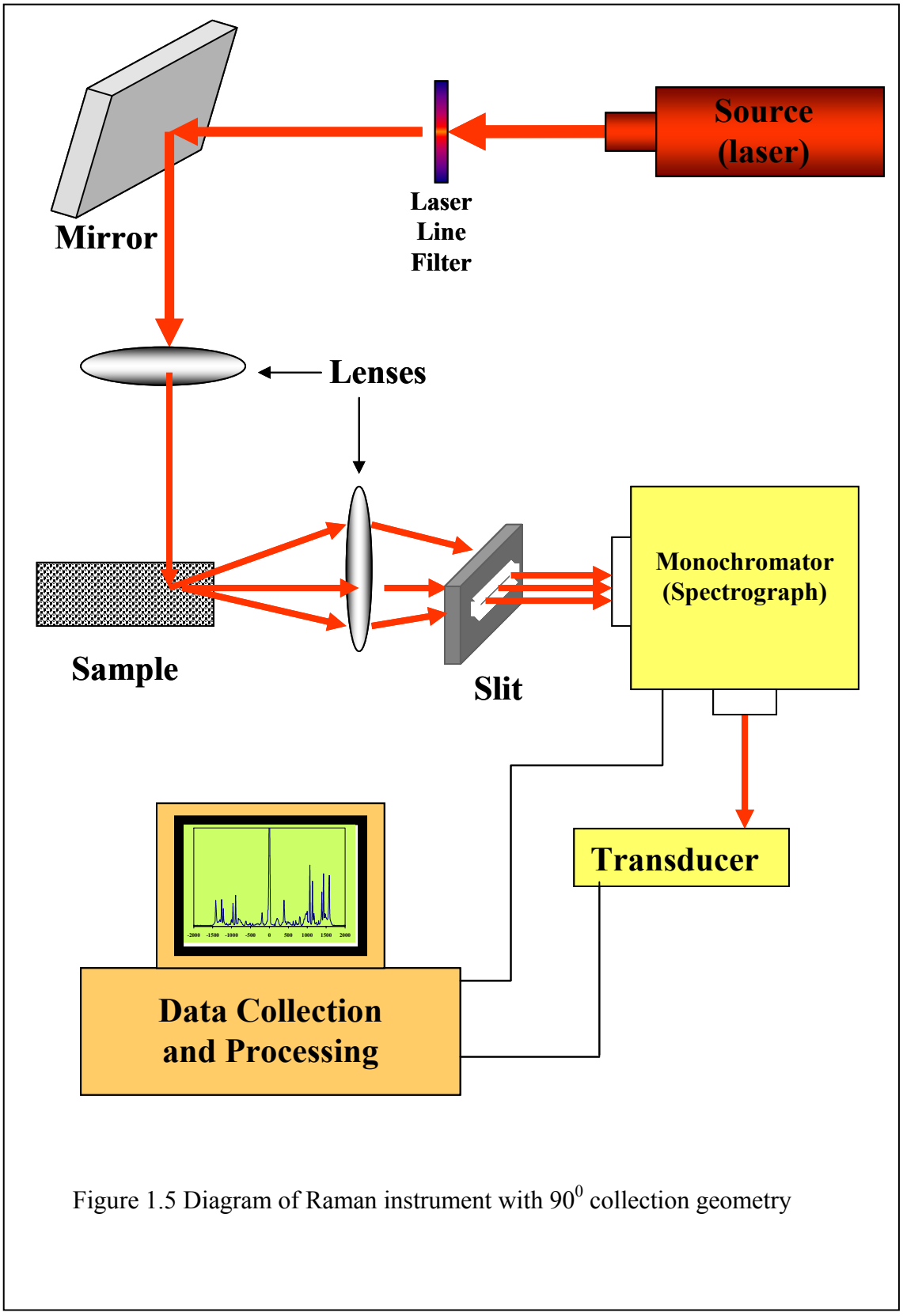


Figure 1.5 Diagram of Raman instrument with 90^0 collection geometry

Sources

C. V. Raman's original instrument utilized a mercury arc lamp as the source. It provided a very intense source with well-defined lines that could be filtered with glass plates. However, many of these bands are close to electronic transitions and fluorescence was an inherent problem. The advent of lasers in the 1960's revived the field by providing stable, coherent, intense sources that did not approach these electronic transitions.[7, 8, 19] Five of the standard lasers now incorporated into instruments, the year of invention, the inventors, and the wavelengths most commonly utilized for Raman spectroscopy are shown in Table 1.2.

Raman scattering varies with ν^4. Traditionally, the argon and krypton lines in the blue and green region of the visible spectrum have been used since they provide a much more intense line than that of a He-Ne laser at the same wattage.[10, 20] This can be very useful for far-from resonant materials which are colorless and are thermally and photolytically stable. As the laser wavelength approaches the near-infrared (NIR), the

Table 1.2 Common lasers for Raman Spectroscopy

Type of Laser	Inventor	Wavelength(s) (nm)
Argon ion (1964)	William Bridges, Hughes Labs	488.0 or 514.5
Helium-Neon (He-Ne) (1961)	Ali Javan William Bennet Jr. Donald Herriot, Bell Labs	632.8
Krypton ion (1964)	William Bridges, Hughes Labs	530.9, 647.1, 676.4
Diode (1962)	Robert Hall, General Electric Labs	782 or 830
Nd/YAG (1965)	J E Geusic H M Markos L G Van Uiteit, Bell Labs	1064

intensity of Raman scattering decreases but the incidence of fluorescence also decreases from both the analyte and the matrix. NIR lasers can often be used at much high powers, however, in certain cases the potential for thermal damage must be accounted for, especially when working with polymers or other photolytically sensitive material.

Transducers

Photomulitplier Tubes. Photomulitplier tubes (PMT) were widely used before the commercial availability of charge-coupled devices (CCD).[11-15] PMTs are highly sensitive detectors for the weak Raman signals. They have relatively inexpensive, wide dynamic range, a linear response, and can amplify signals typically by 10^5 or greater. The weak Raman signals are not swamped by electronic noise from the transducer, have good quantum efficiency, and extremely fast response (1-15 ns) which is necessary since the Raman lifetime is very short. The quantum efficiency (Q.E.) of a PMT (the number of electrons ejected by the photocathode/number of incident photons) is approximately <20% and is wavelength dependant. PMTs are limited by the background noise, dark current noise, of the transducer that can be reduced by Peltier cooling.

These transducers are generally used in a "photon-counting" mode whereby each Raman-scattered photon causes an electrical pulse and is the pulse is measured. This permits the very sensitive discrimination between the dark current noise and the photon pulse, but PMTs can be limited by "pulse pile-ups" for very strong Raman spectroscopic signals. A major limitation of PMTs is that they are single channel detectors. Conventional PMTs can only detect one spectral band pass at a time in the ultraviolet (UV) to blue region of the spectrum. Recent developments for PMTs have enhanced

their capabilities in the red region of the spectrum. Good spectral resolution requires the coordination of the PMT integration time and the monochromator scan rate to optimize the time required to collect a Raman spectrum. PMTs have merit in industrial applications, where often one is concerned quick response times and with a narrow region of the spectrum that is indicative of a specific contaminant.

Photo Diode Arrays. Multichannel detectors were developed to improve the measurement time of a complete spectrum associated with PMTs. A variant of the photo diode arrays (PDA) used for UV-Vis spectroscopy was developed for Raman spectroscopy. By varying the composition of the semiconductor materials, photons with a wide range of energies could be detected. These arrays are arranged linearly on the transducer face and can be electrically charged by to a reverse bias potential by a fast scanning electron beam (vidicons) or they can have on-chip circuitry with amplification by a microchannel plate image (intensified PDA). One PDA can then detect photons from the visible to near infrared (NIR) regions of the spectrum as discrete elements simultaneously. Photons can only be detected by absorption when the energy of the incident photon is greater than the band gap of the semiconductor (the energy difference between the valence and conduction bands) and is greater than the electron affinity (energy required to release an electron from the conduction band into the vacuum). These devices can be used for time-resolved spectroscopy by adjusting the bias of the gating. While these transducers have reduced the time for spectrum measurement, they are less sensitive, much higher inherent noise, are subject to the deleterious effects of silicon as it ages, and they have a more limited dynamic range than PMTs.

Charge-coupled devices. Charge-coupled devices (CCD) have almost completely replaced PDAs as the choice for a detector on most Raman systems. Introduced in the 1970's, they were not commercially viable until the 1990's. Over time, they have proven to be reliable, rugged, and stable. They are comprised typically of a two-dimensional rectangular array of silicon photosites (elements or pixels) on a single chip, typically 512 x 320 pixels. Each element contains two conductive electrodes separated by a thin insulating layer of silica that isolates them from the n-doped silicon substrate and each element surrounded by a non-conductive barrier. These act as capacitors and store the charges when the element is exposed to a photon.

During the collection of a spectrum, the Raman scattered radiation is dispersed over the longest dimension of the chip by a spectrograph or monochromator. Over the course of the accumulation time interval, an element is exposed to incoming radiation and electrons accumulate within the element. This process is often described as an electron well. When the acquisition is completed, the charges from the elements are systematically displaced by a microprocessor in the device via a negative charge applied to the electrodes. This moves the accumulated charges to a shift register located at the end of the array, thus a row by row scan or "bucket brigade" of the transducer is accomplished. The electrons/charges are counted and converted into a measurable voltage that is digitalized and transferred to a readout device.

The CCDs have the multichannel advantages of simultaneous and rapid measurement of a substantial portion of the Raman spectrum (on average ~1000 cm^{-1} wide) and have high quantum efficiency (>20% in the 500-900 nm spectral range and this can be extended to below 200 nm by back illumination or coating with fluorescent

dyes) . The detection area can easily be adjusted per the experimental and instrumental conditions. Although CCDs were designed for the low light conditions, they can be plagued by thermal noise, or dark current noise, from the device itself. To reduce this noise, CCDs are commonly either Peltier or liquid nitrogen cooled.

Pyroelectric Detectors. Fourier Transform **(**FT) Raman instruments commonly use a IR Nd:YAG laser (1064 nm). Most use pyroelectric detectors such as indium-gallium-arsenide (InGaAs) that require cooling, similar to most IR instruments, to reduce noise. The composition of the pyroelectric detectors will determine the reduced long-wavelength cut-off, thus truncating the processed Raman spectrum.

Wavelength Selectors

Line sources, such as the mercury arc lamps, produce a number of wavelengths. Lasers are often considered to be monochromatic, but there can be variations in the linewidth emitted. The radiation emitted from a laser is a narrow continuous group of wavelengths (bands) that are determined by the optical cavity, resonators, and laser medium and are emitted simultaneously by a single laser. The bandwidth of the laser radiation can be narrowed by the insertion of a Fabry-Perot etalon into the optical cavity of the laser itself, which will limit the number of cavity modes oscillating within the laser chamber. Even with Fabry-Perot etalons, all single line lasers exhibit Doppler and other line-broadening effects to some degree. The precise measurement of energy differences intrinsic to Raman spectroscopy requires wavelength line-narrowing of the source and scattered radiation via the rejection of certain. Spectral filters and monochromator gratings can be used to transmit, reject, or reflect selected bands.

Filters. One of the earliest filters, absorbance filters are an inexpensive option for reducing the number of transmitted laser wavelengths and are available for the visible region of the spectrum. These were typically used during the early stages of Raman spectroscopy when mercury arc lamps were used as sources. These filters are typically made from colored glasses or dyed gelatin suspended between two glass plates. This promotes the absorption of portions of the spectrum. Absorption filters are rugged and thermally stable. However, the colored glass absorption filters notoriously fluoresce. Absorbance filter effective bandwidths are generally large, between 30-250 nm. Those filters with the very narrow transmitted bandwidths, generally suffer from very poor transmittance characteristics at the desired wavelengths.

Interference, or laser line filters, are used to reflect unwanted laser wavelength(s) and transmit the desired bands of laser wavelengths in the visible, NIR, and mid-IR spectral regions for the majority of spectrometers.[16, 21-23] Interference filters are comprised of a dielectric layer sandwiched between two layers of metal film covered by glass, quartz, or other transparent material. When a beam hits normal to the surface of the filter, a fraction passes through the first metallic layer while the rest is reflected. Reinforcement of the specific wavelengths and reflection of other out-of-phase wavelengths are reduced via destructive interference. Interference filters are characterized by the narrow transmission of wavelengths and the effective bandwidth determined at the full-width-half-maximum of their transmittance spectrum. Typically, the bandwidths are better than 1.5% of the wavelength with a 10-50% transmittance.

One of the most important revolutions in Raman spectroscopy has been the development of narrow band rejection filters, such as the holographic notch and edge

filters. For both edge and notch filters, the transmission is above 90% at frequencies greater than 400 cm^{-1}. These filters will permit the observation of Raman bands as close as 50 cm^{-1} to the Rayleigh line, although the transmission of the Raman lines will be severely reduced. Holographic filters when combined with single monochromators have an improved through-put of the Raman scattered radiation over spectral rejection systems that require multiple monochromators.

The holographic notch filters (HNF) reject the light from a specific well-defined spectral region, while transmitting all others. With a (HNF), the collected Rayleigh scattered radiation is rejected just prior to the entrance of the spectrograph, while both Stokes and Anti-Stokes shifted lines are transmitted.[16, 21-23] Holographic edge filters pass only the Stokes-shifted Raman radiation, but not the Rayleigh and Anti-Stokes radiation. Holographic filters (HF) are produced by a thin planar film with periodic variations in the refractive index perpendicular to the direction of the film that is deposited on a glass or quartz substrate. These filters are made by illuminating a light sensitive polymer with an appropriate holographic pattern. The laser wavelengths in the near UV to NIR regions of the spectrum require a specialized HF and there are different effective rejection bandwidths (3, 10, or 20 nm FWHM) available and are chosen per the application. Holographic filters are highly susceptible to moisture and thermal damage due to temperatures above 80^0 C for long periods. They can also produce a weak background signal due to fluorescence generation in the polymer film itself, which can be observed when collecting very weak Raman bands. This, however, can be removed by performing a background subtraction.

Atomic vapor-absorption filters can be used as high performance laser filters for tunable lasers. This requires the production of an optically thick metal vapor within an appropriate transparent cell. Absorption of specific wavelengths by the electron orbital transitions in the atomic vapor absorbs the narrow Rayleigh line. However, if the laser or other source frequency shifts, it will pass out of the range of the filter and not be blocked. These filters may have closely spaced absorption bands so that exact tuning can be problematic. A common metal vapor, rubidium, has been used as a tuning media for the tunable Ti: sapphire lasers for the 780 nm line.

Monochromators. Monochromators have rectangular entrance slits that provides a rectangular optical image of the collected radiation, a collimating lens or mirror, a grating or gratings to disperse the collected radiation into its constituent wavelengths via diffration. The first spectral gratings were diamond-scribed flat-glass gratings. Newer monochromators use holographic concave gratings or Echellette-type gratings to eliminate the grating "ghosts" associated with the scribed gratings.

Double and triple monochromators were incorporated into instruments, before the advent of holographic notch and edge filters, to reduce stray light in the spectrometer, reject the laser line from the Raman scattered radiation, and to select the wavelengths of the scattered radiation directed toward the transducer. Early Raman spectrometers often utilized a scanning double monochromator with a PMT for a transducer. The double grating system provided excellent performance (typically ~10^{-10}-10^{-12} reduction of stray light) and have a long focal length (0.75-1.0 m), with a high *f*# (8-10). However, rapid scanning could cause distortions in the spectral patterns.

Triple monochromators can be used in either triple additive or double subtractive modes (Figure 1.6). In the triple additive mode, the first monochromator disperses the collected light and performs the initial stray light rejection. Low frequency bands are generally not detectable in this mode of operation due to less stray light rejection, but subtle chemical shifts and alterations of the band shape are detectable due to the higher spectral resolution. The double subtractive mode uses the first two monochromators as a band pass filter with a variable pass width to reject the stray light. In this arrangement, none of the individual gratings need to have high dispersion characteristics and are applicable for a number of laser wavelengths. The gratings usually have 600-2400 gr/mm, a focal length of 0.5, and are capable of spectral resolution if ~3cm^{-1}. This system of gratings permits the interrogation of the Raman spectrum to within ten wavenumbers of the Rayleigh line. However, the increased number of optics and the lower *f*# of triples, there is a commiserate loss in transmission of the Raman scattering.

Raman Spectrometer Systems

Single channel systems were primarily used during the early part of the twentieth century. As the sources, filters, grating systems, and multichannel detectors became viable, this means of detection was put aside. The goal was to improve through-put, spectral resolution, and measurement time. Below is a discussion of a number of systems that have evolved to answer these requirements.

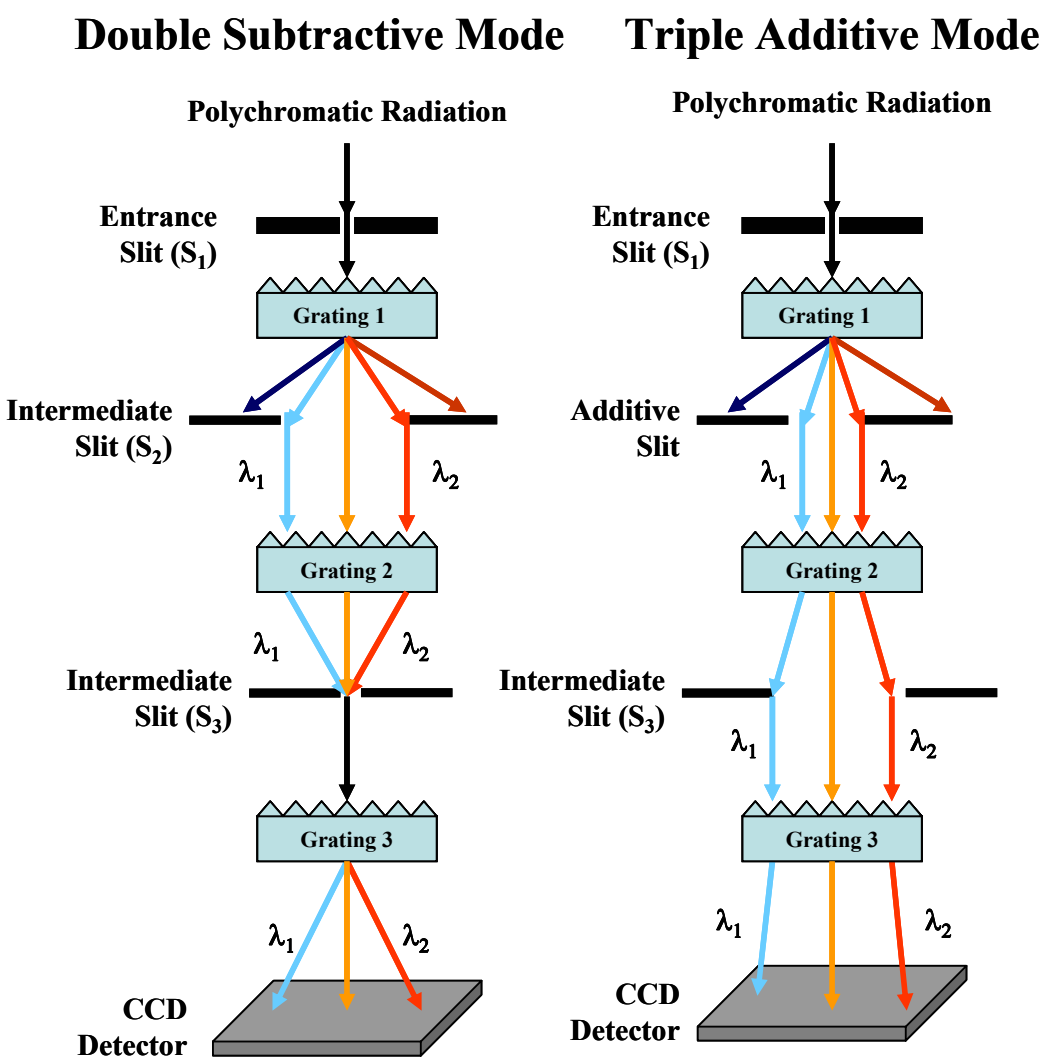


Figure 1.6 Illustration of triple monochromator configurations

Multichannel Dispersive Instruments. By the late 1980's, the triple spectrographs were coupled with the intensified photodiode arrays to create multichannel dispersive Raman spectrometers.[13, 24] These systems permitted the acquisition of a Raman spectrum over a specific wavelength interval. Typically, argon or krypton ion lasers, or helium-neon lasers, where the emitted laser radiation was in the visible region of the spectrum, were used as the sources. Interference filters were used to reject undesirable wavelengths from the laser line to approximately 10 nm (FWHM) of the center line. Power from the lasers could easily be regulated either at the control box or via neutral density filters to prevent damage to the analyte. Groove density and focal length of the spectral grating determine the spectral dispersion for these instruments. An intensified PDA was employed as the transducer.

These dispersive instruments were reconfigured in the early 1990's to include holographic notch filters and CCDs. These greatly improved the measurement time and signal throughput, crucial to SERS and for trace analysis. The first two monochromator stages could be bypassed and a holographic notch filter placed in the path of the incoming radiation to reject the laser line. The transmitted Raman scattered radiation would go through an entrance slit to further collimate the radiation before entering and being dispersed by the third stage monochromator (spectrograph) with a Czerny-Turner configuration. In this way, the Raman radiation was dispersed longitudinally by the grating across the longest axis of the CCD. The resolution of the spectrum was a result of the groove density and quality of the grating and the number of pixels on the CCD's chip. A full spectrum could be collected by adjusting the monochromators to a different setting and overlapping the spectra collected in a multi-window acquisition mode.

The combination of the holographic notch filter and single monochromator lead to the development of field-ready instruments. The sources were no longer the water-cooled noble gas ion lasers, but Peltier-cooled lasers such as the He-Ne and NIR diode lasers. These could then be coupled to fiber optic probes and outfitted with small aspheric lenses. These were typically a bundle of collection fibers surrounding a core illuminating fiber. These unique devices can be used for *in vivo* and environmental studies, process control, as well as remote sensing.

Fourier-Transform Raman Spectrometers. First created in 1984 by Weber, et al in its current commercial configuration, Fourier-transform Raman (FT-Raman) was designed to address many of the same issues as the dispersive spectrometers. They capitalized on the pre-existing software and hardware for FT-IR spectrometers. This instrumental configuration permits the analysis of organic analytes and matrix materials that fluoresce with radiation in the visible region of the spectrum. FT-Raman employs NIR and mid-IR sources prevent the electronic transitions by moving beyond the pre-resonance conditions of these materials. The typical source is a 1064 nm Nd:YAG laser. Similar to an IR spectrometer, the FT-Raman uses an interferometer to disperse the scattered radiation (Figure 1.7). This provides a multiplex advantage, where signals from all the wavelengths are collected simultaneously and permits virtual real-time collection that approaches the shot noise limit. Another advantage is that the amount of signal detected by the interferometer is determined by the entrance aperture. Closing this aperture does not greatly enhance the spectral resolution, as the luminosity of the interferometer is far greater than that of the dispersive systems. In addition to these, the interferometer provides a highly accurate

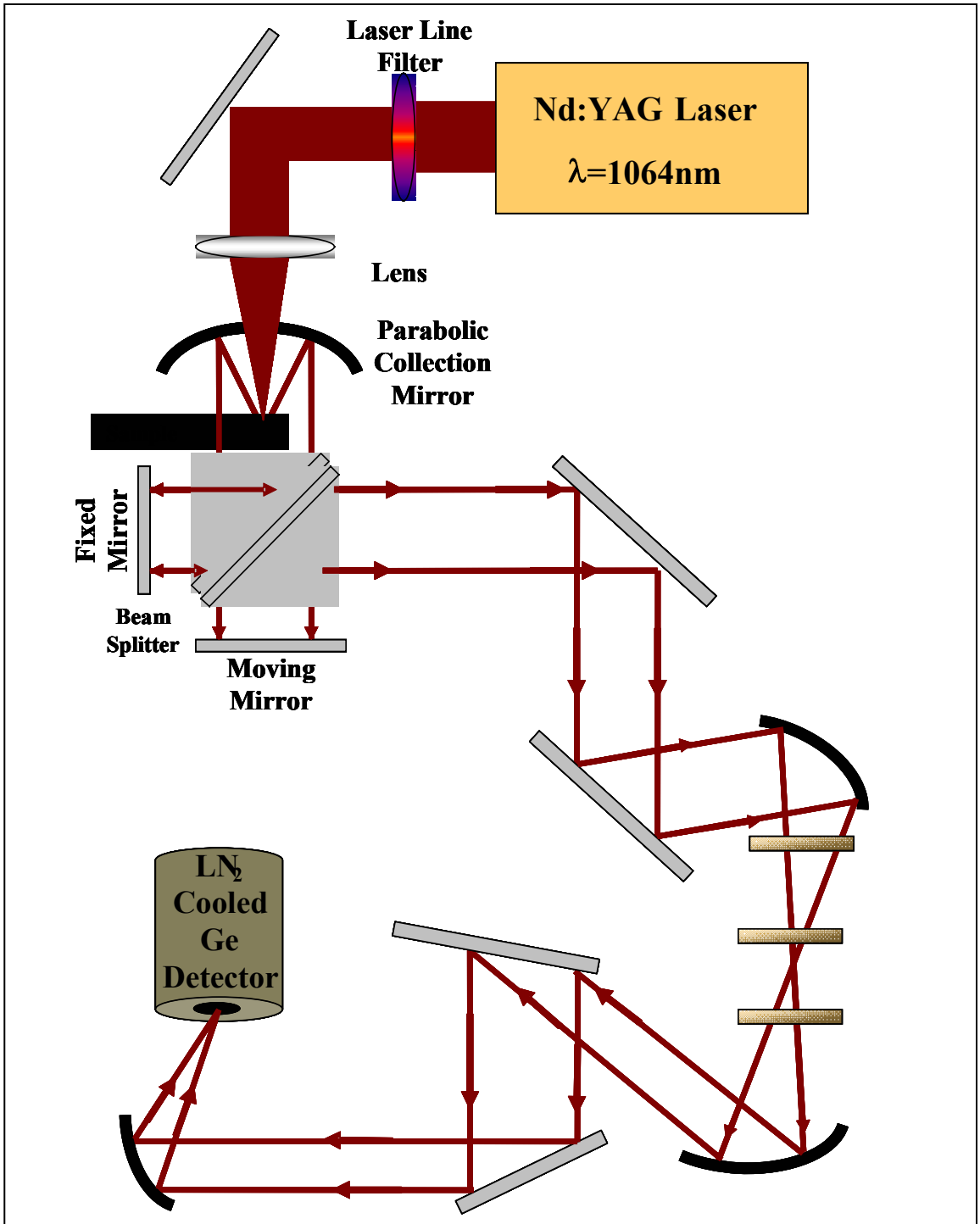


Figure 1.7 Optical diagram of an FT-Raman spectrometer. (Liquid nitrogen (LN_2), Germanium (Ge)).

and precise means of measuring the wavelength, since a He-Ne laser is used as a laser fringe reference. This also allows the direct comparison of spectra and exact background subtraction. The detectors can be multichannel detectors such as liquid nitrogen-cooled germanium transducers, CCDs, or indium gallium arsenide or lithium tantalite pyroelectric transducers.

The ν^4 dependence of the scattering process and the low sensitivity of the pyroelectric detectors can attenuate the overall signal. While the multiplex advantage permits the collection of all the wavelengths simultaneously, shot noise from the entire spectrum tends to be distributed to every spectral element as well. Organic compounds that would otherwise fluoresce with visible wavelength lasers tend to reabsorb the Raman scattered radiation due to an overlap between the Raman emission and the vibrational overtones (1064-1786 nm). Re-absorption of the Raman radiation is most likely when samples are thick and the laser is focused within the sample. In addition, the re-absorption and samples that have high scattering can affect the relative intensities of certain bands and reduce the effectiveness of FT-Raman for quantitative analysis.

Raman Microprobes and Microscopes. Raman microprobes and microscopes can be coupled with most laser sources. One of the earliest discussions of these systems was by Delhaye and Dhamelincourt in 1975. They described a microprobe with a single channel detector, where the diffraction limited laser spot was rapidly scanned back and forth (line-scan), and the output sent to an oscilloscope that was synchronous with the laser scanning. This set-up produced a two-dimensional scan of the sample by translating the sample perpendicular to the line scan while the transducer monitored a specific band of wavelengths.

The microprobe could also be configured with a multichannel detector that also employed the line-scan technique. The illuminated area was imaged onto the entrance slit of the monochromator, set to the Raman wavelength of interest. The axis parallel to the entrance slit of the detector simultaneously detected all of the points on the line. The separate rows of the detector monitored a different point on the illuminated line and, similar to the single channel, the sample was translated perpendicular to the direction of the line scan.

Both of types of microprobes monitored a single Raman line of interest and do not collect a spectrum, which is applicable for industrial process monitoring. While the second microprobe has the multiplex advantage, it requires slightly more laser power to maintain high illumination over the area during the line scan. Later generations of the microprobe have incorporated confocal optics to reduce stray light and improve spatial resolution.

Raman confocal microscopy has tremendous power as a sampling device, especially for small, precious samples. It can achieve high spatial resolution. High numerical aperture optics approaches the diffraction limit and ensure that the collection cone is large. The confocal configuration, an adjustable pinhole placed before the holographic notch filter, limits the amount of radiation collected from the out-of-focus planes and reduces the amount of fluorescence sent into the detector. The laser beam can be focused on the sample anywhere from a Gaussian spot (the diameter of the lens is much greater than the beam diameter) to an Airy disk (the diameter of the lens and beam are equal). Confocal systems were based upon microscopes, thus they utilize an epi-configuration (180^0 collection geometry). Light from the sample is transmitted through

the holographic notch filter to remove the laser line and the Raman radiation is collected onto an entrance slit (open ~100 um). This permits all of the filtered light to enter the multichannel detector, if the monochromator slit is larger than the entrance slit opening, and increases the throughput into the spectrometer.

One version of the Raman confocal microscope that has been available since the early 1990's incorporates infinity-corrected optics and is used for both confocal imaging and mapping procedures. These generally have a single spectrograph (monochromator) with holographic notch filters to improve the throughput of the collected image (Figure 1.8). Samples with complex multiphases can be spatially interrogated with a lateral resolution of about 1 μm and good depth resolution. Matrix materials can be distinguished from the target analyte, which may include areas that fluoresce. Photo-bleaching can be performed before mapping the entire sample to reduce the fluorescence.

The Raman microscope can be configured for global or Airy disk illumination, such that the entire sample is illuminated. Analogous to the microprobes, this configuration monitors only the Raman line of interest. Optical filters, such as acoustic-optic tuning filters (AOTF), liquid-crystal tuning filters (LCTF), and dielectric filters, are used to discriminate this line of interest. These systems are subject to scattered radiation and fluorescence from outside the focal plane that can easily swamp out the Raman signal.

Many of the multichannel instruments permit the collection of a microscopic image of the sample and can collect a series Raman spectra at discrete points on the sample. The sample can be rastered in x, y, and z planes per the users programming. For some instrumental programs, up to three specific Raman bands of interest can be

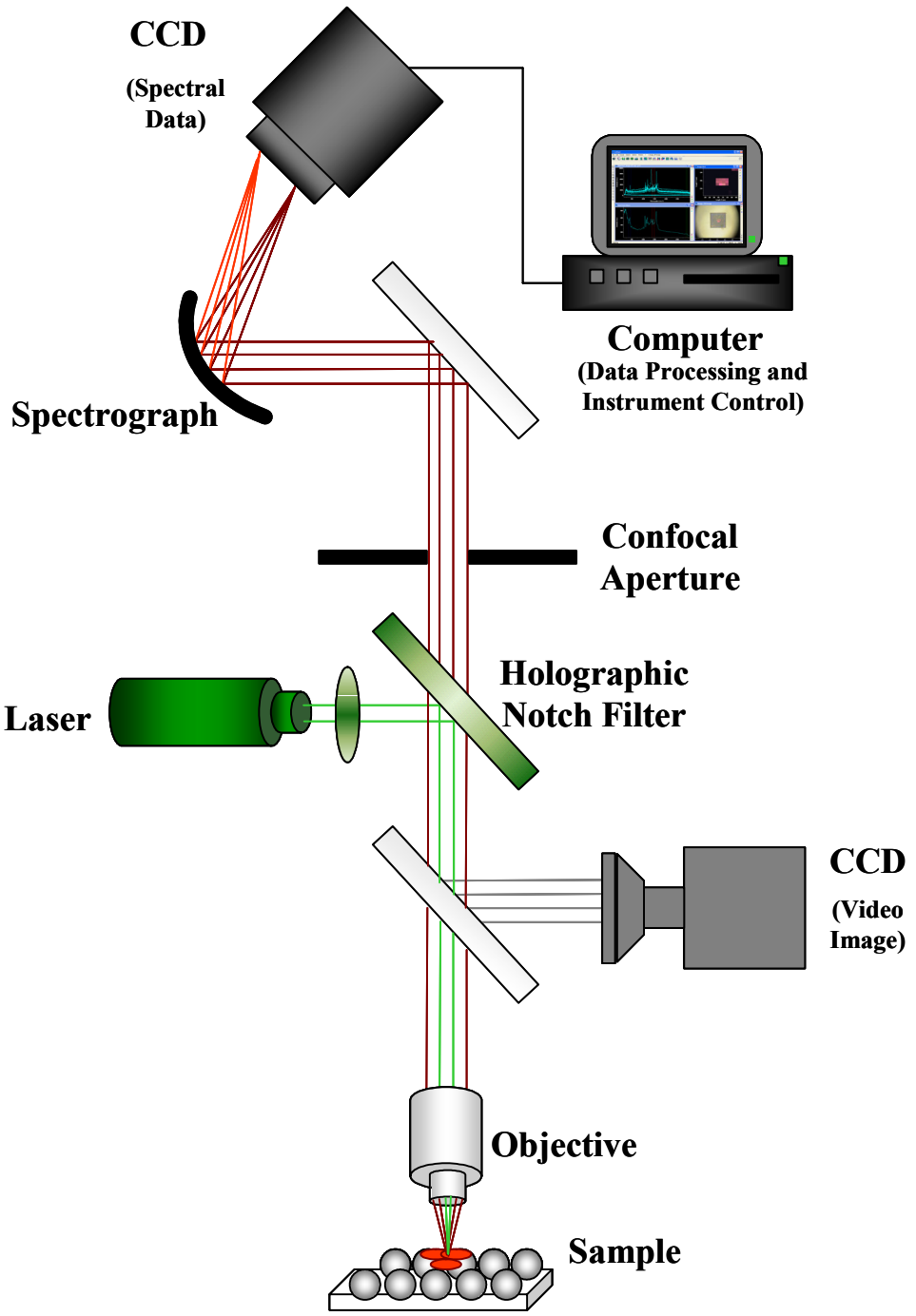


Figure 1.8 Schematic of confocal Raman microscope

monitored simultaneously and the areas of greatest intensity can be overlaid onto the microscopic image for correlation of the chemical nature of the sample on both the surface (x and y) or within the sample (z) (Figure 1.9). Similarly, the global mapping with the optical filters can also produce the correlated image spectra, however, the time for measurement is much longer. This technique is an excellent tool for in vitro cell studies, semiconductor material, alloys, and polymeric blends. The confocal Raman microscopes have been successfully coupled with SERS for both the characterization of SERS substrates, trace analysis, and single molecule detection.

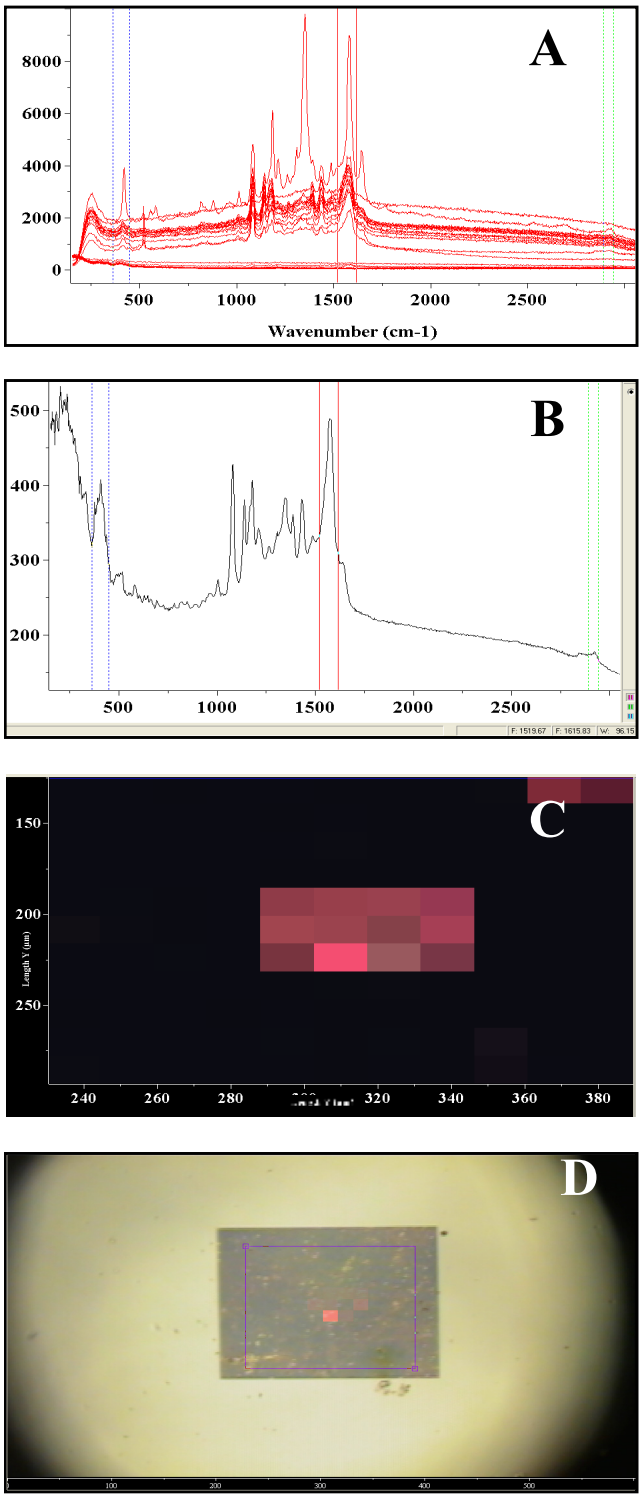


Figure 1.9 Example of Raman mapping of silver-coated nanogratings and pATP. A) All spectra collected at discrete points in two dimensional array, B) Mean of all spectra, C) Raman map for band centered on 1600 cm^{-1}, D) Overlay of Raman map onto the video capture image of the nanogratings

References

(1) Smekal, A. *Annalen der Physik (Berlin, Germany)* **1926**, *81*, 391-406.
(2) Smekal, A. *Annalen der Physik (Berlin, Germany)* **1928**, *87*, 959-964.
(3) Smekal, A. *Naturwissenschaften* **1928**, *16*, 612-613.
(4) Raman, C. V. *Nature (London, United Kingdom)* **1928**, *121*, 619.
(5) Raman, C. V. *Transactions of the Faraday Society* **1929**, *25*, 781-792.
(6) Raman, C. V. *Philosophical Magazine (1798-1977)* **1929**, *7*, 160-161.
(7) Coates, J. *Applied Spectroscopy Reviews* **1998**, *33*, 267-425.
(8) Hathaway, C. E. *Raman Eff.* **1971**, *1*, 183-285.
(9) Kneipp, K. *Single Molecules* **2001**, *2*, 291-292.
(10) Delhaye, M.; Merlin, J. C. *Biochimie* **1975**, *57*, 401-415.
(11) Adar, F. *Practical Spectroscopy* **2001**, *28*, 11-40.
(12) Adar, F.; Geiger, R.; Noonan, J. *Applied Spectroscopy Reviews* **1997**, *32*, 45-101.
(13) Chase, B. *Applied Spectroscopy* **1994**, *48*, 14A-19A.
(14) Chase, D. B. *Chemical Analysis (New York, NY, United States)* **1991**, *114*, 21-43.
(15) Colthup, N. B. *Guide Mod. Methods Instrum. Anal.* **1972**, 195-229.
(16) Davis, K. L.; Tedesco, J. M.; Shaver, J. M. *Proceedings of SPIE-The International Society for Optical Engineering* **1999**, *3608*, 148-156.
(17) Eastwood, D.; Lidberg, R. L.; Simon, S. J.; Vo-Dinh, T. *Environmental Science Research* **1991**, *42*, 97-111.
(18) Felidj, N.; Bernard, S.; Bazzaoui, E. A.; Levi, G.; Aubard, J. *Chimie Nouvelle* **1998**, *16*, 1895-1905.
(19) Clauson, S. L.; Christesen, S. D.; Spencer, K. M. *Proceedings of SPIE-The International Society for Optical Engineering* **2004**, *5269*, 34-41.
(20) Asher, S. A.; Bormett, R. *Springer Series in Materials Science* **2000**, *42*, 35-54.
(21) Asher, S. A.; Flaugh, P. L.; Washinger, G. *Spectroscopy (Duluth, MN, United States)* **1986**, *1*, 26-31.
(22) Carrabba, M. M.; Rauh, R. D.; Spencer, K. M.; Edmonds, R. B.; EIC Labs, Inc.,Norwood,MA,USA., 1992, pp 8 pp.
(23) Hecht, L.; Barron, L. D. *Journal of Molecular Structure* **1995**, *347*, 449-458.
(24) Weesner, F.; Longmire, M. *Spectroscopy (Duluth, MN, United States)* **2001**, *16*, 68-70,72-77.

Part 2

Surface Enhanced Raman Scattering (SERS): History, Theory, and Substrates

History

In 1974 Fleischman, Hendra, and McQuillan reported that they had produced a Ag electrode with high surface area via electrochemical oxidative-reductive cycling.[1] When pyridine was adsorbed onto the surface, an unusually strong signal occurred, approximately a 10^6 fold increase in signal intensity, as compared to standard Raman spectrum of pyridine in either gas phase or non-adsorbed molecules. It was initially attributed to the increased surface area providing the means for additional pyridine molecules to be adsorbed, thus creating a higher surface density of the pyridine.[2] As a result pyridine became one of the "gold standards" for future SERS investigations. The researchers initially hoped that this new techniques would permit Raman be accepted for trace analysis, general chemical analysis, and for environmental and biological studies.

The teams of Van Duyne and Jeanmarie and Creighton and Albrect published simultaneously in 1977 that the effect was not due strictly to the increased surface area.[3] The Raman intensity was found to be 10^5-10^6 times greater than simple calculations would have predicted for the Raman cross-section of pyridine. It was determined that the increased intensity was due to an enhancement of the Raman scattering efficiency, thus, was termed surface enhanced Raman scattering (SERS).

SERS stimulated interest in electrochemistry,[1, 4-18] charge transfer mechanisms,[19-33] chemical aspects of the effect,[5, 7, 34-45] and in metal[26, 46-69] and non-metal colloids[36, 70-73]. It spawned research into classical electrostatic and electromagnetic theories, in particular, as it is applied to small particles,[53, 74-85] the optics of small and single particles,[74, 76, 86-89] surface-photon interactions,[80, 90-92] surface plasmons (SP).[93-103] Additional investigations

were conducted into the optical properties of gratings and regular arrays of metal particles,[83, 93, 104-130] with specific concentration on the interaction of these with the molecules adsorbed or in close proximity to them.

By the mid 1970's to early 1980's, the field began to wane, despite numerous research groups exploring the theoretical aspects of SERS, as SERS had not resulted in hoped for practical applications. The technique was limited initially by the small number of molecules that could be studied, these being mostly aromatic hydrocarbons, laser dyes, or highly polarizable molecules. The electrode substrates had limited concentration ranges, approximately 10^{-1} to 10^{-3} M, which were still well above the goal of trace analysis.

Around 1985, a renaissance of SERS had begun. Physical vapor deposition of coinage metals (Ag, Au, and Cu) onto non-SERS active substrates, such as semiconductors began in earnest.[131-144] Researchers explored Ag and Au electrodes that were electrochemically coated with transition metals such as Ni, Co, Fe, and Pt. In particular, they were interested in the effect of these transition metals and their thickness as an over-coating of the roughened Ag and Au electrodes.[4, 14, 145-153] While thick coatings dampened the SERS effect, it was determined by Weaver, et al that a 3-10 atomic layer coating with minor pinholes provided a unique means to explore the catalytic reactions of these metals and target analytes.[153] By 2001, they overcame the pinhole problem by improving the electrochemical deposition recipes and parameters, often by redesigning the solutions and wave patterns used during the oxidative and reductive cycles. Weaver's group produced ultra-thin films of semiconductors, oxides, and polymers, as well as, the transition metals over SERS substrates. This extended the

capabilities of SERS to study of the behaviors of ultra-thin films in ways that were not possible with conventional Raman.

The research investigated the substrate architecture. Physical, or thermal, vapor deposition (PVD) of metals opened new avenues for SERS substrate production. Roughness of the metal, on the scale of ~50-200 nm for Au and Ag, had been determined as a key to SERS activity. The roughness is generated by adatoms, adclusters, dislocations, and vacancies at the atomic level. Metals could be easily deposited onto a myriad of solid substrates such as glass, frosted glass, quartz, mica, graphite, metals, silicon, gratings, lithographically produced arrays, and polymers. One of the earliest was the vapor deposition of metal onto a monolayer of polystyrene nanospheres coated on quartz slide.[154, 155]

Other groups began to revive what was considered the nearly dead field of colloids.[8, 37, 143, 156-167] Early attempts at colloid preparation suffered from inhomogeneous particle size distribution.[168-175] Over time, direct control particle size and shape via sample preparation, and therefore, the surface plasmon resonance, has been achieved (Figure 2.1). These nanoparticles could be used in solution or applied to a solid surface such as glass and chromatographic or photographic papers via nebulization or drop and dry techniques.

However, the non-uniformity of SERS substrates continues to be a crucial issue that affects the applicability and acceptance of SERS. Inhomogeneous substrates, such as electrodes, colloids, and PVD, produce areas with highly localized areas of great

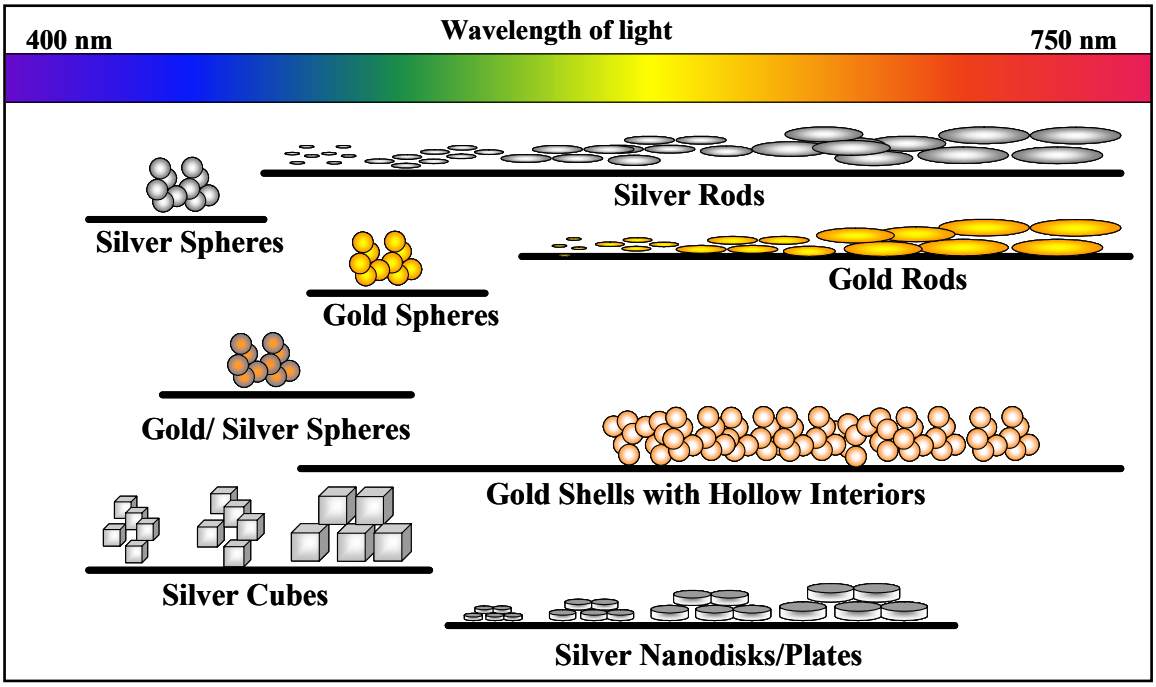


Figure 2.1 Illustration of the unique morphologies and compositions of colloids that have been produced. The surface plasmon resonance for these colloids is located in the visible region of the spectrum and is dependent upon the size and shape of the nanoparticles.

enhancement, also known as hot-spots. Research continues to probe the phenomenon of hot spots, hot nanoparticles, active site, and "blinking". [30, 172, 176-186]

Mathematical models based on the theories of Mie and Maxwell have been developed to describe the optical phenomena associated with PVD and colloid SERS substrates and to guide the iterative process of development.[84, 88, 94, 187-192] Single nanoparticles, dimers, clusters, and aggregates have been characterized by AFM, TEM, and NSOM to correlate the findings of the models and calculations.[56, 60, 61, 65, 69, 80, 88, 193-206] Size, proximity, and shape of the nanoparticles themselves have been explored as parameters that affect SP generation for specific wavelengths.[85, 125, 169, 170, 172, 195, 207-212] It is generally agreed that Ag can be used with a wide range of analytes and exhibits a

highest degree of SERS activity, especially particles with 90 nm diameter and with a spacing of ~5 nm between particles.[213-216] However, Ag substrates are easily oxidized and do not remain active for long periods, in addition, Ag can act as a catalyst for certain analytes.[213-216] Au is nearly as SERS active when the particles are in the 60 nm range with similar spacing and Au exhibits unique affinity for amine, imine, and nitro functional groups.[158, 189, 217-223] This makes it particularly attractive for biological and cellular investigations without the potential for apoptosis. Recently, the alkalis have shown that they may have greater long-term potential, such that they may eventually rival or exceed Ag for practical applications, due in part to a chemical enhancement factor and the potential of "Click-type" chemistry.[224-228]

As discussed in the first chapter, the development of the holographic notch filter with a single spectrograph configuration, as well as, the confocal Raman microscopes improved the throughput of the Raman scattering and it sensitivity. It became possible to work with nearly nanomolar concentrations for most analytes and for some the drive toward single molecule (SM) detection had begun.[92, 180, 184, 229-238] Enhancements of on the order of 10^{14}-10^{15} have been reported with SM for analytes located on or near or "hot spots".[92, 179, 180, 182]

With continued research and development of SERS substrates, the technique has studied heretofore unsolvable problems in electrochemistry,[1, 4-7, 9, 11, 14, 27, 152, 239-249] environmental chemistry,[178, 250, 251] catalysis,[44, 213, 214, 228, 252-257] and others areas under ambient, ultra-high vacuum,[258-263] and cryogenic conditions.[142, 264-269] Electrochemical, biological, and other interfaces were developed as diagnostic probes for molecular structure, orientation of the molecule on or near the SERS substrates,[270-278] charge

transfer,[19, 20, 22, 25, 27-29, 32, 279-283] and for reaction by-products and degradation by-products that are formed due to adsorbate/metal interactions.[131, 134, 284, 285] Researchers have begun to address the issues of the figures of merit for SERS and the homogeneous analyte environments so that it may become an accepted analytical technique. [154, 286, 287]

SERS Theories

While SERS has grown as a technique, there still does not exist a consensus as to the exact mechanism behind the phenomenon. This next section will offer an overview of the two main theories have been put forth to explain the SERS, but should not be considered definitive. The historical electromagnetic (EM) explanation was grounded in the classical optics theory of the early 20th century developed by Maxwell and Mie to explain the behavior of colloids and other small particles.[84, 88, 94, 187-192] A more recent and still quite controversial theory, is the chemical enhancement mechanism. This was developed to explain the high enhancment results that contradicted the initial predicted calculated values from early EM theory. A full discussion of these theories can be found in the literature and reviews on the subject.[19, 22, 30, 74, 78, 84, 90, 94, 162, 191, 192, 267, 281, 282, 288-307]

Electromagnetic Theory

Three conditions are necessary, according to EM theory, for strong enhancement of the Raman signal.[78, 90, 94, 130, 291, 297, 308, 309] First, the particle sizes must be smaller than the incident wavelength. As particles approach size of the incident wavelength, all enhancements decrease and eventually cease. Second, the frequency of the incident radiation must satisfy the conditions for surface plasmon resonance. Surface plasmons

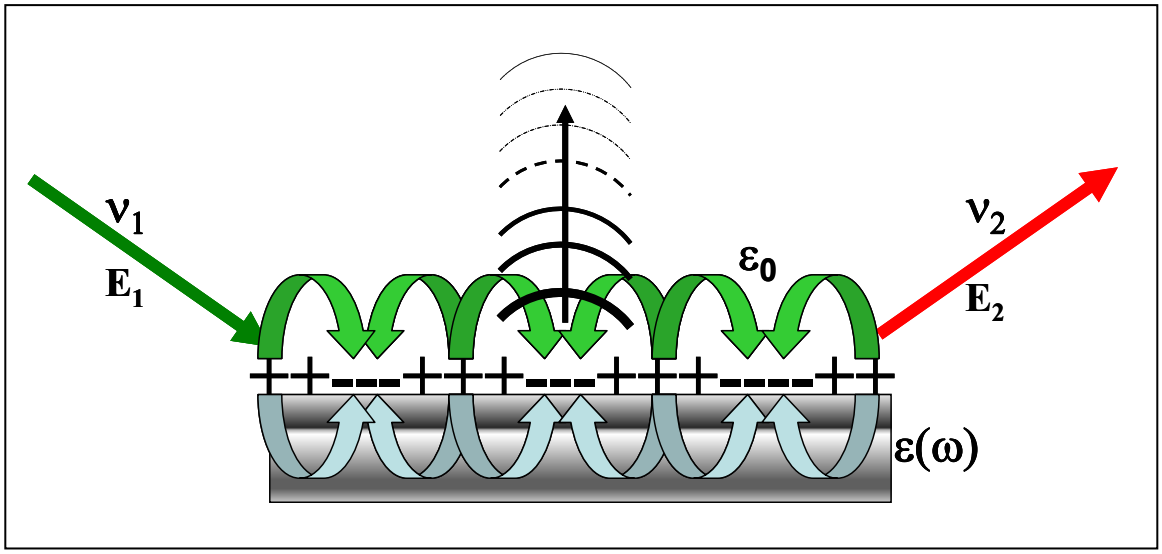


Figure 2.2 Illustration of the charges and electromagnetic field of surface plasmons propagating in the *x* direction on a surface. The electromagnetic field has an exponential dependence and dissipates normal to the surface.

can be excited in the surface of the metal particles and radiate outward as dipolar plasmons that act as a time varying dipole. A fraction of the energy of the dipole is transferred to the surface of the metal particle and will be dissipated as heat when off-resonance. Finally, these fields decay exponentially $1/r^3$ away from the surface, thus a molecule does not need to be in direct contact with the substrate, but if it is too distant from the substrate it will not be enhanced by the EM fields (Figure 2.2).

The incident radiation initiates the oscillation of the surface electrons, a surface plasmon (SP), in the Fermi level, or conduction band, of the rough or nanostructured metal nanoparticles. This oscillation, in turn, produces a large EM field that is localized to the metal nanoparticles and partially polarizes them. The Raman signal is amplified at the SP resonance frequency, which further polarizes the metal and acts as a transmitting antenna. The molecule experiences an EM field that is much larger than the

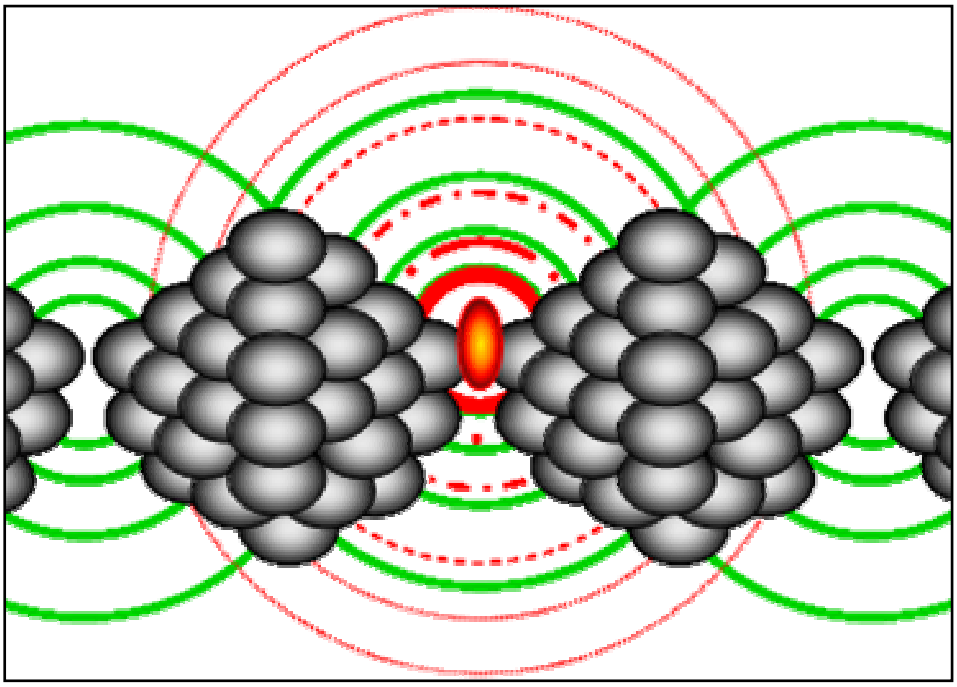


Figure 2.3. Illustration of the electromagnetic enhancement of a "hot spot" or "lightening rod" effect between adclusters. The incident electromagnetic field is shown in green and the induced electromagnetic field is in red.

actual applied field due to large field-induced polarizations and large local fields (localized surface plasmons (LSP)) from the interstices and clefts of the metal nanoparticles. In a similar fashion, the oscillating dipole moment of the molecule at the Raman frequency can polarize the metal nanoparticles. If the oscillation is in resonance with the LSP, there is an additional enhancement of the inelastic scattered photons and is known as the image effect. EM fields can be generated at high-curvature points, e.g. at the tips or near the waist of a prolate ellipsoid or adcluster (Figure 2.3). This is known as the lightening rod effect.[92, 179, 181, 184, 186, 302, 310-316]

Enhancement of the signals can occur without radiation. If an analyte is bonded onto the metal surface, as in a monolayer or more, its inherent oscillating dipole (or

quadrapole) will alter the reflectivity of the metal surface. This will also shift reflected Raman radiation from other sites.

A fundamental knowledge of the generation of SPs can be gained by understanding the propagation of SPs along the bulk surface of a metal. The EM resonance of the flat surface (surface plasmon) has a frequency and momentum parallel to the surface and is described by equation 2.1.

$$\mathbf{k}^2_{\parallel} = (\omega/c)^2 \ \mathrm{Re}\left[\varepsilon_0 \varepsilon (\varepsilon_0 + \varepsilon)^{-1}\right] \qquad \text{Eqn. 2.1}$$

Such that:

$\mathbf{k}^2_{\parallel}$ is the parallel momentum of SP

ω is the frequency of the SP

$\varepsilon(\omega)$ is the dielectric function of the conductor (metal surface)

ε_0 is the dielectric of the ambient surroundings (air, water, solution)

c is the speed of light (2.997 924 58 x 10^8 m/s)

In this equation, both frequency and momentum are conserved when the plane wave that is incident from the ambient dielectric excites the plasmon. Under ambient conditions, either air or vacuum, this condition is not generally met, thus the SP wave is confined to the metal surface and is dissipated as heat, which is why these do not perform well as SERS substrates.

The morphology of a substrate will ultimately affect the generation of SP resonance. Over the last thirty years many groups used Mie and Maxwell's theories to explain their empirical data.[84, 88, 94, 187-192] However, complex surfaces like randomly roughed surfaces are difficult to model due to the potential number of complex

resonances these surfaces can generate. It is also difficult to account for the interactions of these resonances with charged metal particles and the incident plane wave. A fundamental understanding of SERS EM theory, in particular the optical extinction phenomenon, has been derived from the calculations for isolated or small two dimensional arrays with spherical, ellipsoidal, or other simple-geometric particles embedded in a dielectric medium.[130, 317] Other groups have utilized the equations borrowed from the optical properties of two-dimensional gratings as another means to understand this effect.[288, 289, 318, 319]

When the condition of the Rayleigh limit is met, all dimensions of the particle are much smaller than the incident wavelength, the effective electric field inside the particle (E_{eff}) is related to the applied field (E_{appl}) by equation 2.2.

$$E_{eff} = \frac{1}{1+\left[\varepsilon(\omega)/\varepsilon_0 - 1\right]\alpha} E_{appl} \qquad \text{Eqn. 2.2}$$

Where:

α = depolarization factor that is dependant on shape, but not size

$\varepsilon(\omega)$ = dielectric constant of bulk metal

ε_0 = dielectric constant of the surrounding medium

In the visible region of the spectrum, the dielectric constant of the bulk metal is a complex expression, $\varepsilon(\omega) = \varepsilon_1(\omega) + i\varepsilon_2(\omega)$. Enhancement will only occur when E_{eff} is much greater than E_{appl} and when E_{eff} is at its maximum intensity. This will occur when the conditions required for the generation of surface plasmons are satisfied ($\varepsilon(\omega) = \varepsilon_0(1-\alpha^{-1}) = 0$).

By considering the particle as a small sphere for simplification, the enhancement factor can be written

$$E_{eff} = \frac{\varepsilon(\omega) - \varepsilon_0}{\varepsilon(\omega) + 2\varepsilon_0} E_{appl} \qquad \text{Eqn. 2.3}$$

The surface plasmon resonance will be achieved when the real part of the denominator in equation 2.3 is equal to zero. Thus, the real part of $\varepsilon(\omega) = -2\varepsilon_0$ and E_{eff} will be large only when the imaginary aspect is very small.

The dipole decay law dictates that field will decay exponentially with distance away from the surface of the metal nanosphere. While the molecule will experience the greatest intensity field when in direct contact with the metal nanosphere, enhancement of its signals will occur within a range of distances.

$$E_{metal} = \left[\frac{\varepsilon(\omega) - \varepsilon_0}{\varepsilon(\omega) + 2\varepsilon_0}\right] + \left[\frac{r^3}{r + d}\right] \qquad \text{Eqn. 2.4}$$

Where:

E_{metal} = Effective field induced by the metal nanoparticle

r = radius of the metal nanoparticle

d = distance between analyte and surface of the metal nanoparticle

More recent SERS models are based on spheroids and ellipsoids to characterize random substrates. Spheroidal particles can be prolate or oblate (egg-shaped) ellipsoids. Most coinage metals and alkali metal prolate ellipsoids can have SPs in the visible region and produce SERS enhancement. This is done by adjusting the size and aspect ratios of the spheroids. Individual particles will have two distinct peaks in an extinction spectrum from the incident and Raman scattered radiation. The separation between the two peaks

is the difference in energy that corresponds to the frequency of the vibrational mode produced by the Raman scattering. The spectrum will be become much more complicated, especially if the surrounding media has a dielectric greater than one and is a finite thickness.

A more accurate determination of the EM fields near the surface of a small prolate spheroid was completed by Zeman and Schatz.[90] They established the optimal sizes and shapes for ten metals in Groups 1, 11, 12, and 13 as a function of the excitation frequency. These spheroids had an aspect ratio of b/a, where b was the major axis along which the incident radiation was coupled. Molecules of the analyte were randomly distributed over the surface of the molecule so that an average enhancement (R(ω)) using the EM field peripheral to the spheroid (E_{out}) could be determined by equation 2.5.

$$R(\omega) = \frac{\left\langle \left| E_{out,b}^2 \right| \right\rangle}{E_0^2} \qquad \text{Eqn. 2.5}$$

The Raman enhancement, $R(w, w_s) = R(w)R(w_s)$, is the product of the enhancement from the EM field generated by the Stokes shifted frequencies and the incident radiation frequency. When the field is uniformly distributed inside a spheroid with three axes, under the same conditions as above, the subsequent field will be

$$E_{inside,\xi}(\omega) = E_{0,\xi(\omega)} \frac{1}{1 + [\varepsilon(\omega) - 1]\alpha_\xi} \qquad \text{Eqn. 2.6}$$

where ζ = the axes a,b,c.

When a molecule is very distant, the field distribution is the combination of the applied field and the induced dipole at the center of the spheroid. The most interesting

effect seen with these prolate spheroids occurs just outside of their metal tips. The lightening rod effect can be described by

$$E_{outside,\xi(\omega)} = \gamma E_{dipole,\xi(\omega)} + E_{0,\xi(\omega)} \qquad \text{Eqn. 2.7}$$

where the EM field of the dipole (E_{dipole}) is based on the major axis and on a lightening rod factor (γ) that describes the concentration of the field at the tip of the spheroid.

$$\gamma = \frac{3}{2}\left(\frac{b}{a}\right)^2 \left(1 - \alpha_\xi\right) \qquad \text{Eqn. 2.8}$$

This factor increases almost exponentially with an increase in the aspect ratio for prolate spheroids, but only linearly for oblate spheroids. Since only a small fraction of the surface area is bounded by the tips, there is a small quenching of the overall enhancement.

The PVD substrates with random roughness have a wide particle size distribution. Most particles are below the Rayleigh limit and can be accounted for via the aforementioned equations. However, for nanoparticles above the Rayleigh limit, these approximations are no longer valid and more complex calculations are required. In this case the enhancement could be completed by using the computer intensive Lorentz-Mie equations.[318, 320, 321] This treats the molecule as a classical dipole outside of the metal nanosphere that will radiate at a shifted frequency from that of the irradiated by a plane wave. The far-field amplitude of the Raman electric field squared would determine the scattered intensity. This model has worked well for nanospheres, such that it has shown that Ag nanospheres with diameters less than 10 nm will have the strongest SERS enhancement on the order of 10^6 when irradiated with 382 nm light.[322] This may be due to energy losses by the Fermi electrons of the metal as they collide with the surface of the

metal particles due to scattering. As the Ag particles increase in size, the enhancement reduces, the extinction spectrum becomes much broader (due to multipolar SPs), and it is bathochromatically shifted. Above 500 nm, the enhancement is calculated to be only about one to two orders of magnitude in the visible region of the spectrum. For these larger particles, radiation dampening induces losses from the particle dipole's electric field.[75, 323]

Another model looks at spheroids on a solid substrate as hemispherical "bumps", which is similar to what is seen with PVD metal on glass substrates. Under certain conditions the enhancement of a single bump can be up to 16-fold over that of free spheroids. Large groups of hemispherical bumps will have multiple resonances and the SP will shift from the red to the NIR. The extinction spectra will be broad, a "near-continuum" of SP resonance. The EM contribution is calculated to be only about 10^2 (not the 10^6-10^8) for single bumps.[106, 324-326]

More recent models have been developed to mathematically describe the lithographically produced substrates. These permit the probing of particle spacing, size, shape, and dielectric media for two-dimensional arrays. In contrast to irregularly rough surfaces, line gratings and cross-gratings concentrate the scattered intensity to a near diffraction limited maxima. If the aspect ratio of the grating and arrays are increased, light emission and changes in light dispersion will occur. Resonant enhancement alters the electromagnetic field, as was seen with the smooth and rough surfaces and is dependent upon the angle of incidence. If the amplitude of a grating increases, the EM field will be dampened due to radiative losses into the air. However, under very unique conditions, primary SPs can be reflected at the grating interface and the reflected and

primary SPs can couple with each other producing standing waves with specific energy gaps. This inhibits further propagation of SPs along the surface.

Chemical Enhancement Theory

The EM models are responsible for up to 10^{11} increases in the signal enhancement, but this description of the SERS phenomenon excludes the chemical nature of adsorbed molecules. The EM theories describe the nature of the diminishing EM field as a result of proximity to the metal surface; it does not consider the effect of analyte adsorption. This can significantly alter the nature of both the metal substrate and the nature of the analyte and can radically improve the signal enhancement. Several chemical enhancement models, such as charge transfer, atomic roughness, first-layer or short-range chemical effects, have been offered by theoreticians to elucidate these aspects of SERS.[19, 21, 22, 28, 29, 281-283, 327-333]

Charge Transfer (CT) and bond formation between analyte and metal can considerably increase the polarizability of a molecule. This mechanism is associated with an overlap of the electron wavefronts. In this process, a charge can be transferred from the Fermi level of the metal to the lowest unoccupied molecular orbital (LUMO) of the analyte. Figure 2.4 illustrates this effect when the metal is struck by a photon, an electron is excited and can tunnel into the CT state (LUMO) of the analytes. This will form a negative ion of the adsorbate and alter its equilibrium geometry. A retro-donation of the charge from the highest occupied molecular orbital (HOMO) of the adsorbate to the LUMO of the metal can occur due to nuclear relaxation. The excited analyte will emit a Raman-shifted photon and the electron will tunnel back to the metal. Metal

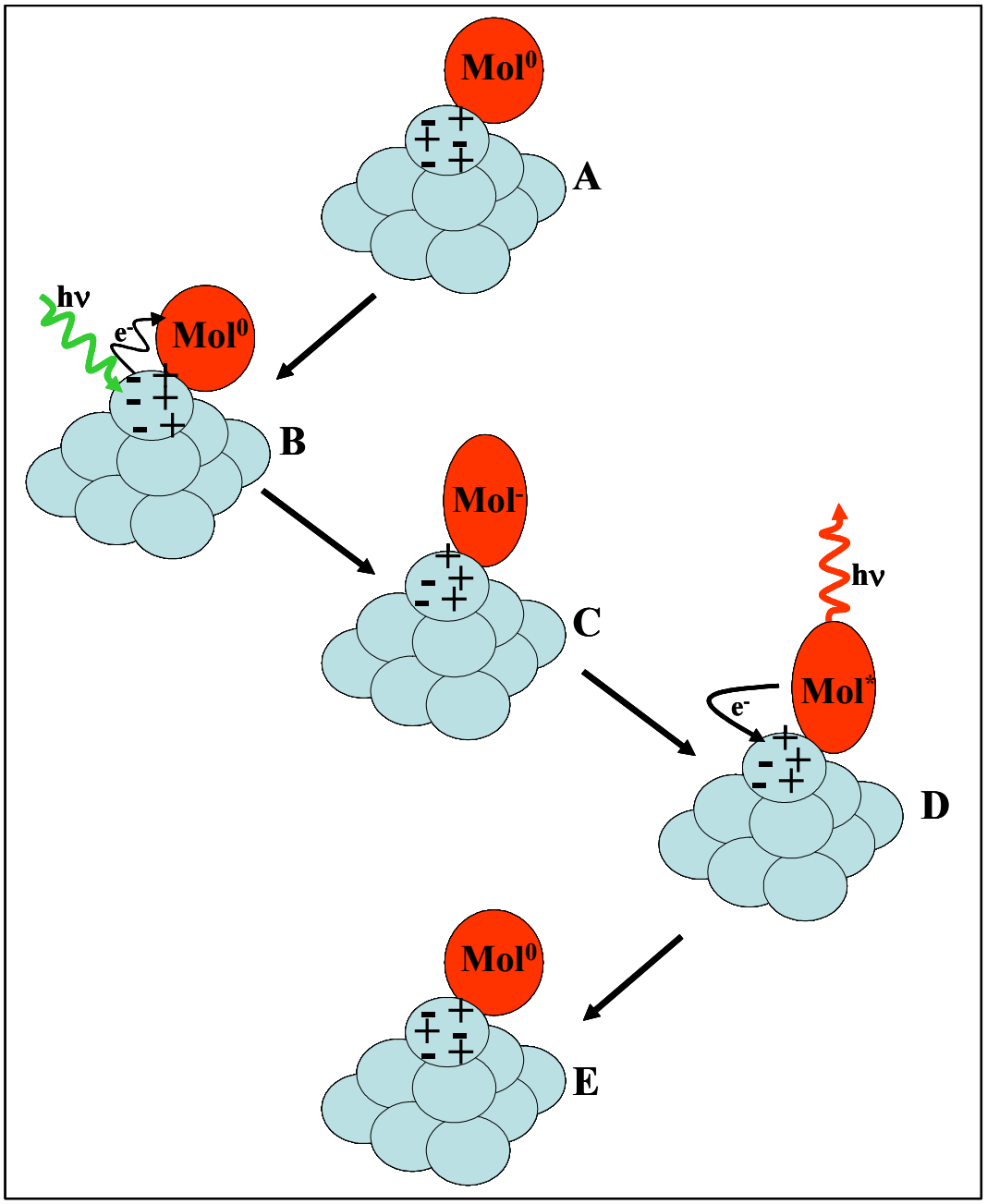


Figure 2.4. Charge Transfer Model is based on an overlap of the HOMO and LUMO of the electron wavefronts for both the adsorbate and metal. A) Molecule adsorbed onto metal surface, B) Electron of metal surface is excited by incident radiation and tunnels into the charge transfer state of adsorbate C) Formation of negative ion of adsorbate with alteration of equilibrium geometry, D) Nuclear relaxation of adsorbate discharges electron back to metal and, simultaneously, emits Raman shifted photon. Equilibrium geometry is re-established, E) Molecule and metal return to neutral state.

substrates have inherent dislocations, defects, and vacancies which provide the sites for adsorption. Atomic-scale roughness (ASR) theories suggest that the formation of adatoms and adclusters may facilitate the CT enhancement phenomenon. It is not restricted to single metal atoms, but up to clusters of 5-6 atoms, a roughness scale much smaller than that of conventional EM theory, which is based on roughness on the scale of 10-100 nm. These loci provide additional momentum for the scattering of electron-hole pairs and relaxation momentum conservation by the ubiety of the adsorbate and ASR. This may affect the interaction of the electrons of the metal and the vibrational modes of the adsorbate.

The chemical enhancement theories are contingent on the adsorption sites, bonding geometries, and the potential overlap energy levels between the adsorbate and metal. The short-range or first-layer effects of increased polarizability of the adsorbate and metal are on the scale of 0.1 to 0.5 nm, or by definition, a monolayer. Thus only a limited number of vibrational modes will experience this form of enhancement. The exact nature of the metal-adsorbate system can affect the degree of enhancement, which has been calculated to be on the order of $10\text{-}10^3$, due to it's a unique electronic excitation spectrum.

Neither the electromagnetic or chemical enhancement theory singularly describe SERS phenomenon; studies have shown that both are factors to the intense enhancements that are seen and that further study is required. However, both models point toward the importance of the conditions that satisfy the generation of SPs as the key to increasing the enhancement by orders of magnitude. Future substrate development will tailor the SP resonance for specific laser wavelengths and ensure identical analyte environments across

an entire substrate by controlling the dielectric materials of the substrates and the shape, size, and proximity of metallic nanoparticles.

Substrates

Since the discovery of SERS more than thirty years ago, the development of substrates has often out-stripped the theoretical modeling. The most common SERS substrates (colloids and PVD substrates) are disordered complex surfaces with often wide particle size and shape distributions. The random nature of these substrates may induce a series of interference patterns that affect the uniform distribution of surface plasmons and the EM field. This complicates the deconvolution and modeling of the multitude of plasmon modes for these inexpensive and relatively dependable SERS substrates.

Hot spots and dampening effects plague most SERS substrates such that spot to spot relative standard deviations (RSD) can approach more than 20% due to their inherent inhomogeneity. Despite the aforementioned limitations, trace analysis and single molecule detection have been demonstrated by many groups for a variety of analytes.[92, 156, 182, 231, 234-236, 238, 287, 327, 334-342] Table 2.1 illustrates the myriad of substrates that have been developed to meet the demands of the growing SERS community. This is not a complete tabulation of all the substrates that have been developed, but it does indicate the ingenuity and resourcefulness of researchers in the field.

Periodic nanostructures produced by electron beam lithography (EBL) and nanosphere lithography (NSL) offer the advantage of controlled array parameters such as size, shape,[84, 90, 170-172, 177, 200, 208, 211, 304, 343-348] geometric pattern,[325, 349] grating constant[126, 181, 304, 318, 350-354] as well as substrate dielectric function.[86, 211, 347, 355-359] These can

Table 2.1 Comparison of SERS substrates

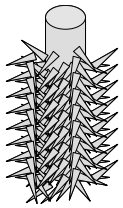
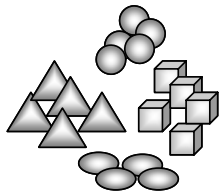
Illustration	Metal	Type	Substrate	Preparation	Comments
	Ag, Au, Pt, and Cu	Etched Metal	Metal Electrodes and flat surfaces	Cyclic oxidation-reduction	First SERS substrate. Inhomogeneous protrusions on the surface of electrode (~25-500nm). Potential can be cycled during SERS to study CT interactions[1, 6-8, 10, 142, 143, 162, 242, 249, 322, 360-367]
	Ag & Au	Colloids	Solution, solid supports, membranes, photographic and chromatography papers	Solution, Drop and dry, nebulization	One of the best SERS substrates. Shape and size are very controllable and do not require specialized equipment. Colloidal solutions can coagulate, which diminishes functionality.[47, 54, 64, 168, 171, 172, 211, 368-379]

Table 2.1 Continued

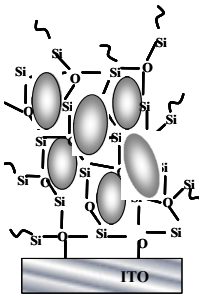
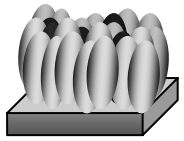
Illustration	Metal	Type	Substrate	Preparation	Comments
	Ag & Au	Sol-gels	Metal colloids in transparent polymer matrix can be spun-coated onto solid support or used as virtual gel.	Hydrolysis and subsequent polymerization of silica precursor..	Used as a selective barrier to prevent oxidation of Ag. Inherently inhomogeneous and irreproducible SERS substrates Porosity and selectivity of polymers are determined by selection of precursors.[375, 380-392]
	Ag	Etched Quartz	Prolate SiO_2 post	SiO_2 PVD and annealed on quartz support PVD Ag is flash heated to form globules of Ag for plasma-etch mask. Substrate is etched with CF_3 and Ag coated for SERS.	A potentially reusable substrate with controlled particle shape. A time consuming process that did not exhibit a high SERS enhancement.[106, 359, 393-395]

Table 2.1 Continued

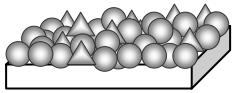
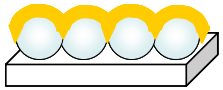
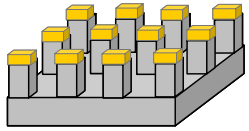
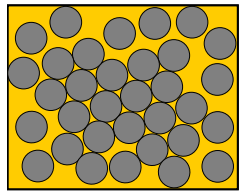
Illustration	Metal	Type	Substrate	Preparation	Comments
	Ag, Au, and Cu	Metal-coated Surfaces	Quartz (untreated and etched), silicon, glass, polymers, membranes, and chromatographic papers	Physical Vapor deposited films	ASR, particle size, and proximity are controlled by deposition rate, film thickness, deposition rate, film thickness, and vacuum pressure and choice of substrate. Most films on solid supports are limited to 10 nm thickness. [132, 134, 139, 147, 150, 224, 287, 341, 342, 396-408]
	Ag, Au, and Cu	Metal-coated Nanoparticle	TiO_2, fumed SiO_2, AlO_2, and other oxides	PVD or spin-coating of oxides and PVD of metal over-coats	Irregular roughness determined by the application process of oxide coating and PVD parameters (deposition rate, film thickness, and vacuum pressure) [401, 409-411]

Table 2.1 Continued

Illustration	Metal	Type	Substrate	Preparation	Comments
	Ag & Au	Metal-coated Nanospheres	Teflon, silica, polystyrene and other polymers	Spin-coated spheres and PVD of metal	Early attempt to produce controlled roughness for substrates. Sphere size and metal thickness affect SERS response. Stronger enhancement than roughened electrodes.[139, 405, 412, 413]
 	Ag & Au	Metal-coated nanostructures	Gratings, cross-gratings, 2-D arrays	E-beam lithography (EBL, RIE, and lift-off techniques) for silicon wafers , spun-coated polymers for imprinting, and nanosphere lithography (NSL)	Uniform 2-D arrays of isolated metal particles.[106, 304, 351, 414, 415] Silicon molds can be used for imprinting polymers.[416-428] NSL: less expensive 2-D array of truncated tetrahedrons (but limited to a single geometric pattern).[113, 114, 129, 429-438]

produce substrates with a high density of comparable analyte environments and provide a means to perform a more direct modeling that may further knowledge about the mechanisms of SERS.[123, 297, 351]

Early attempts at periodic nanostructuring included stochastic silica posts, [106, 359, 393-395] silica nanospheres (Table 2.1), [139, 405, 412, 413] micro-contact printing,[439-442] and covalent tethering of monolayers of colloids.[355, 443-445] These approaches were limited by the instrumentation available at the time, whose resolution was limited to 100 nm.

Calculations by many groups indicate that the field enhancement increases dramatically as the gap between nanoparticles decreases to near molecular dimensions. Meir, Wokaun, and Liao have established via calculations that very strong dipolar interactions for two dimensional square gratings could be tuned by manipulating the grating constant.[446] When the grating constant is slightly above the wavelength of the incident photon, then the substrate will have both an evanescent field and the benefit of the in-phase scattered light field. Additional calculations performed by Garcia-Vidal and Pendry have shown that enhancements can be up to 10^6 for nanostructured substrates.[297] Wei et al has calculated that 2-D Ag nanodisks embedded in dielectric media will yield an average enhancement of 2×10^{11} and 2×10^9 for Ag nanospheres.[130] These are several orders of magnitude greater than disordered substrates at or near the percolation threshold, the point at which a discontinuous metal film become conductive.

The nanosphere lithography technique pioneered by Van Duyne has been used to create periodic SERS substrates, without the costly investment in EBL. [113, 114, 129, 429-438] However, this technique produces nanoparticles whose shape, size, and arrangement pre-determined strictly by the interstices of the nanospheres and with only limited areas of a

monolayer of nanospheres. of the nanosphere. These have produced substrates with particles beyond the optimum spacing.

Figure 2.5 presents several of the most common schemes for producing lithographic SERS substrates. These include etching, lift-off, and imprinting techniques. However, the extreme cost, mostly due to instrumentation and instrument time costs, of EBL has limited its wide spread application for SERS. Previously mentioned, Wei et al have produced Ag nanodisks embedded in a dielectric media by EBL, vapor deposition, followed by etching. EBL has been coupled with reactive-ion etching (RIE) and lift-off by Kahl and coworkers to produce two dimensional ensembles of particles with highly reproducible particle size, shape, and grating constants.[318, 351, 353, 354] Their Au and Ag "cross-gratings" of circular, triangular, and square silver particles have demonstrated the importance of reducing inter-particle distance and the limitation of the instrumentation, however, their resulting spectra are not overly impressive when compared to colloids and thin films.

To date, large substrates (greater than 50 x 50 μm) with homogeneous distributions of very small grating constants and a variety of unique nanoparticle shapes are difficult and very expensive to achieve due to the current limits of instrumentation. In addition, while EBL-RIE substrates are very useful for correlation with SERS mathematical modeling, these produce single application and use substrates.

Silicon wafers coated with polymeric resists can be patterned with EBL and then coated with thin metal films by vapor deposition. These can be employed as reusable SERS substrates. A number of the negative resists on the market are resistant to a wide

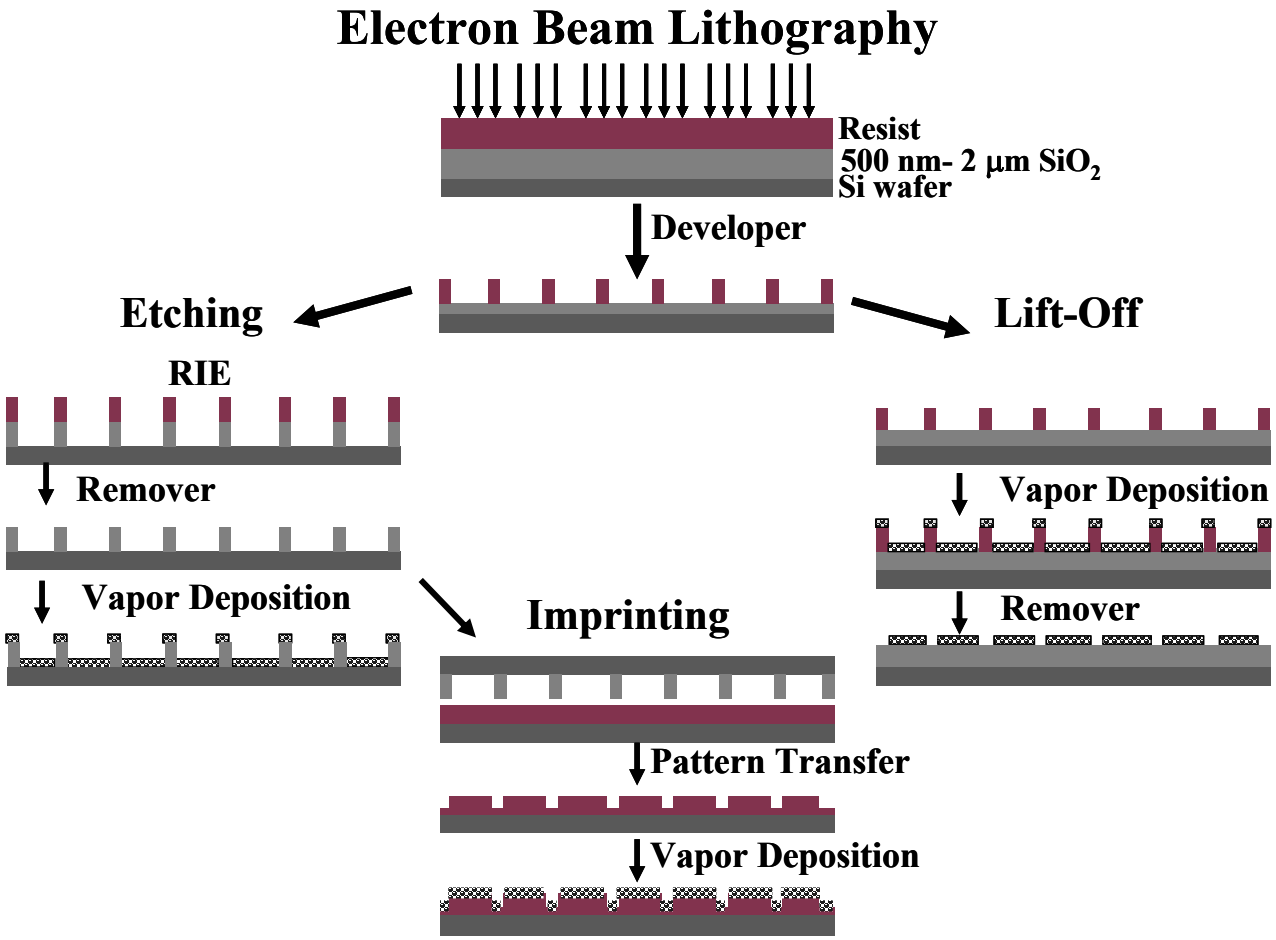


Figure 2.5. Schemes for etching, imprinting, and lift-off methods for substrate preparation via electron beam lithography on Si wafers

range of pH. Thus, nitric acid and aqua regia can be applied for the removal of metal films and the substrates recoated with metal for additional studies.

Despite the high investiture of EBL, it has the inherent capability to produce periodic substrates with unique geometries and patterns and it is ideal for the production of durable silicon molds for imprinting polymeric substrates. A number of groups have demonstrated the ability to imprint polymers with sub-10nm features.[416, 419, 425, 428, 447-461] By combining EBL and imprinting, it may be possible to mass-produce homogeneously responsive substrates for SERS applications such as trace analysis.

The future of nanostructured substrates may include the use of extreme ultraviolet (EUV), deep ultraviolet (DUV), x-ray, near-field, and small-angle neutron scattering (SANS) lithography as well as scanning probe microscopes to improve the spatial resolution of the pattern writing. Other avenues that are being examined include improvements to the polymeric resists, development of block co-polymer resists, and self-assembled multi-layer etch resists. EBL suffers from low-throughput, to this end, Canon is investigating multiplexed electron beams for simultaneous multiple pattern writing to reduce the expense of EBL.

Statement of the Problem

Surface Enhanced Raman Spectroscopy (SERS) has proven to be a promising technique. There are numerous advantages of SERS over other analytical techniques, such as low detection limits and the unambiguous identification of compounds due to the vibrational spectra generated. An additional benefit is that of small sample requirements.

However, it has not been established as a general analytical technique due the analytical figures of merit, such as reproducibility and dynamic range, and to the selectivity of the substrates toward specific functional groups. A key factor in improving the analytical capabilities of SERS resides in the performance characteristics of the substrates. This research will consider the effect of solid support, the pitch, depth, and dimensions of nanogratings on silicon wafers, as well as, the physical vapor deposition parameters to optimize SERS response and the figures of merit.

While some groups have demonstrated single molecule detection with specific analytes, this has generally been on single colloidal metal particles with unique features. Most of the current conventional SERS substrates have a distribution analyte environments across a substrate due to the irregular propagation of surface plasmons. This is endemic to colloidal and physically vapor deposited substrates. This inhomogeneity can directly affect the adsorption of the analyte and the dynamic range of SERS substrates.

To address the issue of surface plasmon generation and propagation, control needs to be exerted over the noble metal nanoparticle size, shape, and proximity. Homogeneous substrates may produce strong electromagnetic fields, such that analytes would not need to be adsorbed onto the surface to have their vibrational signals amplified. Electron beam lithographically produced substrates may offer a means design substrates for specific laser wavelengths and induce a consistent electromagnetic field across an entire substrate. Solid supports, such as glass, limit number of available sites for complexation and charge transfer. Semi-permeable polymers may generate a three-

dimensional network of nanoparticles that are embedded with in the polymer matrix, thus providing additional electromagnetic and chemical enhancement sites.

References

References

(1) Fleischmann, M.; Sundholm, G.; Tian, Z. Q. *Electrochimica Acta* **1986**, *31*, 907-916.

(2) Van Duyne, R. P.; Haller, K. L.; Altkorn, R. I. *Chemical Physics Letters* **1986**, *126*, 190-196.

(3) Van Duyne, R. P. *Journal de Physique, Colloque* **1977**, 239-252.

(4) Chang, R. K.; Yale Univ.,New Haven,CT,USA., 1982, pp 38 pp.

(5) Cotton, T. M.; Kaddi, D.; Iorga, D. *Journal of the American Chemical Society* **1983**, *105*, 7462-7464.

(6) Pettinger, B.; Moerl, L. *Journal of Electroanalytical Chemistry and Interfacial Electrochemistry* **1983**, *150*, 415-424.

(7) Van Duyne, R. P.; Janik-Czachor, M. *Journal of the Electrochemical Society* **1983**, *130*, 2320-2323.

(8) Weaver, M. J.; Hupp, J. T.; Barz, F.; Gordon, J. G., II; Philpott, M. R. *Journal of Electroanalytical Chemistry and Interfacial Electrochemistry* **1984**, *160*, 321-333.

(9) Taniguchi, I.; Umekita, K.; Yasukouchi, K. *Journal of Electroanalytical Chemistry and Interfacial Electrochemistry* **1986**, *202*, 315-322.

(10) Cross, N. A.; Pemberton, J. E. *Journal of Electroanalytical Chemistry and Interfacial Electrochemistry* **1987**, *217*, 93-100.

(11) Weaver, M. J.; Corrigan, D. S.; Gao, P.; Gosztola, D.; Leung, L. W. H. *Journal of Electron Spectroscopy and Related Phenomena* **1987**, *45*, 291-302.

(12) Chang, R. K. *NATO ASI Series, Series C: Mathematical and Physical Sciences* **1990**, *320*, 155-180.

(13) Markwort, L.; Hendra, P. *Journal of Electroanalytical Chemistry* **1995**, *397*, 225-240.

(14) Tian, Z. Q.; Ren, B.; Mao, B. W. *Journal of Physical Chemistry B* **1997**, *101*, 1338-1346.

(15) Cai, W.-B.; She, C.-X.; Ren, B.; Yao, J.-L.; Tian, Z.-W.; Tian, Z.-Q. *Journal of the Chemical Society, Faraday Transactions* **1998**, *94*, 3127-3133.

(16) Bazzaoui, E. A.; Aeiyach, S.; Aubard, J.; Felidj, N.; Levi, G.; Sakmeche, N.; Lacaze, P. C. *Journal de Chimie Physique et de Physico-Chimie Biologique* **1998**, *95*, 1526-1530.

(17) Mrozek, M. F.; Weaver, M. J. *Journal of Physical Chemistry B* **2001**, *105*, 8931-8937.

(18) Mrozek, M. F.; Wasileski, S. A.; Weaver, M. J. *Journal of the American Chemical Society* **2001**, *123*, 12817-12825.

(19) Lippitsch, M. E. *Physical Review B: Condensed Matter and Materials Physics* **1984**, *29*, 3101-3110.

(20) Irish, D. E.; Guzonas, D.; Atkinson, G. F. *Surface Science* **1985**, *158*, 314-324.

(21) Pettenkofer, C.; Eickmans, J.; Ertuerk, U.; Otto, A. *Surface Science* **1985**, *151*, 9-36.

(22) Lombardi, J. R.; Birke, R. L.; Lu, T.; Xu, J. *Journal of Chemical Physics* **1986**, *84*, 4174-4180.

(23) Chang, R. K. *Berichte der Bunsen-Gesellschaft* **1987**, *91*, 296-305.

(24) Otto, A.; Bornemann, T.; Ertuerk, U.; Mrozek, I.; Pettenkofer, C. *Surface Science* **1989**, *210*, 363-386.
(25) Osawa, M.; Matsuda, N.; Yoshii, K.; Uchida, I. *Journal of Physical Chemistry* **1994**, *98*, 12702-12707.
(26) Hildebrandt, P.; Epding, A.; Vanhecke, F.; Keller, S.; Schrader, B. *Journal of Molecular Structure* **1995**, *349*, 137-140.
(27) Kudelski, A.; Bukowska, J. *Chemical Physics Letters* **1996**, *253*, 246-250.
(28) Arenas, J. F.; Tocon, I. L.; Woolley, M. S.; Otero, J. C.; Marcos, J. I. *Journal of Raman Spectroscopy* **1998**, *29*, 673-679.
(29) Grochala, W.; Kudelski, A.; Bukowska, J. *Journal of Raman Spectroscopy* **1998**, *29*, 681-685.
(30) Otto, A. *Physica Status Solidi A: Applied Research* **2001**, *188*, 1455-1470.
(31) Katayama, K.; Shibamoto, K.; Sawada, T. *Chemical Physics Letters* **2001**, *345*, 265-271.
(32) Guo, L.; Zhang, X.; Du, Z.; Huang, Y.; Mo, Y. *Guangpuxue Yu Guangpu Fenxi* **2001**, *21*, 16-18.
(33) Xie, Y.; Wu, D. Y.; Liu, G. K.; Huang, Z. F.; Ren, B.; Yan, J. W.; Yang, Z. L.; Tian, Z. Q. *Journal of Electroanalytical Chemistry* **2003**, *554-555*, 417-425.
(34) Schultz, S. G.; Janik-Czachor, M.; Van Duyne, R. P. *Surface Science* **1981**, *104*, 419-434.
(35) Allen, C. S.; Van Duyne, R. P. *Journal of the American Chemical Society* **1981**, *103*, 7497-7501.
(36) Heard, S. M.; Grieser, F.; Barraclough, C. G. *Chemical Physics Letters* **1983**, *95*, 154-158.
(37) Kneipp, K.; Hinzmann, G.; Fassler, D. *Chemical Physics Letters* **1983**, *99*, 503-506.
(38) Stacy, A. M.; Van Duyne, R. P. *Chemical Physics Letters* **1983**, *102*, 365-370.
(39) Kerker, M.; Wang, D. S. *Chemical Physics Letters* **1984**, *104*, 516-519.
(40) Moskovits, M.; Suh, J. S. *Journal of the American Chemical Society* **1985**, *107*, 6826-6829.
(41) Austin, J. C.; Hester, R. E. *Journal of the Chemical Society, Faraday Transactions 1: Physical Chemistry in Condensed Phases* **1989**, *85*, 1159-1168.
(42) Thornton, J.; Force, R. K. *Applied Spectroscopy* **1991**, *45*, 1522-1526.
(43) Kabasawa, A.; Matsuda, N.; Sawaguchi, T.; Matsue, T.; Uchida, I. *Denki Kagaku oyobi Kogyo Butsuri Kagaku* **1992**, *60*, 986-991.
(44) Tolia, A.; Wilke, T.; Weaver, M. J.; Takoudis, C. G. *Chemical Engineering Science* **1992**, *47*, 2781-2786.
(45) Hill, W.; Wehling, B.; Klockow, D. *Sensors and Actuators, B: Chemical* **1994**, *18*, 188-191.
(46) Lee, P. C.; Meisel, D. *Chemical Physics Letters* **1983**, *99*, 262-265.
(47) Von Raben, K. U.; Chang, R. K.; Laube, B. L.; Barber, P. W. *Journal of Physical Chemistry* **1984**, *88*, 5290-5296.
(48) Kneipp, K.; Hinzmann, G.; Fassler, D. *Journal of Molecular Liquids* **1984**, *29*, 197-206.

(49) Garrell, R. L.; Schultz, R. H. *Journal of Colloid and Interface Science* **1985**, *105*, 483-491.
(50) Kneipp, K.; Flemming, J. *Studies in Physical and Theoretical Chemistry* **1987**, *45*, 451-457.
(51) Ahern, A. M.; Garrell, R. L. *Analytical Chemistry* **1987**, *59*, 2813-2816.
(52) Hildebrandt, P.; Spiro, T. G. *Journal of Physical Chemistry* **1988**, *92*, 3355-3360.
(53) Kerker, M.; Clarkson Univ.,Potsdam,NY,USA., 1988, pp 4 pp.
(54) Angel, S. M.; Myrick, M. L.; Milanovich, F. P. *Applied Spectroscopy* **1990**, *44*, 335-336.
(55) Sutherland, W. S.; Laserna, J. J.; Angebranndt, M. J.; Winefordner, J. D. *Analytical Chemistry* **1990**, *62*, 689-693.
(56) Liang, E.; Wang, Y.; Wang, Y.; Hao, Q.; Zhang, P. *Chinese Physics Letters* **1992**, *9*, 73-76.
(57) Philip, D.; Eapen, A.; Aruldhas, G. *Indian Journal of Physics, B* **1994**, *68B*, 463-467.
(58) Xu, H.; Tseng, C.-H.; Vickers, T. J.; Mann, C. K.; Schlenoff, J. B. *Surface Science* **1994**, *311*, L707-L711.
(59) Philip, D.; Aruldhas, G. *Journal of Solid State Chemistry* **1995**, *116*, 427-431.
(60) Sanchez-Cortes, S.; Garcia-Ramos, J. V.; Morcillo, G.; Tinti, A. *Journal of Colloid and Interface Science* **1995**, *175*, 358-368.
(61) Solecka-Cermakova, K.; Vlckova, B.; Lednicky, F. *Journal of Physical Chemistry* **1996**, *100*, 4954-4960.
(62) Freeman, R. G.; Hommer, M. B.; Grabar, K. C.; Jackson, M. A.; Natan, M. J. *Journal of Physical Chemistry* **1996**, *100*, 718-724.
(63) Vlckova, B.; Solecka-Cermakova, K.; Matejka, P.; Baumruk, V. *Journal of Molecular Structure* **1997**, *408-409*, 149-154.
(64) Nickel, U.; zu Castell, A.; Poeppl, K.; Schneider, S. *Langmuir* **2000**, *16*, 9087-9091.
(65) Pignataro, B.; De Bonis, A.; Compagnini, G.; Sassi, P.; Cataliotti, R. S. *Journal of Chemical Physics* **2000**, *113*, 5947-5953.
(66) Rivas, L.; Sanchez-Cortes, S.; Garcia-Ramos, J. V.; Morcillo, G. *Langmuir* **2001**, *17*, 574-577.
(67) Torres La Porte, R.; Silva Moreno, D.; Castillejo Striano, M.; Martin Munoz, M.; Garcia-Ramos, J. V.; Sanchez Cortes, S.; Koudoumas, E. *Laser Chemistry* **2002**, *20*, 23-32.
(68) Marques, C.; Alves, E.; da Silva, R. C.; Silva, M. R.; Stepanov, A. L. *Nuclear Instruments & Methods in Physics Research, Section B: Beam Interactions with Materials and Atoms* **2004**, *218*, 139-144.
(69) Fang, J.; Huang, Y.; Li, X.; Dou, X. *Journal of Raman Spectroscopy* **2004**, *35*, 914-920.
(70) Mou, C.; Chen, D.; Wang, X.; Zhang, B.; He, T.; Xin, H.; Liu, F. *Spectrochimica Acta, Part A: Molecular and Biomolecular Spectroscopy* **1991**, *47A*, 1575-1581.
(71) Reimer, H.; Fischer, F. *Physica Status Solidi B: Basic Research* **1984**, *124*, 61-67.
(72) Abel, H. B.; Fischer, F. *Physica Status Solidi B: Basic Research* **1987**, *144*, 875-884.

(73) Abel, H. B. *Physica Status Solidi B: Basic Research* **1990**, *161*, 435-445.
(74) Wang, D. S.; Chew, H.; Kerker, M. *Applied Optics* **1980**, *19*, 2256-2257.
(75) Wokaun, A.; Gordon, J. P.; Liao, P. F. *Physical Review Letters* **1982**, *48*, 957-960.
(76) Pack, A.; Hietschold, M.; Wannemacher, R. *Optics Communications* **2001**, *194*, 277-287.
(77) Taneja, P.; Ayyub, P.; Chandra, R. *Physical Review B: Condensed Matter and Materials Physics* **2002**, *65*, 245412/245411-245412/245416.
(78) Kerker, M.; Clarkson Univ.,Potsdam,NY,USA., 1985, pp 6 pp.
(79) Kovacs, G. J.; Loutfy, R. O.; Vincett, P. S.; Jennings, C.; Aroca, R. *Langmuir* **1986**, *2*, 689-694.
(80) Orenda, H.; Knobloch, H.; Aust, E. F.; Knoll, W. *RIKEN Review* **1993**, 49-50.
(81) Yang, W.-H.; Schatz, G. C.; Van Duyne, R. P. *Journal of Chemical Physics* **1995**, *103*, 869-875.
(82) Keating, C. D.; Kovaleski, K. K.; Natan, M. J. *Journal of Physical Chemistry B* **1998**, *102*, 9414-9425.
(83) Cotton, T. M.; Sokolov, K.; Chumanov, G.; (Mediflor, Ltd., Switz.). Application: WO
WO, 1998, pp 35 pp.
(84) Jensen, T.; Kelly, L.; Lazarides, A.; Schatz, G. C. *Journal of Cluster Science* **1999**, *10*, 295-317.
(85) Hao, E.; Schatz, G. C. *Journal of Chemical Physics* **2004**, *120*, 357-366.
(86) Park, S.-H.; Im, J.-H.; Im, J.-W.; Chun, B.-H.; Kim, J.-H. *Microchemical Journal* **1999**, *63*, 71-91.
(87) Shahbazyan, T. V.; Parakis, I. E. *Condensed Matter Theories* **2000**, *14*, 317-324.
(88) Cho, S. H.; Lee, S.; Ku, D. Y.; Lee, T. S.; Cheong, B.; Kim, W. M.; Lee, K. S. *Thin Solid Films* **2004**, *447-448*, 68-73.
(89) Sandoghdar, V. *Abstracts of Papers, 227th ACS National Meeting, Anaheim, CA, United States, March 28-April 1, 2004* **2004**, PHYS-544.
(90) Zeman, E. J.; Schatz, G. C. *Jerusalem Symposia on Quantum Chemistry and Biochemistry* **1984**, *17*, 413-424.
(91) Corio, P.; Brown, S. D. M.; Marucci, A.; Pimenta, M. A.; Kneipp, K.; Dresselhaus, G.; Dresselhaus, M. S. *Physical Review B: Condensed Matter and Materials Physics* **2000**, *61*, 13202-13211.
(92) Kneipp, K. *Single Molecules* **2001**, *2*, 291-292.
(93) Jha, S. S.; Kirtley, J. R.; Tsang, J. C. *Physical Review B: Condensed Matter and Materials Physics* **1980**, *22*, 3973-3982.
(94) Gersten, J.; Nitzan, A. *Journal of Chemical Physics* **1980**, *73*, 3023-3037.
(95) Novotny, L.; Hecht, B.; Pohl, D. W. *Journal of Applied Physics* **1997**, *81*, 1798-1806.
(96) Treacy, M. M. J. *Applied Physics Letters* **1999**, *75*, 606-608.
(97) Goodrich, G. P.; Musick, M. D.; Natan, M. J.; Keating, C. D. *Abstracts of Papers, 220th ACS National Meeting, Washington, DC, United States, August 20-24, 2000* **2000**, COLL-138.
(98) Sarychev, A. K.; Shalaev, V. M. *Physics Reports* **2000**, *335*, 275-371.

(99) Setala, T.; Kaivola, M.; Friberg Ari, T. *Physical review letters* **2002**, *88*, 123902.
(100) Setala, T.; Kaivola, M.; Friberg, A. T. *Physical Review Letters* **2002**, *88*, 123902/123901-123902/123904.
(101) Maier, S. A.; Kik, P. G.; Atwater, H. A.; Meltzer, S.; Harel, E.; Koel, B. E.; Requicha, A. A. G. *Nature Materials* **2003**, *2*, 229-232.
(102) Crouse, D. T.; Lo, Y.-H. *Journal of Applied Physics* **2004**, *95*, 4163-4172.
(103) Pendry, J. B.; Martin-Moreno, L.; Garcia-Vidal, F. J. *Science (Washington, DC, United States)* **2004**, *305*, 847-849.
(104) Wheeler, C. E.; Arakawa, E. T.; Ritchie, R. H. *Physical Review B: Solid State* **1976**, *13*, 2372-2376.
(105) Wokaun, A.; Bergman, J. G.; Heritage, J. P.; Glass, A. M.; Liao, P. F.; Olson, D. H. *Physical Review B: Condensed Matter and Materials Physics* **1981**, *24*, 849-856.
(106) Liao, P. F. *Springer Series in Optical Sciences* **1981**, *30*, 420-424.
(107) Girlando, A.; Knoll, W.; Philpott, M. R. *Solid State Communications* **1981**, *38*, 895-898.
(108) Liao, P. F.; Stern, M. B. *Optics Letters* **1982**, *7*, 483-485.
(109) Harris, T. D.; Glass, A. M.; Olson, D. H. *Analytical Chemistry Symposia Series* **1984**, *19*, 49-52.
(110) Wirgin, A. *Physica A: Statistical Mechanics and Its Applications (Amsterdam, Netherlands)* **1989**, *157*, 382-387.
(111) Smith, M. T.; Hulteen, J. C.; Ratner, M. A.; Van Duyne, R. P. *Book of Abstracts, 210th ACS National Meeting, Chicago, IL, August 20-24* **1995**, PHYS-195.
(112) Scheihing, J. E.; Dodd, M. A. *Proceedings - Electrochemical Society* **1995**, *94-5*, 136-143.
(113) Hulteen, J. C.; Van Duyne, R. P. *Book of Abstracts, 210th ACS National Meeting, Chicago, IL, August 20-24* **1995**, PHYS-025.
(114) Hulteen, J. C.; Treichel, D. A.; Smith, M. T.; Duval, M. L.; Jensen, T. R.; Van Duyne, R. P. *Journal of Physical Chemistry B* **1999**, *103*, 3854-3863.
(115) Popov, E.; Neviere, M.; Enoch, S.; Reinisch, R. *Physical Review B: Condensed Matter and Materials Physics* **2000**, *62*, 16100-16108.
(116) Wei, A.; Kim, B.; Sadtler, B.; Tripp, S. L. *ChemPhysChem* **2001**, *2*, 743-745.
(117) Maier, S. A.; Brongersma, M. L.; Kik, P. G.; Meltzer, S.; Requicha, A. A. G.; Atwater, H. A. *Advanced Materials (Weinheim, Germany)* **2001**, *13*, 1501-1505.
(118) Schider, G.; Krenn, J. R.; Gotschy, W.; Lamprecht, B.; Ditlbacher, H.; Leitner, A.; Aussenegg, F. R. *Journal of Applied Physics* **2001**, *90*, 3825-3830.
(119) Ormonde, A. D.; Van Duyne, R. P. *Abstracts of Papers, 222nd ACS National Meeting, Chicago, IL, United States, August 26-30, 2001* **2001**, ANYL-092.
(120) Kim, B.; Tripp, S. L.; Wei, A. *Materials Research Society Symposium Proceedings* **2002**, *676*, Y6 1 1-Y6 1 7.
(121) Garcia-Vidal, F. J.; Martin-Moreno, L. *Physical Review B: Condensed Matter and Materials Physics* **2002**, *66*, 155412/155411-155412/155410.
(122) Grebel, H. *Proceedings - Electrochemical Society* **2002**, *2002-4*, 79-87.
(123) Sarychev, A. K.; Genov, D. A.; Wei, A.; Shalaev, V. M. *Proceedings of SPIE-The International Society for Optical Engineering* **2003**, *5218*, 81-92.

(124) Felidj, N.; Aubard, J.; Levi, G.; Krenn, J. R.; Hohenau, A.; Schider, G.; Leitner, A.; Aussenegg, F. R. *Applied Physics Letters* **2003**, *82*, 3095-3097.
(125) Hanarp, P.; Kaell, M.; Sutherland, D. S. *Journal of Physical Chemistry B* **2003**, *107*, 5768-5772.
(126) Vallius, T.; Jefimovs, K.; Turunen, J.; Vahimaa, P.; Svirko, Y. *Applied Physics Letters* **2003**, *83*, 234-236.
(127) Van Duyne, R. P.; Haes, A. J.; McFarland, A. D. *Proceedings of SPIE-The International Society for Optical Engineering* **2003**, *5223*, 197-207.
(128) Wei, A.; Kim, B.; (USA). Application: US
US, 2003, pp 17 pp.
(129) Schmidt Jason, P.; Cross Sarah, E.; Buratto Steven, K. *Journal of chemical physics* **2004**, *121*, 10657-10659.
(130) Genov, D. A.; Sarychev, A. K.; Shalaev, V. M.; Wei, A. *Nano Letters* **2004**, *4*, 153-158.
(131) Boerio, F. J.; Tsai, W. H.; Montaudo, G. *Journal of Polymer Science, Part B: Polymer Physics* **1989**, *27*, 1017-1027.
(132) Boerio, F. J. *Thin Solid Films* **1989**, *181*, 423-433.
(133) Venkatachalam, R. S.; Boerio, F. J.; Roth, P. g.; Tsai, W. H. *Journal of Polymer Science, Part B: Polymer Physics* **1988**, *26*, 2447-2461.
(134) Venkatachalam, R. S.; Boerio, F. J.; Carnevale, M. R.; Roth, P. G. *Applied Spectroscopy* **1988**, *42*, 1207-1213.
(135) Rothenhaeusler, B.; Knoll, W. *Surface Science* **1987**, *191*, 585-594.
(136) Roth, P. G.; Boerio, F. J. *Journal of Polymer Science, Part B: Polymer Physics* **1987**, *25*, 1923-1933.
(137) Lueth, H. *Surface Science* **1986**, *168*, 773-786.
(138) Jennings, C.; Aroca, R.; Hor, A. M.; Loutfy, R. O. *Analytical Chemistry* **1984**, *56*, 2033-2035.
(139) Goudonnet, J. P.; Begun, G. M.; Arakawa, E. T. *Chemical Physics Letters* **1982**, *92*, 197-201.
(140) Aroca, R.; Jennings, C.; Kovac, G. J.; Loutfy, R. O.; Vincett, P. S. *Journal of Physical Chemistry* **1985**, *89*, 4051-4054.
(141) Garoff, S.; Weitz, D. A.; Alvarez, M. S.; Chung, J. C. *Journal de Physique, Colloque* **1983**, 345-348.
(142) Dornhaus, R. *Journal of Electron Spectroscopy and Related Phenomena* **1983**, *30*, 197-202.
(143) Dornhaus, R. *Vib. Surf., [Proc. Int. Conf.], 2nd* **1982**, 445-455.
(144) Seki, H. *Journal of Vacuum Science and Technology* **1981**, *18*, 633-637.
(145) Yao, J. L.; Pan, G. R.; Xue, K. H.; Wu, D. Y.; Ren, B.; Sun, D. M.; Tang, J.; Xu, X.; Tian, Z. Q. *Pure and Applied Chemistry* **2000**, *72*, 221-228.
(146) Wasileski, S. A.; Zou, S.; Weaver, M. J. *Applied Spectroscopy* **2000**, *54*, 761-772.
(147) Ren, B.; Yao, J. L.; She, C. X.; Huang, Q. J.; Tian, Z. Q. *Internet Journal of Vibrational Spectroscopy [online computer file]* **2000**, *4*, No pp given.
(148) Luo, H.; Weaver, M. J. *Langmuir* **1999**, *15*, 8743-8749.
(149) Chan, H. Y. H.; Zou, S.; Weaver, M. J. *Journal of Physical Chemistry B* **1999**, *103*, 11141-11151.

(150) Zou, S.; Weaver, M. J. *Analytical Chemistry* **1998**, *70*, 2387-2395.
(151) Wilke, T.; Gao, X.; Takoudis, C. G.; Weaver, M. J. *Langmuir* **1991**, *7*, 714-721.
(152) Tadayyoni, M. A.; Farquharson, S.; Weaver, M. J.; Dep. Chem.,Purdue Univ.,Lafayette,IN,USA., 1983, pp 10 pp.
(153) Weaver, M. J.; Kizhakevariam, N.; Jiang, X.; Villegas, I.; Stuhlmann, C.; Tolia, A.; Gao, X. *Journal of Electron Spectroscopy and Related Phenomena* **1993**, *64-65*, 351-362.
(154) Vo Dinh, T.; Alak, A.; Moody, R. L. *Spectrochimica Acta, Part B: Atomic Spectroscopy* **1988**, *43B*, 605-615.
(155) Moody, R. L.; Vo Dinh, T.; Fletcher, W. H. *Applied Spectroscopy* **1987**, *41*, 966-970.
(156) Hu, J.-w.; Zhao, B.; Xu, W.-q.; Xie, Y.-t.; Fan, Y.-g.; Li, B.-f.; Wang, H. *Gaodeng Xuexiao Huaxue Xuebao* **2002**, *23*, 123-125.
(157) Kvitek, L.; Fichna, P.; Barosova, I.; Novotny, R. *Acta Universitatis Palackianae Olomucensis, Facultas Rerum Naturalium, Chemica* **1997**, *36*, 29-33.
(158) Wang, J.; Zhu, T.; Tang, M.; Cai, S. M.; Liu, Z. F. *Japanese Journal of Applied Physics, Part 2: Letters* **1996**, *35*, L1381-L1384.
(159) Roark, S. E.; Semin, D. J.; Rowlen, K. L. *Analytical Chemistry* **1996**, *68*, 473-480.
(160) Sanchez-Cortes, S.; Garcia-Ramos, J. V. *Journal of Raman Spectroscopy* **1990**, *21*, 679-682.
(161) Pettinger, B.; Krischer, K.; Ertl, G. *Chemical Physics Letters* **1988**, *151*, 151-155.
(162) Creighton, J. A. *Surface Science* **1986**, *173*, 665-672.
(163) Campion, A.; Mullins, D. R. *Surface Science* **1985**, *158*, 263-270.
(164) Moskovits, M.; Suh, J. S. *Journal of Physical Chemistry* **1984**, *88*, 1293-1298.
(165) Kerker, M.; Siiman, O.; Wang, D. S. *Journal of Physical Chemistry* **1984**, *88*, 3168-3170.
(166) Lee, P. C.; Meisel, D. *Journal of Physical Chemistry* **1982**, *86*, 3391-3395.
(167) Sun, Y.; Xia, Y. *Journal of the American Chemical Society* **2004**, *126*, 3892-3901.
(168) Yang, C.; Yang, H.; Shi, Z.; Zhu, L.; Sheng, R.; Hu, J. *Chinese Chemical Letters* **1992**, *3*, 919-922.
(169) Sestak, O.; Matejka, P.; Vlckova, B. *Journal of Molecular Structure* **1995**, *348*, 297-300.
(170) Felidj, N.; Aubard, J.; Levi, G. *Journal of Raman Spectroscopy* **1998**, *29*, 651-664.
(171) Mock, J. J.; Barbic, M.; Smith, D. R.; Schultz, D. A.; Schultz, S. *Journal of Chemical Physics* **2002**, *116*, 6755-6759.
(172) Futamata, M.; Maruyama, Y.; Ishikawa, M. *Vibrational Spectroscopy* **2002**, *30*, 17-23.
(173) Xia, Y. S. a. Y. *Advanced Materials* **2003**, *15*, 695-699.
(174) Lee, M.-S.; Nam, S.-I.; Min, E.-S.; Kim, S.-B.; Shin, H.-S.; (Postech Foundation, S. Korea). Application: WO
WO, 2002, pp 32 pp.
(175) Xia, Y. S. a. Y. *Analyst* **2003**, *128*, 686-691.

(176) Andersen, P. C.; Jacobson, M. L.; Rowlen, K. L. *Journal of Physical Chemistry B* **2004**, *108*, 2148-2153.
(177) Futamata, M.; Maruyama, Y.; Ishikawa, M. *Journal of Physical Chemistry B* **2003**, *107*, 7607-7617.
(178) Andersen, P. C.; Jacobson, M. L.; Rowlen, K. L. *Preprints of Extended Abstracts presented at the ACS National Meeting, American Chemical Society, Division of Environmental Chemistry* **2003**, *43*, 702-705.
(179) Moskovits, M.; Tay, L.-L.; Yang, J.; Haslett, T. *Topics in Applied Physics* **2002**, *82*, 215-226.
(180) Kneipp, K.; Kneipp, H.; Itzkan, I.; Dasari, R. R.; Feld, M. S.; Dresselhaus, M. S. *Topics in Applied Physics* **2002**, *82*, 227-247.
(181) Quinten, M. *Applied Physics B: Lasers and Optics* **2001**, *73*, 245-255.
(182) Moskovits, M.; Tay, L.; Yang, J.; Haslett, T. *Proceedings of SPIE-The International Society for Optical Engineering* **2001**, *4258*, 43-49.
(183) Gadenne, P.; Berini, B.; Buil, S.; Quelin, X.; Anceau, C.; Gresillon, S.; Ducourtieux, S.; Rivoal, J.-C.; Breit, M.; Bourdon, A.; Sarychev, A. K.; Shalaev, V. M. *Proceedings of SPIE-The International Society for Optical Engineering* **2001**, *4467*, 288-296.
(184) Armstrong, R. L.; Shalaev, V. M.; Shay, T. M.; Kim, W.-t.; Ying, Z. C.; (New Mexico State University Technology Transfer Corporation, USA). Application: WO
WO, 2001, pp 55 pp.
(185) Shalaev, V. M.; Editor *Optical Properties of Nanostructured Random Media. [Top. Appl. Phys., 2002; 82]*, 2002.
(186) Shalaev, V. M. *Topics in Applied Physics* **2002**, *82*, 93-112.
(187) Hao, E.; Hupp, J. T.; Schatz, G. C. *Abstracts of Papers, 227th ACS National Meeting, Anaheim, CA, United States, March 28-April 1, 2004* **2004**, PHYS-356.
(188) Kelly, K. L.; Coronado, E.; Zhao, L. L.; Schatz, G. C. *Journal of Physical Chemistry B* **2003**, *107*, 668-677.
(189) Dong, W.-F.; Sukhorukov, G. B.; Moehwald, H. *Physical Chemistry Chemical Physics* **2003**, *5*, 3003-3012.
(190) Zheng, M.; Gu, M.; Jin, Y.; Jin, G. *Materials Research Bulletin* **2001**, *36*, 853-859.
(191) Felidj, N.; Aubard, J.; Levi, G. *Journal of Chemical Physics* **1999**, *111*, 1195-1208.
(192) Kreibig, U. *Handbook of Optical Properties* **1997**, *2*, 145-190.
(193) Zhao, Y.; McCarthy, B. P.; Yamnitskiy, K. M.; Sarid, D. *Proceedings of SPIE-The International Society for Optical Engineering* **2004**, *5363*, 54-64.
(194) Ormonde, A. D.; Hicks, E. C. M.; Castillo, J.; Van Duyne, R. P. *Langmuir* **2004**, *20*, 6927-6931.
(195) Sun, Y.; Xia, Y. *Materials Research Society Symposium Proceedings* **2003**, *776*, 31-36.
(196) Smejkal, P.; Siskova, K.; Vlckova, B.; Pfleger, J.; Sloufova, I.; Slouf, M.; Mojzes, P. *Spectrochimica Acta, Part A: Molecular and Biomolecular Spectroscopy* **2003**, *59A*, 2321-2329.

(197) Seitz, O.; Chehimi, M. M.; Cabet-Deliry, E.; Truong, S.; Felidj, N.; Perruchot, C.; Greaves, S. J.; Watts, J. F. *Colloids and Surfaces, A: Physicochemical and Engineering Aspects* **2003**, *218*, 225-239.
(198) Rivas, L.; Sanchez-Cortes, S.; Garcia-Ramos, J. V.; Morcillo, G. *Langmuir* **2000**, *16*, 9722-9728.
(199) Ramirez-Aguilar, K. A.; Rowlen, K. L. *Langmuir* **1998**, *14*, 2562-2566.
(200) Felidj, N.; Levi, G.; Pantigny, J.; Aubard, J. *New Journal of Chemistry* **1998**, *22*, 725-732.
(201) Heilmann, A.; Werner, J.; Schwarzenberg, D.; Henkel, S.; Grosse, P.; Theiss, W. *Thin Solid Films* **1995**, *270*, 103-108.
(202) Wentrup-Byrne, E.; Fredericks, P. M.; Aubard, J.; Pantigny, J.; Levi, G. *Int. Conf. Spectrosc. Biol. Mol., 5th* **1993**, 259-260.
(203) Van Duyne, R. P.; Hulteen, j. C.; Treichel, D. A. *Journal of Chemical Physics* **1993**, *99*, 2101-2115.
(204) Roark, S. E.; Rowlen, K. L. *Chemical Physics Letters* **1993**, *212*, 50-56.
(205) Boerio, F. J.; Hong, P. P.; Clark, P. J.; Okamoto, Y. *Langmuir* **1990**, *6*, 721-727.
(206) Hickel, W.; Rothenhaeusler, B.; Knoll, W. *Journal of Applied Physics* **1989**, *66*, 4832-4836.
(207) Xu, X.-H. N.; Huang, S.; Brownlow, W.; Salatia, K.; Jeffers, R. B. *Journal of Physical Chemistry B* **2004**, *108*, 15543-15551.
(208) Su, K.-H.; Wei, Q.-H.; Zhang, X.; Mock, J. J.; Smith, D. R.; Schultz, S. *Proceedings of SPIE-The International Society for Optical Engineering* **2003**, *5221*, 108-115.
(209) Sun, Y.; Xia, Y. *Analytical Chemistry* **2002**, *74*, 5297-5305.
(210) Link, S.; El-Sayed, M. A. *International Reviews in Physical Chemistry* **2000**, *19*, 409-453.
(211) Felidj, N.; Aubard, J.; Levi, G. *Trends in Physical Chemistry* **1999**, *7*, 103-113.
(212) Chang, S.-S.; Shih, C.-W.; Chen, C.-D.; Lai, W.-C.; Wang, C. R. C. *Langmuir* **1999**, *15*, 701-709.
(213) Kalkan, A. K.; Fonash, S. J.; (The Penn State Research Foundation, USA). Application: WO
WO, 2004, pp 52 pp.
(214) Doblhofer, K.; Flatgent, G.; Radhakrishnan, G.; Pettinger, B.; Savinova, E.; Wasle, S. *Transactions of the SAEST* **1999**, *34*, 88-92.
(215) Gu, X. J.; Akers, K. L.; Moskovits, M. *Journal of Physical Chemistry* **1992**, *96*, 383-387.
(216) Gu, X. J.; Akers, K. L.; Moskovits, M. *Journal of Physical Chemistry* **1991**, *95*, 3696-3700.
(217) Jang, S.; Park, J.; Shin, S.; Yoon, C.; Choi, B. K.; Gong, M.-s.; Joo, S.-W. *Langmuir* **2004**, *20*, 1922-1927.
(218) Pendell Jones, J.; Fell, N. F., Jr.; Alexander, T. A.; Dorschner, K.; Tombrello, C.; Reis, B. R.; Fountain, A. W., III *Proceedings of SPIE-The International Society for Optical Engineering* **2003**, *5071*, 205-211.
(219) Alexander Troy, A.; Pellegrino Paul, M.; Gillespie James, B. *Applied spectroscopy* **2003**, *57*, 1340-1345.

(220) Demers, L. M.; Oestblom, M.; Zhang, H.; Jang, N.-H.; Liedberg, B.; Mirkin, C. A. *Journal of the American Chemical Society* **2002**, *124*, 11248-11249.
(221) Zhao, B.; Ozaki, Y. *Dianhuaxue* **2001**, *7*, 185-188.
(222) Freeman, R. G.; Grabar, K. C.; Allison, K. J.; Bright, R. M.; Davis, J. A.; Guthrie, A. P.; Hommer, M. B.; Jackson, M. A.; Smith, P. C.; et al. *Science (Washington, D. C.)* **1995**, *267*, 1629-1631.
(223) Koh, T. Y.; Greaves, S. J.; Griffith, W. P. *Spectrochimica Acta, Part A: Molecular and Biomolecular Spectroscopy* **1994**, *50A*, 857-873.
(224) Boss, P. A.; Boss, R. D.; Lieberman, S. H.; (United States Dept. of the Navy, USA). Application: US
US, 2002, pp 14 pp.
(225) Maynard, K. J.; Moskovits, M. *Journal of Chemical Physics* **1989**, *90*, 6668-6679.
(226) Maynard, K. J.; Moskovits, M. *Chemical Physics Letters* **1987**, *142*, 298-301.
(227) Hartmuth C. Kolb, M. G. F., and K. Barry Sharpless *Angew. Chem. Int. Ed.* **2001**, *40*, 2004 - 2021.
(228) Tian, Z.-Q.; Ren, B.; Wu, D.-Y. *Journal of Physical Chemistry B* **2002**, *106*, 9463-9483.
(229) Doering, W. E.; Nie, S. *Analytical Chemistry* **2003**, *75*, 6171-6176.
(230) Despotuli, A. L.; Andreeva, A. V. *Chemistry Preprint Server, Physical Chemistry* **2003**, 1-13, CPS: physchem/0309001.
(231) Kneipp, K.; Kneipp, H.; Itzkan, I.; Dasari, R. R.; Feld, M. S. *Abstracts of Papers, 221st ACS National Meeting, San Diego, CA, United States, April 1-5, 2001* **2001**, PHYS-113.
(232) Michaels, A. M.; Nirmal, M.; Brus, L. E. *Journal of the American Chemical Society* **1999**, *121*, 9932-9939.
(233) Kneipp, K.; Kneipp, H.; Itzkan, I.; Dasari, R. R.; Feld, M. S. *Chemical Physics* **1999**, *247*, 155-162.
(234) Kneipp, K.; Kneipp, H.; Manoharan, R.; Itzkan, I.; Dasari, R. R.; Feld, M. S. *Journal of Raman Spectroscopy* **1998**, *29*, 743-747.
(235) Nie, S.; Emory, S. R. *Science (Washington, D. C.)* **1997**, *275*, 1102-1106.
(236) Kneipp, K.; Wang, Y.; Kneipp, H.; Perelman, L. T.; Itzkan, I.; Dasari, R. R.; Feld, M. S. *Physical Review Letters* **1997**, *78*, 1667-1670.
(237) Emory, S. R.; Nie, S. *Book of Abstracts, 213th ACS National Meeting, San Francisco, April 13-17* **1997**, PHYS-459.
(238) Kneipp, K.; Wang, Y.; Kneipp, H.; Dasari, R. R.; Feld, M. S. *Experimental Technique of Physics (Lemgo, Germany)* **1995**, *41*, 225-234.
(239) Pemberton, J. E.; Joa, S. L.; Woelfel, K. J. *Journal of the Chemical Society, Faraday Transactions* **1996**, *92*, 3683-3691.
(240) Shimizu, T.; Oblonsky, L. J.; Devine, T. M. *Proceedings - Electrochemical Society* **1995**, *94-26*, 114-126.
(241) Feilchenfeld, H.; Weaver, M. J. *Journal of Physical Chemistry* **1989**, *93*, 4276-4282.
(242) Holze, R. *Zeitschrift fuer Physikalische Chemie (Muenchen, Germany)* **1988**, *160*, 45-58.

(243) Gao, P.; Gosztola, D.; Weaver, M. J. *Journal of Physical Chemistry* **1988**, *92*, 7122-7130.
(244) Taniguchi, I.; Yasukouchi, K. *Studies in Organic Chemistry (Amsterdam)* **1987**, *30*, 393-396.
(245) Rubim, J. C. *Journal of Electroanalytical Chemistry and Interfacial Electrochemistry* **1987**, *220*, 339-350.
(246) Chang, R. K.; Henrich, V. E.; Yale Univ.,New Haven,CT,USA., 1986, pp 45 pp.
(247) Guy, A. L.; Pemberton, J. E. *Langmuir* **1985**, *1*, 518-525.
(248) Farquharson, S.; Milner, D.; Tadayyoni, M. A.; Weaver, M. J.; Dep. Chem.,Purdue Univ.,Lafayette,IN,USA., 1984, pp 24 pp.
(249) Philpott, M. R.; Barz, F.; Gordon, J. G., II; Weaver, M. J. *Journal of Electroanalytical Chemistry and Interfacial Electrochemistry* **1983**, *150*, 399-314.
(250) Dai, S.; Bao, L.-L.; Mahurin, S.; Gu, B. *Preprints of Extended Abstracts presented at the ACS National Meeting, American Chemical Society, Division of Environmental Chemistry* **2004**, *44*, 515-517.
(251) Mosier-Boss, P. A.; Lieberman, S. H. *Preprints of Extended Abstracts presented at the ACS National Meeting, American Chemical Society, Division of Environmental Chemistry* **2001**, *41*, 377-382.
(252) Lee, S. J.; Kim, K. *Chemical Physics Letters* **2003**, *378*, 122-127.
(253) Han, S. W.; Lee, I.; Kim, K. *Langmuir* **2002**, *18*, 182-187.
(254) Joo, S. W.; Han, S. W.; Kim, K. *Journal of Physical Chemistry B* **1999**, *103*, 10831-10837.
(255) Chan, H. Y. H.; Williams, C. T.; Weaver, M. J.; Takoudis, C. G. *Journal of Catalysis* **1998**, *174*, 191-200.
(256) Weaver, M. J.; Corrigan, D. S.; Gao, P.; Gosztola, D.; Leung, L. W.; Dep. Chem.,Purdue Univ.,West Lafayette,IN,USA., 1987, pp 14 pp.
(257) Dorain, P. B.; Von Raben, K. U. *Surface Science* **1985**, *160*, 164-170.
(258) Litorja, M.; Haynes, C. L.; Haes, A. J.; Jensen, T. R.; Van Duyne, R. P. *Journal of Physical Chemistry B* **2001**, *105*, 6907-6915.
(259) Chan, H. Y. H.; Takoudis, C. G.; Weaver, M. J. *Journal of Catalysis* **1997**, *172*, 336-345.
(260) Van Duyne, R. P. *Book of Abstracts, 212th ACS National Meeting, Orlando, FL, August 25-29* **1996**, COLL-078.
(261) Child, C. M.; Foster, M.; Ivanecky, J. E., III; Perry, S. S.; Campion, A. *Proceedings of SPIE-The International Society for Optical Engineering* **1995**, *2547*, 2-11.
(262) Akemann, W.; Otto, A. *Langmuir* **1995**, *11*, 1196-1200.
(263) Akers, K. L.; Cousins, L. M.; Moskovits, M. *Chemical Physics Letters* **1992**, *190*, 614-620.
(264) Hinde, R. J.; Sepaniak, M. J.; Compton, R. N.; Nordling, J.; Lavrik, N. *Chemical Physics Letters* **2001**, *339*, 167-173.
(265) Douketis, C.; Wang, Z.; Haslett, T. L.; Moskovits, M. *Physical Review B: Condensed Matter* **1995**, *51*, 11022-11031.
(266) Wolkow, R. A.; Moskovits, M. *Journal of Chemical Physics* **1992**, *96*, 3966-3980.

(267) Gass, A. N.; Kapusta, O. I.; Klimin, S. A.; Mal'shukov, A. G. *Solid State Communications* **1989**, *71*, 749-753.
(268) Blue, D.; Helwig, K.; Moskovits, M. *Journal of Physical Chemistry* **1989**, *93*, 8080-8089.
(269) Otto, A. *Indian Journal of Pure and Applied Physics* **1988**, *26*, 141-158.
(270) Vogel, E.; Gessner, R.; Hayes, M. H. B.; Kiefer, W. *Journal of Molecular Structure* **1999**, *482-483*, 195-199.
(271) Menikh, A.; Bouraoui, A. *Journal of Molecular Structure* **1997**, *403*, 189-197.
(272) Matejka, P.; Mojzes, P.; Vlckova, B. *Journal of Molecular Structure* **1995**, *349*, 121-124.
(273) Garrell, R. L.; Herne, T. M.; Szafranski, C. A.; Diederich, F.; Ettl, F.; Whetten, R. L. *Journal of the American Chemical Society* **1991**, *113*, 6302-6303.
(274) Kneipp, K.; Kneipp, H.; Rentsch, M. *Journal of Molecular Structure* **1987**, *156*, 331-340.
(275) Koglin, E.; Sequaris, J. M.; Fritz, J. C.; Valenta, P. *Journal of Molecular Structure* **1984**, *114*, 219-223.
(276) Goulet, P. J. G.; Aroca, R. F. *Canadian Journal of Chemistry* **2004**, *82*, 987-997.
(277) Wu, Y.; Zhao, B.; Xu, W.; Li, G.; Li, B.; Ozaki, Y. *Langmuir* **1999**, *15*, 1247-1251.
(278) Koglin, E.; Kreisig, S. M.; Copitzky, T. *Progress in Colloid & Polymer Science* **1998**, *109*, 232-243.
(279) Weiss, A.; Haran, G. *Journal of Physical Chemistry B* **2001**, *105*, 12348-12354.
(280) Guo, L.; Zhang, X.; Du, Z.; Huang, Y.; Mo, Y. *Guang pu xue yu guang pu fen xi = Guang pu* **2001**, *21*, 16-18.
(281) Choi, J. H.; Kim, H. *Bulletin of the Korean Chemical Society* **1993**, *14*, 388-392.
(282) Ueba, H. *Surface Science* **1983**, *131*, 347-366.
(283) Otto, A. *Journal of Electron Spectroscopy and Related Phenomena* **1983**, *29*, 329-342.
(284) Constantino, C. J. L.; Aroca, R. F.; He, J. A.; Zucolotto, V.; Li, L.; Oliveira, O. N., Jr.; Kumar, J.; Tripathy, S. K. *Applied Spectroscopy* **2002**, *56*, 187-191.
(285) He, L.; Mulvaney, S. P.; St. Angelo, S. K.; Baker, B. E.; Natan, M. J. *ACS Symposium Series* **2000**, *761*, 366-373.
(286) Vo-Dinh, T.; Hiromoto, M. Y. K.; Begun, G. M.; Moody, R. L. *Analytical Chemistry* **1984**, *56*, 1667-1670.
(287) de Jesus, M. A.; Giesfeldt, K. S.; Sepaniak, M. J. *Journal of Raman Spectroscopy* **2004**, *35*, 895-904.
(288) Yamashita, M.; Tsuji, M. *Journal of the Physical Society of Japan* **1983**, *52*, 2462-2471.
(289) Garcia, N. *Journal of Electron Spectroscopy and Related Phenomena* **1983**, *29*, 421-425.
(290) Neviere, M.; Reinisch, R. *Springer Series in Chemical Physics* **1983**, *33*, 94-96.
(291) Kerker, M. *Studies in Physical and Theoretical Chemistry* **1987**, *45*, 3-14.
(292) Zeman, E. J., 1987.
(293) Kim, Y. S.; Leung, P. T.; George, T. F. *Surface Science* **1988**, *195*, 1-14.
(294) Linder, B.; Kromhout, R. A. *Molecular Physics* **1989**, *67*, 1181-1194.

(295) Polubotko, A. M. *Physics Letters A* **1993**, *173*, 424-432.
(296) Yonezawa, Y.; Miyama, T.; Sato, T. *Nippon Shashin Gakkaishi* **1995**, *58*, 109-121.
(297) Garcia-Vidal, F. J.; Pendry, J. B. *Progress in Surface Science* **1995**, *50*, 55-64.
(298) Yang, W.-h.; Hulteen, J.; Schatz, G. C.; Van Duyne, R. P. *Journal of Chemical Physics* **1996**, *104*, 4313-4323.
(299) Hornyak, G. L.; Patrissi, C. J.; Martin, C. R. *Nanostructured Materials* **1997**, *9*, 705-708.
(300) Felidj, N.; Bernard, S.; Bazzaoui, E. A.; Levi, G.; Aubard, J. *Chimie Nouvelle* **1998**, *16*, 1895-1905.
(301) Oldenburg, S. J.; Westcott, S. L.; Averitt, R. D.; Halas, N. J. *Journal of Chemical Physics* **1999**, *111*, 4729-4735.
(302) Podolskiy, V. A.; Shalaev, V. M. *Laser Physics* **2001**, *11*, 26-30.
(303) Hu, B.; Xu, W.-q.; Wang, K.-x.; Xie, Y.-t.; Zhao, B. *Jilin Daxue Ziran Kexue Xuebao* **2001**, 57-61.
(304) Felidj, N.; Aubard, J.; Levi, G.; Krenn, J. R.; Salerno, M.; Schider, G.; Lamprecht, B.; Leitner, A.; Aussenegg, F. R. *Physical Review B: Condensed Matter and Materials Physics* **2002**, *65*, 075419/075411-075419/075419.
(305) Iliescu, T.; Bolboaca, M.; Pacurariu, R.; Maniu, D.; Kiefer, W. *Journal of Raman Spectroscopy* **2003**, *34*, 705-710.
(306) Suh, Y. D.; Schenter, G. K.; Zhu, L.; Lu, H. P. *Ultramicroscopy* **2003**, *97*, 89-102.
(307) Hao, E.; Li, S.; Bailey, R. C.; Zou, S.; Schatz, G. C.; Hupp, J. T. *Journal of Physical Chemistry B* **2004**, *108*, 1224-1229.
(308) Ye, Q.; Fang, J.; Sun, L. *Journal of Physical Chemistry B* **1997**, *101*, 8221-8224.
(309) Hildebrandt, P.; Stockburger, M. *Journal of Physical Chemistry* **1984**, *88*, 5935-5944.
(310) Gadenne, P.; Quelin, X.; Ducourtieux, S.; Gresillon, S.; Aigouy, L.; Rivoal, J.-C.; Shalaev, V.; Sarychev, A. *Physica B: Condensed Matter (Amsterdam)* **2000**, *279*, 52-55.
(311) Wei, Q.-H.; Su, K.-H.; Zhang, X.-X.; Zhang, X. *Proceedings of SPIE-The International Society for Optical Engineering* **2003**, *5221*, 92-99.
(312) Kim, W.-T.; Safonov, V. P.; Shalaev, V. M.; Armstrong, R. L. *AIP Conference Proceedings* **2002**, *622*, 306-316.
(313) Shubin, V. A.; Sarychev, A. K.; Clerc, J. P.; Shalaev, V. M. *Physical Review B: Condensed Matter and Materials Physics* **2000**, *62*, 11230-11244.
(314) Sarychev, A. K.; Shalaev, V. M. *Proceedings of SPIE-The International Society for Optical Engineering* **2001**, *4467*, 207-218.
(315) Wang, Z.; Pan, S.; Krauss, T. D.; Du, H.; Rothberg, L. J. *Proceedings of the National Academy of Sciences of the United States of America* **2003**, *100*, 8638-8643.
(316) Sarychev, A. K.; Shalaev, V. M. *Topics in Applied Physics* **2002**, *82*, 169-184.
(317) Sauer, G.; Brehm, G.; Schneider, S.; Graener, H.; Seifert, G.; Nielsch, K.; Choi, J.; Goring, P.; Gosele, U.; Miclea, P.; Wehrspohn, R. B. *Journal of Applied Physics* **2005**, *97*, 024308/024301-024308/024306.

(318) Kahl, M.; Voges, E. *Physical Review B: Condensed Matter and Materials Physics* **2000**, *61*, 14078-14088.
(319) Wirgin, A.; Maradudin, A. A. *Progress in Surface Science* **1987**, *22*, 99 pp.
(320) Jelski, D. A.; Leung, P. T.; George, T. F.; Dep. Chem.,State Univ. New York,Buffalo,NY,USA., 1988, pp 68 pp.
(321) Zhao, X.; Ando, Y.; Qin, L.-C.; Kataura, H.; Maniwa, Y.; Saito, R. *Applied Physics Letters* **2002**, *81*, 2550-2552.
(322) Kerker, M.; Wang, D.-S.; Chew, H. *Applied Optics* **1980**, *19*, 4159-4174.
(323) Shahbazyan, T. V.; Perakis, I. E. *Physical Review B: Condensed Matter and Materials Physics* **1999**, *60*, 9090-9099.
(324) Schatz, G. C.; Lazarides, A. A.; Kelly, K. L. *Abstracts of Papers, 224th ACS National Meeting, Boston, MA, United States, August 18-22, 2002* **2002**, PHYS-027.
(325) Schatz, G. C. *Theochem* **2001**, *573*, 73-80.
(326) Schatz, G. C. *Theochem* **2001**, *573*, 73-80.
(327) Doering, W. E.; Nie, S. *Journal of Physical Chemistry B* **2002**, *106*, 311-317.
(328) Lecomte, S.; Matejka, P.; Baron, M. H. *Langmuir* **1998**, *14*, 4373-4377.
(329) Otto, A.; Billmann, J.; Eickmans, J.; Ertuerk, U.; Pettenkofer, C. *Surface Science* **1984**, *138*, 319-338.
(330) Sandroff, C. J.; Herschbach, D. R. *Langmuir* **1985**, *1*, 131-135.
(331) Gao, P.; Weaver, M. J. *Journal of Physical Chemistry* **1986**, *90*, 4057-4063.
(332) Kim, Y. D.; Chung, E. C.; Jung, C. S. *Sae Mulli* **1991**, *31*, 216-222.
(333) Kruszewski, S.; Skonieczny, J. *Acta Physica Polonica, A* **1991**, *80*, 611-620.
(334) Laserna, J. J. *Analytica Chimica Acta* **1993**, *283*, 607-622.
(335) Bjerneld, E. J.; Johansson, P.; Kall, M. *Single Molecules* **2000**, *1*, 239-248.
(336) Corni, S.; Tomasi, J. *Journal of Chemical Physics* **2002**, *116*, 1156-1164.
(337) Lemma, T.; Aroca, R. F. *Journal of Raman Spectroscopy* **2002**, *33*, 197-201.
(338) Jiang, J.; Bosnick, K.; Maillard, M.; Brus, L. *Journal of Physical Chemistry B* **2003**, *107*, 9964-9972.
(339) Otto, A.; Bruckbauer, A.; Chen, Y. X. *Journal of Molecular Structure* **2003**, *661-662*, 501-514.
(340) Futamata, M.; Maruyama, Y.; Ishikawa, M. *Vibrational Spectroscopy* **2004**, *35*, 121-129.
(341) De Jesus, M. A.; Sepaniak, M. J.; Giesfeldt, K. S. *Abstracts of Papers, 228th ACS National Meeting, Philadelphia, PA, United States, August 22-26, 2004* **2004**, ANYL-047.
(342) de Jesus, M. A.; Giesfeldt, K. S.; Sepaniak, M. J. *Applied Spectroscopy* **2004**, *58*, 1157-1164.
(343) Saito, Y.; Wang, J. J.; Batchelder, D. N.; Smith, D. A. *Langmuir* **2003**, *19*, 6857-6861.
(344) Alexander, T. A.; Wickenden, A. E. *Proceedings of SPIE-The International Society for Optical Engineering* **2004**, *5588*, 78-86.
(345) Li, X.; Zhang, J.; Xu, W.; Jia, H.; Wang, X.; Yang, B.; Zhao, B.; Li, B.; Ozaki, Y. *Langmuir* **2003**, *19*, 4285-4290.

(346) Kottmann, J. P.; Martin, O. J. F.; Smith, D. R.; Schultz, S. *New Journal of Physics [Electronic Publication]* **2000**, *2*, No pp given, Article No 27.
(347) Felidj, N.; Aubard, J.; Levi, G. *Physica Status Solidi A: Applied Research* **1999**, *175*, 367-372.
(348) Kruszewski, S. *Proceedings of SPIE-The International Society for Optical Engineering* **1998**, *3320*, 281-293.
(349) Hao, E.; Schatz George, C. *Journal of chemical physics* **2004**, *120*, 357-366.
(350) Zou, S.; Janel, N.; Schatz, G. C. *Journal of Chemical Physics* **2004**, *120*, 10871-10875.
(351) Kahl, M. *Fortschritt-Berichte VDI, Reihe 9: Elektronik* **2001**, *343*, i-x, 1-158.
(352) Gunnarsson, L.; Bjerneld, E. J.; Xu, H.; Petronis, S.; Kasemo, B.; Kall, M. *Applied Physics Letters* **2001**, *78*, 802-804.
(353) Kahl, M.; Voges, E.; Hill, W. *Spectroscopy Europe* **1998**, *10*, 8,10,12-13.
(354) Kahl, M.; Voges, E.; Kostrewa, S.; Viets, C.; Hill, W. *Sensors and Actuators, B: Chemical* **1998**, *B51*, 285-291.
(355) Grabar, K. C.; Allison, K. J.; Baker, B. E.; Bright, R. M.; Brown, K. R.; Freeman, R. G.; Fox, A. P.; Keating, C. D.; Musick, M. D.; Natan, M. J. *Langmuir* **1996**, *12*, 2353-2361.
(356) Bar, G.; Rubin, S.; Cutts, R. W.; Taylor, T. N.; Zawodzinski, T. A., Jr. *Langmuir* **1996**, *12*, 1172-1179.
(357) Wachter, E. A.; Storey, J. M. E.; Sharp, S. L.; Carron, K. T.; Jiang, Y. *Applied Spectroscopy* **1995**, *49*, 193-199.
(358) Enlow, P. D.; Vo-Dinh, T. *Analytical Chemistry* **1986**, *58*, 1119-1123.
(359) Stern, M. B.; Craighead, H. G.; Liao, P. F.; Mankiewich, P. M. *Applied Physics Letters* **1984**, *45*, 410-412.
(360) Froelicher, M.; Froment, M.; Hugot-Le Goff, A.; Vansam, A. M. *Raman Spectrosc., Proc. Int. Conf., 8th* **1982**, 83-84.
(361) Weaver, M. J.; Hupp, J. T.; Barz, F.; Gordon, J. G., II; Philpott, M. R.; Dep. Chem.,Purdue Univ.,Lafayette,IN,USA., 1983, pp 26 pp.
(362) Otto, C.; Van den Tweel, T. J. J.; De Mul, F. F. M.; Greve, J. *Journal of Raman Spectroscopy* **1986**, *17*, 289-298.
(363) Kruszewski, S.; Skonieczny, J. *Optica Applicata* **1993**, *23*, 51-60.
(364) Natan, M. J.; Grabar, K. C.; Smith, P. C.; Musick, M. D.; Jackson, M. A. *Book of Abstracts, 210th ACS National Meeting, Chicago, IL, August 20-24* **1995**, COLL-091.
(365) Bilmes, S. A. *Journal of the Chemical Society, Faraday Transactions* **1996**, *92*, 2381-2387.
(366) Niaura, G.; Gaigalas, A. K.; Vilker, V. L. *Journal of Physical Chemistry B* **1997**, *101*, 9250-9262.
(367) Niaura, G.; Gaigalas, A. K.; Vilker, V. L. *Proceedings - Electrochemical Society* **1997**, *97-17*, 409-417.
(368) Siiman, O.; Feilchenfeld, H. *Journal of Physical Chemistry* **1988**, *92*, 453-464.
(369) Zhang, P. X.; Fang, Y.; Wang, W. N.; Ni, D. H.; Fu, S. Y. *Journal of Raman Spectroscopy* **1990**, *21*, 127-131.

(370) Neddersen, J.; Chumanov, G.; Cotton, T. M. *Applied Spectroscopy* **1993**, *47*, 1959-1964.
(371) Baker, B. E.; Kline, N. J.; Treado, P. J.; Natan, M. J. *Journal of the American Chemical Society* **1996**, *118*, 8721-8722.
(372) Keating, C. D.; Kovaleski, K. M.; Natan, M. J. *Journal of Physical Chemistry B* **1998**, *102*, 9404-9413.
(373) Bright, R. M.; Musick, M. D.; Natan, M. J. *Langmuir* **1998**, *14*, 5695-5701.
(374) Emory, S. R.; Haskins, W. E.; Nie, S. *Journal of the American Chemical Society* **1998**, *120*, 8009-8010.
(375) Murphy, T.; Schmidt, H.; Kronfeldt, H. D. *Applied Physics B: Lasers and Optics* **1999**, *69*, 147-150.
(376) Iacob, A. *ACH - Models in Chemistry* **1999**, *136*, 161-169.
(377) Brown, K. R.; Lyon, L. A.; Fox, A. P.; Reiss, B. D.; Natan, M. J. *Chemistry of Materials* **2000**, *12*, 314-323.
(378) Futamata, M.; Maruyama, Y.; Ishikawa, M. *Studies in Surface Science and Catalysis* **2001**, *132*, 263-266.
(379) Li, X.-L.; Xu, W.-Q.; Zhang, J.-H.; Jia, H.-Y.; Zhao, B.; Yang, B. *Gaodeng Xuexiao Huaxue Xuebao* **2003**, *24*, 707-710.
(380) Akbarian, F.; Dunn, B. S.; Zink, J. I. *Proceedings of SPIE-The International Society for Optical Engineering* **1994**, *2288*, 140-144.
(381) Akbarian, F.; Dunn, B. S.; Zink, J. I. *Journal of Raman Spectroscopy* **1996**, *27*, 775-783.
(382) Lee, Y.-H.; Dai, S.; Young, J. P. *Journal of Raman Spectroscopy* **1997**, *28*, 635-639.
(383) Garcia-Rodriguez, F. J.; Gonzalez-Hernandez, J.; Perez-Robels, F.; Vorobiev, Y. V.; Manzano-Ramirez, A.; Jimenez-Sandoval, S.; Chao, B. S. *Journal of Raman Spectroscopy* **1998**, *29*, 763-771.
(384) Li, Y.-S.; Lin, X.; Cao, Y. *Vibrational Spectroscopy* **1999**, *20*, 95-101.
(385) Lee, Y.-H.; Farquharson, S.; Rainey, P. M. *Proceedings of SPIE-The International Society for Optical Engineering* **1999**, *3857*, 76-84.
(386) Volkan, M.; Stokes, D. L.; Vo-Dinh, T. *Journal of Raman Spectroscopy* **1999**, *30*, 1057-1065.
(387) Premasiri, W. R.; Clarke, R. H.; Womble, M. E. *Proceedings of SPIE-The International Society for Optical Engineering* **2002**, *4577*, 205-212.
(388) Farquharson, S.; Smith, W. W.; Lee, V. Y.-H.; Elliott, S.; Sperry, J. F. *Proceedings of SPIE-The International Society for Optical Engineering* **2002**, *4575*, 62-72.
(389) Farquharson, S.; Maksymiuk, P. *Applied Spectroscopy* **2003**, *57*, 479-482.
(390) Bao, L.; Mahurin, S. M.; Haire, R. G.; Dai, S. *Analytical Chemistry* **2003**, *75*, 6614-6620.
(391) Maruszewski, K.; Jasiorski, M.; Hreniak, D.; Strek, W.; Hermanowicz, K.; Heiman, K. *Journal of Sol-Gel Science and Technology* **2003**, *26*, 83-88.
(392) Kang, J. S.; Lee, C. J.; Kim, M. S.; Lee, M. S. *Bulletin of the Korean Chemical Society* **2003**, *24*, 1599-1604.
(393) Liao, P. F. *Surf. Enhanced Raman Scattering* **1982**, 379-390.

(394) Vo Dinh, T.; Meier, M.; Wokaun, A. *Analytica Chimica Acta* **1986**, *181*, 139-148.
(395) Goudonnet, J. P.; Inagaki, T.; Ferrell, T. L.; Warmack, R. J.; Buncick, M. C.; Arakawa, E. T. *Chemical Physics* **1986**, *106*, 225-232.
(396) Roark, S. E.; Rowlen, K. L. *Applied Spectroscopy* **1992**, *46*, 1759-1761.
(397) Baibarac, M.; Cochet, M.; Lapkowski, M.; Mihut, L.; Lefrant, S.; Baltog, I. *Synthetic Metals* **1998**, *96*, 63-70.
(398) Strekal, N.; Oskirko, V.; Stepuro, V.; Maskevich, A.; Maskevich, S.; Nabiev, I. *Spectroscopy of Biological Molecules: New Directions, European Conference on the Spectroscopy of Biological Molecules, 8th, Enschede, Netherlands, Aug. 29-Sept. 2, 1999* **1999**, 569-570.
(399) Wadayama, T.; Aoshima, K.; Kawano, S.; Hatta, A. *Applied Spectroscopy* **2004**, *58*, 299-303.
(400) Sant'Ana, A. C.; Santos, P. S.; Temperini, M. L. A. *Journal of Electroanalytical Chemistry* **2004**, *571*, 247-254.
(401) Kostrewa, S.; Hill, W.; Klockow, D. *Sensors and Actuators, B: Chemical* **1998**, *B51*, 292-297.
(402) Vogel, E.; Kiefer, W.; Deckert, V.; Zeisel, D. *Journal of Raman Spectroscopy* **1998**, *29*, 693-702.
(403) Giesfeldt Kathleen, S.; Connatser, R. M.; De Jesus Marco, A.; Lavrik Nickolay, V.; Dutta, P.; Sepaniak Michael, J. *Applied spectroscopy* **2003**, *57*, 1346-1352.
(404) Li, H.; Patel, P. H.; Cullum, B. M. *Proceedings of SPIE-The International Society for Optical Engineering* **2004**, *5588*, 87-97.
(405) Li, H.; Cullum, B. M. *Proceedings of SPIE-The International Society for Optical Engineering* **2004**, *5261*, 142-154.
(406) De Jesus, M. A.; Giesfeldt, K. S.; Sepaniak, M. J. *Applied spectroscopy* **2003**, *57*, 428-438.
(407) Sepaniak, M. J.; De Jesus, M. A.; Giesfeldt, K. S. *American Pharmaceutical Review* **2004**, *7*, 90, 92-97,37.
(408) Wachter, E. A.; Moore, A. K.; Haas, J. W., III *Vibrational Spectroscopy* **1992**, *3*, 73-78.
(409) Schueler, P. A.; Ives, J. T.; DeLaCroix, F.; Lacy, W. B.; Becker, P. A.; Li, J.; Caldwell, K. D.; Drake, B.; Harris, J. M. *Analytical Chemistry* **1993**, *65*, 3177-3186.
(410) Lacy, W. B.; Williams, J. M.; Wenzler, L. A.; Beebe, T. P., Jr.; Harris, J. M. *Analytical Chemistry* **1996**, *68*, 1003-1011.
(411) Vogel, E.; Meuer, P.; Kiefer, W.; Urlaub, R.; Thull, R. *Journal of Molecular Structure* **1999**, *482-483*, 241-244.
(412) Dick, L. A.; McFarland, A. D.; Haynes, C. L.; Van Duyne, R. P. *Journal of Physical Chemistry B* **2002**, *106*, 853-860.
(413) Zhang, X.; Yonzon, C. R.; Van Duyne, R. P. *Proceedings of SPIE-The International Society for Optical Engineering* **2003**, *5221*, 82-91.
(414) Pio, M. S.; Kwon, S.; Choi, Y.-K.; Lee, L. P. *Materials Research Society Symposium Proceedings* **2002**, *729*, 179-184.
(415) Srituravanich, W.; Fang, N.; Sun, C.; Luo, Q.; Zhang, X. *Nano Letters* **2004**, *4*, 1085-1088.

(416) Schift, H.; Jaszewski, R. W.; David, C.; Gobrecht, J. *Microelectronic Engineering* **1999**, *46*, 121-124.
(417) Studer, V.; Pepin, A.; Chen, Y. *Applied Physics Letters* **2002**, *80*, 3614-3616.
(418) Choi, D.-G.; Jang, S. G.; Yu, H. K.; Yang, S.-M. *Chemistry of Materials* **2004**, *16*, 3410-3413.
(419) Chou, S. Y.; Krauss, P. R.; Renstrom, P. J. *Applied Physics Letters* **1995**, *67*, 3114-3116.
(420) Chou, S. Y.; Krauss, P. R.; Renstrom, P. J. *Journal of Vacuum Science & Technology, B: Microelectronics and Nanometer Structures* **1996**, *14*, 4129-4133.
(421) Chou, S. Y.; Krauss, P. R.; Renstrom, P. J. *Science (Washington, D. C.)* **1996**, *272*, 85-87.
(422) Chou, S. Y.; Krauss, P. R. *Microelectronic Engineering* **1997**, *35*, 237-240.
(423) Tan, H.; Gilbertson, A.; Chou, S. Y. *Journal of Vacuum Science & Technology, B: Microelectronics and Nanometer Structures* **1998**, *16*, 3926-3928.
(424) Li, M.; Chen, L.; Chou, S. Y. *Applied Physics Letters* **2001**, *78*, 3322-3324.
(425) Chou Stephen, Y.; Keimel, C.; Gu, J. *Nature* **2002**, *417*, 835-837.
(426) Yu, Z.; Chou, S. Y. *Nano Letters* **2004**, *4*, 341-344.
(427) Yu, Z.; Gao, H.; Chou, S. Y. *Applied Physics Letters* **2004**, *85*, 4166-4168.
(428) Austin, M. D.; Ge, H.; Wu, W.; Li, M.; Yu, Z.; Wasserman, D.; Lyon, S. A.; Chou, S. Y. *Applied Physics Letters* **2004**, *84*, 5299-5301.
(429) Halteen, J. C.; Van Duyne, R. P. *Journal of Vacuum Science & Technology, A: Vacuum, Surfaces, and Films* **1995**, *13*, 1553-1558.
(430) Hulteen, J. C., 1995.
(431) Van Duyne, R. P. *Book of Abstracts, 213th ACS National Meeting, San Francisco, April 13-17* **1997**, PHYS-290.
(432) Jensen, T. R.; Schatz, G. C.; Van Duyne, R. P. *Journal of Physical Chemistry B* **1999**, *103*, 2394-2401.
(433) Jensen, T. R.; Duval, M. L.; Kelly, K. L.; Lazarides, A. A.; Schatz, G. C.; Van Duyne, R. P. *Journal of Physical Chemistry B* **1999**, *103*, 9846-9853.
(434) Haynes, C. L.; Haes, A. J.; Van Duyne, R. P. *Materials Research Society Symposium Proceedings* **2001**, *635*, C6 3/1-C6 3/6.
(435) Haes, A. J.; Haynes, C. L.; Van Duyne, R. P. *Materials Research Society Symposium Proceedings* **2001**, *636*, D4 8/1-D4 8/6.
(436) Malinsky, M. D.; Kelly, K. L.; Schatz, G. C.; Van Duyne, R. P. *Journal of Physical Chemistry B* **2001**, *105*, 2343-2350.
(437) Whitney, A. V.; Myers, B. D.; Van Duyne, R. P. *Nano Letters* **2004**, *4*, 1507-1511.
(438) Ormonde Anjeanette, D.; Hicks Erin, C. M.; Castillo, J.; Van Duyne Richard, P. *Langmuir: ACS journal of surfaces and colloids* **2004**, *20*, 6927-6931.
(439) Yang, X. M.; Tryk, D. A.; Hasimoto, K.; Fujishima, A. *Applied Physics Letters* **1996**, *69*, 4020-4022.
(440) Yang, X. M.; Tryk, D. A.; Hashimoto, K.; Fujishima, A. *Journal of Raman Spectroscopy* **1998**, *29*, 725-732.

(441) Musick, M. D.; Keating, C. D.; Lyon, L. A.; Botsko, S. L.; Pena, D. J.; Holliway, W. D.; McEvoy, T. M.; Richardson, J. N.; Natan, M. J. *Chemistry of Materials* **2000**, *12*, 2869-2881.
(442) Shin, H. S.; Yang, H. J.; Jung, Y. M.; Kim, S. B. *Vibrational Spectroscopy* **2002**, *29*, 79-82.
(443) Sokolov, K.; Chumanov, G.; Cotton, T. M. *Proceedings of SPIE-The International Society for Optical Engineering* **1995**, *2547*, 117-124.
(444) Grabar, K. C.; Smith, P. C.; Musick, M. D.; Davis, J. A.; Walter, D. G.; Jackson, M. A.; Guthrie, A. P.; Natan, M. J. *Journal of the American Chemical Society* **1996**, *118*, 1148-1153.
(445) Natan, M. J.; Keating, C.; (The Penn State Research Foundation, USA). Application: US
US, 2000, pp 56 pp.
(446) Meier, M.; Wokaun, A.; Liao, P. F. *Journal of the Optical Society of America B: Optical Physics* **1985**, *2*, 931-949.
(447) Scheer, H. C.; Schulz, H.; Hoffmann, T.; Sotomayor Torres, C. M. *Journal of Vacuum Science & Technology, B: Microelectronics and Nanometer Structures* **1998**, *16*, 3917-3921.
(448) Gottschalch, F.; Hoffmann, T.; Torres, C. M. S.; Schulz, H.; Scheer, H.-C. *Solid-State Electronics* **1999**, *43*, 1079-1083.
(449) Khang, D.-Y.; Lee, H. H. *Applied Physics Letters* **2000**, *76*, 870-872.
(450) Schulz, H.; Scheer, H. C.; Hoffmann, T.; Sotomayor Torres, C. M.; Pfeiffer, K.; Bleidiessel, G.; Grutzner, G.; Cardinaud, C.; Gaboriau, F.; Peignon, M. C.; Ahopelto, J.; Heidari, B. *Journal of Vacuum Science & Technology, B: Microelectronics and Nanometer Structures* **2000**, *18*, 1861-1865.
(451) Schulz, H.; Lyebyedyev, D.; Scheer, H. C.; Pfeiffer, K.; Bleidiessel, G.; Grutzner, G.; Ahopelto, J. *Journal of Vacuum Science & Technology, B: Microelectronics and Nanometer Structures* **2000**, *18*, 3582-3585.
(452) Hirai, Y.; Fujiwara, M.; Okuno, T.; Tanaka, Y.; Endo, M.; Irie, S.; Nakagawa, K.; Sasago, M. *Journal of Vacuum Science & Technology, B: Microelectronics and Nanometer Structures* **2001**, *19*, 2811-2815.
(453) Roos, N.; Luxbacher, T.; Glinsner, T.; Pfeiffer, K.; Schulz, H.; Scheer, H.-C. *Proceedings of SPIE-The International Society for Optical Engineering* **2001**, *4343*, 427-435.
(454) Malaquin, L.; Carcenac, F.; Vieu, C.; Mauzac, M. *Microelectronic Engineering* **2002**, *61-62*, 379-384.
(455) Hiroshima, H.; Inoue, S.; Kasahara, N.; Taniguchi, J.; Miyamoto, I.; Komuro, M. *Japanese Journal of Applied Physics, Part 1: Regular Papers, Short Notes & Review Papers* **2002**, *41*, 4173-4177.
(456) Pfeiffer, K.; Fink, M.; Ahrens, G.; Gruetzner, G.; Reuther, F.; Seekamp, J.; Zankovych, S.; Sotomayor Torres, C. M.; Maximov, I.; Beck, M.; Graczyk, M.; Montelius, L.; Schulz, H.; Scheer, H. C.; Steingrueber, F. *Microelectronic Engineering* **2002**, *61-62*, 393-398.
(457) Scheer, H.-C.; Glinsner, T.; Wissen, M.; Pelzer, R. *Proceedings of SPIE-The International Society for Optical Engineering* **2004**, *5374*, 203-208.

(458) Tan, L.; Kong, Y. P.; Pang, S. W.; Yee, A. F. *Journal of Vacuum Science & Technology, B: Microelectronics and Nanometer Structures--Processing, Measurement, and Phenomena* **2004**, *22*, 2486-2492.
(459) Niino, H.; Ding, X.; Kurosaki, R.; Narazaki, A.; Sato, T.; Kawaguchi, Y. *Applied Physics A: Materials Science & Processing* **2004**, *A79*, 827-828.
(460) Cheng, X.; Chang, M.-H.; Guo, L. J. *Proceedings of SPIE-The International Society for Optical Engineering* **2004**, *5374*, 337-347.
(461) Ge, H.; Wu, W.; Li, Z.; Jung, G.-Y.; Olynick, D.; Chen, Y.; Liddle, J. A.; Wang, S.-Y.; Williams, R. S. *Nano Letters* **2005**, *5*, 179-182.

Part 3

Discontinuous Metal Films for SERS Substrates: Theory, Preparation, and Characterization

Introduction

The EM theory of SERS emphasizes the fundamental role that the dielectric of the solid support plays in the enhancement process. Noble metal nanoparticles deposited on solid supports by physical vapor deposition (PVD) have been incorporated into sensors and optical devices, [1-5] surface-enhanced substrates,[6-14] and have been used as model systems for supported nano-metallic catalysts. [15] Numerous materials have been used as solid supports for thin metal films. Silicon, quartz, glass, and thermoplastic polymers have all been used with different degrees of success. These materials produce a surface-bound layer of metal nanoparticles below the percolation threshold, the point of conductivity. While these SERS substrates often have high RSDs from spot to spot, overall, from one substrate to another they are reasonably reproducible. This is due to the controllable parameters for physical vapor deposition.

In contrast to the surface-bound metal nanoparticles, if elastomers and polymers near their glass transition are used, a nanocomposite can be produced. In this genre of substrates, the metal nanoparticles are distributed within the polymer matrix, not unlike the metal sol-gels. Physical vaporization deposition (PVD), ion implantation, and ion exchange have been used to accomplish the formation of metal nanoparticles within the solid support.[16-22]In the previous chapter it was discussed that the surface plasmon resonance of these substrates is the result of the shape, size, and spacing of metallic anoparticles. The deposition and implantation parameters critically affect the initial morphology of the nanoparticles. Thermal annealing[23-26] and laser irradiation [27-31] can be used to further transform the morphology, often by either smoothing the surface or

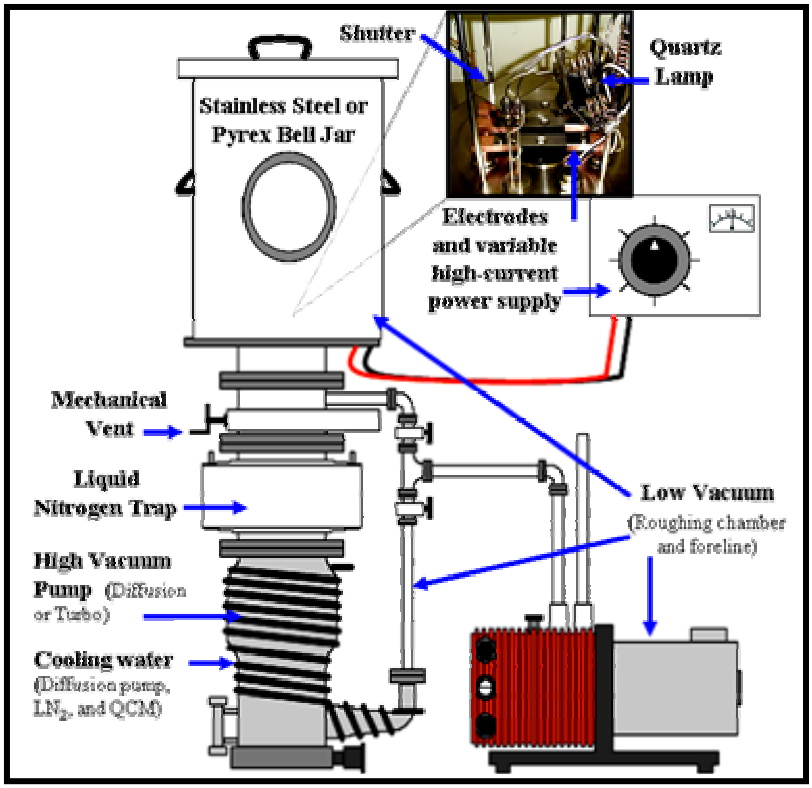


Figure 3.1. Basic physical vapor deposition system with its component parts

inducing aggregation. Physical vapor deposited metal nanoparticles have a distinctive fractal-like morphology that can act as sites for further SERS enhancement.[32-37]

Physical Vapor Deposition Theory

Physical vapor deposition (PVD) uses a resistively heated source under high vacuum (~1 x10^{-6} Torr) to melt or sublime a material depending on its inherent vapor pressure and melting point. A typical configuration of a PVD system can be seen in Figure 3.1. Evaporation or effusion of the material is determined by the choice of the

thermal source. Langmuir (non-equilibrium) evaporation from a droplet, also known as a point source, is isotropic. The nanoparticles produced have a narrow range of kinetic energies and have a more directional plume. Certain materials, such as chromium, do not melt, but merely sublime as they are resistively heated. Polymers, Au, and certain other materials form a molten pool that imparts a wide distribution of kinetic energies and a non-directional plume when vaporized. One means to compensate for this non-uniformity is to place these types of materials into a box-type source with a small hole from which the vapor can escape. Effusion, thus mimics a confocal hole, and allows for particles with a more narrow range of kinetic energies to travel toward the substrate. As the vapor travels in the chamber toward the solid support, agglomeration and condensation processes can form the seeds of the nanoparticles. An illustration of these processes can be seen in Figure 3.2. Condensation of the gas phase to solid (or liquid) occurs only if the system is at a temperature that will create a saturated vapor of the evaporant; this is easily achieved under high vacuum conditions. Control of the substrate temperature is crucial to the organization of the thin permanent thin film. High substrate temperature during deposition results in higher rate of desorption of evaporant, a greater degree of rearrangement, and an annealed metal film will be produced. The substrates can either be heated by quartz lamps that are at the same height as the sources or via thermistor mounted on the verso of the support. Precise control over the substrate temperature is required to prevent the excessive diffusion (reverse evaporation) of the material, which will result in pinholes in the thin film. However, the judicious use of heat before deposition on non-thermally sensitive materials can ensure a better film as this will desorb water, oils, and other contaminants.

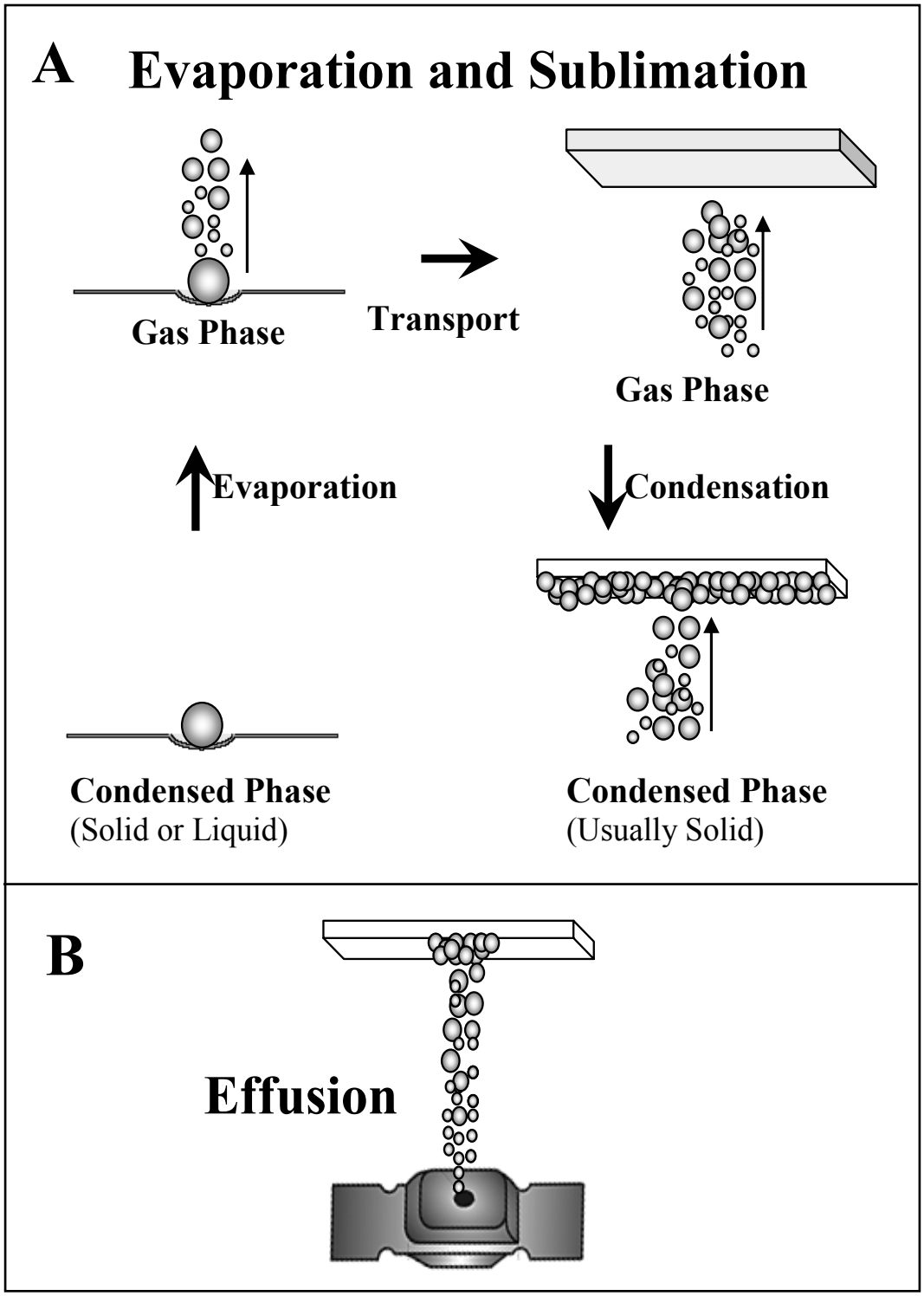


Figure 3.2. Comparison of evaporation (A) and effusion (B) processes during physical vapor deposition. Condensation and agglomeration occur as vapor plume travels toward the solid support producing a wide range of nanoparticle sizes and shapes. Effusion is evaporation or sublimation through an orifice such as the lidded thermal sources is directional.

During the deposition process, molecules, adatoms, and nanoparticles of the evaporant collide with a solid support. The evaporant is adsorbed or reflected by the solid support. This depends critically on its kinetic energy, which is much higher than that of the support and the kinetic energy is determined by the temperature of the resistively-heated source. The amount of kinetic energy will affect the rate at which the evaporant comes to equilibrium with the substrate surface via migration, adhesion, and desorption. Sorption can be defined as the adherence of a particle to a surface either through physisorption or chemisorption. The adatoms, adclusters, and nanoparticles will diffuse or migrate around on the surface gradually losing their thermal (kinetic) energy until they come to equilibrium with surface. At this point, they do not have sufficient energy to escape the surface or desorb, which is known as physisorption. In contrast, chemisorption occurs when energy is lost due to a chemical reaction that creates a permanent bond between the particle and other particles.

Migration of the evaporant results in nucleation and cluster formation. Clusters have lower kinetic energy due to small surface to volume ratio, thus do not desorb as readily as individual molecules, adatoms, or nanoparticles. This process results in the formation of thin films of the desired evaporant.

Thermal Evaporation Sources

Thermal sources for PVD are simple, robust, and widely available. Generally thermal sources are open heaters that expose the SERS substrates to IR radiation during deposition, which may damage sensitive solid support materials. Sources are produced in a myriad of shapes that are designed for specific applications (Figure 3.3). Typically,

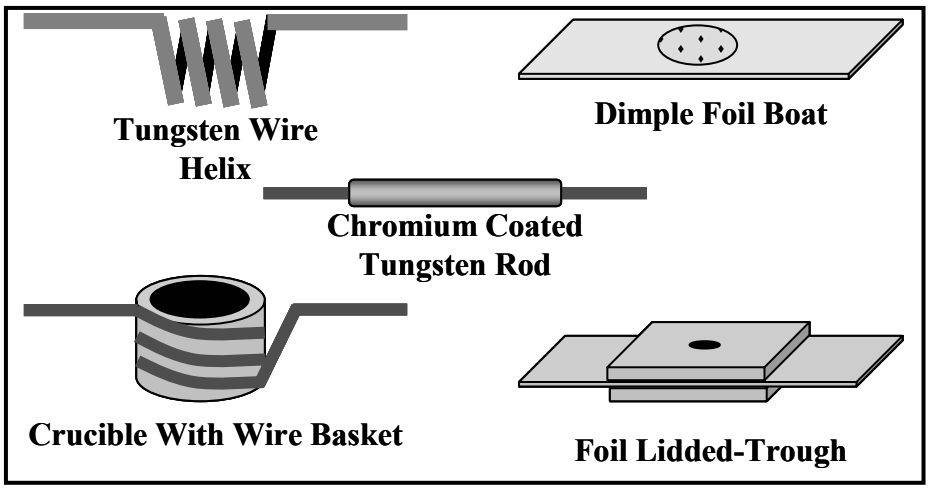


Figure 3.3. Common thermal sources for evaporation and effusion used for physical vapor deposition of materials

these sources are made of refractory metals such as W, Mo, or Ta that can withstand the cyclic heating and cooling process. However, they can only be heated to temperatures of 1800^0C, which limits the types of materials that can be evaporated. The thermal sources are attached to low voltage, high-currents supplies (e.g.,Variacs or rectifiers) that permit deposition rates from 0.1-5.0Å/s.

The evaporant (metal, organic, or inorganic material) is placed in contact with refractory metal boat or filament or placed inside a crucible that is surrounded by a refractory filament. Certain materials such as polymers and chromium require crucibles that are made out of aluminum oxide, quartz, or vitreous carbon. This provides a means to prevent the thermal degradation or undesirable polymerization of the evaporant. As the electrical resistance is vital to the process, the sources are made in several different thicknesses and can be pre-coated with aluminum oxide, notched, or bent to alter the electrical resistance.

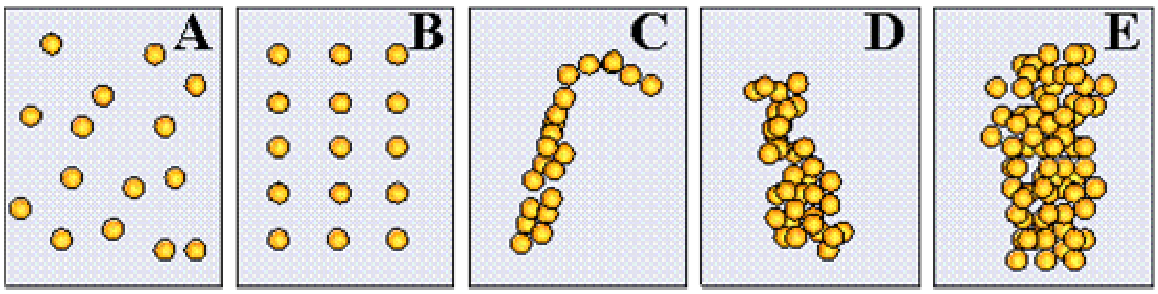


Figure 3.4. The cluster aggregation on the surface of a solid support. A) random topography B) regular topography, C) coagulation aggregate, D) coalescence aggregate, E) nugget or cluster

Thin Film Theory

The observed growth of a thin film begins with the condensation stage at which point the adsorption of monomers and oligomers of polymeric materials, or adatoms, adclusters, and atoms of metals, molecules of inorganic materials begin to form on the support surface. Figure 3.4 shows some of the typical configurations of these clusters. It is rare to find large areas of the regular topography unless the surface of the solid support has been chemically modified.

M. Volmer and A. Weber first described the formation of the adcluster/nanoparticle island formation in 1926.[38] Figure 3.5 illustrates this theoretical growth pattern and that of the subsequent proposed theories. In 1938, J. N. Stranski and L. Krastanov modified Volmer and Weber's island theory to address the potential of distinct layers of metal atoms being formed between the islands when a continuous film was produced.[39] F. C. Frank and J. H. Van der Merwe noted that ideal epitaxy, or layered growth, was a result of vacuum proximity and innate substrate characteristics.[40]

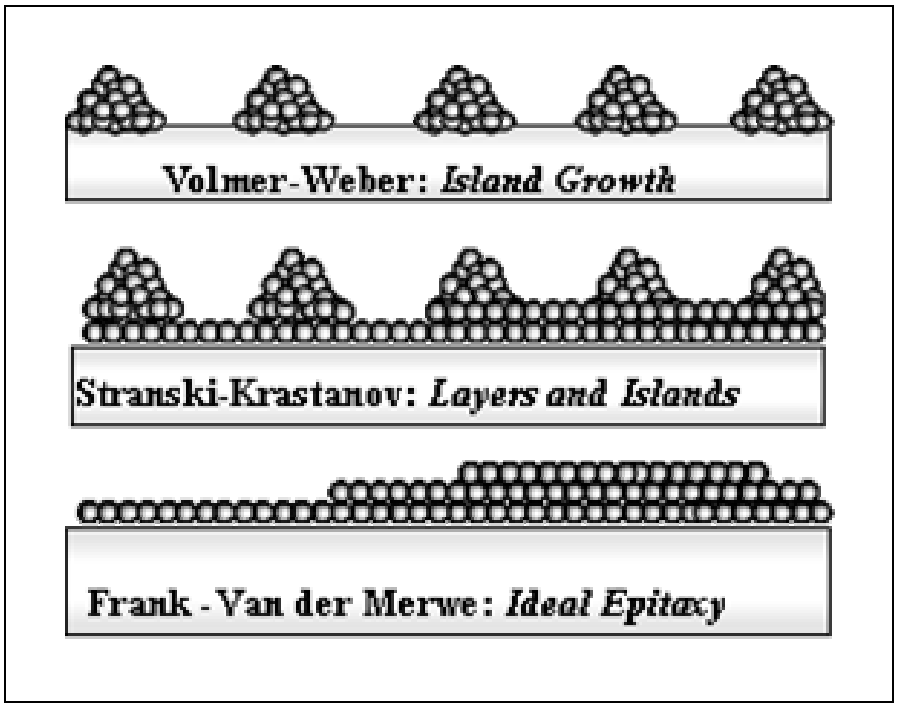


Figure 3.5 Theoretical thin film growth patterns

The current hypothesis in the field is that all of these theoretical growth patterns exist simultaneously on a single substrate.[41-44] The full cycle of film growth is illustrated in Figure 3.6, which incorporates all of these growth patterns. The formation of a thin film is due to the initial kinetics of the vapor imparted by the resistive heating. The nanoparticles will migrate on the surface and when they encounter other nanoparticles they can form nuclei or coalesce. These embryonic nanoparticles grow to a supercritical size by incorporating more deposition material surrounding them, thus the kinetic energy is reduced to potential energy. The nucleation process continues and the nascent nanoparticles form small clusters. With continued evaporant impinging on the support, the clusters fuse into islands. The process of migration, nucleation, and cluster formation

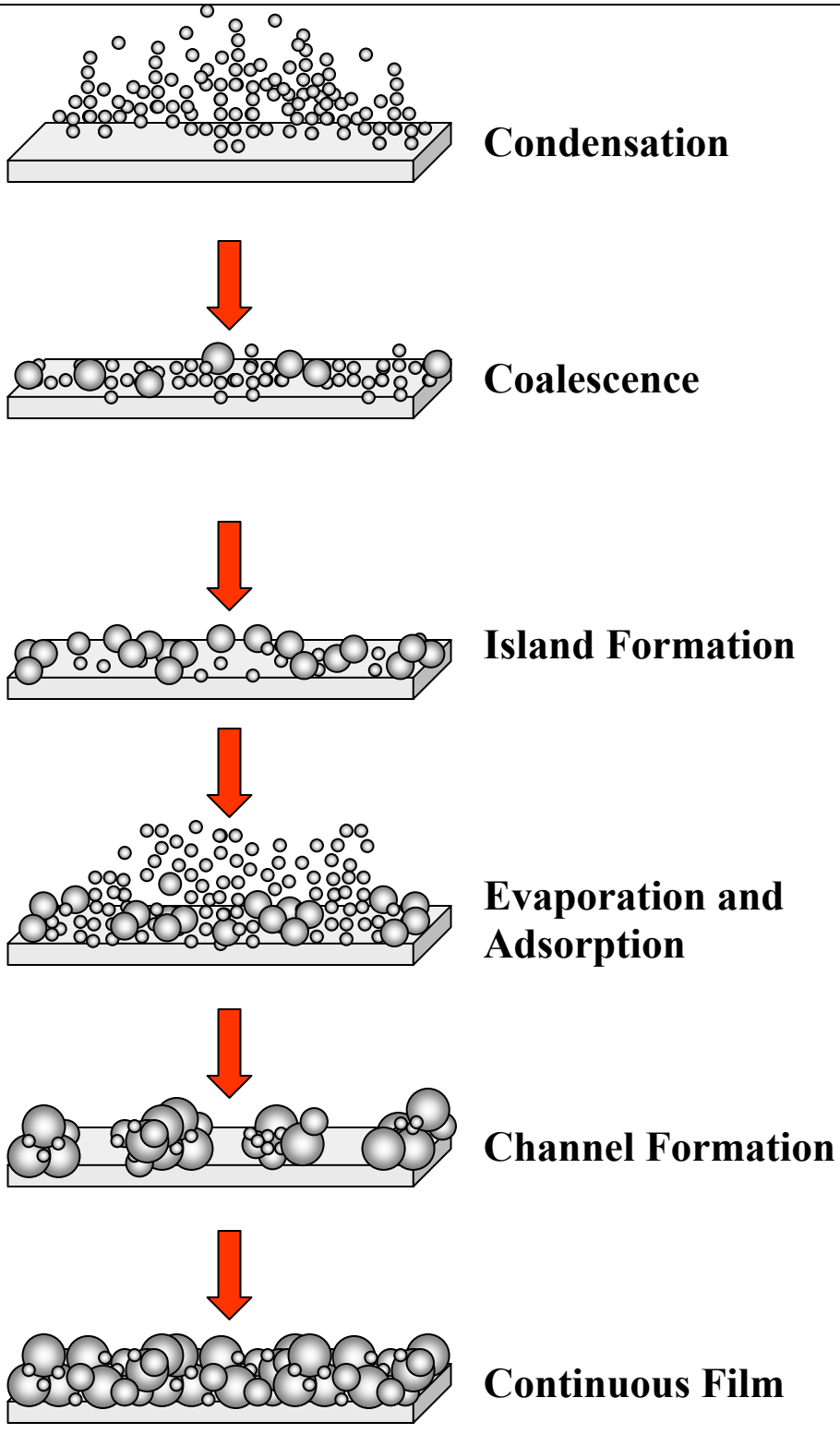


Figure 3.6. Observed formation of a thin metal film by physical vapor deposition

continues, which creates areas devoid of evaporant. As additional evaporant finds its lowest energy sites, the evaporant begins to adhere to these open areas. The cycle continues with a channel stage, such that larger islands are formed that produce holes and channels between the islands. Eventually, with continuous evaporation, a continuous film will be produced that will be electro-conductive and it is known as the percolation threshold.

Considerations for Solid Supports

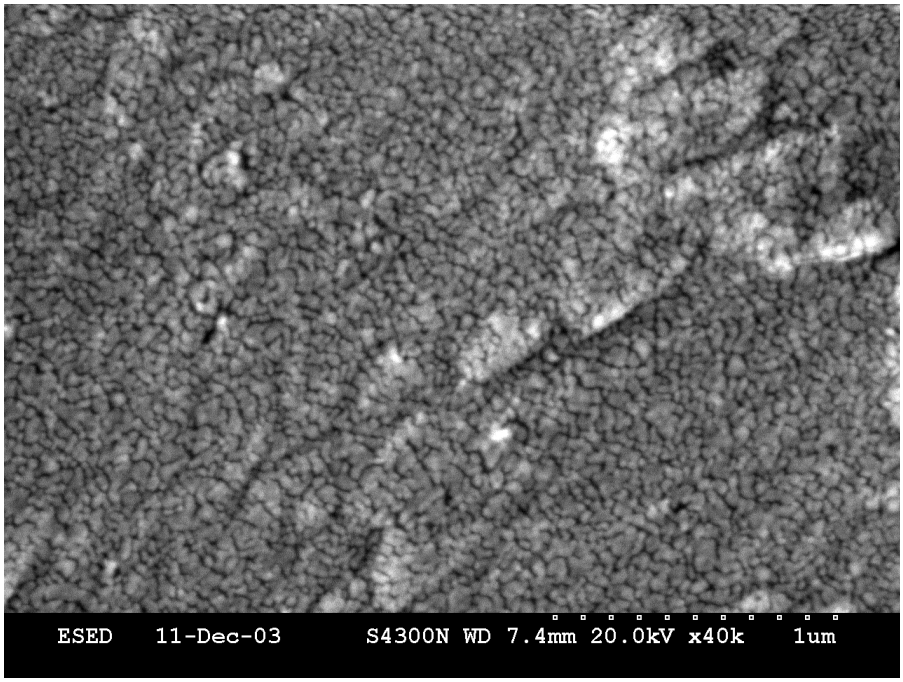
For every potential PVD substrate, there are critical working parameters for each material and final product. Organic and inorganic-based materials, as well as metals and polymers can be used for solid supports. The inherent roughness, inclusions, or flaws of a substrate material can determine potential nucleation sites during PVD. In addition, contamination on the surface, such as particulates, chemical, hydrocarbon, and water film residues, as well as sebaceous deposits from fingerprints provide additional nucleation site. These, in turn, affect the final morphology of the thin film due to the formation of islands, channels, and epitaxial film growth. The mechanical properties of solid supports also need to be accounted for when choosing an appropriate material. Mechanical properties such as stability, ruggedness, thermal response, expansion coefficients, glass transition temperatures, permeability, and most importantly for SERS applications, dielectric constants often need to be balanced against each other, depending on the specific application. Similarly the optical properties of a substrate can influence the choice of materials. Whether a material will absorb light at a specific wavelength, if it is opaque, or if it fluoresces will affect the applicability for a technique.

Surface preparation for PVD is highly dependant upon the chemical composition and mechanical properties of a substrate. Cleaning procedures must be appropriate per type of contamination and for the substrate material. The substrate condition, the degree of roughness, inclusions, or general imperfections, determine the extent to which the material will require either chemical or physical polishing before deposition.

The chemical composition at the surface can be manipulated or permanently altered by pre-treatment with plasmas, UV, or ozone.[16, 45-48] This can change the hydrophobicity/phillicity of polymeric surfaces. Piranha or potassium hydroxide solutions can chemically etch the surfaces of glass, quartz, and silicon.[49] Chemisorption of fluorinated compounds, amines, thiols, silanol can produce self-assembled monolayers (SAMs) that can dramatically affect the final thin film or can be used to manipulate it after deposition.[49, 50]

Organic and inorganic-based materials, metals, and polymers have unique deposition conditions that are depend the temperature sensitivity of the material.[16, 19, 51, 52] This will determine the deposition rate, as the faster the rate, the higher the internal temperature of the chamber. The surfaces of low glass transition temperature polymers, like polydimethylsiloxane (PDMS), often exhibit increased surface roughness after exposure to the IR radiation of the thermal sources. The PVD system geometry can also influence the homogeneity of size and proximity. The closer to the thermal sources the larger and more irregular the nanoparticles will be (Figure 3.7).

Other factors that will influence the morphology of a thin film include the generation of lattice flaws during the migration of nanoparticles on the surface, the extent



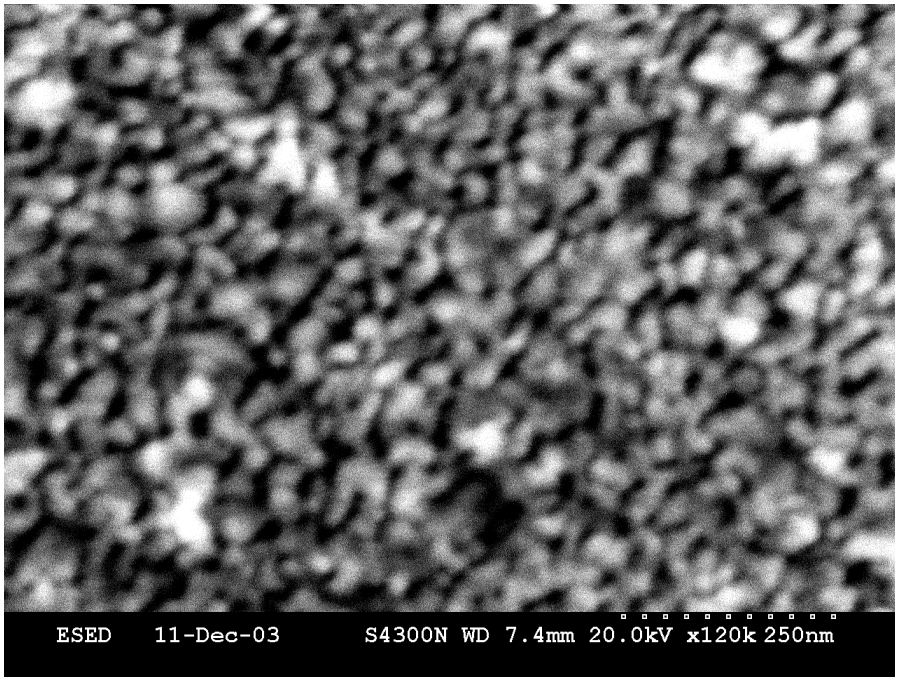


Figure 3.7. A) Example of inherent roughness of Ag-coated PDMS, B) Example of inhomogeneity of nanoparticle size and shape due to the vapor deposited metal film (both samples: ~20 nm Ag, 1Å/s).

of the surface mobility of evaporant, and the formation of oxides during and after deposition. It is imperative that the deposition rate remain constant during PVD as it will induce additional roughness and inhomogeneity in the film (Figure 3.7).

Characterization of Thin Films

Characterization of thin films will establish the critical criteria for consistent results. These range from relatively inexpensive choices such as UV-Vis spectroscopy, DC conductivity, and optical light microscopy, to the very rarified and expensive like Rutherford Back-scattering spectroscopy (RBS) and electron microscopy. Failure and performance analysis is a crucial step to guarantee future reproducibility and reliability; access to appropriate instrumentation ensures correct early diagnosis of system errors and material failures. Systematic errors include deposition rate and thickness, system geometry, vacuum pressure, and proper cleaning procedures. The collection of functional baseline performance per application is necessary to determine acceptable limits for both the materials and the applications. By monitoring the substrates as a function of time, changes in color, weight, resistivity, environmental and chemical stability, as well as, the functionality of the thin films can be detected and appropriate actions can be determined.

As with many analytical techniques, appropriate sampling procedures need to be in place to establish representative samples. Some techniques permit the direct sampling of thin film coated substrates, however, it should be ascertained first whether or not such a technique will render the substrate non-functional for future applications. Stylus-based characterizations, such as profilometry and contact mode atomic force mircroscopy

(AFM), may provide crucial information about film stress and adhesion, but there will be permanent damage to the films. If a solid support is comprised of certain polymers, such as PDMS, that have an adhesive-like layer or the film and substrate morphology are extremely rough, this will also limit the application of certain probe-type instrumentation. Most PVD systems have in-site characterization instrumentation, such as the quartz crystal microbalance to measure film thickness and deposition rate. Electrical resistivity instruments can easily be introduced into the PVD chamber for conductivity measurements.

Table 3.1 references a number of techniques and the sample preparation required for the characterization of thin metal films on solid supports. One of the best, and least expensive, characterization techniques is strictly optical. Visual inspection of substrates before and after deposition to confirm that they are free of contaminants and that the films are homogeneous in color is critical for most applications. Such inspections can show if the color is in the observed range of functionality based on past depositions; this can indicate if there are serious problems with the diffusion pump or liquid nitrogen trap. Additional inspections should ascertain if an entire batch is equivalent, such that the vapor plume evenly interacted with all, or if there are "dead" spots within the chamber due to interior architecture. Illumination of thin films with oblique lighting will often show imperfections, areas of greater roughness, or particulates on the surface. This can assist in choosing areas for sampling.

It is important to monitor thin films over a period of time. For those that are being developed as SERS substrates, the length of time that these materials are functional for both qualitative and quantitative measurements should be determined. This will be a

Table 3.1 Characterization Techniques

Type of Characterization	Instrumentation	Sample Preparation	Comments
Elemental *Surface, bulk, trace, and distribution*	**XPS** (X-ray Photoelectron Spectroscopy)	Small 1 cm^2 samples must be cut from substrates, no additional preparation is necessary. Must be able to tolerate high vacuum pressures.	Surface sensitive characterization tool that provides information about the chemical state and concentration of the elements. Sampling depth is less than 10 nm.
	EDXF (Energy Dispersive X-Ray Fluorescence) **WDXF** (Wavelength Dispersive X-Ray Fluorescence)	Same as above.	EDXF or WDXF are done in conjunction with SEM. Rapid semi-quantitative analysis of elements down to boron in the ppm range. Determines surface composition (1 μm) and bulk composition (>10 μm) by using different emission lines that have unique depth penetration
	SAM (Scanning Auger Microscopy)	Sample size varies from few millimeters to 1-2 cm^2. Conducting materials are directly analyzed. Those below the percolation threshold are difficult due to charging effects. Optimization of the electron beam conditions will minimize this problem. Must be able to tolerate high vacuum pressures.	Surface chemistry characterization and at interfaces between conductive and non-conductive materials. Depth analysis is limited to 1-5 nm. Areas as large as 0.5 mm^2 can be interrogated to determine average composition. Secondary electron images also provide topographical information that can be directly correlated to the surface composition

Table 3.1 Continued

Type of Characterization	Instrumentation	Sample Preparation	Comments
Chemical and Molecular Composition: *bonding, distribution, corrosion, etch rate, stoichiometry, catalytic properti*es	**IR** Infrared Spectroscopy	Must have IR transparent or absorbent solid support. Can be prepared for diffuse reflectance and attenuated total reflectance configurations. Sample requires no preparation.	Semi-quantitative analysis can be performed on both the thin film and solid support materials. Fingerprint regions can confirm if thermal degradation has occurred, especially during the deposition of organics. IR microscopy can provide chemical identification that can be correlated with topographical images.
	Raman Spectroscopy/ Microscopy	No sample preparation is necessary.	Raman and SERS can be used to probe surface chemistry and homogeneity via mapping procedures similar to IR microscopy. Semi-quantitative analysis can be performed on the substrates.
	XPS (X-ray Photoelectron Spectroscopy)	See above in Elemental Analysis	XPS can provide chemical shifts and structure information as well as the oxidation state of the elements on the surface. Can only be used for semi-quantitative analysis.

Table 3.1 Continued

Type of Characterization	Instrumentation	Sample Preparation	Comments
Morphology: Structure and Microstructure: *Surface, bulk, local, micro-porosity, lattice flaws and, defects, size, shape, and proximity*	**(S)TEM** (Transmission Electron Microscopy (Scanning and Conventional))	Sample preparation is an art and is very time consuming. Less than 3mm in diameter and must be less than 100 μm thick. Samples either need to be prepared on TEM grids or solid supports need to be chemically thinned or electropolished before PVD. Ultramicrotomes can be used for cross-sectioning polymeric composite substrates.	(S)TEM is well-suited for the analysis of composite materials, where cross-sectional analysis determines if evaporant has embedded into the substrate. It can be used to determine the crystal structures of the metal nanoparticles. Certain polymers are very sensitive to the electron beam and can be irreversibly damaged. Image resolution is less than 0.2 nm. Elements lighter than neon can only be detected using an ultra-thin EDS detector or energy loss spectrometer (EELS).
	SEM (Scanning Electron Microscopy)	Small 2 cm^2 samples must be cut from substrates, no additional preparation is necessary. Conducting and non-conducting materials can be directly analyzed. Must be able to tolerate high vacuum pressures. Ultramicrotomes can be used for cross-sectioning polymeric composite substrates.	Resolution with most SEMs is ~1.5-3.0 nm, which is less than that of TEMs, however the sample require less preparation. Topography and chemical composition can be determined using SEM and EDS. Nanocomposite materials below the percolation threshold and uncoated polymeric materials can be imaged with an environmental secondary electron detector under variable vacuum modes with reduced beam currents to counteract charging effects.

Table 3.1 Continued

Type of Characterization	Instrumentation	Sample Preparation	Comments
Morphology: Structure and Microstructure (cont.)	**AFM** (Atomic Force Microscopy)	Samples must be relatively flat and non-adhesive. They can be either conductive or non-conductive.	The forces between the probe tip and surface are measured and are determined by the tip geometry, spring constant of the probe, and distance between probe and sample. Standard AFMs can be used in either the repulsive/contact and attractive/imaging modes. Contact modes permanently damage the sample and are not recommended for surface analysis of PVD substrates. Imaging modes oscillate the tip at or near its resonance frequency and monitor the shifts in frequency as tip approaches the sample. AFM is sensitive to electrical and magnetic forces and can be used to determine the Young's modulus of polymeric materials using Force modulation techniques.

Table 3.1 Continued

Type of Characterization	Instrumentation	Sample Preparation	Comments
Morphology: Structure and Microstructure (cont.)	**XRD** (X-ray Crystal Diffraction)	Small 25 μm to 1 mm thick samples of up to ~2 $cm^{2.}$	XRD can identify compounds as well as the crystal structure and can be used to perform crystalline phase analysis. It can be used to determine the preferred chain conformations in polymeric solid supports and if they are altered due to PVD.
Physical Properties: *Density, thickness, surface area*	**Microscopy:** Light, electron, and probe	Sample preparation will depend on type of microscopy chosen. See above for electron and probe. Light microscopy will not require sample preparation.	Density and thickness can be determined with optical light microscopy (OLM). It is one of the oldest characterization techniques. Resolution is limited to 0.2 μm. Bright and dark-field imaging, transmitted (sample <5 μm thick) and reflected light, polarized light microscopy are just a few imaging modes available. Differential contrast and phase contrast are particularly useful for nanocomposites. Depth of field is determined by the numerical aperture of the objective and can range from 0.4 to 8 μm.

Table 3.1 Continued

Type of Characterization	Instrumentation	Sample Preparation	Comments
Physical Properties: (cont.)	**Profilometer**	Similar to AFM preparation Profilometers can either use a metal stylus or a laser beam to interrogate the surface. Samples must not be adhesive when using metal stylus. .	Metal styluses can impart damage to the surface which results in a possible error of up to 30%. These are spatially limited, due to the tip geometry and size and are very sensitive to ambient vibrations. Roughness can only be measure if greater than 0.05 μm. With laser profilometers, roughness measurements on the order of angstroms can be achieved for nearly all surfaces, including soft and adhesive. As with many optical devices, precise alignment of the instrument is crucial to the accuracy and precision of its data.
	RBS (Rutherford Backscattering Spectroscopy)	Small 2 cm^2 samples must be cut from substrates, no additional preparation is necessary. However, several samples should be interrogated in order to ensure representative sampling.	RBS can be used for elemental analysis and for collecting a collision cross-section, and for the analysis of near-surface regions. This can be used to model a surface without using calibration standards for thin films where the original composition is unknown. It can be used for quantitative analysis with depth profiling up to several thousand angstroms (depending on the mass of the particles) without destroying or altering the substrates.

Table 3.1 Continued

Type of Characterization	Instrumentation	Sample Preparation	Comments
Physical Properties: (cont.)	**RBS** (Rutherford Backscattering Spectroscopy)		RBS, however, has a very limited lateral resolution (~ 1mm) due to the beam size, and rough surfaces further diminish its resolution. RBS can also be used for the non-destructive study of material diffusion at an interface as a function of time and temperature.
Optical Properties: *absorption, reflection, color, index of refraction*	**UV-Vis** spectrophotometry	No additional sample preparation is required. It is best to place the sample with the thin film toward the beam. Tape or create a holder for sample in front of detector.	A scanning or photodiode UV-Vis is used to determine the optical extinction and the bandwidth of surface plasmon resonance. a function of time on the substrates.
	UV-Vis spectrophotometry		Derivative spectrophotometry can reveal the lambda max of the surface plasmon band. UV-Vis can be utilized to study the effect of oxide formation as
	PLM (Polarized Light Microscopy)	Light microscopy will not require sample preparation. Cargill refractive index oils can be used to determine refractive index of substrate and thin film, respectively.	The crystal system and its incipient growth history can be resolved with PLM. Refractive index of thin films and substrates (pleochroisim and dichroism), birefringence, color, size, "purity", morphology, microstructure, and can be determined.

Table 3.1 Continued

Type of Characterization	Instrumentation	Sample Preparation	Comments
Optical Properties (cont.)	**Colorimetry & Colorimetric Imaging**	No sample preparation is required for conventional colorimetry. Colorimetric imaging will require treating a thin film with fuming HCl, then covering with dephenylcarbizide in gelatin-glycerin, which will form a film for analysis.	Changes in nucleation will be apparent by non-uniform coloration. Characterization with colorimetry can quantify the appearance of the thin metal films on glass or other transparent materials. Interfacial material can also be determined after chemical etching, such as chromium oxide. Colorimetric imaging can measure micro-porosity, pinhole density, and corrosion by-products
Mechanical Properties: *Young's (elastic) modulus, hardness, yield stress, fracture toughness, wear resistance*	**SThM** (Scanning Thermal Microscopy)/ **AFM** (Atomic Force Microscopy)	Solid surfaces are best for this technique. Elastomeric polymers and thin polymer films are not suitable.	AFM tip acts as a miniature thermocouple, making temperature measurements with a resolution of 1 μm - 100 nm. Topographical imaging can be done simultaneously to correlate with the thermal maps. Microscope can be combined with hot and cold stages for the determination of amorphous and crystalline regions of polymeric substrates and thin metal films or to determine whether adherence of thin film to a surface.

Table 3.1 Continued

Type of Characterization	Instrumentation	Sample Preparation	Comments
Mechanical Properties (cont.)	**Nanoindentation**	Features less than 100 nm across and thin films less than 5 nm thick can be evaluated. Solid samples are best. Some elastomer-based nanocomposites are not suitable (PDMS) if they have an adhesive surface.	Nanoindentation uses a hard tip, typically a diamond that is pressed into the sample with a known load. This allows for depth-sensing in the sub micrometer range with very high accuracy and precision. Load displacement data can be interpreted to obtain hardness, elastic modulus, and other mechanical properties. Can be used in conjunction with AFM imaging for corroboration
Electrical Properties: *Resistivity, dielectric constant, carrier mobility and lifetime*	**Resistivity and Sheet Resistivity**	No sample preparation is required	Generally a four point configuration of probes such that the two outer most probes inject the current across the film and the voltage drop is measure by the two inner probes. Commercial instruments can measure resistance from 1mΩ to 500kΩ and pin separation a small as 0.025 inches.

Table 3.1 Continued

Type of Characterization	Instrumentation	Sample Preparation	Comments
Electrical Properties (cont.)	**DC Conductance/ Impedance**	Substrates should be prepared for PVD	Substrate needs to be masked off and initial PVD to create thick film to make small electrodes. After mask is removed, wires are attached to the substrate and to the chart recorder. A second deposition is completed while monitoring the rise of conductance across the surface. This will be used to determine the percolation threshold for different deposition rates and substrates.
	TCR (Temperature Coefficient of Resistivity)	Similar to DC Conductance/Impedance	Measurement of how resistivity changes with temperature. TCR can be used on metal films on non-conductive substrates and can be used to monitor nucleation of metal nanoparticles, the percolation threshold, and the development of oxides.
Barrier Properties	**Permeation**	No sample preparation is required	Determination of pinholes in coatings via a weight or volume of analyte per unit of time per unit area. Oxygen and water vapor transmission are the ASTM standards. Permeation is dependant upon temperature, substrate material, adsorption and desorption of analyte, solubility within substrate, diffusivity and thickness of substrate. Often used in conjunction with conductivity measurements.

Table 3.1 Continued

Type of Characterization	Instrumentation	Sample Preparation	Comments
Barrier Properties (cont.)	**Diffusion**	No sample preparation is required	Diffusion is temperature and molecule size dependent. As some thin films and polymer-metal nanocomposites can be used as diffusion barriers, determination of the grain structure is necessary. (Amorphous grain structure work best.) Diffusion is driven by chemical gradients, the analyte (H_2, O_2, H_2O, etc.) would need to be monitored across the film from the source (both normal to and laterally away from the source)

function of the type of solid support and the metal chosen for the thin film. Chemical treatments can also alter the substrate, cleaning procedures with potassium hydroxide, piranha, nitric acid, or even aqua regia can have detrimental effects on certain materials. Some of the lithographic resists and glass substrates can be recycled a number of times, but eventually they, too, will degrade to a point where qualitative measurements can not be collected.

References

References

(1) Kostrewa, S.; Hill, W.; Klockow, D. *Sensors and Actuators, B: Chemical* **1998**, *B51*, 292-297.

(2) Heilmann, A.; Kiesow, A.; Spohn, U.; Janasek, D.; (Fraunhofer-Gesellschaft zur Foerderung der Angewandten Forschung e.V., Germany). Application: DE DE, 2000, pp 6 pp.

(3) Culha, M.; Lavrik, N.; Sepaniak, M. J. *Abstracts of Papers, 223rd ACS National Meeting, Orlando, FL, United States, April 7-11, 2002* **2002**, ANYL-041.

(4) Li, H.; Patel, P. H.; Cullum, B. M. *Proceedings of SPIE-The International Society for Optical Engineering* **2004**, *5588*, 87-97.

(5) Li, H.; Cullum, B. M. *Proceedings of SPIE-The International Society for Optical Engineering* **2004**, *5261*, 142-154.

(6) DiLella, D. P.; Moskovits, M. *Journal of Physical Chemistry* **1981**, *85*, 2042-2046.

(7) Goudonnet, J. P.; Begun, G. M.; Arakawa, E. T. *Chemical Physics Letters* **1982**, *92*, 197-201.

(8) Dornhaus, R. *Vib. Surf., [Proc. Int. Conf.], 2nd* **1982**, 445-455.

(9) Vo-Dinh, T.; Hiromoto, M. Y. K.; Begun, G. M.; Moody, R. L. *Analytical Chemistry* **1984**, *56*, 1667-1670.

(10) Vo Dinh, T.; Meier, M.; Wokaun, A. *Analytica Chimica Acta* **1986**, *181*, 139-148.

(11) Davies, J. P.; Pachuta, S. J.; Cooks, R. G.; Weaver, M. J. *Analytical Chemistry* **1986**, *58*, 1290-1294.

(12) Alak, A. M.; Vo-Dinh, T. *Analytical Chemistry* **1987**, *59*, 2149-2153.

(13) Zeman, E. J.; Carron, K. T.; Schatz, G. C.; Van Duyne, R. P. *Journal of Chemical Physics* **1987**, *87*, 4189-4200.

(14) Vo Dinh, T.; Alak, A.; Moody, R. L. *Spectrochimica Acta, Part B: Atomic Spectroscopy* **1988**, *43B*, 605-615.

(15) Doblhofer, K.; Flatgent, G.; Radhakrishnan, G.; Pettinger, B.; Savinova, E.; Wasle, S. *Transactions of the SAEST* **1999**, *34*, 88-92.

(16) Burger, R. W.; Gerenser, L. J. *Metallized Plastics* **1992**, *3*, 179-193.

(17) Kreutz, E. W.; Frerichs, H.; Stricker, J.; Wesner, D. A. *Nuclear Instruments & Methods in Physics Research, Section B: Beam Interactions with Materials and Atoms* **1995**, *105*, 245-249.

(18) Feldmann, K.; Beitinger, G. *Metalloberflaeche* **1996**, *50*, 400-402.

(19) Zaporojtchenko, V.; Strunskus, T.; Behnke, K.; v. Bechtolsheim, C.; Thran, A.; Faupel, F. *Microelectronic Engineering* **2000**, *50*, 465-471.

(20) Beitinger, G.; Kolbeck, G.; Feldmann, K. *Metalloberflaeche* **2001**, *55*, 40-45.

(21) Zaporojtchenko, V.; Zekonyte, J.; Biswas, A.; Faupel, F. *Surface Science* **2003**, *532-535*, 300-305.

(22) Wang, B.; Eberhardt, W.; Kueck, H. *Journal of Adhesion Science and Technology* **2004**, *18*, 883-891.

(23) Werner, J.; Heilmann, A.; Hopfe, V.; Homilius, F.; Steiger, B.; Stenzel, O. *Thin Solid Films* **1994**, *237*, 193-199.

(24) Stepanov, A. L.; Hole, D. E.; Townsend, P. D. *Nuclear Instruments & Methods in Physics Research, Section B: Beam Interactions with Materials and Atoms* **1999**, *149*, 89-98.
(25) Ohara, T.; Hayashi, S.; (Toshiba Corp., Japan). Application: JP
JP, 1999, pp 7 pp.
(26) Markevich, M. I.; Chaplanov, A. M. *Fizika i Khimiya Obrabotki Materialov* **2002**, 90-93.
(27) Libenson, M. N.; Karpman, I. M.; Suslov, G. P.; Veiko, V. P.; Shpuntova, E. N.; Yakovlev, E. B. *Mikroelektronika* **1974**, *3*, 235-238.
(28) Sheng, R.; Zhou, G.; Xiong, J.; Xu, Z.; Morris, M. D.; Zeng, Y. e. *Wuhan University Journal of Natural Sciences* **1997**, *2*, 101-104.
(29) Tabuchi, S.; Tabata, H.; Kawai, T. *Japanese Journal of Applied Physics, Part 1: Regular Papers, Short Notes & Review Papers* **2000**, *39*, 1268-1271.
(30) Lengl, G.; Plettl, A.; Ziemann, P.; Spatz, J. P.; Moller, M. *Applied Physics A: Materials Science & Processing* **2001**, *72*, 679-685.
(31) De Jesus, M. A.; Giesfeldt, K. S.; Sepaniak, M. J. *Applied spectroscopy* **2003**, *57*, 428-438.
(32) Siiman, O.; Feilchenfeld, H. *Journal of Physical Chemistry* **1988**, *92*, 453-464.
(33) Yang, C.; Yang, H.; Shi, Z.; Zhu, L.; Sheng, R.; Hu, J. *Chinese Chemical Letters* **1992**, *3*, 919-922.
(34) Douketis, C.; Haslett, T. L.; Wang, Z.; Moskovits, M.; Iannotta, S. *Progress in Surface Science* **1995**, *50*, 187-195.
(35) Douketis, C.; Wang, Z.; Haslett, T. L.; Moskovits, M. *Physical Review B: Condensed Matter* **1995**, *51*, 11022-11031.
(36) Michely, T.; Ye, G.-X.; Weidenhof, V.; Wuttig, M. *Surface Science* **1999**, *432*, 228-238.
(37) Shalaev, V. M. *Handbook of Nanostructured Materials and Nanotechnology* **2000**, *4*, 393-449.
(38) Weber, M. V. a. A. *Z. Phys. Chem.* **1926**, *119*, 277.
(39) Krastanov., J. N. S. a. L. *Ber. Akad Wiss. Wen.* **1938**, *146*, 797.
(40) Merwe, F. C. F. a. J. H. V. d. *Proc. R. Soc. London, Ser. A.* **1949**, *198*, 205.
(41) Robins, J. L.; Donohoe, A. J. *Thin Solid Films* **1972**, *12*, 255-259.
(42) Usher, B. F. *Applications of Surface Science (1977-1985)* **1985**, *22-23*, 506-511.
(43) Hendricks, J. H.; Aquino, M. I.; Maslar, J. E.; Zachariah, M. R. *Chemistry of Materials* **1998**, *10*, 2221-2229.
(44) Wu, F.; Liu, Y.; Wang, X.; Wu, Z. *Proceedings of SPIE-The International Society for Optical Engineering* **2000**, *4086*, 330-333.
(45) Musick, M. D.; Keating, C. D.; Lyon, L. A.; Botsko, S. L.; Pena, D. J.; Holliway, W. D.; McEvoy, T. M.; Richardson, J. N.; Natan, M. J. *Chemistry of Materials* **2000**, *12*, 2869-2881.
(46) Berdichevsky, Y.; Khandurina, J.; Guttman, A.; Lo, Y. H. *Sensors and Actuators, B: Chemical* **2004**, *B97*, 402-408.
(47) Kim, S. D.; Torkelson, J. M. *Polymeric Materials Science and Engineering* **2001**, *85*, 2-3.

(48) Ng, J. M. K.; Gitlin, I.; Stroock, A. D.; Whitesides, G. M. *Electrophoresis* **2002**, *23*, 3461-3473.
(49) Boss, P. A.; Boss, R. D.; Lieberman, S. H.; (United States Dept. of the Navy, USA). Application: US
US, 2002, pp 14 pp.
(50) Fisher, G. L.; Walker, A. V.; Hooper, A. E.; Tighe, T. B.; Bahnck, K. B.; Skriba, H. T.; Reinard, M. D.; Haynie, B. C.; Opila, R. L.; Winograd, N.; Allara, D. L. *Journal of the American Chemical Society* **2002**, *124*, 5528-5541.
(51) Faupel, F.; Willecke, R.; Thran, A.; von Bechtolsheim, C.; Kiene, M.; Strunskus, T. *International Congress on Adhesion Science and Technology, Invited Papers, Festschrift in Honor of Dr. K. L. Mittal on the Occasion of his 50th Birthday, 1st, Amsterdam, Oct. 16-20, 1995* **1998**, 747-761.
(52) Giesfeldt Kathleen, S.; Connatser, R. M.; De Jesus Marco, A.; Lavrik Nickolay, V.; Dutta, P.; Sepaniak Michael, J. *Applied spectroscopy* **2003**, *57*, 1346-1352.

Part 4

Studies of the Optical Properties of Metal-Pliable Polymer Composite Materials

This chapter is a revised version of an article under the same name published in Applied Spectroscopy by Kathleen S. Giesfeldt, R. Maggie Connatser, Marco A. De Jesús, Nickolay V. Lavrik, Pampa Dutta, and Michael J. Sepaniak:

Giesfeldt Kathleen, S.; Connatser, R. M.; De Jesus Marco, A.; Lavrik Nickolay, V.; Dutta, P.; Sepaniak Michael, J., **Studies of the optical properties of metal-pliable polymer composite materials.** *Applied Spectroscopy (***2003),** 57(11), 1346-52.

;

My use of "we" in this chapter refers to my co-authors and myself. My primary contributions to this article included: (A) design of the project and development the experimental protocols to characterize the Ag-PDMS system (B) Fabrication of several series of Ag-PDMS and Ag-Glass flat substrates under various deposition conditions (C) design of the experimental methods and protocols, (D) collection and interpretation of the analytical data (E) collection and interpretation of the cited literature, (F) most of the writing.

Introduction

Intense interest in noble metallic nanoparticles has arisen due to their application for optical devices, surface-enhanced spectroscopies, biological and chemical sensors, nanoscopic tethering agents, single molecule detection, and as model systems for supported metallic catalysts.[1-5] An interesting class of nanostructured materials involves the creation of dielectric material-nanometallic composites. In these composites, the metallic nanoparticles are usually dispersed within the dielectric rather than surface confined. The dielectric material is often a polymer that is metallized by processes that include physical vapor deposition (PVD), ion implantation, and ion exchange.[6-8]

The optical properties of these composites depend critically on the morphology of the system. This, in turn, is influenced by the conditions used for their formation and by subsequent treatment. With regard to the latter, thermal annealing[9, 10] and laser irradiation[11, 12] can be used to alter the morphology through changes in the size, shape,

and proximity of the nano-metallic-particles. The unique optical responses of these structures are determined to a large degree by their surface plasmon resonances (frequency and intensity) that are strongly dependent on both the morphology and dielectric properties of the composite material.[13, 14] Polycarbonate, poly(methyl methacrylate), polyethylene, poly(ethylene teraphthalate), epoxy, and other thermoplastics have been used as the base materials for creating metallic nanoparticle composites.[15-20] Surface plasmon resonance can be tailored by controlling the shape, size, and spacing of metallic nanoparticles.[21, 22] This control can be achieved via lithographic techniques when the particles are surface confined, however, lithographic methods can be costly and are not amenable to the creation of bulk amounts of composite materials.

The optical properties of nano-metallic-particle composites have been studied by optical extinction spectroscopy and interpreted using Mie and Maxwell theories, particularly for regular arrays and for individual localized particles.[23, 24] When nano-metallic-particles are physically or chemically vapor deposited within polymeric matrices, they can be polydisperse or assume a fractal-like morphology. Predictions regarding the plasmon resonance responses of such disordered systems can be more complex.[25, 26]

Herein, we report novel composites made from physical vapor deposition (PVD) of silver onto the elastomer polydimethylsiloxane (PDMS). This polymer is comprised of a saturated silicone-oxygen backbone that has high resistance to degradation due to temperature, ozone, radiation, and high-voltage ionization. With its unique phase-separated layer,[27, 28] PDMS is considered a "self-healing" polymer. PDMS is more dielectrically stable in comparison to typical organic polymers. The inclusion of vinyl-

terminal groups at low concentrations increases cross-linking efficiency; thus the PDMS has high tensile strength, potential for elongation, and abrasion resistance. Nano-metallic-particle composites are formed by using PVD to create effective average Ag thicknesses of 10-50 nm and studied primarily by optical methods. A unique and relevant feature of this pliable Ag-PDMS material is that it can be physically manipulated with fair reproducibly and reversibly to alter the nano-Ag-particle morphology. Thus, the optical properties of the composites can be optimized. Another characteristic of these materials is that they can be molded into practical functional devices. For example, we have created titer-well plates from Ag-PDMS.[29]

Experimental

Materials. Ag (99.999%, 2-3mm diameter pellets) was purchased from Alfa Aesar and glass microscope slides from Fischer Scientific. Microscope slides for Ag-glass were sonicated with a 5% KOH in methanol solution for ten minutes, copiously rinsed with 18 MΩ, deionized water (Barnstead, E-Pure, Dubuque, IA) and allowed to air dry. Dow Sylgard 184 compounds were used for the polymer synthesis with A to B (w/w) ratio 10:1. The A component is a 250 unit dimethylvinyl terminated siloxane (18500Da). The B component is a short hydrosilane cross-linker. The cure temperature and time were 70^0C and thirty minutes, respectively. Prior to curing, films a few mm thick were cast onto glass microscope slides and degassed for fifteen minutes.

Ag Deposition. Ag films were deposited on PDMS films and in one case glass slides with a Cooke Vacuum Products, Inc. vapor deposition chamber with a base pressure ~10^{-7} torr. Mass thickness and deposition rate were measured for each film with

a quartz-crystal microbalance (Maxtek, Inc, Model TM-100R, Santa Fe Springs, CA) that was calibrated by ellipsometry (DRE, Model EL X-02C, Ratzeburg, Germany). Samples are mounted 24 cm above the effusive source.

Extinction Spectra. All extinction spectra were collected on a Thermospectronic Biomate 5 UV-Visible spectrometer with the automatic cell tray removed. All spectra were collected from 350 to 800 nm. Background spectra of PDMS and the polarization filter were collected and manually subtracted from the appropriate spectra. The stretched PDMS substrate experiments utilized a modified Vernier caliper onto which the substrates were attached and stretched before Ag deposition. These substrates were slowly collapsed to the original, pre-stretched, length of the substrate.

DC Conductivity Measurements. The DC conductivity of the nanocomposites was monitored as the composites were formed by first depositing thick layers of Ag (200 nm) as conduction strips, separated by a 7 mm gap, onto films of cured PDMS. Connections to these strips were fed through the thermocouple port of the PVD apparatus. By this means, a DC voltage of 2.2 V was applied across the strips and the current was monitored using a Keithley Model 485 autoranging picoammeter as silver was deposited (as described above) at different rates.

Scanning Electron Microscopy. A Hitachi S4300-E SEM with a field-emission gun at 2kV with an electron beam diameter of ~2.5nm was used to obtain the high-resolution images in secondary and backscattered modes presented herein. Low-voltage scanning electron microscopy reduced the sample damage and the charge build up while producing high-resolution images of "neat" surfaces with negligible beam damage.

X-Ray Photoelectron Spectrometry. The XPS measurements were performed using a Perkin Elmer 5500LS ESCA spectrometer with a non-monochromatized Mg Kα X-ray excitation source (1253.6 eV line) with a power of 300 watts and a pass energy of 89.45 eV. The diameter of the X-ray spot was set to 400 μm for small area analysis. All the samples were held under vacuum (10^{-9} torr) for 2 hours before measurements were performed in order to remove surface contamination. The operating pressure was also 10^{-9} torr. Depth profiles of the films were observed with continuous Ar^+ sputtering, operating the Ar^+ ion gun at a beam voltage of 3000V. During sputtering, the analysis chamber was kept at a vacuum of $2x10^{-8}$ torr. The sputter area was approx 10 mm in diameter.

For the estimation of the etching rate for Ag-PDMS composite material, the etch rates of silver (Ag) as well as PDMS films were determined separately by analyzing the depth profiles of a 12 nm Ag film (deposited by thermal evaporation under vacuum, see above) and a 87 nm PDMS film (that was spin-cast from a mixture of 10 mg/mL of uncured PDMS in chloroform at a speed of 4000 rpm using spin coater model PWM32-PS-R790 from Headway Research, Inc., Garland, TX, USA). In both cases the backing material was a silicon wafer that provided signature XPS bands at the point of breakthrough. The thicknesses of the silver (Ag) and PDMS films on silicon wafer were measured using ellipsometry. From the depth profile of Ag and PDMS films, the etch rates were determined to be 3.8 and 3.4 Å/min, respectively, and the rough estimate of etch rate for the composite material was considered to be 4 Å/min in this work.

Surface Enhanced Raman Spectrometry. The SERS spectra were acquired using a LabRam Spectrograph from JY-Horiba. The instrument uses an Olympus

microscope with a 10X (0.25 n. a.) objective to deliver up to 9 mW of the 632.8 nm line from an electrically cooled He-Ne laser. The confocal hole and slit of the instrument were opened to 500 μm and 200 μm, respectively. All spectra were acquired in a 180° scattering geometry with a 2936 cm^{-1} spectral window centered at 1700 cm^{-1}. The scatter was dispersed with a 600-groove/mm grating, imaged with a 1024 x 256 thermoelectrically cooled CCD camera, and processed using Labspec 4.03 software. A computer controlled x-y-z stage was used to adjust the focusing of the microscope objective as well as the positioning of the laser spot on the SERS substrates.

Macro Simulation. A 1.5 cm W x 2.5 cm L x 0.1mm piece of cured PDMS was placed into a modified Vernier calipers and stretched to 4.5 cm. To simulate the Ag nanoparticle morphology and packing as seen in the SEM micrographs, a thin coating of fresh PDMS was spread onto the substrate to act as an adhesive for the randomly placed glass beads that ranged in size from 1.8 mm to 2.6 mm. An Intel QX3 digital microscope was used to capture images of the substrate as it was slowly relaxed to its original length. These images were imported into MS PowerPoint. Due to the nature of the microscope, the original images lacked high contrast, thus the image of each bead was overlaid with transparent circles of appropriate dimensions and the outlines of the substrate edges were elucidated. After grouping the transparent circles and outlines, they were copied to another PowerPoint slide. This was repeated for each of the individual micrographs to clarify the movement of the beads parallel and perpendicular to the direction of stretching.

Results and Discussion

Noble metals generally exhibit only a weak chemical interaction with polymers, thus permitting diffusion within the polymer upon vapor deposition. Due to the noble metal's high cohesive energy, agglomeration of the metal within or on the surface of the polymer competes with the random diffusion processes on or within the polymer.[30, 31] At higher deposition rates there are greater concentrations of free atoms or very small clusters on or near the surface. This enhances the probability that free atoms or very small atom clusters encounter each other and form nanoparticles of Ag that are sufficiently large so as to exhibit negligible diffusivity. A narrow distribution of nanoparticle size and shape will produce a more distinct plasmon resonance.[32-34] Control of parameters, such as, deposition rate and thickness, that influence nanoparticle size and distribution are important. These can be used to tune the surface plasmon resonance characteristics of the composite material.

Thickness and Deposition Rate Studies

Driven by entropic processes, the PDMS used in these studies is known to phase separate wherein non-crosslinked polymer chains can rise to the surface.[27, 28] The "self-healing" characteristic of PDMS is a result of this process. As evidence of this, the surface of our PDMS films has an obvious adhesive quality. When treated with UV light in an ozone environment the surface becomes more rigid and less tacky. Deposition of Ag onto a UV treated PDMS surface results in Ag layers that are easily rubbed off. With time, the surfaces again become tacky and any deposited Ag is more difficult to rub off. Silver deposited on non-UV treated PDMS was not rubbed off as readily.

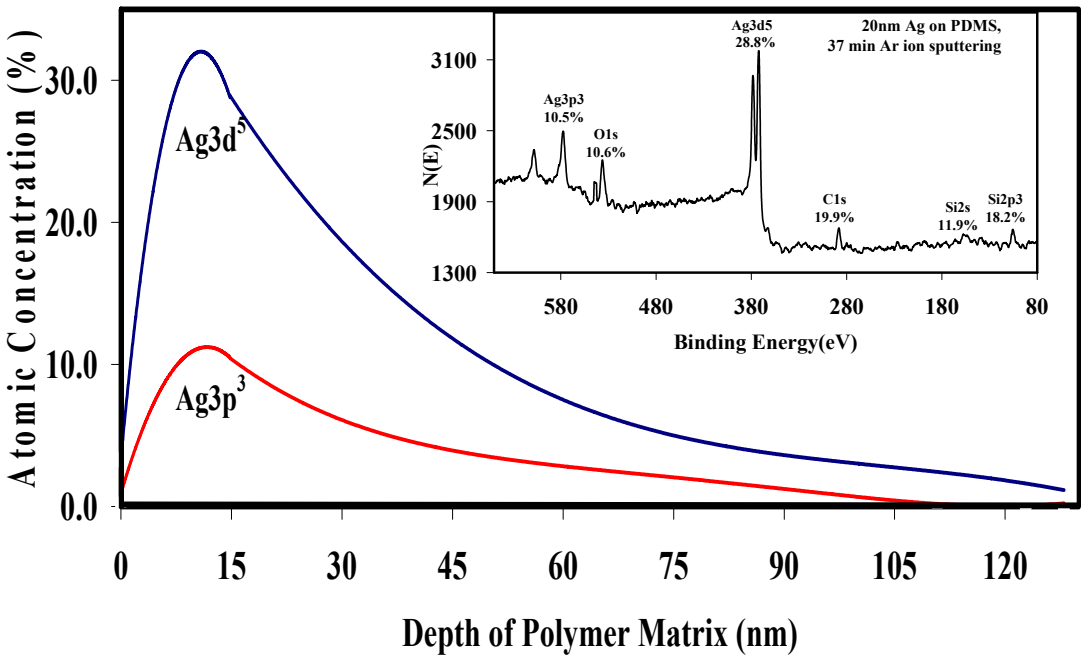


Figure 4.1. The XPS depth profiles of 20 nm Ag on PDMS showing area percent for two Ag lines. The inset is the XPS spectrum of the film after 37 minute Ar ion sputtering.

Figure 4.1 presents an XPS depth profile for a 20 nm average thickness of Ag on PDMS demonstrating the change of silver content with depth from the surface of the composite material. The silver content as demonstrated in the profiles seen in the figure were estimated as peak area percent based on the Ag 3d binding energy at 372 eV or the Ag 3p binding energy at 577 eV. The C 1s binding energy at 287.5 eV, the O 1s binding energy at 536 eV, the Si 2s binding energy at 155 eV and the Si 2p binding energy at 105 eV were among the polymer peaks used to determine the area percent of Ag as the surface was sputtered at approximately 4 Å/min. From Figure 4.1, it appears that the

amount of silver content increases from a very small amount at the surface to a maximum at around 10-15 nm below from the surface and then trails off to an undetectable amount by approximately 100 nm depth. The physical characteristics of these surfaces as described above and the XPS data provide strong evidence that the Ag nanoparticles are at least partially submerged into the phase-separated surface layer of the PDMS. Two generalized features arise from this surface morphology. Unlike silver island films on glass, which are more traditionally used in surface enhanced spectroscopy techniques, the Ag-PDMS system has some depth and thus the accessible metal surface area is increased. Moreover, the PDMS itself can act as a solid-phase extractor of analyte from sample environments and also strongly determines the dielectric properties of the medium in contact with the surface of the noble metal.

The optical properties of the composite material change as the proximity among particles is altered.[21] Monitoring the DC conductivity is one way to observe gross changes in metal nanoparticle proximity and, thereby, characterize the composites we have created. To determine at what nominal metal thickness percolation, i.e. the creation of macroscopic electrical pathways,[35] occurs during the physical vapor deposition of silver onto the PDMS films, we applied a constant DC voltage across our substrate-electrode system (see Experimental Section) during the deposition process while measuring an output current. Figure 4.2 demonstrates that the DC conductivity in the composite dramatically increased at 38 nm and 46 nm average silver thicknesses for deposition rates of 0.2 Å /sec and 1 Å /sec, respectively. Since the point of measurable percolation within the composite is considerably beyond the thickness at which we

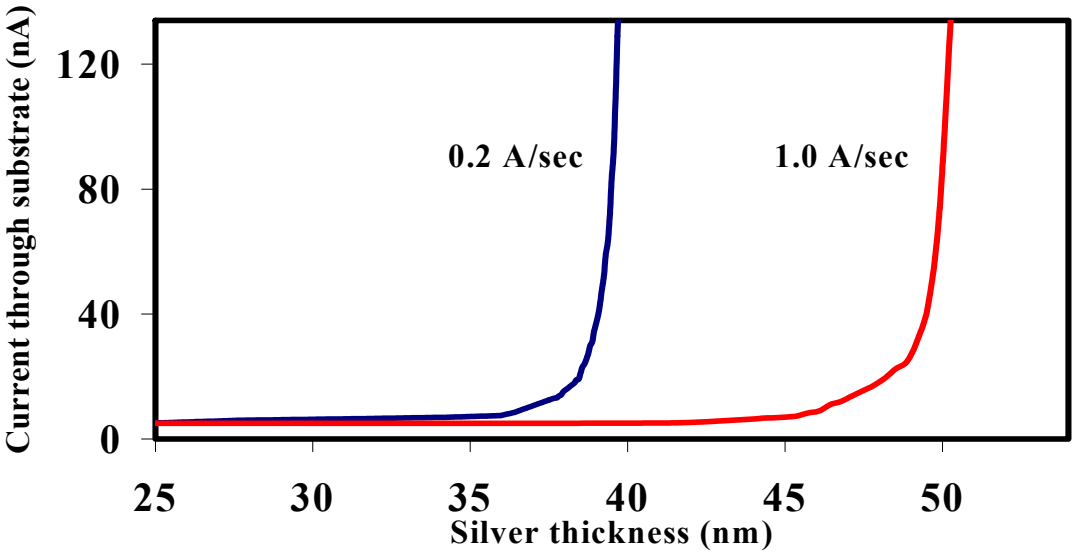


Figure 4.2. DC conductivity curves obtained during deposition at 0.2 and 1.0 Å/s

observe optimum optical behavior (see below), we believe our composites do not exhibit behavior indicative of an electrically conductive film.

Upon deposition, the competition between agglomeration and diffusion involving Ag results in the random formation of nanoparticles. For PDMS, the presence of an uncrosslinked layer near the surface may enhance the probability of forming sub-surface nanoparticles. UV curing or the addition of a higher percentage of hydrosilane cross-linker increased the surface modulus, tensile strength and altered, for a period of time, the physical and optical properties of the Ag-PDMS composite.

The composite materials were also investigated by SEM. Uncoated and partially metal-coated polymers build up a negative charge when bombarded by electron beams at the voltages used for SEM imaging. Samples deposited with less than approximately 20

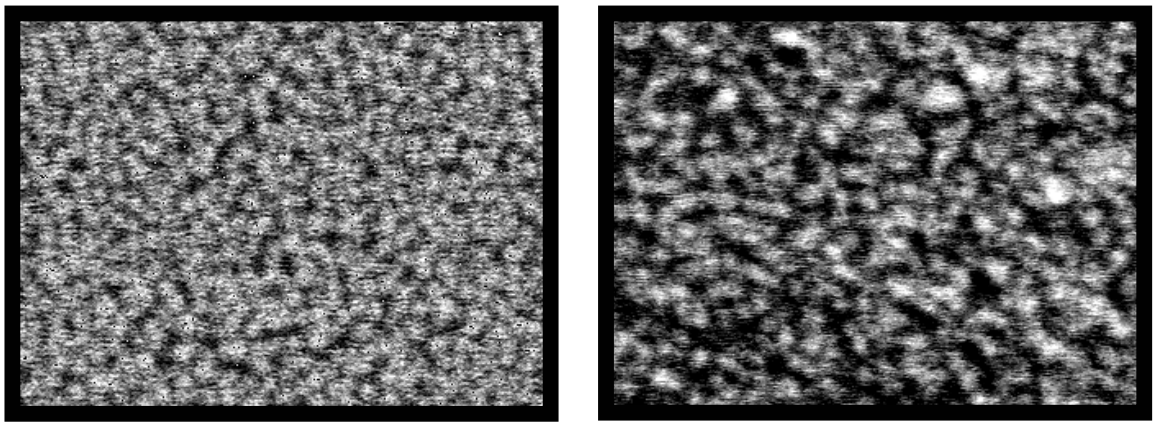


Figure 4.3. Scanning electron micrographs of Ag-PDMS surface at 90,000 fold magnification for deposition rates of 1.0 Å/s (left) and 0.2 Å/s (right).

nm Ag, thus well below the percolation threshold, suffered from charge build-up, even at low voltages and vacuum. Above this Ag thickness, pathways may have been generated to draw off excess charge and more authentic images were obtained. The micrographs in Figure 4.3 indicate that deposition rate affects the regularity of the surface morphology. Slow deposition rates, ~0.2 Å/s, produce larger irregular features that may be more fractal in nature. Higher rates increase the probability of a more regular surface with more uniform and distinct, more nearly spherical particles. Since the depth profiling (Figure 4.1) shows a maximum Ag content at a depth less than the apparent radii of the nanoparticles seen in the SEM (particles appear to be in the 50 -100 nm range), the particles may assume an ellipsoidal shape with respect to dimensions parallel and perpendicular to the composite's surface. Visual appearances of the two deposition rates are consistent with the lower percolation threshold for the slower deposition rate (see Figure 4.2). The optical extinction band of the 1 Å/s deposition rate is higher but slightly broader than that of the slower rate (Figure 4.4).

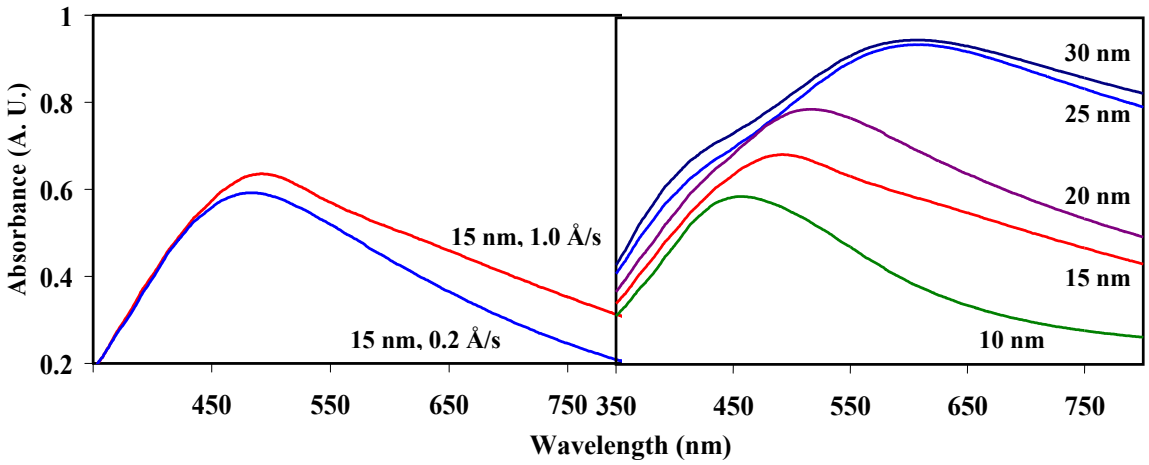


Figure 4.4. Optical extinction curves for 15 nm average Ag thickness Ag-PDMS substrates at the two different deposition rates (left). Optical extinction curves for Ag-PDMS obtained at a deposition rate of 1.0 Å/s for several different average thicknesses of Ag (right).

Effective Ag thickness has a noticeable effect on reflectivity and other optical properties as well. The intensity and frequency of plasmon resonances are expected to change when nanoparticle size is increased and the proximity of nanoparticles is reduced.[1, 13, 36] Morphological changes that are expected with large average thicknesses complicate this effect; e.g., the plasmon resonances may be diminished as particles begin to engage when the average Ag layer thickness is too great. By engagement we mean direct contact between nanoparticles or the creation of crowded nanoparticle arrangements wherein additive and subtractive electromagnetic field effects are observed. The extinction curves shown in Figure 4.4 cover a wide range of Ag thicknesses. These curves result from plasmon resonances (probably involving multiple overlapping bands due to morphological heterogeneity), reflectivity (expected to be rather broad), and absorption. The bathochromatic shift in the 10, 15, 20 nm series indicates increasing

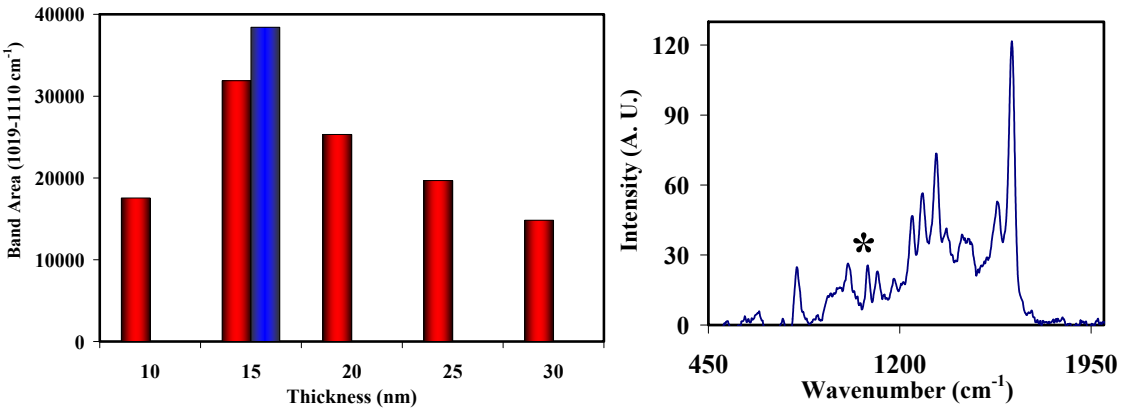


Figure 4.5. Band areas (left) of 1 x 10^{-5} M *p*-ATP on Ag-PMDS at deposition rate of 1.0 Å/s (blue bar for 0.2 Å/s). Spectrum (right) is of 1 x 10^{-8} M *p*-ATP (conditions: 1 second acquisition time; background and baseline corrected; excitation of 2.1 mW at 633 nm; 18 nm average Ag thickness deposited at 1.0 Å/s).

nanoparticle size.[1] The 20 nm thickness still resembles a strong distinct band, unlike the higher thicknesses which seem to be dominated by broad reflectivity. In fact, the 15 - 20 nm thickness range provides the greatest SERS activity when excited using 633 nm light (see below). The 25 and 30 nm thicknesses also show the beginning of a known Ag absorption band appearing at about 400 nm.[37] The tailing effect at long wavelengths may be due to fractal-like morphology.[25]

Because of complications resulting from absorption, reflection, and heterogeneous morphology, a strict correlation between observed optical extinction profiles and the magnitude of surface plasmon related responses may not be observed. Nevertheless, these extinction profiles are a useful start in interpreting SERS responses. SERS spectra of *p*-aminothiol phenol, *p*-ATP, were obtained for Ag-PDMS composites using a He-Ne (633 nm) laser excitation as shown in Figure 4.5. A typical spectrum at low concentration (50 μL of 1 x 10^{-8} M spotted into a composite molded as a micro-titer well)

is shown in the figure. Also shown in the figure are the areas of the band centered at about 1050 cm^{-1} for the different average Ag thicknesses using a concentration of *p*-ATP that is expected to saturate the surface of the noble metal with a self assembled monolayer of the thiolated compound. Consistent with the extinction curves shown in Figure 4.4, the data for the He-Ne laser excitation showed the best response for the 15 nm thickness with the response for the 20 nm thickness being nearly the same. The band area data in the figure represents an average of three experiments; an optimum response in the 15 - 20 nm average thickness was observed for the individual experiments as well. It should be noted that spatial variations in deposition rate within the PVD chamber make these average thicknesses only a rough approximation. Although a thickness study was not conducted for the slower deposition rate (0.2 Å/s), good response (better than for 1.0 Å/s) at an average thickness of 15 nm was observed (Figure 4.5). The superior performance for the slower deposition rate at this thickness is not obvious when considering the extinction curves in Figure 4.4**,** but was consistently observed.

Since Ag islands on glass represent one of the most traditionally used substrates, we made a direct comparison of spectra obtained on an optimal 8 nm average thickness Ag on glass substrate to a 20 nm average thickness Ag-PDMS substrate (see Figure 4.6). At high concentrations of *p*-ATP, the signal levels for Ag-glass are about a factor of two less than the Ag-PDMS. Since *p*-ATP binds to the surface of the metal and sufficient analyte was present to achieve a monolayer, the ratio of signal levels in Figure 4.6A is indicative of the relative inherent surface enhancements of the two substrates. However, it should be noted that the particle proximity was not optimized for the Ag-PDMS case (see below). The spectra for *p*-aminobenzoic acid, *p*-ABA, demonstrate the unique

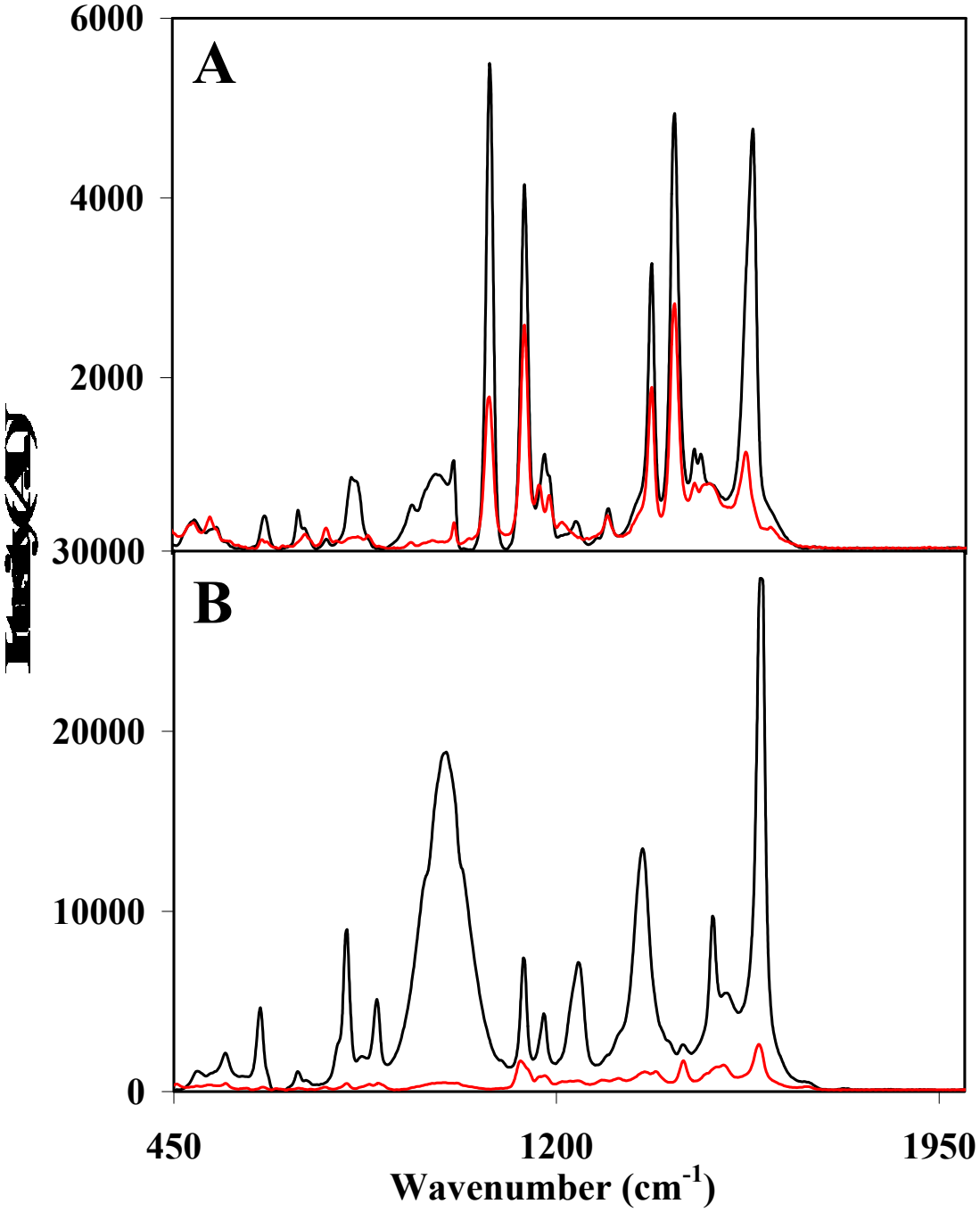


Figure 4.6. Spectra (A) of 1x 10^{-5} M *p*-ATP on Ag-PDMS (black line) and Ag-Glass (red). Spectra (B) of 1 x 10^{-4}M *p*-ABA on Ag-PDMS (black line) and Ag-Glass (red) (conditions for both A &B: 1 second acquisition time; mean of 10 spectra, background and baseline corrected; excitation 2.1 mW at 633 nm; 18 nm Ag deposited at 1 Å/s on PDMS; 8 nm Ag deposited at 1 Å/s on glass).

advantage of PDMS as a solid phase extractor of analyte. Due to the efficient partitioning of the *p*-ABA with the PDMS, and subsequent interaction with the Ag layer, the spectra for Ag-PDMS substrate are far more intense than for the Ag-glass substrate (Figure 4.6B).

Optimization of Particle Proximity

A series of Ag-PDMS substrates were used to study changes in optical extinction and surface-enhanced Raman responses with mechanical manipulation. Individual substrates were mechanically stretched up to approximately 150% of the original post-cured length prior to PVD of Ag at 1.0 Å/s. An average Ag thickness of 15 nm, at the lower end of optimum (see above), was used in these studies. The optical properties of the substrate were then investigated while it was systematically relaxed to its original dimension in order to manipulate inter-nanoparticle spacing. We noted in our experiments when relaxing (contracting) in one dimension, the composite expands a factor of about one-fifth of the contraction change in the perpendicular direction. The optical experiments were conducted with perpendicular or parallel polarization orientations using the inherent polarization of the laser (SERS experiments) or a polarizing film (optical extinction experiments).

Our initial notion in these experiments is that the nanoparticles look somewhat like the SEM shown in Figure 4.3 (left). Specifically, particle shapes are spherical to oblong (surface view) with surface irregularities and possessing a range of sizes of 50 – 100 nm. The particles are generally isolated or appear as small isolated aggregates of nanoparticles (not engaged). The fact that they are isolated is supported by the fact that

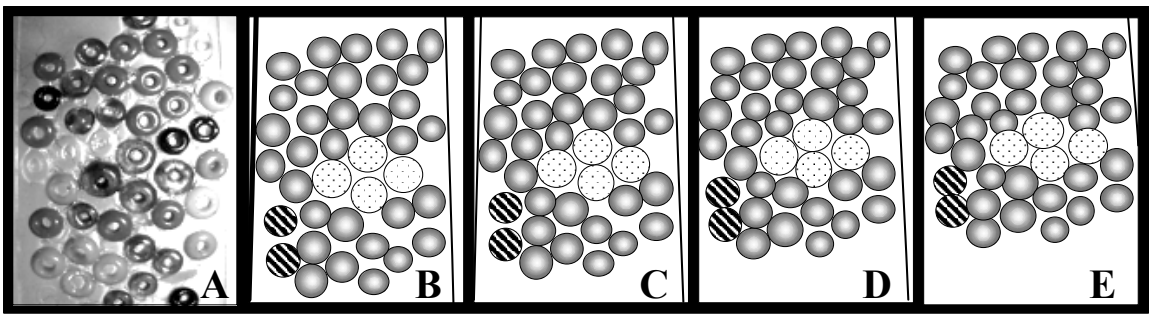


Figure 4.7. A: image of the macro-simulation. B-D: graphically enhanced images as PDMS is allowed to relax from the original ~ 150% stretched state (B, ~147%; C, ~134%; D, ~125%; E, ~119%). The direction of substrate manipulation is vertical and the lines within the images are the edges of the PDMS.

at 20 nm average thickness the system is far from the percolation threshold (see Figure 4.2). Additionally, there may be some depth to the system (i.e., the centers of mass of the nanoparticles have a range of depths relative to the composite surface). The first and most general change when relaxing the composite is that a greater number of nanoparticles and a greater Ag surface area will be in the field of view of our optics. Thus, in optical extinction experiments greater reflectivity and absorption is expected and in SERS experiments a general increase in signal might also be anticipated. The subtler and less predictable effects involve inter-nanoparticle spacing and arrangements. These morphological changes may be expected to have a profound effect on the generation of surface plasmons and SERS activity and, as such, mask the general effects mentioned above.

In order to better visualize what morphological changes might occur, a macro-simulation experiment was performed (see Experimental Section for details). The results of that simulation are seen in Figure 4.7. A pair of striped particles and a nearly close-packed grouping of four dotted particles are highlighted. As the macro-simulation

relaxation (contraction) occurs, several observations about the spacings and arrangements of particles can be made. (i) The striped particles move closer together in the stretch direction, then eventually touch and overlap akin to tectonic plates. In prior theoretical work, shortening the gap between two isolated spherical nanoparticles of Ag resulted in a large increase in surface plasmon related fields between the particles when the polarization of the incident radiation was parallel to the gap.[36] (ii) Within the dotted grouping the two particles that are aligned in the stretch direction move closer and the two aligned perpendicularly move apart. Eventually, the overlap of the former pair occurs. (iii) In the fully collapsed state (Figure 4.7E) there are many contact pathways in any direction across the assembly of particles whereas this is not the case in Figure 4.7B. (iv) There is limited depth to the penetration of Ag into our substrates (Figure 4.1), therefore, these systems are not strictly a two-dimensional arrangement of nanoparticles (such as Ag islands on glass). This further complicates the situation. (v) Finally, many morphological changes that can be expected to influence optical responses, positively or negatively, occur simultaneously upon relaxation. Thus, while physical manipulation can be readily performed to experimentally optimize optical responses, predicting what conditions will be optimum will be very difficult for these relatively disorganized systems.

Figure 4.8 provides the polarized extinction curves during actual Ag-PDMS substrate relaxation. The perpendicular and parallel peak absorbencies (average of three experiments) are roughly equal (in the 0.60 – 0.65 A. U. range). It is the changes within each polarization orientation when the substrate is relaxed that are seen in the figure that are significant. The perpendicular orientation shows only small changes. Upon relaxing

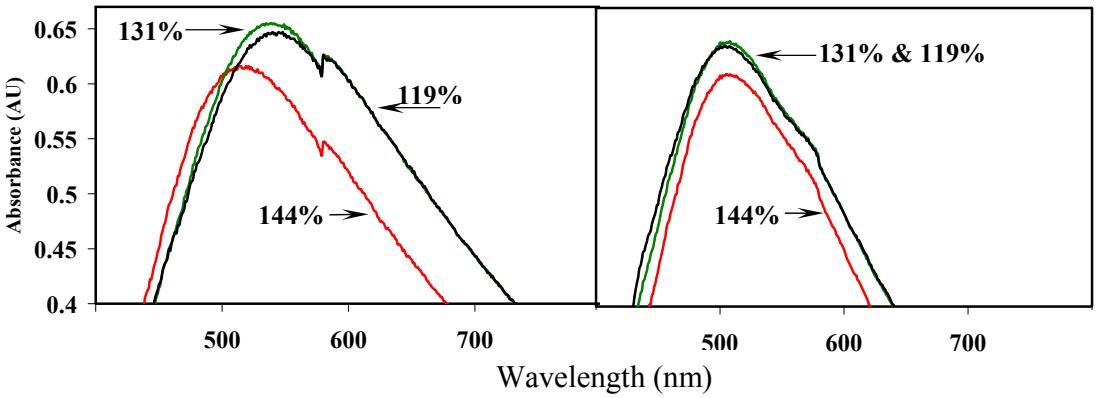


Figure 4.8. Optical extinction curves of Ag-PDMS substrate with excitation beam polarization parallel (left) and perpendicular (right) to direction of stretch.

from 144% to 119% there is a slight hypsochromic shift in the λ_{max} of approximately 5 nm. The relative transmission at λ_{max} decreases by less than 5% over the 144% to 119% range, less than would be expected based on the increased density of particles in the optical beam (note we are quoting λ_{max} transmission changes not the integrated extinction curve area). The effects for the parallel orientation are more dramatic. A bathochromic shift (toward the laser wavelength) of about 25 nm is observed when relaxing from 144% to 131% with an additional shift of 5 nm when the substrate is further relaxed to 119%. When going from 144% to 131% there is a significant 10% relative reduction in transmission at λ_{max}. The transmission at λ_{max} then reverses and increases slightly with further relaxation despite an increase in the density of nanoparticles within the optical beam. This extinction data points indicates the creation of morphology for parallel interrogation that should exhibit an optimum plasmon resonance for intermediate stretch values.

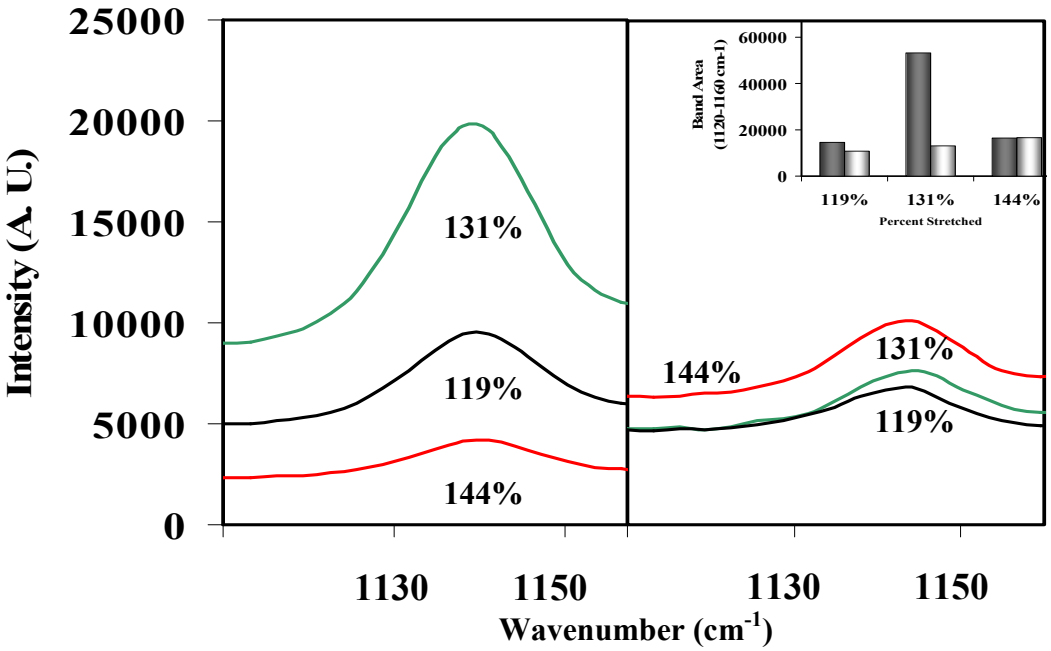


Figure 4.9. SERS band profiles of 1 x 10^{-5} M *p*-ATP with excitation beam polarization parallel (left) and perpendicular (right) of pre-stretched Ag-PDMS substrate (15 nm Ag, 1.0 Å/s). The baseline corrected band areas appear as an insert.

The SERS profiles for the p-ATP band centered at 1150 cm^{-1} are shown in Figure 4.9 for a relaxation experiment (average of three experiments). These Ag-PDMS substrates were not the exact same ones used in generating Figure 4.8, but were prepared under the same conditions. The SERS data is consistent with the extinction curves, in that the perpendicular to stretch polarization shows less dramatic effects and no maximum in signal magnitude during the relaxation. The 144% perpendicular polarization band area is about the same as the parallel orientation at that stretch value. However, upon relaxation the perpendicular polarization decreases in band area whereas the parallel polarization shows a dramatic increase in band area and a distinct optimum for the intermediate stretch.

A final set of experiments were performed by relaxing substrates similar to those used for Figure 4.9 (deposition at 1.0 Å/s and 15 nm thickness performed at 150% stretched condition) to a stretch value that previously seemed to be optimum for the parallel polarization orientation (~130%). The Ag-PDMS substrates were then cycled between 150% and 130% four times and the band areas of *p*-ATP recorded. Table 4.1 presents the results of a representative cycling experiment.

The data in the table indicates that optimization of SERS activity via physical manipulation is moderately reversible and repeatable. There seems to some hysteresis effect, however, wherein nano-metallic-particles rearrange in response to physical manipulation but do not fully assume the prior orientation when the process is reversed. An additional source of variability in these cycling experiments arises from difficulty in probing the same region of the substrate for each measurement.

Table 4.1. The 1050 cm^{-1} band areas (arbitrary units) of *p*-ATP for a substrate cycled between stretches.

Trial	1	2	3	4	mean	CV
130%	1080	1780	1510	1690	1520	20%
150%	640	690	870	920	780	17%

References

References

(1) Emory, S. R.; Haskins, W. E.; Nie, S. *Journal of the American Chemical Society* **1998**, *120*, 8009-8010.

(2) Maier, S. A.; Brongersma, M. L.; Kik, P. G.; Meltzer, S.; Requicha, A. A. G.; Atwater, H. A. *Advanced Materials (Weinheim, Germany)* **2001**, *13*, 1501-1505.

(3) Mulvaney, P. *Langmuir* **1996**, *12*, 788-800.

(4) Haes, A. J.; Chang, L.; Klein, W. L.; Van Duyne, R. P. *Journal of the American Chemical Society* **2005**, *127*, 2264-2271.

(5) Kneipp, K. *Single Molecules* **2001**, *2*, 291-292.

(6) Beitinger, G.; Kolbeck, G.; Feldmann, K. *Metalloberflaeche* **2001**, *55*, 40-45.

(7) Korol, E. N.; Manoylo, M. A. *Molecular Crystals and Liquid Crystals Science and Technology, Section A: Molecular Crystals and Liquid Crystals* **1994**, *248*, 645-649.

(8) Kreutz, E. W.; Frerichs, H.; Stricker, J.; Wesner, D. A. *Nuclear Instruments & Methods in Physics Research, Section B: Beam Interactions with Materials and Atoms* **1995**, *105*, 245-249.

(9) Heilmann, A.; Werner, J. *Thin Solid Films* **1998**, *317*, 21-26.

(10) Stepanov, A. L.; Hole, D. E.; Townsend, P. D. *Nuclear Instruments & Methods in Physics Research, Section B: Beam Interactions with Materials and Atoms* **1999**, *149*, 89-98.

(11) Kaempfe, M.; Graener, H.; Kiesow, A.; Heilmann, A. *Applied Physics Letters* **2001**, *79*, 1876-1878.

(12) Tabuchi, S.; Tabata, H.; Kawai, T. *Japanese Journal of Applied Physics, Part 1: Regular Papers, Short Notes & Review Papers* **2000**, *39*, 1268-1271.

(13) Gunnarsson, L.; Bjerneld, E. J.; Xu, H.; Petronis, S.; Kasemo, B.; Kall, M. *Applied Physics Letters* **2001**, *78*, 802-804.

(14) Kahl, M.; Voges, E.; Kostrewa, S.; Viets, C.; Hill, W. *Sensors and Actuators, B: Chemical* **1998**, *B51*, 285-291.

(15) Stepanov, A. L.; Popok, V. N.; Khaibullin, I. B.; Kreibig, U. *Nuclear Instruments & Methods in Physics Research, Section B: Beam Interactions with Materials and Atoms* **2002**, *191*, 473-477.

(16) Dirix, Y.; Bastiaansen, C.; Caseri, W.; Smith, P. *Journal of Materials Science* **1999**, *34*, 3859-3866.

(17) Lee, M.-S.; Nam, S.-I.; Min, E.-S.; Kim, S.-B.; Shin, H.-S.; (Postech Foundation, S. Korea). Application: WO
WO, 2002, pp 32 pp.

(18) Henry, A. C. *Journal of Physcial Chemistry B* **2001**, *37*.

(19) Lavrik, N. V.; Tipple, C. A.; Datskos, P. G.; Sepaniak, M. J. *Proceedings of SPIE-The International Society for Optical Engineering* **2001**, *4560*, 152-161.

(20) Rao, Y.; Shi, S. H.; Wong, C. P. *Proceedings - Electronic Components & Technology Conference* **1999**, *49th*, 784-789.

(21) Jensen, T. R.; Duval, M. L.; Kelly, K. L.; Lazarides, A. A.; Schatz, G. C.; Van Duyne, R. P. *Journal of Physical Chemistry B* **1999**, *103*, 9846-9853.

(22) Malinsky, M. D.; Kelly, K. L.; Schatz, G. C.; Van Duyne, R. P. *Journal of Physical Chemistry B* **2001**, *105*, 2343-2350.
(23) Malinsky, M. D.; Kelly, K. L.; Schatz, G. C.; Van Duyne, R. P. *Journal of the American Chemical Society* **2001**, *123*, 1471-1482.
(24) Pack, A.; Hietschold, M.; Wannemacher, R. *Optics Communications* **2001**, *194*, 277-287.
(25) Kim, W.; Safonov, V. P.; Shalaev, V. M.; Armstrong, R. L. *Physical Review Letters* **1999**, *82*, 4811-4814.
(26) Markel, V. A.; Shalaev, V. M.; Zhang, P.; Huynh, W.; Tay, L.; Haslett, T. L.; Moskovits, M. *Physical Review B: Condensed Matter and Materials Physics* **1999**, *59*, 10903-10909.
(27) Dou, Y.-H.; Bao, N.; Xu, J.-J.; Chen, H.-Y. *Electrophoresis* **2002**, *23*, 3558-3566.
(28) Kim, S. D.; Torkelson, J. M. *Polymeric Materials Science and Engineering* **2001**, *85*, 2-3.
(29) De Jesus, M. A.; Giesfeldt, K. S.; Sepaniak, M. J. *Applied Spectroscopy* **2003**, *57*, 428-438.
(30) Faupel, F. *Diffusion and Defect Data--Solid State Data, Pt. A: Defect and Diffusion Forum* **1993**, *95-98*, 1201-1206.
(31) Limoge, Y. *NATO ASI Series, Series E: Applied Sciences* **1990**, *179*, 601-624.
(32) Andersen, P. C.; Rowlen, K. L. *Applied Spectroscopy* **2002**, *56*, 124A-135A.
(33) Mandal, S. K.; Roy, R. K.; Pal, A. K. *Journal of Physics D: Applied Physics* **2002**, *35*, 2198-2205.
(34) F. Nordin, G. L., J. Pantigny, J. Aubard *New Journal of Chemistry* **1998**, *22*.
(35) Kilbride, B. E.; Coleman, J. N.; Fraysse, J.; Fournet, P.; Cadek, M.; Drury, A.; Hutzler, S.; Roth, S.; Blau, W. J. *Journal of Applied Physics* **2002**, *92*, 4024-4030.
(36) Hinde, R. J.; Sepaniak, M. J.; Compton, R. N.; Nordling, J.; Lavrik, N. *Chemical Physics Letters* **2001**, *339*, 167-173.
(37) Zheng, M.; Gu, M.; Jin, Y.; Jin, G. *Materials Research Bulletin* **2001**, *36*, 853-859.

Part 5

Gold-Polymer Nanocomposites: Studies of their Optical Properties and Their Potential as SERS Substrates

This chapter is a revised version of an article with additional material on the effects of pH and anions under the same name by Kathleen S. Giesfeldt, R. Maggie Connatser, Marco A. De Jesús, Pampa Dutta, and Michael J. Sepaniak:

Giesfeldt, Kathleen, S.; Connatser, R. M.; De Jesus Marco, A.; Dutta, P.; Sepaniak Michael, J., **Gold-Polymer Nanocomposites: Studies of Their Optical Properties and Their Potential as SERS Substrates.** Submitted to *Journal of Raman Spectroscopy*. Currently under review.

My use of "we" in this chapter refers to my co-authors and myself. My primary contributions to this article included: (A) design of the project and development the experimental protocols to characterize the Au-PDMS system (B) Fabrication of several series of Au-PDMS and Au-Glass flat substrates under various deposition conditions (C) design of the experimental methods and protocols, (D) collection and interpretation of the analytical data (E) collection and interpretation of the cited literature, (F) most of the writing.

Introduction

There has been an increase in the number of publications concerning noble metal nanoparticles, in particular those based on Ag and Au, for optical devices, surface-enhanced spectroscopies, as well as biological and chemical sensors.[1-5] One class of nanostructured materials includes composites comprised of dielectric media and metal nanoparticles that are either dispersed within the material or confined to the surface. The dielectric material, generally a polymer, is metallized via physical vaporization deposition (PVD), ion implantation, or ion exchange.[6-8]

Our research group has recently reported on the optical properties of Ag-PDMS nanocomposites and their potential Surface Enhanced Raman Spectroscopy (SERS) applications.[9-11] Those studies showed a marked improvement in the SERS signals, in part due the fact that PDMS is an elastomer with a unique phase-separated layer that

strongly determines the dielectric properties of the medium in contact with the surface of the noble metal, a known efficient solid-phase micro-extractor (SPME) of analytes from sample environments, and provides a means of molding a plethora of substrates for the analysis of aqueous phase analytes. These unique features of PDMS facilitate the formation of a three-dimensional distribution of the noble metal particles within the phase-separated polymer matrix that improves of the linear dynamic range of SERS substrates.[9-11]

Surface plasmon resonance of these noble metal nanocomposites was manipulated through several experimental variables such as the vapor deposition parameters and effective thickness of the noble metals deposited. In this work, we extend our previous efforts and demonstrate that PVD of gold on PDMS can produce nanocomposites with tunable surface plasmon resonance characteristics and unique analyte selectivity. Motivation for extending the nanocomposites approach to gold resides in the greater stability of Au, relative to Ag, and a compatibility with biological systems.

The optical properties of these nanocomposites depend critically on the type of noble metal and the morphology of the substrate and metal particles. Thermal evaporation is one of the oldest, well-characterized, and inexpensive methods to produce metallic nanocomposites. Precise control over deposition parameters such as effective metal thickness, deposition rate, temperature, and pressure can affect the reproducibility of the optical properties of the nanocomposites.

For noble metal particles in the 10-100 nm diameter range, the optical absorption and scattering of incident electromagnetic radiation from the nanoparticles can result in

the collective oscillation of surface electrons, i.e. surface plasmons. Surface plasmon resonance can be tailored by controlling the shape, size, and proximity of metallic nanoparticles.[12-15] Greater optical coupling occurs at the surface plasmon resonance wavelengths, which is the basis of the aforementioned applications. For silver substrates, the plasmon resonance is within the visible range of the electromagnetic spectrum, whereas gold substrates generally exhibit a red-shifted surface plasmon resonance often in the near-infrared region of the electromagnetic spectrum.[16-18]

Mie and Maxwell theories have been used to explain the optical extinction spectra of regular arrays, individual localized particles, and metallic dimers.[19, 20] For certain elastomeric polymers metallized by physical vapor deposition techniques, the metallic nanoparticles are no longer confined to the surface of the substrate. These nanoparticles can be polydisperse and may assume a fractal-like morphology. Such disordered systems complicate the theoretical interpretations regarding the plasmon resonance responses.[21, 22]

The extremely large enhancement of the Raman signal upon the positioning of the sample analytes on or very near the surface of certain noble metal structures with nanoscale features has greatly improved the sensitivity of the technique. However, only a modest number of significant organic chemicals and possible adsorption sites on most SERS substrates can exploit the full power of resonant, chemical, and electromagnetic surface enhancement factors. Considerable work has been done in the area of SERS substrate design to maximize enhancements. Among the approaches are Au and Ag islands on glass,[23] colloidal metal solutions,[24] colloidal particles encapsulated in sol-gels,[25] silver coated microspheres,[26] metallized polymers,[2] and more regular structures such as those created by nanosphere lithography.[27] Metal-polymer nanocomposites, such

as our previously reported Ag-PDMS substrates, [9-11] have proven to be effective in reducing the oxidation of the Ag nanoparticles and exhibit unique optical and pre-concentrating properties.

Most Raman studies of biological analytes are performed in the NIR due to minimal fluorescence interferences. [28] Silver SERS substrates generally are not used for many biological applications due to apoptosis. Cellular and biological Au-SERS studies are performed commonly with colloids or as vapor deposited films on glass slides.[5, 18, 29-31] A distinct limitation is that these colloids are only loosely bound on the glass surface and, therefore, rearrange upon deposition of aqueous solutions. This rearrangement can induce the destabilization of the SERS "hot spots" reducing the enhancement of the Raman signal. Surface modifications to the glass substrates to tether the colloids have been attempted to minimize this issue. These techniques compromise the sensitivity of SERS by altering the dielectric properties of the substrate and may produce strong optical backgrounds.[31]

An often underestimated problem for relevant biological analytes is the sensitivity to the thermal and photolytic processes inherent to SERS. Continuous irradiation of the laser beam over a SERS substrate has been shown to cause the gross decomposition and/or fragmentation of the sample, alter observed spectral bands, and reduce the signal reproducibility.[32, 33] A rotary cell was designed by Kiefer and Bernstein in 1971 to minimize these effects under Resonance Raman (RR) conditions.[34] Our research group has extended this sample translation technique (STT) to SERS by producing 50 μL volume PDMS titerwells that have been vapor deposited with noble metals. These micro-titerwells are rapidly rotationally translated and interrogated with the Raman microprobe.

This creates a solid of revolution, a torus-like surface that is "viewed" by detector during data acquisition. The STT-SERS technique averages out microscopic aberrations and the high relative standard deviations (RSD) in signals that are endemic to SERS substrates. The purpose of our current work is to characterize the properties of Au-PDMS nanocomposites, comparing and contrasting to prior studies with Ag-PDMS, particularly as applied to STT-SERS.

Experimental

Materials. Methods for the preparation of polydimethylsiloxane (PDMS) substrates and glass substrates have been reported previously.[9-11]

Au Deposition. Au films were deposited on PDMS micro-titerwell arrays and quartz microscope slides (Fischer Scientific). Each array or quartz substrate was physically vapor deposited under similar conditions[11] with 10-50 nm 99.999% Au (Gatewest, Canada), at a rate of 0.2 or 1.0Å/s.

Extinction Spectra. All extinction spectra were collected from 350 to 1000 nm on a Thermospectronic Biomate 5 UV-Visible spectrometer. The background spectrum of PDMS was collected and manually subtracted from the analyte spectra.

DC Conductivity Measurements. The DC conductivity of the nanocomposites was determined while vapor depositing at 0.2 and 1.0 Å/s, per our earlier publication. [11]

Scanning Electron Microscopy. All micrographs were collected with Hitachi S4300-E SEM with field-emission gun, at 150 Pa chamber conditions, and detected with an Environmental Secondary Electron Detector (ESED).

X-Ray Photoelectron Spectrometry. The XPS measurements were performed using a Perkin Elmer 5500LS ESCA spectrometer with a non-monochromatized Mg Kα X-ray excitation source (1253.6 eV line) with a power of 300 watt and a pass energy of 89.45 eV. The diameter of the X-ray spot was set to be 400 μm for small area analysis. Depth profiles of the films were observed with continuous Ar^+ sputtering, operating the Ar^+ ion gun at a beam voltage of 3000V. The sputter area was approx 10 mm in diameter.

For the estimation of the etching rate for Au-PDMS composite material, the etch rate of gold (Au) was determined separately by analyzing the depth profiles of a 30 nm Au film on a clean silicon wafer which provided signature XPS bands. The exact thickness of the Au film on silicon wafer was measured using ellipsometer. The etch rate of PDMS was determined in a similar manner as was done for the Ag-PDMS. From the depth profile of Au and PDMS films, the etch rates were determined to be 1.8 and 3.4 Å/min, respectively, and the rough estimate of etch rate for the composite material was considered to be 3 Å/min in this work.

Surface Enhanced Raman Spectrometry. All SERS spectra were acquired using a modified version of a LabRam Spectrograph from JY-Horiba which has been previously described.[9] The STT instrumentation allows the translation of the sample at spin rates from 0 up to 8000 rpm.

Sample Preparation and Data Analysis. A series of $1x10^{-3}$ M stock solutions of p-aminobenzoic acid, p-ABA, (analytical grade, Nutritional Biomedicals), p-aminothiolphenol, p-ATP, (90+%, Aldrich,), n phenyl-1,2 diphenylene diamine, 1,2-PDA, (98%, Aldrich), p-nitroaniline (Eastman), 1,10 o-phenanthroline (G. Fredrick

Smith), and p-nitrophenol (Fisher) were prepared with deionized water (18Ω, Barnstead E-Pure) and 1% Methanol (99.9%, Acros Inc.). These stock solutions were used to prepare standards of $1x10^{-5}$ M.

A 50 μL aliquot of each sample solution was transferred to the Au-PDMS well, precisely centered on the top of the sample translator, and covered with a glass cover slip. The samples were generally translated at 2800 rpm and the light microscope images were aligned relative to dead center of the bottom of the microtiter well. The point of maximum SERS signal was obtained by fine-focusing the microscope objective after moving the illuminated spot 150 μm off-center. Once the signal was brought into focus the SERS spectra of the sample were acquired by moving the stage at 50 μm intervals (1 spectral acquisition of 5 sec per step) to a maximum distance of 1400 μm from the dead center. Experiments were performed to determine the working parameters for the Au-PDMS substrates such as acquisition time, laser power, and exposure time to analytes prior to the collection of the analytical data. Corrections of the baseline and the background were performed in order to compensate for the changes in refractive index of the sample solutions and the optical background signal from the substrate.

Results and Discussion

Noble metals exhibit a high agglomeration tendency, as their cohesive energy is at least two orders of magnitude higher than that of polymers, and have a low solubility in polymers under equilibrium conditions.[35-37] Despite noble metals weak chemical interaction with polymers, they have been shown to diffuse into the polymers during

vapor deposition. The extent to which this diffusion occurs depends on the nature of the polymer and its glass transition temperature. The melting point of a metal under vacuum directly affects the temperature within the PVD chamber, as well as the diffusion and morphology of the nanoparticles At slower depositions, there is a greater probability that free atoms or very small atom clusters encounter each other and form larger and more irregular nanoparticles of metal before impinging the substrate and the deposition chamber may remain below the glass transition temperature of the polymer. Thus, random diffusion and clustering into the bulk polymer can be inhibited. This may produce a highly surface-oriented film similar to that seen with metal-Si and metal-glass substrates.[8, 38] Fast deposition rates result in higher temperatures within the deposition chamber. The increased deposition rate also is expected to increase the concentration of free atoms or very small clusters that are formed in the PVD plume. In order to produce a more distinct and tunable plasmon resonance, there needs to be control over the nanoparticles size and shape and the distribution of these should be very narrow. This may be influenced via control of deposition parameters. [12, 13, 15, 39, 40]

Studies of Nanocomposite Properties Related to Metal Thickness and Deposition Rate

When heated in tungsten boats Au wets the surface, thus, unlike Ag, it is not a true point source for vapor deposition. A gradient of kinetic energies is created and this affects the distribution of nanoparticle sizes before they encounter the polymer substrate. The Au-PDMS substrates are not as homogeneous in particle size and shape as those of the Ag-PDMS nanocomposites.[11] The vapor transition temperature for gold is much

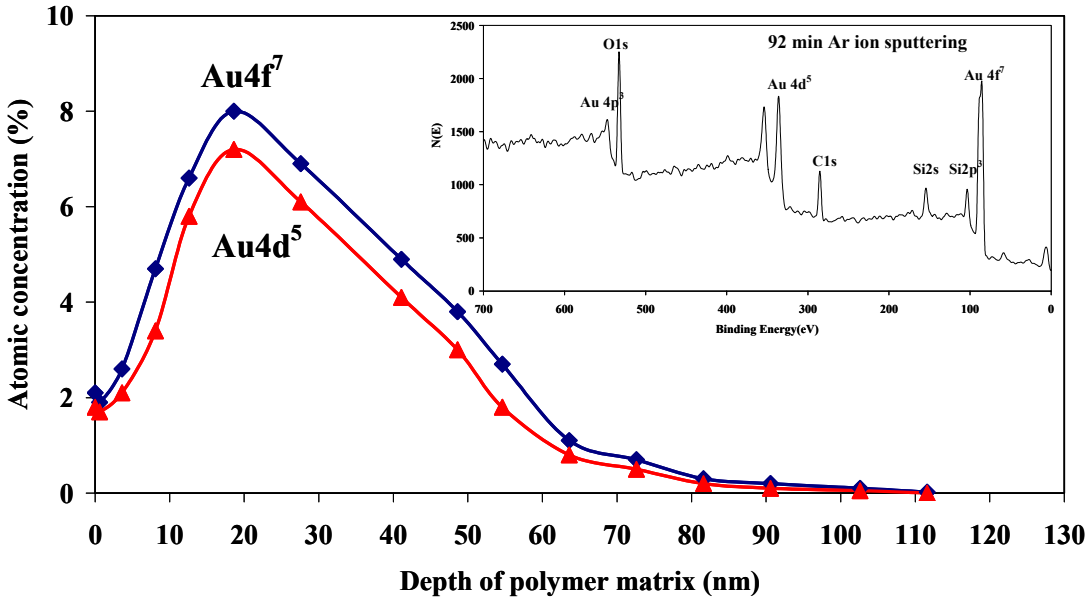


Figure 5.1. The XPS depth profiles of 30 nm Au on PDMS showing atomic percent for two Au lines. The inset is the XPS spectrum of the film after 37 minute Ar ion sputtering. The majority of the Au nanoparticles can be found within the top 60 nm of the PDMS matrix.

higher than that of silver, this coupled with higher deposition rates may allow the temperature in the deposition chamber to approach the glass transition temperature of the phase separated layer of the PDMS. This could affect the diffusion of gold atoms and nanoparticles into the polymer.

Figure 5.1 presents an XPS depth profile for a 30 nm average thickness of Au on PDMS demonstrating the change of gold content with depth from the surface of the composite material. The gold content as demonstrated in the profiles seen in the figure were estimated as peak area percent based on the Au $4d^5$ binding energy at 335-353 eV or the Au $4f^7$ binding energy at 86 eV. The C 1s binding energy at 287.5 eV, the O 1s binding energy at 536 eV, the Si 2s binding energy at 155 eV and the Si 2p binding energy at 105 eV were among the polymer peaks used to determine the area percent of

Au as the surface was sputtered at approximately 3 Å/min. From Figure 5.1, it appears that the amount of gold content increases from a very small amount at the surface to a maximum at around 15-20 nm below from the surface and then trails off to an undetectable amount by approximately 85 nm depth. The physical characteristics of these surfaces as described above and the XPS data provide evidence that the Au nanoparticles have a broad distribution submerged within the phase-separated surface layer of the PDMS. In comparison, the Ag-PDMS nanocomposites made under similar conditions also indicate that the metal nanoparticles diffused into the polymer, but that the distribution of particles extended further into the polymer (100 nm). [11] This apparent difference between Au and Ag may be due to the size of the nanoparticles upon impingement of the substrates, which may also affect the depth of penetration as well. The XPS data supports the supposition that the Au-PDMS system, like that of Ag-PDMS, has some depth within the polymer and that the accessible metal surface area is increased.

The optical properties of the composite material change due to the choice of noble metal, as well as alterations in the size and proximity among particles. [11] DC conductivity is one way to observe gross changes in metal nanoparticle proximity and determine at what thickness the percolation threshold, i.e. the creation of macroscopic electrical pathways, [41] occurs during the physical vapor deposition of gold onto the PDMS films. A constant DC voltage was applied across our substrate-electrode system during the deposition process while measuring an output current. Figure 5.2 demonstrates that the DC conductivity in the composite dramatically increased at 25 nm average gold thicknesses for deposition rates of 0.2 Å /sec and 1 Å /sec. The 1.0 Å/s

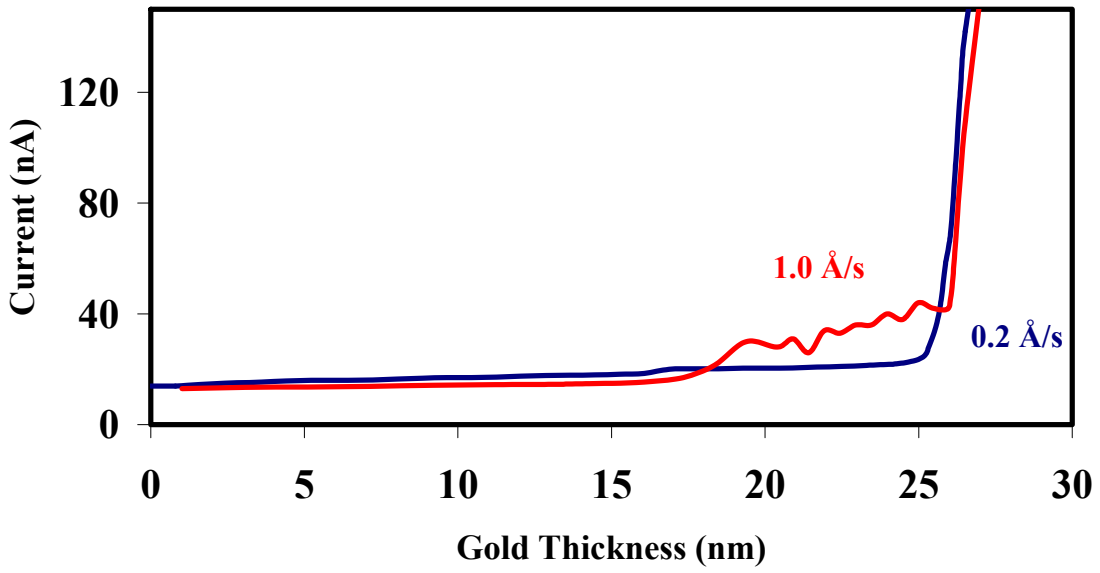


Figure 5.2. DC conductivity curves obtained during the deposition of Au at 0.2 and 1.0 Å/s. Relatively constant conductivity occurs ~25 nm for both deposition rates.

exhibits a unique pattern of temporary conductivity, whereby conductive paths are formed but the nanoparticles may not fully coalesce into a permanent continuous film.

The micrographs in Figure 5.3 indicate that deposition rate affects the regularity of the surface morphology. Slow deposition rates, ~0.2 Å/s, produce larger irregular features that may be more fractal in nature due to the lower kinetic energy of the nanoparticles. The particle sizes for 1.0 Å/s deposition range from 10 to 30 nm in diameter and range from 15 to 50 nm for the 0.2 Å/s depositions. From the micrographs and XPS, one may surmise that the particles are not spherical, but are more likely to be ellipsoidal shape with a small aspect ratio (~1.5:1 to 2:1). [11]

Effective Au thickness has a noticeable effect on reflectivity and other optical properties. The intensity and frequency of plasmon resonances are expected to shift with

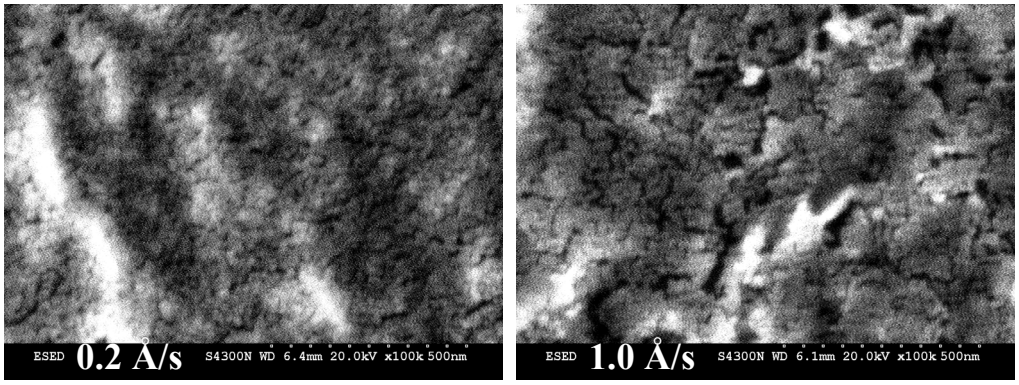


Figure 5.3. Scanning electron micrographs of 30 nm Au-PDMS surface at 100,000 fold magnification for deposition rates of 0.2 Å/s (left) and 1.0 Å/s (right).

increased size and proximity of nanoparticles.[1, 16, 42] The extinction curves shown in Figure 5.4 cover a wide range of Au thicknesses. The broad nature of the observed bands may result from multiple overlapping plasmon resonance bands due to morphological heterogeneity, reflectivity (expected to be rather broad), and absorption. The 25 nm thickness shows the beginning of a known Au absorption band appearing at about 530 nm (see Figure 5.4) and have a λ_{max} of 578 nm.[21] The λ_{max} for 20 nm was 584 and 594 for the 0.2 and 1.0 Å/s, respectively. Similarly, for 30 nm the λ_{max} was 594 and 605 nm for the two deposition rates. It is interesting to note that there is a substantial hypsochromic shift in the $\lambda_{max,}$, to 578 nm for 25 nm Au, near the percolation threshold for these nanocomposites. The optical extinction band of the 25 nm, 0.2 Å/s deposition rate is higher and slightly narrower than that of the faster rate (Figure 5.4). This may be due to the slightly larger size of the nanoparticles themselves and a change in the aspect ratio of the ellipsoidal particles. A tailing effect at long wavelengths may be due to fractal-like

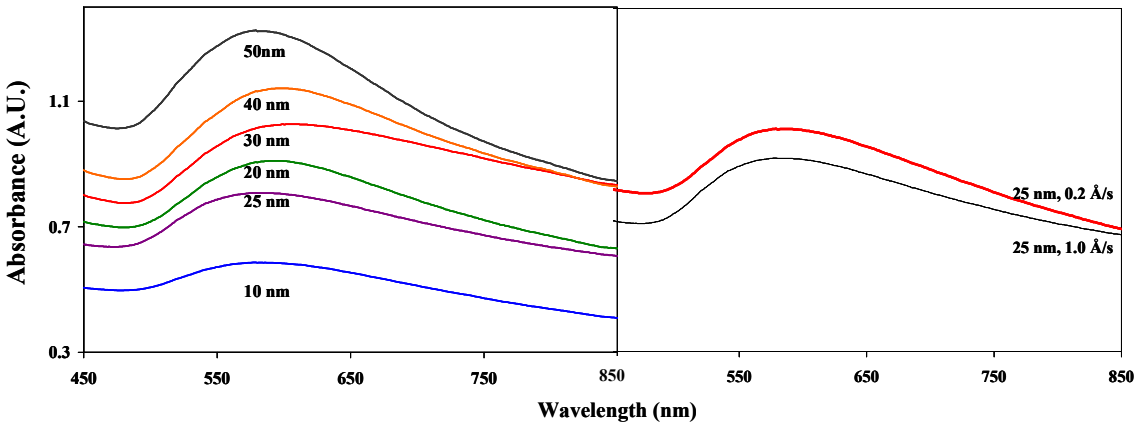


Figure 5.4. Optical extinction curves for Au-PDMS obtained at a deposition rate of 1.0 Å/s for six different average thicknesses of Au (left). Optical extinction curves for 25 nm average Au thickness Au-PDMS substrates at the two different deposition rates (right).

morphology similar to that seen with the Ag-PDMS substrates. [11, 21] These are comparable trends as those observed for the Ag-PDMS substrates.

Absorption, reflection, and heterogeneous morphology complicate any strict correlation between observed optical extinction profiles and the magnitude of surface plasmon resonance at a desired laser wavelength. Nevertheless, these extinction profiles provide a crude means to interpret SERS responses. SERS spectra of 1,2-PDA at a concentration that is expected to saturate the surface of the noble metal were obtained for Au-PDMS composites. The areas of the band centered at about 1151 cm^{-1} are plotted in Figure 5.5 for the different effective thicknesses of Au at two deposition rates to determine the best Au-PDMS parameters when using a He-Ne (633nm) laser for excitation. A typical spectrum of 50 μL of 1.4 x 10^{-4} M 1,2-PDA spotted into an Au-

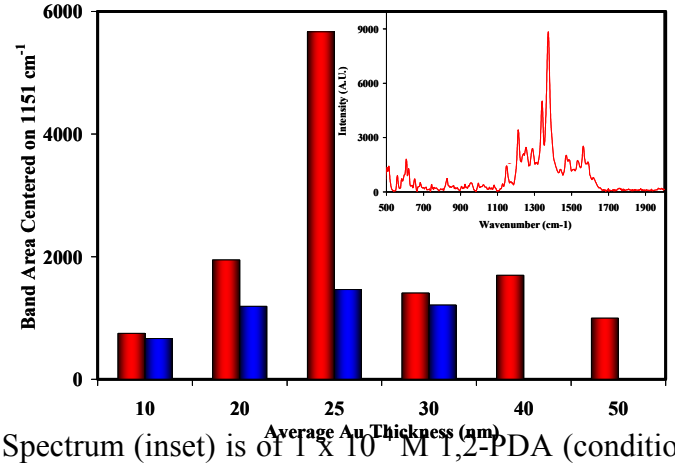


Figure 5.5. Spectrum (inset) is of 1 x 10^{-4} M 1,2-PDA (conditions: 5 second acquisition time; mean of 21 spectra; 2800 rpm; background and baseline corrected; excitation of 4.5 mW at 633 nm; 25 nm average Au thickness deposited at 1.0 Å/s). Comparison of 1151 cm^{-1} band areas of 1 x 10^{-4} M 1,2-PDA on Au-PMDS at a deposition rate of 1.0 Å/s (blue bar for 0.2 Å/s) to determine the optimum effective thickness and deposition rate for Au-PDMS substrates

PDMS microtiter well is shown as an insert in Figure 5.5, the asterisk denotes the 1151 cm^{-1} band.

Consistent with the extinction curves shown in Figure 5.4, the data for the He-Ne laser excitation showed the best response for the 25 nm thickness for both deposition rates (Figure 5.5), however, it is evident that the 1.0 Å/s deposition rate produced a much more intense SERS response. The band area data in the figure represents an average of three experiments with the He-Ne laser (633 nm); an optimum response in the 25 nm average thickness was observed for the individual experiments as well. The hypsochromic shift away from the laser wavelength in the λ_{max} (578 nm) for 25 nm Au occurs near the percolation threshold for these nanocomposites. This may account for the improved coupling of the excitation laser and the substrate and, thus, the increased SERS

activity at this particular metal thickness. In contrast, Ag-PDMS showed optimum SERS activity well below the percolation threshold.[11]

Since Au islands on glass represent one of the more traditionally used substrates, we made a direct comparison of spectra obtained on Au-glass and Au-PDMS. Both substrates were produced under their optimal conditions: 7 nm, 0.2 Å/s Au on glass substrate [12, 13, 29] and 25 nm, 1.0 Å/s for the Au-PDMS substrate (Figure 5.6). At 7.0×10^{-5} M *p*-ATP, the signal levels for Au-glass are almost a factor of two less than the Au-PDMS for most bands. Since *p*-ATP binds to the surface of the metal and sufficient analyte was present to achieve a monolayer, the ratio of signal levels in Figure 5.6A is indicative of the relative inherent surface enhancements of the two substrates. The spectra for 1,2-PDA demonstrate the unique advantage of PDMS as a solid phase extractor of analyte. Due to the efficient partitioning of the 1,2-PDA with the PDMS and the subsequent interaction with the Au layer, the spectrum for Au-PDMS substrate is far more intense than for the Au-glass substrate (Figure 5.6B). In addition, more spectral bands are enhanced, which improves the possibility of correct identification when performing qualitative analysis.

Translation Rate/ STT

As previously stated, our goal was to optimize Au-PDMS SERS substrates for the 633 nm He-Ne laser line. The Au-PDMS substrates are relatively durable and stable. They remain functional for more than six months for both qualitative and quantitative studies even when exposed to light and atmosphere. (Figure 5.7) In contrast, Ag-PDMS

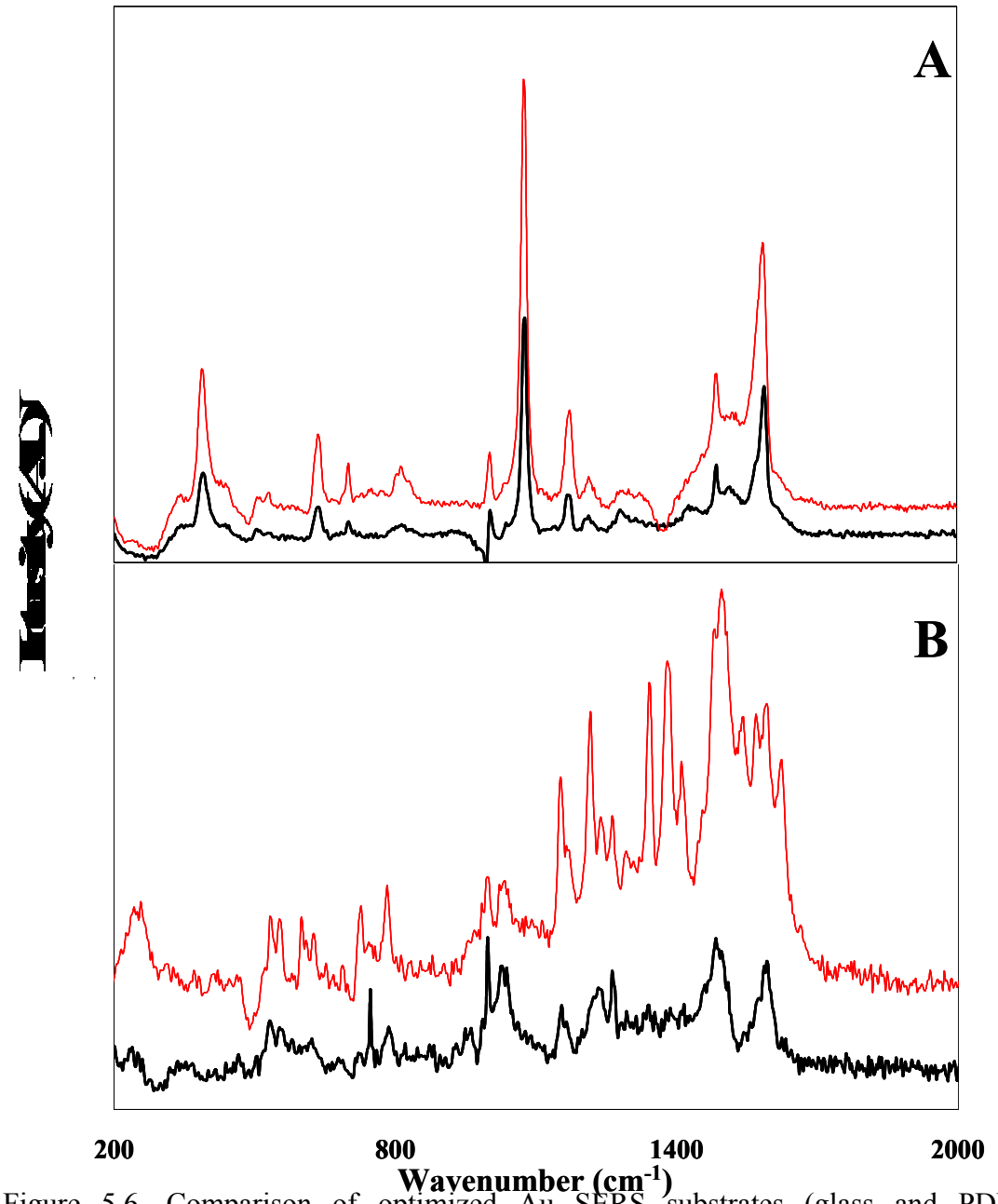


Figure 5.6. Comparison of optimized Au SERS substrates (glass and PDMS substrates) under STT conditions to illustrate improved SERS signal intensity and functional group affinity. Spectra (A) of 6.9 x 10-5 M *p*-ATP on Au-PDMS (Red) and Au-Glass (black). Spectra (B) of 1.9 x 10-5M 1,2-PDA. Conditions for both A & B: 5 second acquisition time; mean of 21 spectra; 2800 rpm; background and baseline corrected; excitation 4.5 mW at 633 nm; 25 nm Au deposited at 1 Å/s on PDMS; 7 nm Au deposited at 0.2 Å /s on glass).

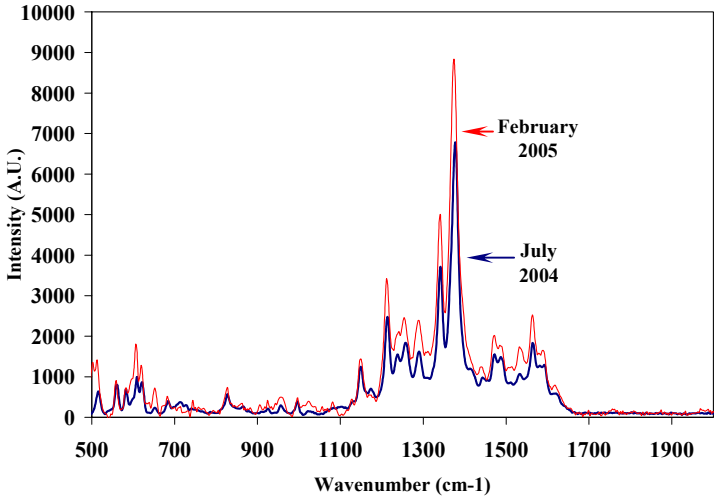


Figure 5.7. A study of the long-term viability of the Au-PDMS substrates. Spectra of 1,2 PDA (1.26 x 10^{-4}M) under STT conditions. First spectrum taken the day substrates were prepared (bold blue). Second spectrum was taken more than six months later using a microtiter well from the same set of substrates that were kept under ambient conditions (red).

substrates are functional for quantitative studies only during the initial five days and are remain viable for qualitative work for up to two weeks when held under vacuum and in the dark.

These noble metal nanocomposites are inherently inhomogeneous, have intrinsic band broadening, and are susceptible to thermal and photolytic decomposition effects. These concerns lead to substantial differences in the SERS spectra under stationary and STT conditions. While these noble metal nanocomposites are made with the same elastomer, the choice of noble metal effects the STT working parameters such as laser power tolerance, acquisition time, translation rates, and functional group affinity. The potential benefits for improved qualitative and quantitative analysis using STT with Ag-PDMS have been previously presented by our group.[9, 10] In this work, we have applied

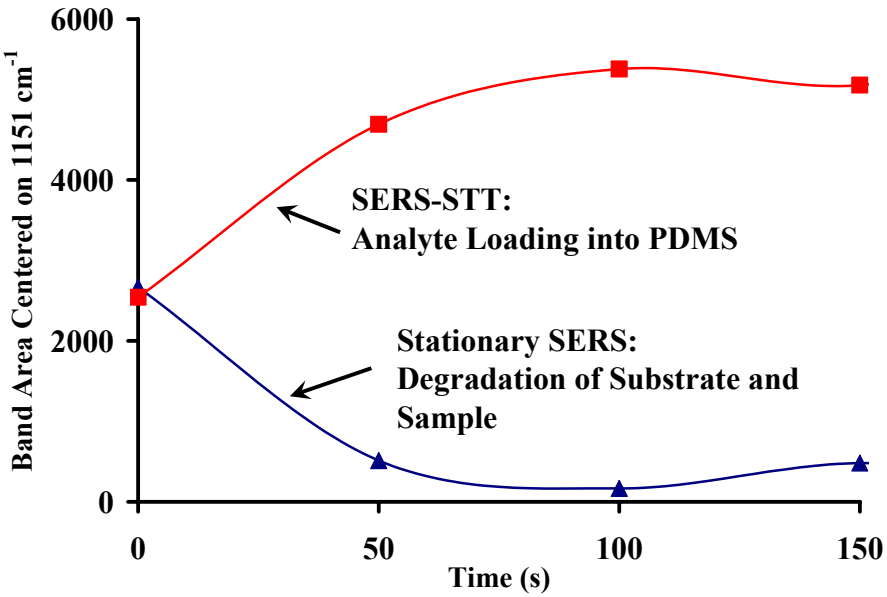


Figure 5.8. Temporal study of the effect of 8.9 mW of laser irradiation on substrate and analyte under stationary and STT-SERS conditions.

this technique to the Au-PDMS substrates to reduce the deleterious effects of stationary SERS and improve the S/N of Au-PDMS.

While Ag-PDMS substrates are more SERS active, they are visibly damaged with at low power densities with the 633 nm He-Ne laser during a 1 s acquisition. The inherent robustness of the Au substrates permitted longer acquisitions of 5 s at a 4.9 mW of laser power. This compensated for the lower Au SERS enhancements without visible damage to the substrates under both stationary and STT conditions.

The degradation of both the analyte and substrate is reduced with translation. Figure 5.8 compares a series of 1 s acquisitions over the course of 150 s under stationary and STT conditions on the growth of the 1151 cm^{-1} spectral band, which is associated with the breathing mode of the benzene ring. This region of was selected since it exhibits modest thermal and photolytic effects, which result in a reduction in band area. In this

study, bands at 1330 and 1580 cm^{-1} (graphitic carbon bands) were also tracked to follow the degradation rate of the analyte. Under stationary conditions at the highest laser power tested (8.9 mW), decay of the 1151 cm^{-1} band is very rapid and more than 90% of the band area is lost within the first 100s. Simultaneously, the graphitic carbon bands rapidly increase, suggesting the degradation of the analyte and substrate. Similar to the Ag-PDMS, the translation of Au-PDMS microtiter wells containing the sample at 2800 rpm, roughly 10^5 μm/s and a residency time of 0.1 ms or less, with the same laser power produced a more consistent band area. The slight rise in band area during the initial 50 s may be due the kinetics of analyte loading into the PDMS, after the initial period the 1151 cm^{-1} spectral band remains relatively stable.

Reproducibility of SERS spectra and spectral resolution for Ag-PDMS microtiter wells under STT conditions has been demonstrated.[9] While the intensity of the signal from the Au-PDMS substrate is reduced in comparison to the Ag-PDMS substrates, the overall background features are minimal and can be easily subtracted from the analytical signal. Studies of a $1.0x10^{-3}$ M solution of 1,2-PDA as a model biological compound show an intra-well RSD (n=21) of less than 16%, and an inter-well RSD (n=5) of less than 10% using the 1149 cm^{-1} band.

As a surface-based technique, SERS offers discrete sampling capabilities that are a function of the available number of nanoparticles per unit area. The limited number of adsorption sites and the rapid decay of the induced electromagnetic field in SERS sets the maximum loading capacity of the substrate close to a monolayer of analyte per unit area. With the nanocomposites, the encapsulated nature of the gold within the polymer increases the available surface area for SERS and can extend the saturation point of the

substrates. The results in Figure 5.9 indicate that the limit of detection (3 x S/N) and linear range of these substrates are promising for the qualitative and the quantitative analysis of biologically relevant analytes and better than typically observed for gold islands on glass. [28]

Selectivity

Gold is considered one of the most inert metals. Since only a modest number of organic chemicals and substrate adsorption sites can exploit the full potential of SERS chemical and electromagnetic enhancement factors, this relative inertness reduces the potential for analyte degradation or complexation at the metal surface. The SAMs produced by disulfides, thiols, and alkylamines have been well characterized and have been exploited for many sensor-based technologies.[43, 44] The interaction of other functional groups, such as aromatic amines, imines, and nitro, to Au is considered to be a relatively weak non-covalent bond when attached to colloidal Au nanoparticles.[28] It has been suggested that electrostatic and hydrophobic interactions of these functionalities, especially in biologically-based studies, dominate. Despite this limited chemisorption, Au-based SERS permits the detection of many biologically relevant analytes such as penicillin, amphetamines, cocaine, heroin, 3-4 methylenedioxymethamphetamine (MDMA, also known as ecstasy), and other analgesics in aqueous media, as well as cellular-based SERS studies.[5, 18, 28, 29]

Even though Au-based substrates generally produce weaker SERS enhancements in the visible wavelength range than Ag, it may have lower detection limits for certain analytes due to selectivity of the metal and the concomitant chemical enhancement

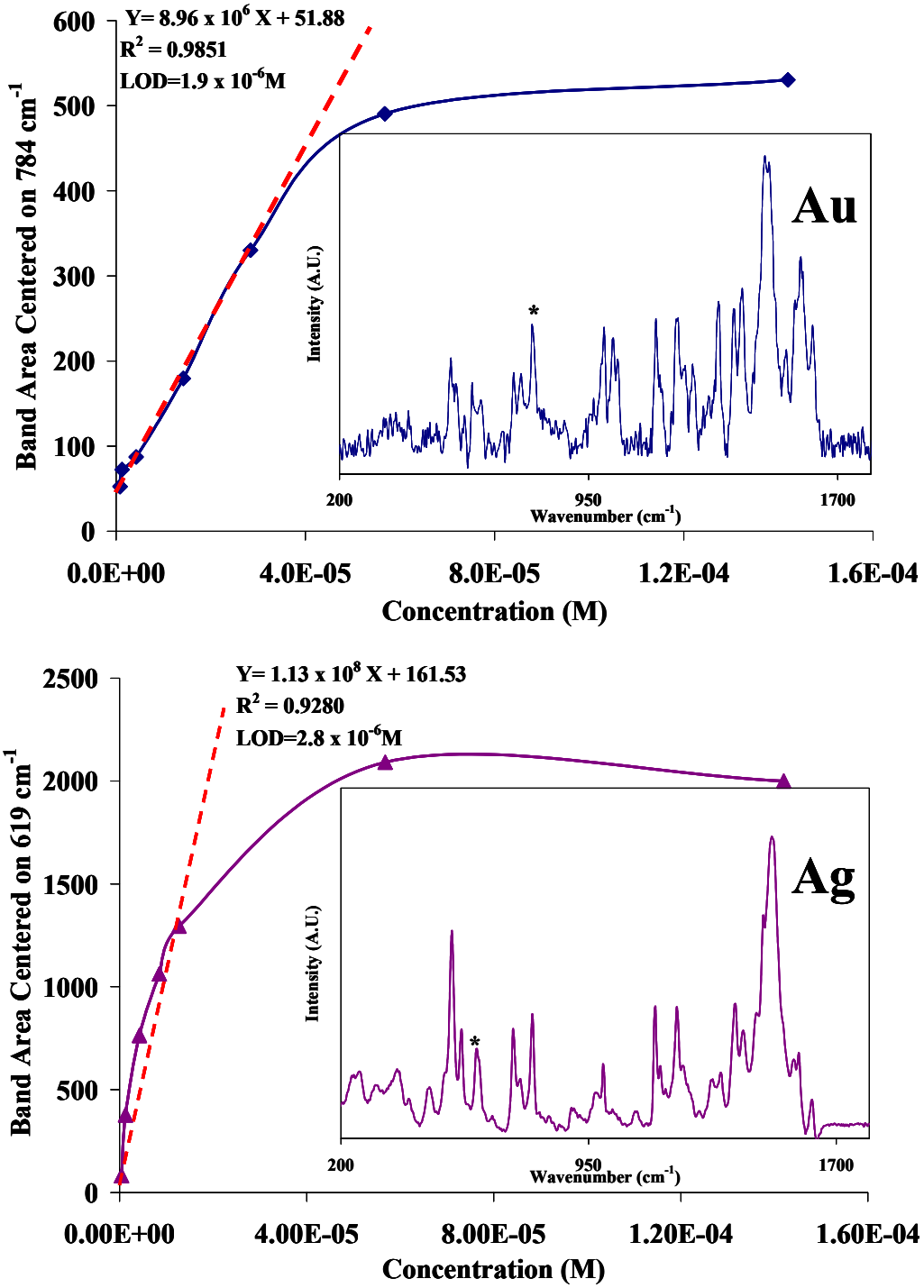


Figure 5.9. Calibration plots for 1,2-PDA with Au (top) and Ag (bottom) nanocomposites substrates. (Conditions for Au-PDMS: 5 second acquisition time; mean of 21 spectra; 2800 rpm; background and baseline corrected; excitation 4.5 mW at 633 nm; 25 nm Au deposited at 1 Å/s on PDMS. Conditions for Ag-PDMS: 1 second acquisition time; mean of 21 spectra; 2000 rpm; background and baseline corrected; excitation 2.2 mW at 633 nm; 20 nm Ag deposited at 1 Å/s on PDMS.)

effects.[28] A comparison of calibration plots with gold and silver nanocomposites using the aromatic amine, 1,2-PDA, as a model biological analyte shows the potential for a lower detection limit with Au-PDMS. The insets of spectra of 1,2-PDA in Figure 5.9 on both nanocomposite substrates illustrate that the binding of the analytes to the nanoparticles results in the enhancement of different bands depending on the metal. This is probably due to the orientation of the analyte to the nanoparticles due to covalent bonding and the secondary electromagnetic field effects.

In a previous study it was found that functional groups such as amine, nitro, or carboxyl groups compete for the binding sites on the Ag nanoclusters.[45] The differences in the spectral bands in Figure 5.10 also illustrates that Au and Ag SERS substrates exhibit unique selectivities for naphthalene derivatives with a 1,5 substitution pattern and other bi-functional analytes. Specifically, the Au substrates show a high affinity for analytes with the amine functional group (Figure 5.10 B, C, D).

The Effect of pH and Anions on Analyte Absorption and SERS Activity

As PDMS is often used for solid-phase micro-extractions, it is useful to understand how the manipulation of pH and anion concentration can be applied to improve SERS intensity. Ionized organic species such as carboxylic acids, phenols, and amines will not readily partition into the nonpolar PDMS. Likewise, large multi-ringed analytes may not absorb or diffuse into the PDMS uncross-linked surface. Sometimes this selectivity is desirable if the ionized species would otherwise interfere with the analysis. Partitioning of ionizable organic compounds into the PDMS substrates can be manipulated as a function of pH and anion concentration. Adjusting the pH into the

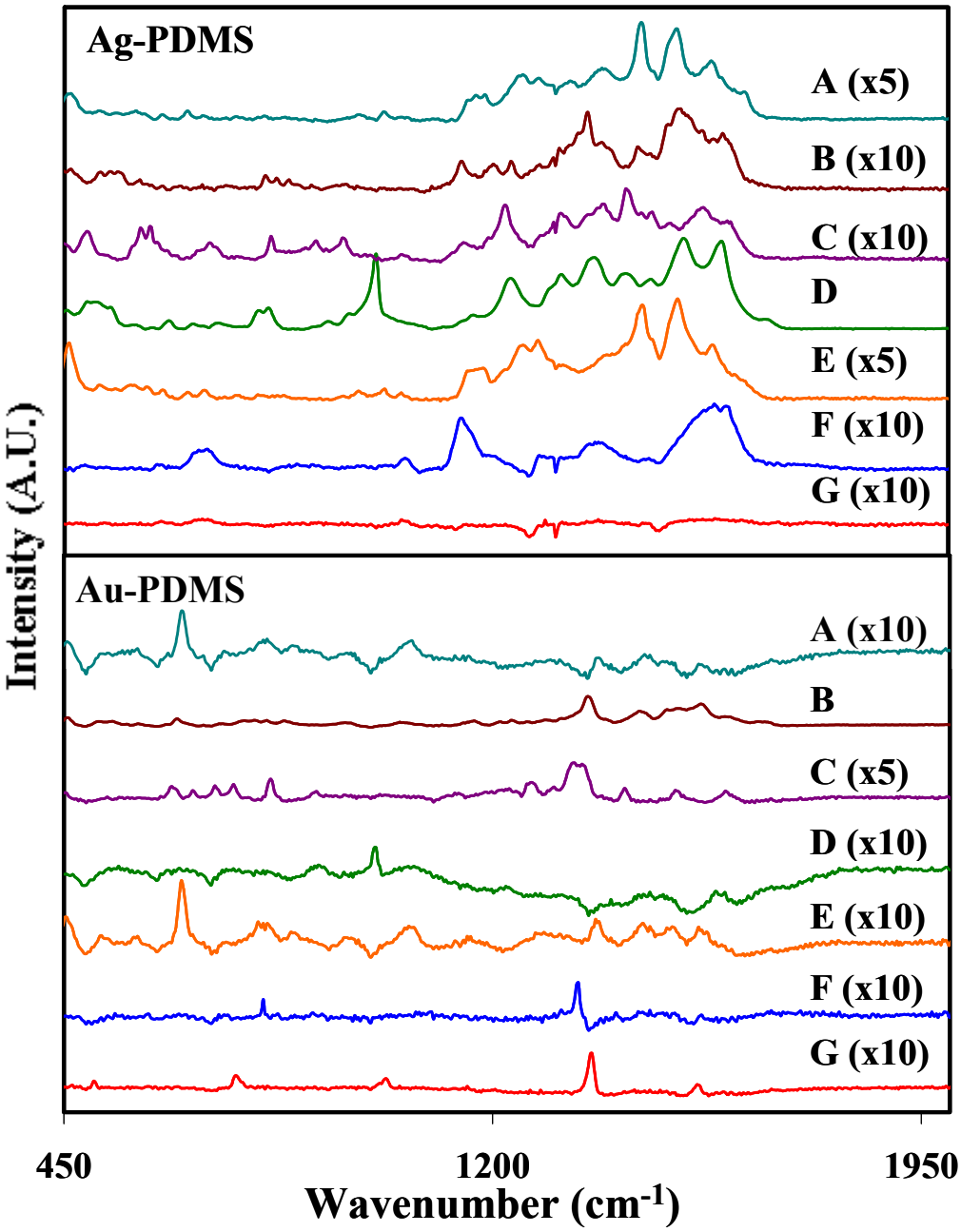


Figure 5.10. Comparison of selectivities of Ag-PDMS (upper) and Au-PDMS (lower) for a series of naphthalene derivatives that show the affinity of Au-PDMS for amine and nitro functionalities. Note that some SERS spectra have been multiplied by an integer for clarification of the spectra. A) 1,5 Dihydronaphthalene; B) 1,5 Diaminonaphthalene; C) 4 Chloro-nitroaniline; D) 3 Amino benzoic acid; E) 1,5 Naphthalenediol; F) 1,5 Dinitronaphthalene; G) Naphthalene.

acidic range can enhance partitioning and extraction of phenols and carboxylic acids via protonation and bring them into close proximity to the gold nanoparticles. Similarly, by the simple adjustment of the sample to a pH into the basic range, many basic compounds will more easily extracted. Some research groups have found that moderate amounts of polar organic solvents in a solution will not affect the partioning of these organic species into the PDMS, which may facilitate the preparation of certain analytes for SERS analysis. We have, in previous studies, utilized acetonitrile as such an agent to improve the solubility of an analyte.

The Effect of pH on SERS Intensity. In studies with the Ag-PDMS system, we have shown the PDMS inhibits the oxidation of the silver and promotes the adsorption of a wide range of analytes via a solid-phase extraction process (Figure 5.10). This was thought to be due to the favorable ionization of the analytes such that their diffusion into the PDMS and the simultaneous ionization of the silver nanoparticles which would improve the physisorption process. It is known that changes in pH can also affect the distribution of silanol groups on the surface of the PDMS, thus altering its permeability. These experiments resulted in improved SERS signals for specific analytes under different conditions.

The PDMS in the Au-PDMS system provides a matrix for the three-dimensional distribution of the nanoparticles and act as the solid-phase extractor. Gold is inherently stable and oxidizes only under very harsh conditions, such as when gold is exposed to aqua regia. It is believed that the chloride ion facilitates the ionization of Au to the auric ion Au^{+3}.[46, 47] In this series of experiments the pH and the anion concentrations were in a

range well below that of where oxidation of the gold might occur. The adsorption and diffusion of the analyte to the gold nanoparticles and the concomitant increase in SERS signal could therefore be argued due to the manipulation of the PDMS partioning process itself. As previously discussed and illustrated in Figure 5.10, all gold substrates have a more limited functional group affinity. Amines have the strongest affinity to these surfaces and, consequently, we have chosen n phenyl-1,2 diphenylene diamine (1,2 PDA) as the model analyte for this series of partioning experiments. Figure 5.11A illustrates the effect of pH on the analyte, n phenyl-1,2 diphenylene diamine. The native 1,2 PDA solution had a pH of 5.62 and was manipulated with 1 M nitric acid and 1 M sodium hydroxide. As the pH of the solution approached the pK_a, there was an increase in the SERS intensity from the analyte. Unlike the studies with the silver, nearly all of the bands were enhanced equivalently.

By noting the effect that the Au deposition had on the PDMS bands, it provided a baseline from which the effect of pH on both the analyte and the polymer could be discerned. We tracked the increase in the band areas of 485 and 1151 cm^{-1} (Figure 5.10B) for the bands corresponding to the Si-O-C asymmetric deformation vibration and the =C-H in-plane deformation vibration, respectively. The native surface of the uncoated PDMS had a very sharp and intense signal before the vapor deposition of the Au at 485 cm^{-1}, which became broad and the band area was reduced by nearly 33%. Below a pH of 7, the surface of the Au-PDMS may be permanently altered as the silanol groups are modified or decreased. In contrast, the band center on 1150 cm^{-1} associated with the analyte, increases as the pH approaches the pK_a. This may be due to the formation of a soft Lewis base via ionization that improved the adsorption onto and

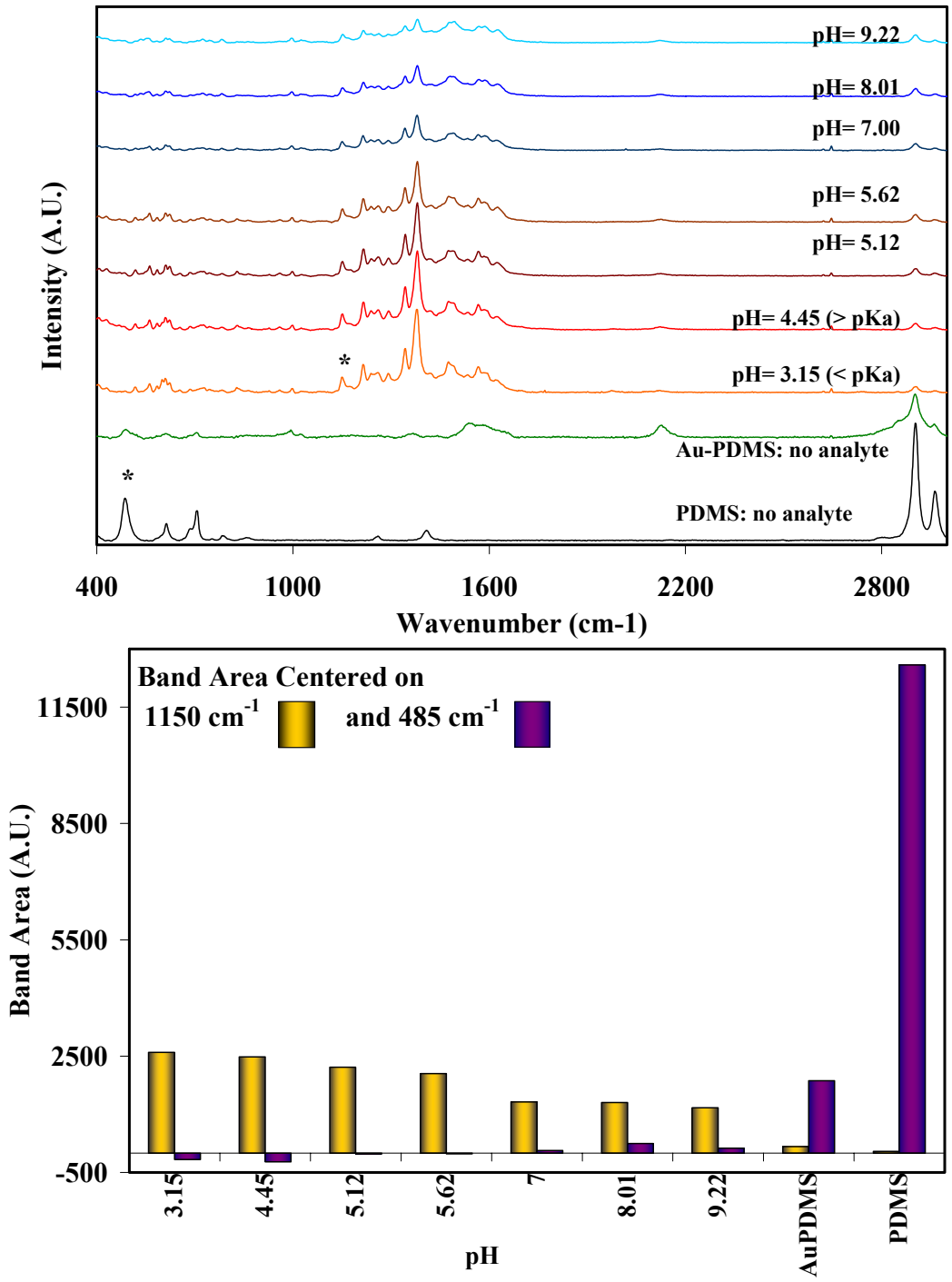


Figure 5.11. A) The SERS intensity as a function of pH. A 5.97 x 10^{-4}M solution of n phenyl-1,2 diphenylene diamine (pK_a=4.45) was analyzed under STT conditions (2800 rpm and incident laser power of 4.5 mW). B) Comparison of band areas centered on 485 cm^{-1} and 1150 cm^{-1} as a function of pH (band areas marked with an asterisk.) Spectra and band areas for Au-PDMS and PDMS without analyte are included as a reference for the background.

diffusion into the polymer. This would necessarily bring the analyte in closer proximity to the gold nanoparticles where they could then be physisorbed.

Inorganic Anions and the effect on Partioning. Inorganic anions in the matrix of analyte solutions can alter their solubility in water and their subsequent partioning into the PDMS. Unlike Ag, gold does not tend to form complexes with the halides and other anions, which has been shown to severely reduce the effectiveness of the Ag-island substrates. A series of experiments were performed on Au-PDMS and Au-glass substrates to differentiate between the effect of increased partioning and true chemical enhancement due to the anions. Samples were prepared by using a series of sodium salts of the type (NaX), where X was one of the following: phosphate, acetate, sulfate, carbonate, nitrate, bromide, chloride, or fluoride. The total concentration of the 1,2 PDA was held at 1 x 10^{-4}M in solutions of increasing concentration of the NaX anions. The control samples were prepared with de-ionized water.

In order to more fully characterize the partioning process, the band near 777(782) cm^{-1} was tracked on both the Au-PDMS and Au-Glass systems (Figure 5.12). The 777(782) cm^{-1} that was tracked is characteristic of a 1,2 di-substituted aromatic compound's out of plane (OOP) deformation vibration. There is a slight shift in the center wavenumber of the band between the Au-PDMS and Au-Glass that may be due to the difference in the dielectric properties of these materials. Overall, the addition of the anion solutions reduced the SERS band area for the OOP vibration in comparison to the control on Au-Glass of the 1,2-PDA without the addition of the NaX salts. This may be

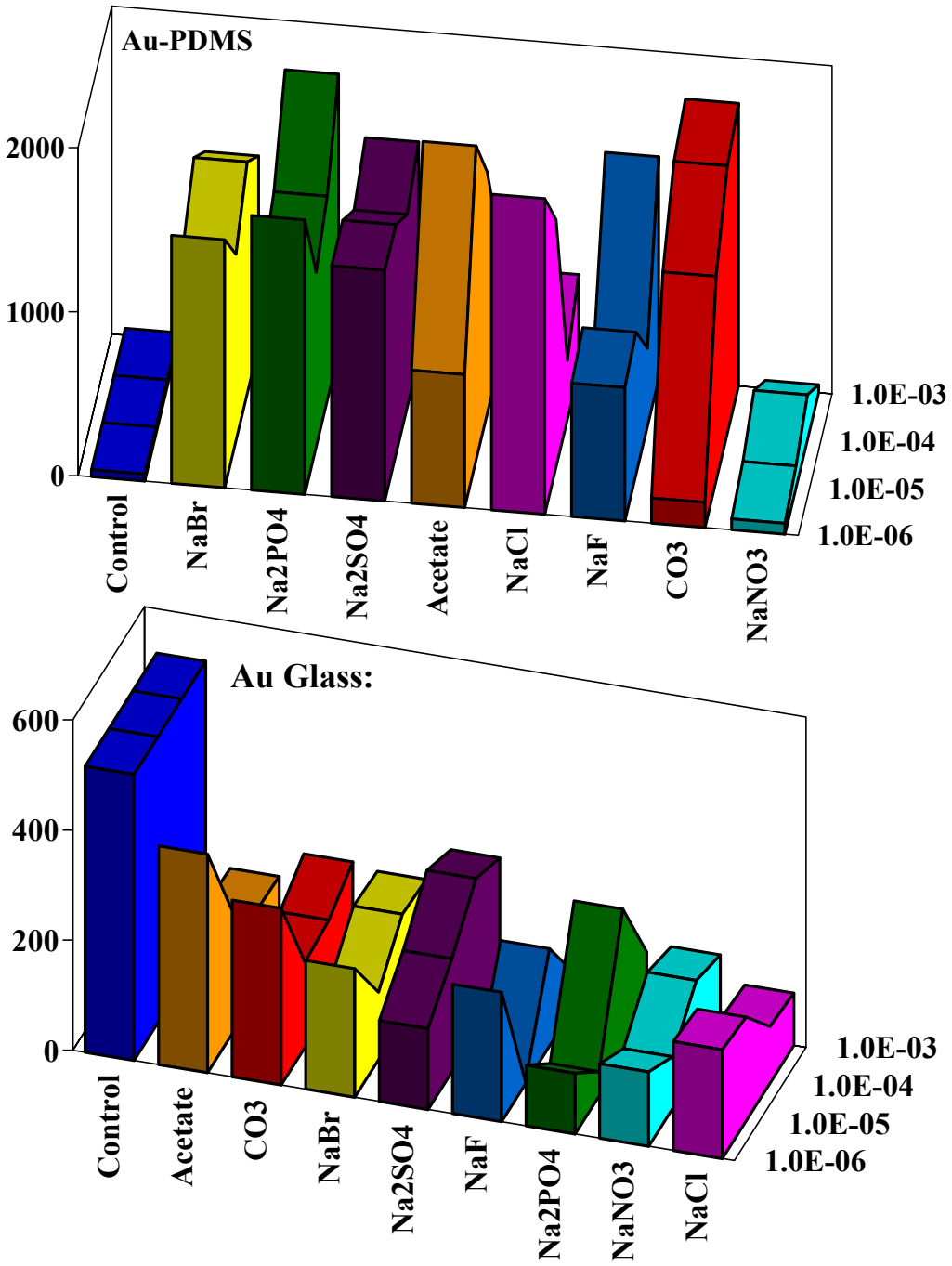


Figure 5.12. Comparison of band areas on Au-Glass (782 cm^{-1}, 7 nm, 0.5 Å/s, stationary conditions (N=21)) and Au-PDMS (777 cm^{-1}, 25 nm, 1.0 Å/s, STT-SERS conditions (N=21)). The concentration of the 1,2 PDA was held at 1 x 10^{-4}M prepared in solutions of increasing sodium salts.

due to the formation of a monolayer that overcoats the metal film and prevent the close contact of the analyte to the metal nanoparticles. In contrast, the Au-PDMS system showed a marked increase in the band areas for all the NaX salts at all concentrations at 777 cm^{-1}. This may be indicative of an improved partioning effect or as there may be a change in the orientation or geometry of the molecule due to the formation of complexes that would also improve the partioning .

Table 5.1 shows the correlation between the anion concentration and its subsequent change in pH. The red highlighted pHs are near or above (+/- 0.2 accuracy of the meter), which according to the previous pH study should result in a reduction of the spectrum, if the partioning process is solely governed by pH. It is interesting to note that the 777 cm^{-1} band shows overall improvement for the Au-PDMS with all of the anions, despite the elevated pH.

These studies may provide the basis for future experiments for the identification of single analytes in a mixture of analytes. We have shown with the Ag-PDMS system that the manipulation of the solid-phase extraction capabilities of the PDMS, this selective sorption of an analyte may be achievable. Although there is more limited palette of functional groups that have affinity for gold, we believe that this will expand the applications for this system, especially in the realm of biologically relevant analytes and for biological systems.

Table 5.1 pH of NaX solutions

Anion	10^{-3}M	10^{-4}M	10^{-5}M	10^{-6}M
Br^{-1}	6.27	6.18	6.01	5.82
Cl^{-1}	6.30	6.05	5.90	5.99
F^{-1}	7.05	6.66	6.37	6.23
$Acetate^{-1}$	6.86	6.62	6.42	6.38
CO_3^{-2}	9.95	6.91	6.11	5.85
PO_4^{-2}	7.52	6.88	6.48	6.80
SO_4^{-2}	6.89	6.72	6.47	6.03
NO_3^{-2}	5.87	6.11	7.03	7.10
1,2 PDA		6.51		

References

References

(1) Emory, S. R.; Haskins, W. E.; Nie, S. *Journal of the American Chemical Society* **1998**, *120*, 8009-8010.
(2) Kneipp, K. *Single Molecules* **2001**, *2*, 291-292.
(3) Maier, S. A.; Brongersma, M. L.; Kik, P. G.; Meltzer, S.; Requicha, A. A. G.; Atwater, H. A. *Advanced Materials (Weinheim, Germany)* **2001**, *13*, 1501-1505.
(4) Murphy, T.; Schmidt, H.; Kronfeldt, H. D. *Applied Physics B: Lasers and Optics* **1999**, *69*, 147-150.
(5) Sockalingum, G. D.; Beljebbar, A.; Morjani, H.; Manfait, M. *Proceedings of SPIE-The International Society for Optical Engineering* **1998**, *3260*, 58-62.
(6) Beitinger, G.; Kolbeck, G.; Feldmann, K. *Metalloberflaeche* **2001**, *55*, 40-45.
(7) Kreutz, E. W.; Frerichs, H.; Stricker, J.; Wesner, D. A. *Nuclear Instruments & Methods in Physics Research, Section B: Beam Interactions with Materials and Atoms* **1995**, *105*, 245-249.
(8) Zaporojtchenko, V.; Zekonyte, J.; Biswas, A.; Faupel, F. *Surface Science* **2003**, *532-535*, 300-305.
(9) De Jesus, M. A.; Giesfeldt, K. S.; Sepaniak, M. J. *Applied Spectroscopy* **2003**, *57*, 428-438.
(10) de Jesus, M. A.; Giesfeldt, K. S.; Sepaniak, M. J. *Journal of Raman Spectroscopy* **2004**, *35*, 895-904.
(11) Giesfeldt, K. S.; Connatser, R. M.; De Jesus, M. A.; Lavrik, N. V.; Dutta, P.; Sepaniak, M. J. *Applied Spectroscopy* **2003**, *57*, 1346-1352.
(12) Gupta, R.; Dyer, M. J.; Weimer, W. A. *Journal of Applied Physics* **2002**, *92*, 5264-5271.
(13) Gupta, R.; Weimer, W. A. *Chemical Physics Letters* **2003**, *374*, 302-306.
(14) Malinsky, M. D.; Kelly, K. L.; Schatz, G. C.; Van Duyne, R. P. *Journal of Physical Chemistry B* **2001**, *105*, 2343-2350.
(15) Semaltianos, N. G.; Wilson, E. G. *Thin Solid Films* **2000**, *366*, 111-116.
(16) Gunnarsson, L.; Bjerneld, E. J.; Xu, H.; Petronis, S.; Kasemo, B.; Kall, M. *Applied Physics Letters* **2001**, *78*, 802-804.
(17) Kalyuzhny, G.; Schneeweiss, M. A.; Shanzer, A.; Vaskevich, A.; Rubinstein, I. *Journal of the American Chemical Society* **2001**, *123*, 3177-3178.
(18) Sockalingum, G. D.; Beljebbar, A.; Morjani, H.; Angiboust, J. F.; Manfait, M. *Biospectroscopy* **1998**, *4*, S71-78.
(19) Kelly, K. L.; Coronado, E.; Zhao, L. L.; Schatz, G. C. *Journal of Physical Chemistry B* **2003**, *107*, 668-677.
(20) Link, S.; El-Sayed, M. A. *International Reviews in Physical Chemistry* **2000**, *19*, 409-453.
(21) Kim, W.; Safonov, V. P.; Shalaev, V. M.; Armstrong, R. L. *Physical Review Letters* **1999**, *82*, 4811-4814.
(22) Malinsky, M. D.; Kelly, K. L.; Schatz, G. C.; Van Duyne, R. P. *Journal of the American Chemical Society* **2001**, *123*, 1471-1482.
(23) Lee, Y.-H.; Farquharson, S.; Rainey, P. M. *Proceedings of SPIE-The International Society for Optical Engineering* **1999**, *3857*, 76-84.

(24) Odziemkowski, M.; Koziel, J. A.; Irish, D. E.; Pawliszyn, J. *Analytical Chemistry* **2001**, *73*, 3131-3139.
(25) Habuchi, S.; Cotlet, M.; Gronheid, R.; Dirix, G.; Michiels, J.; Vanderleyden, J.; De Schryver, F. C.; Hofkens, J. *Journal of the American Chemical Society* **2003**, *125*, 8446-8447.
(26) Doering, W. E.; Nie, S. *Journal of Physical Chemistry B* **2002**, *106*, 311-317.
(27) Moskovits, M.; Tay, L.-L.; Yang, J.; Haslett, T. *Topics in Applied Physics* **2002**, *82*, 215-226.
(28) Faulds, K.; Smith, W. E.; Graham, D.; Lacey, R. J. *Analyst (Cambridge, United Kingdom)* **2002**, *127*, 282-286.
(29) Jennings, C. A.; Kovacs, G. J.; Aroca, R. *Journal of Physical Chemistry* **1992**, *96*, 1340-1343.
(30) Khlebtsov, N. G.; Bogatyrev, V. A.; Dykman, L. A.; Melnikov, A. G. *Journal of Colloid and Interface Science* **1996**, *180*, 436-445.
(31) Seitz, O.; Chehimi, M. M.; Cabet-Deliry, E.; Truong, S.; Felidj, N.; Perruchot, C.; Greaves, S. J.; Watts, J. F. *Colloids and Surfaces, A: Physicochemical and Engineering Aspects* **2003**, *218*, 225-239.
(32) Sheng, R.; Zhou, G.; Xiong, J.; Xu, Z.; Morris, M. D.; Zeng, Y. e. *Wuhan University Journal of Natural Sciences* **1997**, *2*, 101-104.
(33) Suh, J. S.; Jeong, D. H.; Lee, M. S. *Journal of Raman Spectroscopy* **1999**, *30*, 595-598.
(34) Kiefer, W.; Bernstein, H. J. *Applied Spectroscopy* **1971**, *25*, 500-501.
(35) Dou, Y.-H.; Bao, N.; Xu, J.-J.; Chen, H.-Y. *Electrophoresis* **2002**, *23*, 3558-3566.
(36) Kim, S. D.; Torkelson, J. M. *Polymeric Materials Science and Engineering* **2001**, *85*, 2-3.
(37) Smithson, R. L. W.; McClure, D. J.; Evans, D. F. *Thin Solid Films* **1997**, *307*, 110-112.
(38) Kuban, P.; Flowers, H. *Analytica Chimica Acta* **2001**, *437*, 115-122.
(39) Kaschl, A.; Romheld, V.; Chen, Y. *Environmental Toxicology and Chemistry* **2002**, *21*, 1775-1782.
(40) McMurry, J.; Castellion, M. E. *Fundamentals of General, Organic, and Biological chemistry, Third Edition*, 1999.
(41) Kilbride, B. E.; Coleman, J. N.; Fraysse, J.; Fournet, P.; Cadek, M.; Drury, A.; Hutzler, S.; Roth, S.; Blau, W. J. *Journal of Applied Physics* **2002**, *92*, 4024-4030.
(42) Hinde, R. J.; Sepaniak, M. J.; Compton, R. N.; Nordling, J.; Lavrik, N. *Chemical Physics Letters* **2001**, *339*, 167-173.
(43) Grabar, K. C.; Freeman, R. G.; Hommer, M. B.; Natan, M. J. *Analytical Chemistry* **1995**, *67*, 735-743.
(44) Kumar, A.; Mandal, S.; Selvakannan, P. R.; Pasricha, R.; Mandale, A. B.; Sastry, M. *Langmuir* **2003**, *19*, 6277-6282.
(45) Sepaniak, M. J.; De Jesus, M. A.; Giesfeldt, K. S. *American Pharmaceutical Review* **2004**, *7*, 90, 92-97,37.
(46) Filippov, A. A.; Volkova, G. V. *Sin., Ochistka Anal. Neorg. Mater., Tr. Konf. \"Nauka-Proizvod.\"* **1971**, 163-170.

(47) Carlsson, L.; Lundgren, G. *Acta Chemica Scandinavica (1947-1973)* **1967**, *21*, 819.

Part 6
Preliminary Investigations of Polymer-Based SERS Substrates with Uniform Morphology

Introduction

In chapter two, it was shown that the incident electromagnetic radiation can initiate surface plasmons and, thus induce electromagnetic fields, which are the basis of the signal enhancement seen with Surface Enhanced Raman Spectroscopy (SERS). Unfortunately, substrate selectivity and issues with the analytical figures of merit, such as reproducibility and dynamic range have not garnered the general acceptance of the technique for routine analytical applications. Nevertheless, SERS has been shown to be very useful for qualitative analysis, due to narrow spectral bands which result in unique spectral fingerprints and structural information. The drive for uniform morphologies will produce SERS substrates with large homogeneous EM fields that may improve the Raman cross-section, and therefore, lower the detection limits by increasing Raman scattering.

The disordered complex surfaces from colloids and thin film type substrates have a multitude of plasmon modes that are difficult to deconvolute and model. The random nature of these types of substrates induces a series of interference patterns that affects the uniform distribution of surface plasmons. Gaps, dislocations, and anomalous-sized nanoparticles can dampen the generation and propagation of surface plasmons (SPs) across a surface. Periodic dielectric nanostructures offer the means to determine a more direct correlation between the computer-generated models of the magnitude of SERS and the experimentally-determined optimal structures. Array parameters such as size, shape, geometric pattern, grating constant, as well as substrate dielectric function can be manipulated to produce substrates with a high density of identical analyte environments.

Early attempts at periodic nanostructuring included stochastic silica posts,[1] silica nanospheres,[2, 3] micro-contact printing,[4-15] and self-assembled monolayers of colloids.[16-22] These approaches were limited by of the instrumentation available at the time, which had, at best, a limited resolution of approximately 100 nm. Our prior calculations and those of many others indicate that the field enhancement increases dramatically as the gap between nanoparticles decreases to near molecular dimensions.[23-28]

Electron beam lithography (EBL) continues to evolve and each subsequent generation of the EBL instruments have improved resolution.[29, 30] Structures considerably smaller than 50 nm with gaps of less than 50 nm have been made, but their size and shape is frequently limited by imperfections in the thin films and by damage induced by the developing processes. The resolution of EBL is limited by the beam diameter, the brightness of the electron source, and the beam current. The shortest-focal length electron lenses currently available are about 0.5 mm. In theory, when a 50 keV electron beam is focused, the resulting beam has a minimum diameter of approximately 0.56 nm. However, in practice the beam is generally larger in diameter by at least 20% depending on the source of the electrons. The practical resolution of EBL is determined by the choice of resist, thickness of the film, the beam current and the resultant generation of secondary electrons. As the beam current is increased, the forward scattered radiation is narrowed and becomes nearly negligible below the typical 0.1 μm thick layer resist for nanolithography. Correspondingly, as the incident energy of the beam increases, the area from which the backscattered electrons are generated also increases. At a typical 50 keV, the diameter due to forward and backscattered electrons can be as large as 10 nm, which can obscure a very dense pattern by reducing the contrast

between elements. This limitation is crucial for the production of penultimate SERS substrates, wherein the gap between nanoparticles needs to be far below this dimension.

In this chapter, we will show our preliminary investigations into the optical properties and SERS responses for a series of nanowell cross-gratings (NCG) and two-dimensional arrays of nanoparticles produced via EBL. We plan to cast and imprint elastomeric polymers using the NCGs as the mold. This would permit the mass-production of pillar-like polymeric structures with unique geometries and patterns that would be metallized via physical vapor deposition. While the imprinting of polymers with silicon molds has become virtually routine in the semi-conductor industry, it has not, to our knowledge, been applied to the fabrication of SERS substrates. We are also exploring EBL as a means of generating the nanoparticle arrays and directly vapor depositing metal on to the arrays, such that they can be used to transfer the ordered metal films onto the elastomers. As with the imprinting, this will facilitate the rapid generation of homogeneous SERS substrates. Imprinting of the polymers and the metal transfer by the EBL substrates will allow us to probe nanoparticle proximity with the unique elastomeric properties of PDMS, the stretching or relaxation of the polymer films. Molecular probes will be used to determine the optimum Ag metal film thickness and grating periodicity to generate SPs with 633 nm He-Ne laser excitation. In addition, the selectivity of these substrates due to metal film will be explored and the SERS response of these systems can be compared to that of disordered systems. With continued refinement, it is desired that these studies will eventually guide the generation of designs for future high performance SERS substrates.

Experimental

Nanowell cross-gratings. The nanowell cross-grating were produced at the Cornell facility by Dr. Nickolay Lavrik (Oak Ridge National Laboratory, Oak Ridge, Tennessee). A 4" Si (100) wafer with 1 μm thick SiO_2 was used as a substrate for e-beam lithography. These wafers were cleaned with piranha (3:1, H_2SO_4 and H_2O_2) solution for 3 minutes, rinsed with deionized water, and dried with a stream of dry nitrogen. Poly-methyl methacrylate (PMMA) 950K (MicroChem) electron-beam resist was spun-coated at 1500 rpm for 45 sec, which resulted in a 250 nm thick layer. The PMMA was soft-baked for 45 min at 160^{o}C using contact heating on a hotplate.

A Leica VB-6HR electron-beam writing tool was used to transfer the cross-grating patterns onto the PMMA. The e-beam dose was ramped in the range of 800 to 2580 μC/cm^2. This yielded a series of patterns with 10 mm spacing in x and y directions. Thus, the wafer was divided into 25 10x10 mm areas with patterns differed by the e-beam dose only. Each of such 10x10 mm areas contained four elemental 50x50 μm NCGs with slightly different pitch parameters. The gap/pitch for all four NCGs, in both x and y directions were as follows: 200/400 nm, 200/350 nm, 300/450 nm, and 300/500 nm (Figure 6.1). All NCGs have a well depth of 250 nm.

The e-beam resist was developed with a 1:1 dilution of methyl isopropyl butyl ketone (MIBK): isopropyl alcohol (IPA) for 2 minutes. After which the patterned resist

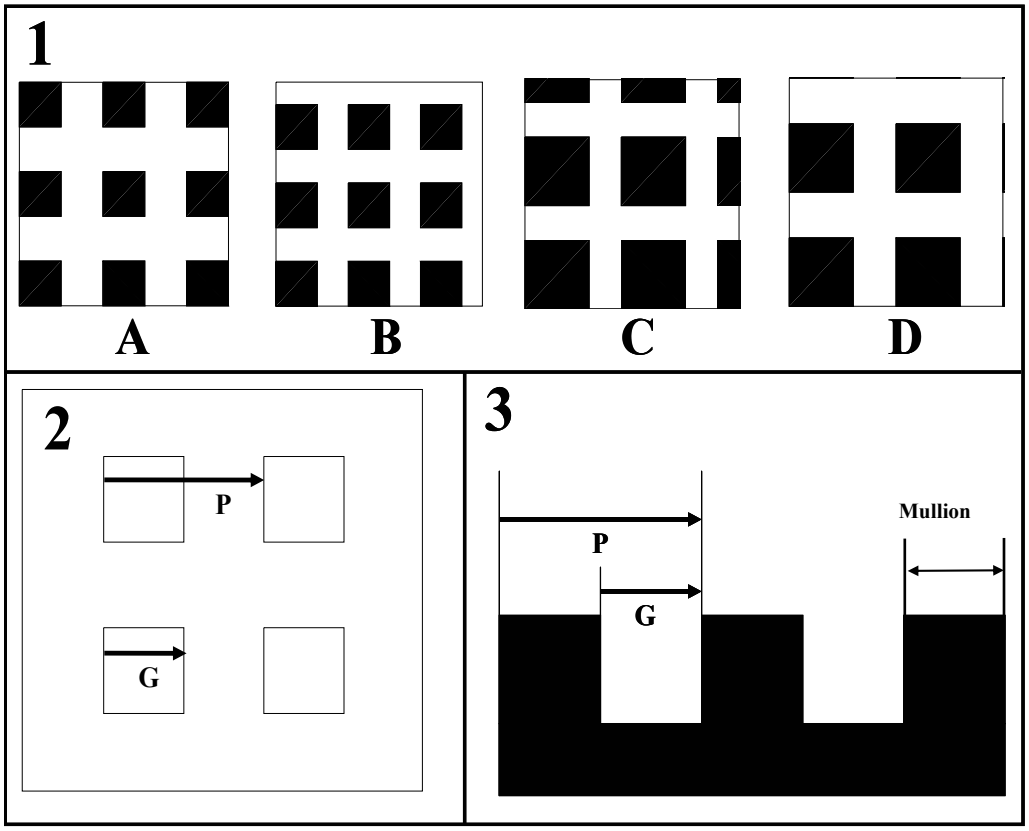


Figure 6.1. 1) A 1 μm area of the AutoCad patterns to show a comparison of the four nanowell cross-gratings. Gap/Pitch: A)200/400;B) 200/350; C)300/450; D) 300/500. 2) Illustration of Gap (G) and Pitch (P) of nanowell cross-gratings and nanoparticle arrays. 3) Cross-sectional illustration of Gap (G) and Pitch (P) of nanowell cross-gratings.

was dried for 45 min at 90°C on a hot plate. The patterned e-beam resist layer was used as a dry etch mask for reactive ion etching. The dry etch of oxide was conducted in capacitively-induced CHF_3 plasma (150 W, 20 mTorr) for 25 min using a Plasma Therm 72 tool. Due to relatively poor selectivity of PMMA resist versus oxide etch; the resist layer was also partially etched away during this step.

Nanoparticle Arrays. These arrays were produced in the EBL facilities at the University of Tennessee by Dr. Marco De Jesús and myself. 2" Si (110) wafers were cleaned with a piranha solution (2:1, H_2SO_4 and H_2O_2) for 5-10 minutes, rinsed with deionized water, and dried with a stream a dry nitrogen. Residual moisture was removed by placing in a 200^0C oven for 30 minutes, and then removed to a glass desiccators to cool. The wafer was spun-coated with a negative resist of MA-N 2403 (methacrylate) (MicroChem) at ~3000 rpm for 30 s. This resulted in a 250 nm thick layer. The MA-N 2403 was soft-baked for 60 s at 90°C using contact heating on a hotplate.

AutoCad LT 2000 was used to generate the four patterns for the nanoparticle cross-gratings based on the negative parameters from the NCGs and imported into a Jeol JBX-6000 FS/E electron-beam writer. The e-beam dose was 120 $\mu C/cm^2$. Six sets of the four cross-gratings with 100 μm spacing in x and 50 μm y directions. The patterns were developed with a ma-D 332; a sodium hydroxide based solution for 30 s and rinsed with copious amounts of water. The patterned resists were imaged before and after physical vapor deposition of 10 nm Ag and Au (1.0 Å/s) for characterization with SEM, optical reflectance spectroscopy, and SERS. Subsequent experiments were done with 20 nm Ag and Au (1.0 Å/s) for improved SERS response.

Imprinted PDMS. The NCGs were used as a silicon mold for PMDS. The small sections of patterned Si wafer were attached to a glass microscope slide with paraffin. A metal laser slit to act as a container for the molding compound was positioned over a set of NCG using the video imaging of a JY Horriba LabRam instrument. Sylgard 184 was prepared 10:1, per the manufacturer directions and poured into the laser slit. The ensemble was placed in a vacuum desiccators and brought to ~10^{-2} Torr and held there for twenty-four hours until fully cured. The imprinted polymer was carefully removed from the silicon mold, UV-ozone treated for 5 minutes, and then vapor deposited with 20 nm Ag and Au (1.0 Å/s) for characterization with SEM, optical reflectance spectroscopy, optical extinction, and SERS.

Ag Deposition. Ag (99.999%, 2-3mm diameter pellets, Alfa Aesar) and Au (99.999%, Gatewest, Canada) films were deposited on nanowells cross-gratings, MA-N 2403, and PDMS with a Cooke Vacuum Products, Inc. vapor deposition chamber which has been previously described.

Extinction Spectra and Optical Reflection Spectroscopy. All extinction spectra were collected on a Thermospectronic Biomate 5 UV-Visible spectrometer with the automatic cell tray removed. All spectra were collected from 350 to 800 nm. Background spectra of glass and PDMS were collected and manually subtracted from the appropriate spectra.

Optical reflection spectra of the NCGs with several thicknesses of Ag were collected with a JY-Horiba LabRam with the holographic notch filter removed. A 50x objective (Olympus) was used to focus the white light source onto the surface of the nanowell cross-gratings (NCG) and nanoparticle arrays, which probes ~7 μm diameter

area. The slit width was set to 20 μm and the confocal hole set to 500 μm. All spectra were collected from 350 to 800 nm, in three sections. The three individual spectra were collected for 1 s and combined into a single spectrum, post-collection. A reference spectrum from each metal and thickness in a non-nanostructured area was collected to calculate the ratio spectrum (sample spectrum/ reference spectrum).

Scanning Electron Microscopy. Micrographs were collected with Hitachi S4300-E SEM with field-emission gun, at 150 Pa chamber conditions, and detected either with an Environmental Secondary Electron (ESED) or Backscattered Scattered Electron (BSE) detector. Under high vacuum conditions a Secondary Electron detector (SE) was used.

Surface Enhanced Raman Spectrometry. SERS spectra were acquired using a modified version of a LabRam Spectrograph from JY-Horiba which has been previously described. For the comparison of laser wavelengths and SERS on Au-coated NCGs, a Dilor XY Raman spectrometer (Instruments SA Inc., Edison, NJ) was used in double additive mode with a 1200-groove/mm grating and 100-μm slits, giving a band-pass of 2 nm. The EG &G OMA 4 CCD detector (Trenton, NJ) was cooled with liquid nitrogen. The 100 mW of a 1514.5nm 20 W argon ion laser Coherent Innova 200 (Palo Alto, CA) and a 676.4 nm 5 W krypton laser Coherent Innova (Palo Alto, CA) were attenuated to ~86% at the sample. The spectra were collected over the 1137-1740 cm^{-1} range on each nanowell cross-grating and integrated for 5 s for each. All reported spectra are an average of quadruplicate measurements to improve S/N.

Nanowell Cross-gratings and Nanoparticle Arrays

While the cross-gratings and those of the nanoparticles in our EBL arrays herein are larger than the theoretically calculated individual localized particles for the optimal conditions for SP resonance, these nanostructured areas were designed to be similar in dimensions to the nanoparticles found on polymeric nanocomposites, metallic gratings, and metal oxide films cited in the literature. We have utilized relatively high deposition rates, so that the films would be smoother at the nanoscopic scale in comparison to EBL and imprinted nanostructuring. All of our preliminary substrates have been deposited with either Ag or Au at 1.0 Å/s with film thicknesses (20-60 nm) that exceed the percolation threshold of silicon wafers. This was done to minimize generation of SERS signals in areas that were not modified by EBL, imprinting, etc.

Absorption, reflection, and diffraction of light from these well defined, periodic nanostructures can be monitored by optical extinction spectroscopy in either transmission or reflection geometry. Mie theory has been used to explain the observed surface plasmon resonance effects with localized and regular arrays of nanoparticles. It has been calculated that dislocations (gaps) and irregular particle sizes of the substrate can dampen the propagation of SPs across a surface.

We have seen with our PDMS-based nanocomposites, the optical extinction profiles furnished a crude means to interpret the viability of certain structures for SERS at specific excitation wavelengths. While most SERS analytes do not fluoresce in the 500-600 nm laser wavelengths, many of the biologically relevant compounds, in vivo studies, and nanocomposites must address this issue by moving further into the NIR. The different pitch/gaps of the nanowell cross-gratings and the nanoparticle arrays are

believed satisfy the conditions for surface plasmon resonance at particular excitation wavelengths. Further study into the optimal size and proximity with different lasers will assist in future designs for particular applications.

As indicated in the previous chapters, it is well documented that the conditions for surface plasmons resonance and the subsequent SERS enhancement of analyte signals depend critically on interparticle spacing and the dielectric constants of the substrate, surrounding medium, and analyte. These separate dielectric constants combine to form a unique dielectric environment to such an extent that the individual dielectric constants cannot be decoupled from one another. Depending on the type of solid support, the metal nanoparticles can be affected by all three simultaneously, or in the case of our nanocomposites, most of the embedded nanoparticles are affected by the dielectric of the polymer and the adsorbed analytes.

The deposition of thin dielectric materials, such as silicon dioxide or polymers, over noble metal nanoparticles can act as a protective or as a selective semi-permeable layer that are can either be physisorbed or chemisorbed. Similarly, analytes in solvent with different refractive indices on these same types of substrates have also been shown to exhibit shifts in the plasmon resonance as a result of the changing dielectric environment. Only the non-bound surfaces of the nanoparticles deposited on solid support, such as glass or thermo-plastics, are in direct contact with this thin surrounding dielectric medium. The dielectric properties of the over-layers, molecular analytes, and solvents, as well as their thicknesses, can directly affect the refractive index, and therefore, the SERS response. A number of research groups have proposed biological and chemical sensors based on measuring small shifts (~ 5nm) in the localized surface

plasmon resonance (LSPR). However, these very narrowly tuned LSPR substrates have not been demonstrated to have the performance characteristics essential for analytical applications with SERS detection.

As we have stated, our objective is to create uniform analyte environments with relatively narrow SP resonance and a consistent EM field across an entire SERS substrate. The effect of the dielectric environment will need to be considered, as the LSPR shifts due to changes in this environment can be as great as 200 nm, which may affect the conditions for surface plasmon resonance at a given excitation wavelength. Our EBL nanostructured substrates may provide the means create substrates to this goal and permit the investigation into adsorption of an analyte or of a solvent and the subsequent effect on SERS activity. As our substrates are not transparent, optical reflection spectra and SERS mapping may help to elucidate this connection.

Nanowell Cross-Gratings

In the early stages of design, it was anticipated that the nanowell cross-gratings (NCGs) could perform as nano-titer wells. It was hypothesized that the vapor deposition process would form cushions of Ag along the mullions and at the bottoms of the wells. These additional metal sites would then serve as adsorption sites that would improve the linear dynamic range of the substrate. In addition, these sites would be well within the desired spacing to generate localized SPs and, therefore, produce a large EMF (Figure 6.2). This would enhance the Raman signals for analytes adsorbed on the interstices and in solution. However, hydrophobicity of the surface was radically increased due to the nanostructuring, the efficient excitation of SPs was not realized and the EMF generated

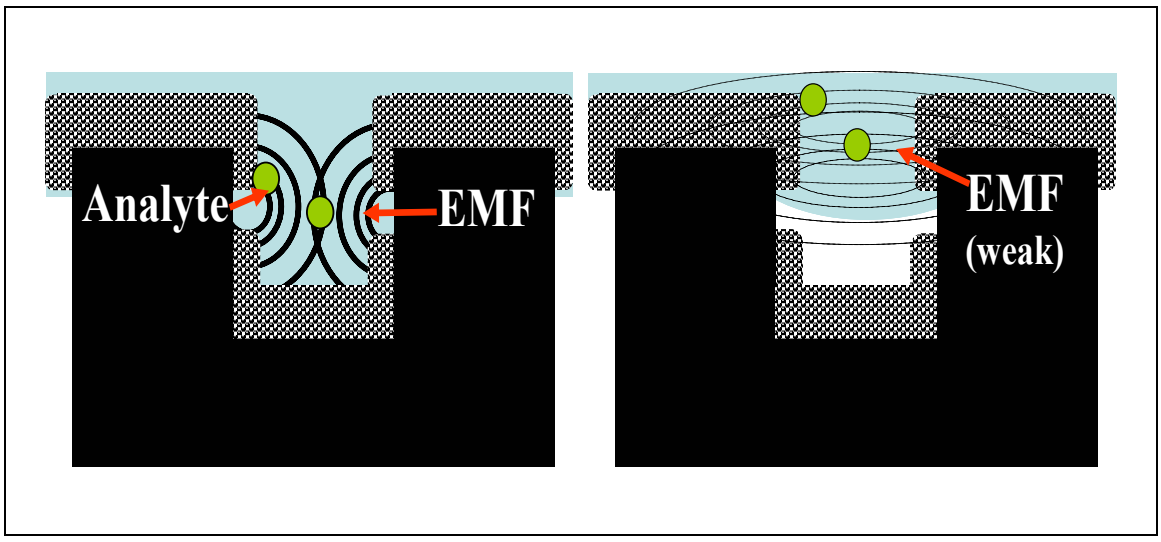


Figure 6.2. Illustration of the theorized nano-titer well function (left) and what the empirical data suggests (right).

seemed to be much weaker due to the non-ideal spacing between the tops of the metal-coated mullions and the poor coverage at the bottom of the wells.

The effect of film thickness, approaching the percolation threshold, was explored with the NCGs. The SEM images in Figure 6.3 show the inherent surface roughness with the growth in film thickness. It is evident from the SEM micrographs that despite the relatively thick metal coating, the nanowells were not occluded by the Ag nanoparticles. With high magnification and tilting of the samples, it was clear that there were gaps between the metal coating the mullions and the metal at the bottom of the wells. It was concluded that the high aspect ratio of the wells did prevent a contiguous metal film from being formed, and that potentially even thicker metal films could be applied before we would reach a true percolation threshold for the nanostructured areas.

A series of SERS experiments were performed with the set of NCGs at the different metal film thicknesses seen in the SEM micrographs. After each Ag deposition,

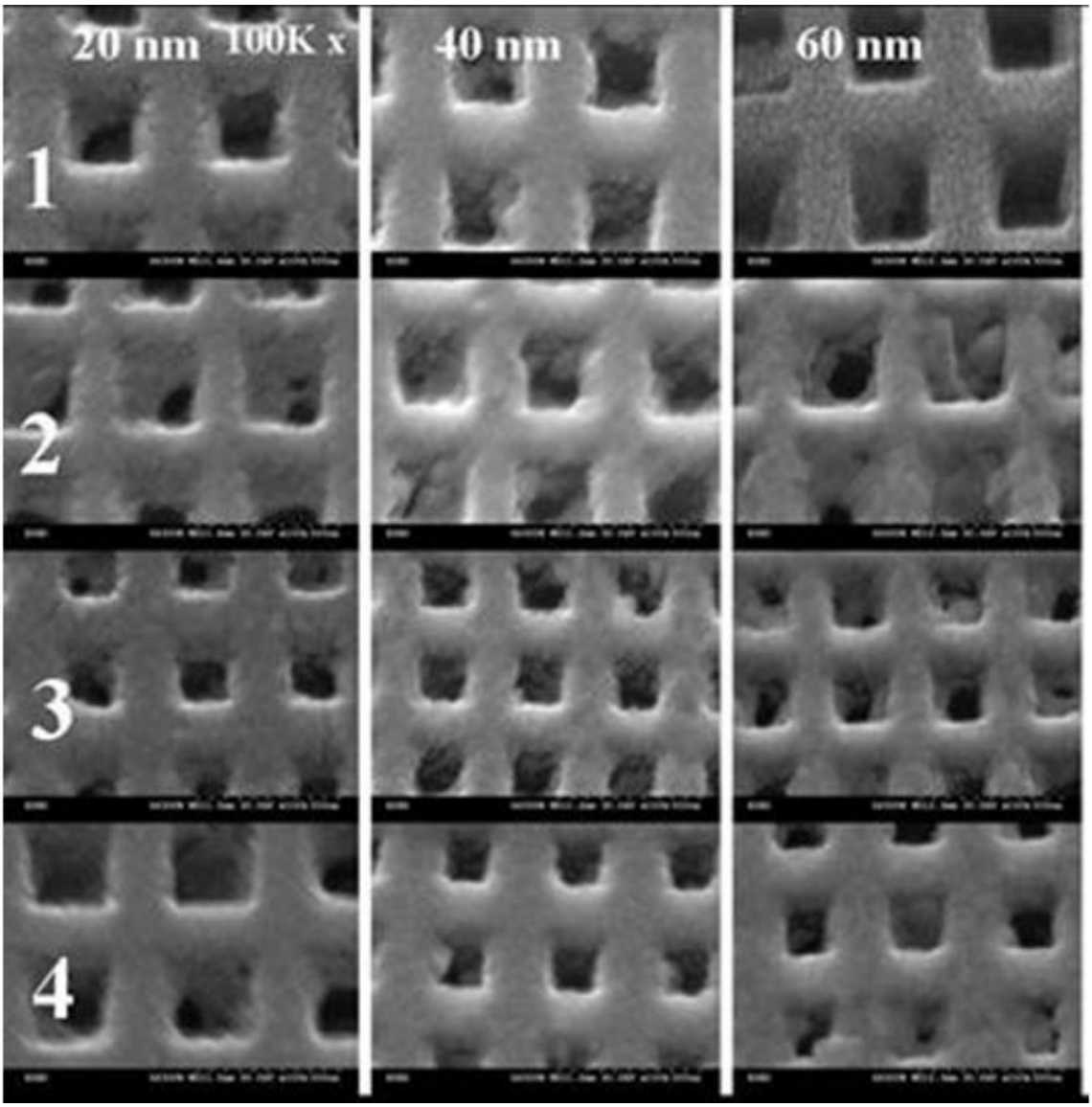


Figure 6.3. SEM micrographs illustrating the effect of metal film thickness on the inherent roughness of the Ag film

the NCGs were vapor treated with p-ATP. This analyte was chosen because it is easily chemisorbed on the surface of the NCGs, thus would create a unique dielectric environment. Spectra were collected on and off the NCGs decouple the enhancement mechanism due to the fractal-like nature of the thick metal films and the nanostructuring. The band centered on 1558 cm^{-1}, a -C=C- stretching vibration, was monitored for all the samples. Figure 6.4 shows a unique response for each pitch/gap per the metal film thickness with little or negligible response from the areas off the nanostructuring. Due to the low intensity of the SERS signals overall, we concluded that the well structures seemed to have interrupted the propagation of the SPs and the generation of the evanescent fields in all directions from the point of incidence. While the SPs could propagate along the mullions of these structures, the field may have been dampened due to the non-ideal particle separation across the expanse of the well itself. Similarly, analytes may not have been able to experience the fields that generated between the mullions and the bottoms of the well due to the aforementioned hydrophobicity issue. At some future point, we plan to repeat the thickness study with Au to confirm if it has a comparable trend, or as seen with the PDMS-based nanocomposites, that the optimum thickness is greater for Au. However, for consistency and comparative purposes, it was determined that a 20 nm film would be used for both metals in these preliminary investigations.

It was noted that as the pitch/gap changes for the Ag-NCGs, exhibited a radical color shift from yellow to magenta with increased film thickness for the 300/500 pitch/gap when illuminated by a white light source (Figure 6.5). A similar trend was seen

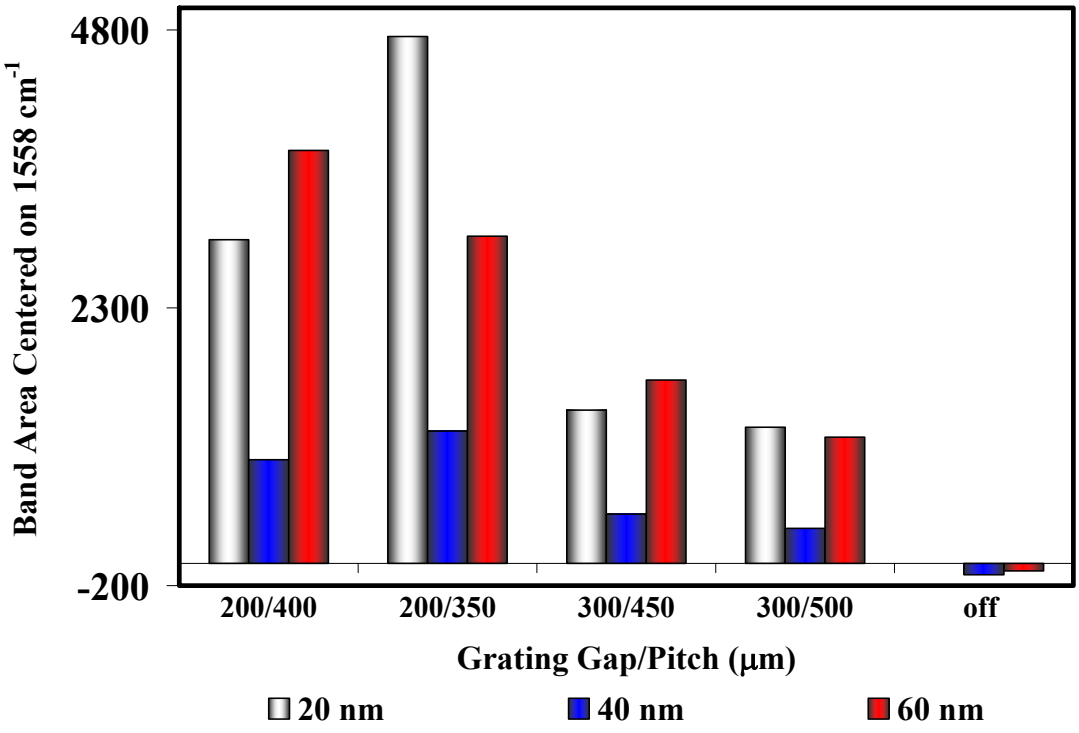


Figure 6.4. Comparison of Ag film thickness and SERS spectral band areas.

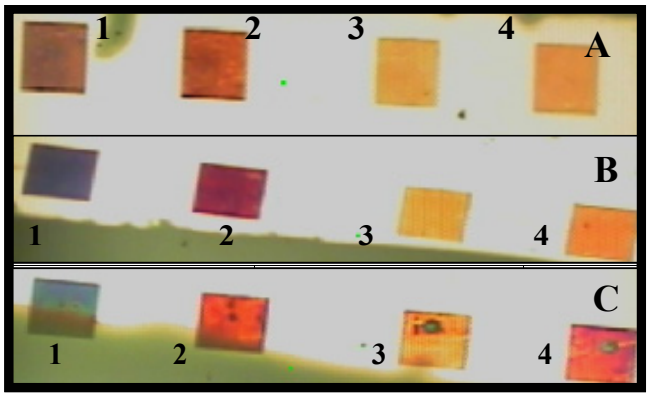


Figure 6.5. Comparison of white light illumination of Ag-coated nanowell cross-gratings. A) 20 nm; B) 40 nm C) 60 nm. [Pitch/Gap: 1) 200/400;2) 200/350; 3)300/450; 4) 300/500]

with the all the other NCGs with different pitch/gaps. These colors were thought to be the result of absorption, reflection, and, potentially, surface plasmon resonance (SPR).

Optical extinction spectroscopy is the conventional means to asses the wavelength and width of the SPR. The opacity of our NCGs prevented the collection of optical extinction spectra with our current instrumentation. We devised a means to collect the reflectance spectra as a means to correlate these spectra with observed the SERS intensities of analyte signals at the He-Ne (633 nm) SP excitation wavelength. There was noticeable bathochromatic shifts with the 200/400 gap/pitch NCG in the reflectance spectra. All of the reflectance spectra for the 2 nm Ag deposition did not have a well-defined λ_{maxes}, exhibited multiple peaks possibly due to the increased reflectivity of the surface. All of the 20 nm Ag NCGs had a peak located near ~600 nm with different degrees of intensity. The reflection spectra did not, however, directly correlate to the SERS activity seen in Figure 6.4, and was determined not to be an accurate means to determine the SPR.

LSPR are known to shift toward the longer wavelengths with an increase in nanoparticle size. One set 20 nm Au-coated NCGs with 1 x10^{-4}M 1,2 PDA were prepared for a series of SERS experiments with three laser wavelengths: with a 514 nm (Ar^{+}), 676 nm (Kr^{+}), and 633 nm (He-Ne) lasers to test if the width of the mullions would respond in a similar manner as nanoparticles. The argon and krypton lasers were used with the Dilor XY Raman instrument (a dispersive Raman instrument) and the He-Ne (spectrograph and notch filter). The comparison of the response of the band areas centered on 1156 cm^{-1}, the =C-H in-plane deformation vibration, must acknowledge the difference in throughput due to the instrumental configurations.

It was determined that for each laser wavelength there is a different gap/pitch for the 20 nm Au deposition thickness that points toward the satisfying of the conditions for surface plasmon resonance and the generation of an EM field (Figure 6.6). The argon laser appears to be fairly sensitive to the width of the mullion areas of the NCGs, with the optimum being the 150 nm, as the width increases to 200 nm, the band area decreases. It

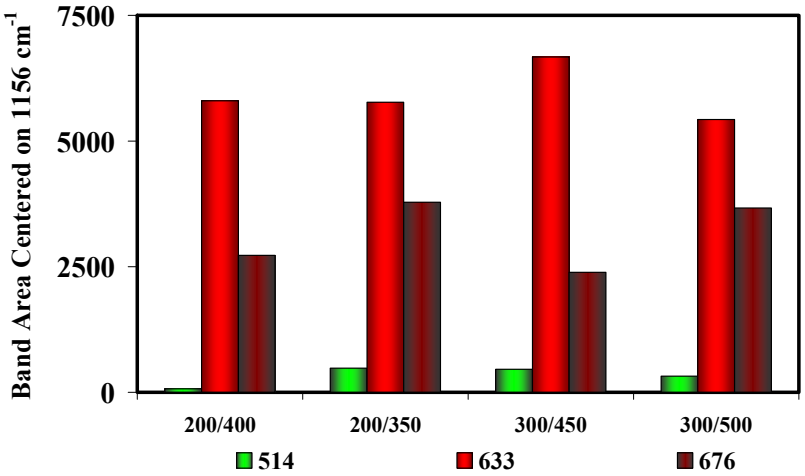


Figure 6.6 Effect of source laser on the generation of surface plasmons and SERS intensity with 20 nm Au-coated NCGs and 1 x 10^{-4}M 1,2 PDA

is interesting to note that SERS response for the 300/500 was much higher than that of the 200/400, where the only difference is the expanse of the well. The small difference (~50 nm) in the mullion widths may account for the lack of discernable patterns in the band areas of the different gaps/pitches of the NCGs with 633 nm and 676 nm wavelength excitation. [31, 32]

Nanoparticle Arrays via EBL

The lack-luster SERS performance of the NCGs prompted the move toward nanoparticle arrays. EBL offers reasonable control over the nanoparticle shape and excellent control of size, but the proximity of the nanoparticles remains an issue. Most groups employ lift-off and RIE techniques for their nanoparticle arrays because they produce substrates where the interstices are devoid of metal and can be more directly correlated to theoretical calculations.

We have endeavored to create reusable nanoparticle arrays with the EBL resists that have high aspect ratios. Our process will produce polymeric "posts" or "pillars" that will be vapor deposited, but the height of the pillars will prevent the formation of continuous metal films with up to 100 nm of deposited metal. The methacrylate resist will permit the removal and recoating of metal relatively easily as it is impervious to a wide range of pH solutions. Solutions of 5% of nitric acid or aqua regia can be used to remove the Ag and Au films, respectively.

The initial patterns for this series of experiments were based on the gap/pitch schemes of the NCGS. In this application, the dimensions of the wells are now those of

the nanoparticles. Figure 6.7 shows the micrographs of one of our first sets of these nanoparticle arrays. We believe that the irregularity of the nanoparticles was due to irregularities in the resist film, beam focusing, and the development process. The larger nanoparticles are relatively square (300/450 and 300/500). The SEM image shows the tracks between the nanoparticles due to the rastering of the beam between particles. With the smaller nanoparticles (200/400) there is a peculiar aberration in the particle shape and size from the original computer-generated pattern. This is probably due to corrugations in the film thickness, as the 200/400 cross-grating does not have the same clear interstices that the larger nanoparticle arrays have. Included in the Figure 6.7 are the white light illumination images of before and after the Ag film deposition. As we have seen with the NCGs, this does not necessarily indicate future SERS performance.

The nanoparticle arrays were vapor deposited with only 10 nm of Ag to facilitate SEM imaging. We attempted to collected SERS spectra with this set, although we realized that metal film thickness for both Ag and Au will need to be optimized. Background spectra were collected from each of the nanoparticle arrays and off the nanostructured areas before vapor treatment with p-ATP. The SERS spectra were collected before and after vapor treating with p-ATP and can be seen in Figure 6.8. The methacrylate resist bands dominate the background spectra and the SERS spectra of the analyte. From our previous experience with metal-coated polymeric SERS substrates, the spectra of thinly coated polymers (discontinuous films with areas devoid of metal) will still exhibit strong conventional Raman bands from the solid support and a reduced SERS intensity of the analyte signal. As the metal approaches an optimum SERS thickness, the bands from the polymer are severely reduced and the analyte signal increases.

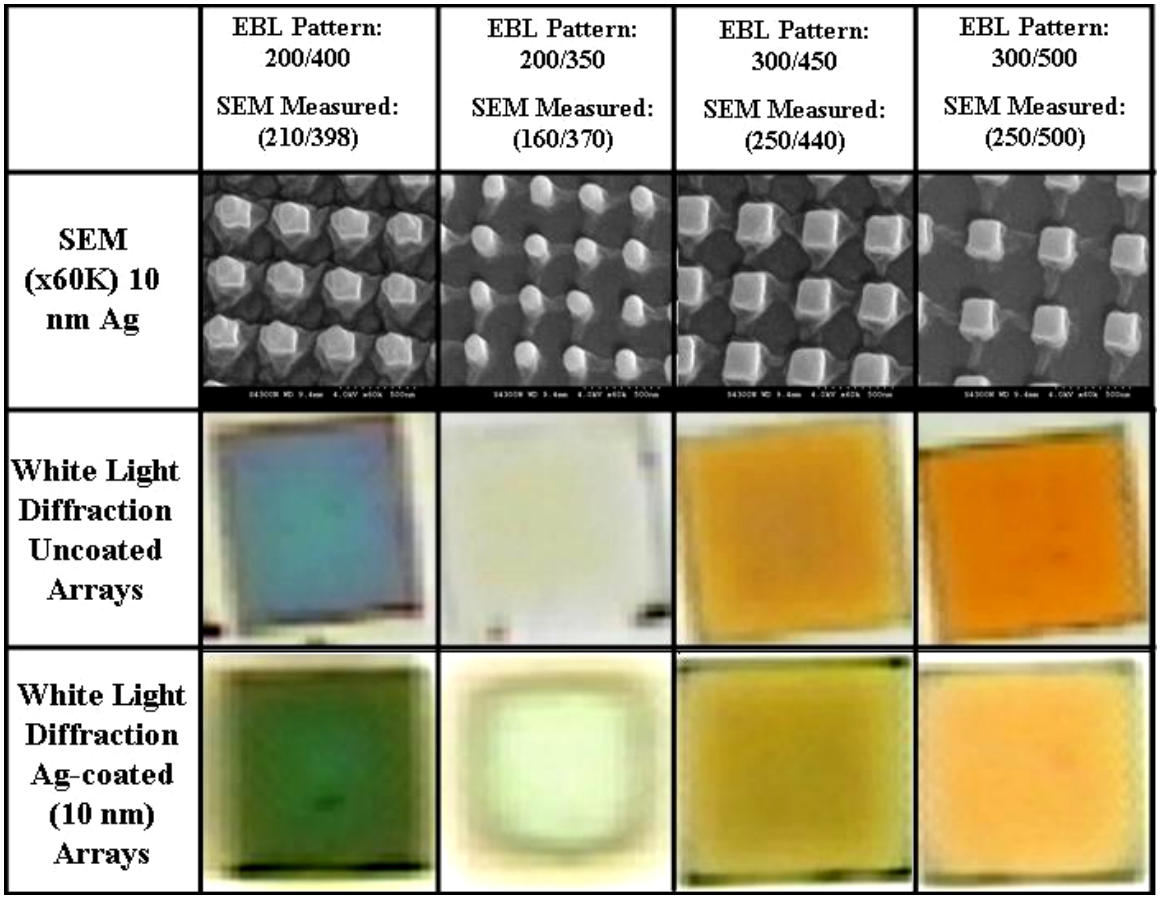


Figure 6.7. Micrographs and white-light illumination images of 10 nm Ag coated nanoparticle cross-gratings

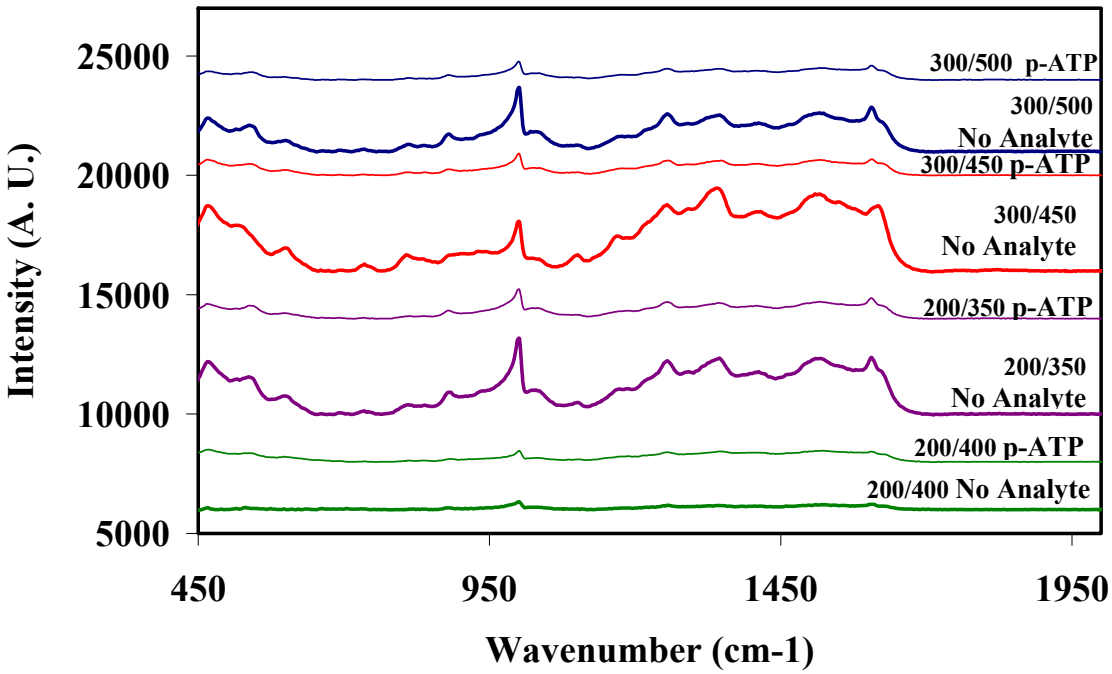


Figure 6.8. 10 nm Ag-coated set of nanoparticle cross-gratings that were vapor-treated with p-ATP. Note that the background is dominated by the spectral bands of the resist and overwhelms the spectral bands of the p-ATP.

Imprinting and Casting

We have begun to investigate other means to produce polymer-based SERS substrates with homogeneous morphology. Nano-imprint lithography, used in the semi-conductor industry, employs EBL and RIE to produce reusable silicon molds for imprinting and casting polymers (Figure 6.9). While the NCGs were not high performance SERS substrates, we plan to utilize their unique well design to produce arrays of low aspect pillars via imprinting and casting.

Chou, et al have developed several methods for imprinting polymers, in particular PMMA, with silicon molds with 10 nm features and 40 nm periods over an area of ~1 square inch.[33-37] For most polymers, a surface treatment with fluoro-chlorosilanes is required to alter the hydrophobicity of the surface and act as the release agent. A thin film of polymer, often a thermal plastic resist, is spin-coated onto a separate wafer. The mold and polymer-coated wafer are pressed together under pressure and heat. The temperature is maintained just below the glass transition temperature of the thermal plastic for the duration of the imprinting to reduce its viscosity. Both mold and wafer are slowly cooled to room temperature before separation. Pattern transfer via RIE can be used to remove the residual polymer between the nanostructures to improve the aspect ratio. Both the imprinted substrates and the RIE pattern transferred substrates can be vapor deposited with metal to create SERS substrates. To our knowledge, no one has attempted this procedure for the fabrication of SERS substrates.

Other groups have investigated submicron-scale patterns with PDMS molds and cast structures. PDMS is an ideal polymer as it does not adhere to silicon wafers and does not require additional surface treatments to the nanostructured Si wafers. This

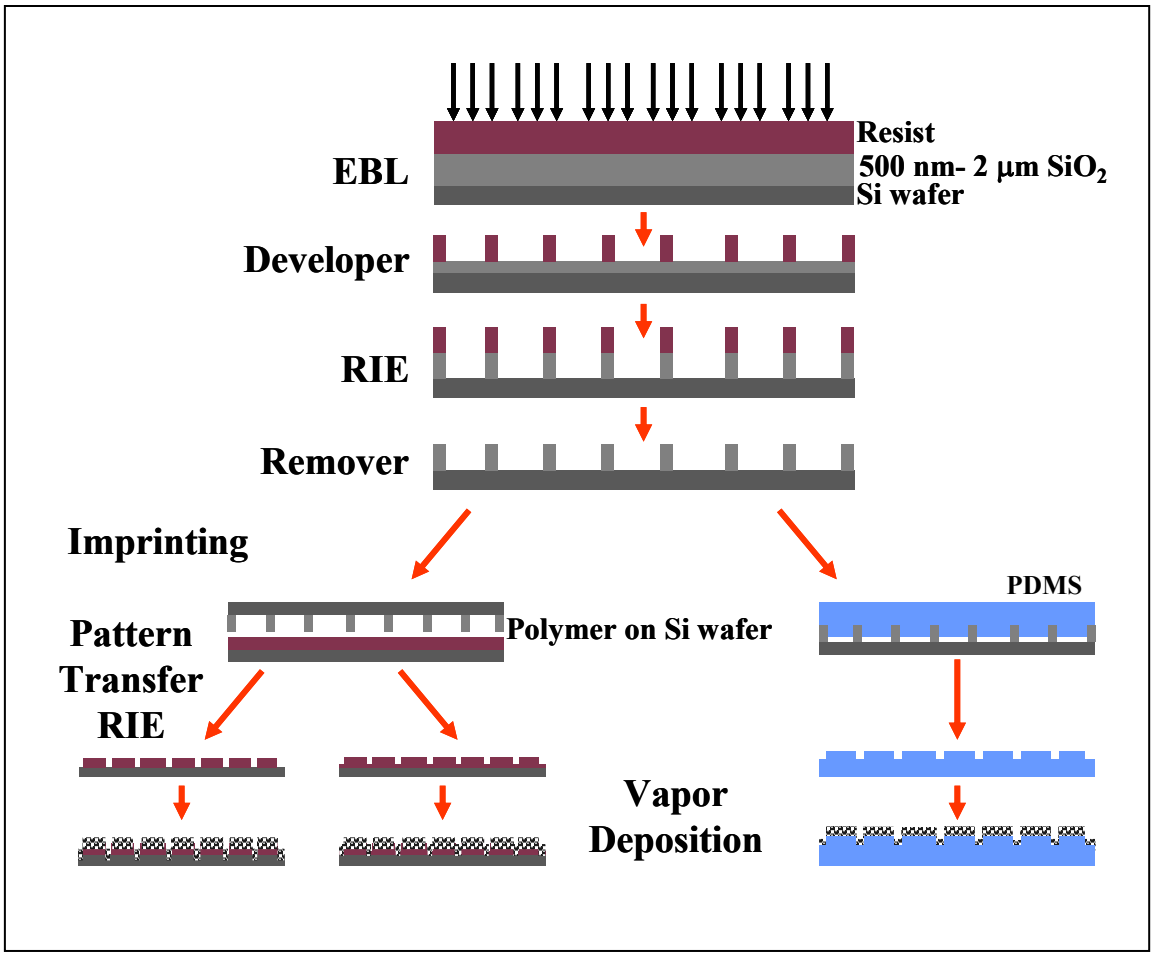


Figure 6.9. Process of imprinting and casting nanostructured polymer substrates.

would permit the simultaneous advantages of the solid-phase micro-extraction capabilities of PDMS and the controlled nanostructuring via EBL. Other options for future substrates may include creating a positive mold, like our NCGS, and cast PDMS on to this. The negative PDMS mold can then be used to cast other UV curable polymers such as PMMA and MA, thereby rapidly produce many solid substrates. Multiple PDMS molds can be produced and the original EBL resist master can be stored until the PDMS molds degrade. The surface of the PDMS will be permanently altered after a number of castings due to the increased silanol groups on the surface generated by the UV curing process, which will affect the release properties of the molds themselves. Over time and multiple castings, the precise shape of the cast pillars will degrade, and the interstices enlarge. However, since we are vapor depositing over these substrates, which inherently rounds the final nanoparticle shape, this degradation of the mold may be compensated for by the deposition thickness.

Polymer-based SERS substrates provide a unique venue to explore dielectric environments, particle proximity, morphology, ad(ab)sorption phenomena. As have been shown in the previous chapters, the elastomeric substrates can be molded into a wide variety of shapes and can be used for micro-fluidic devices. We are currently investigating the potential to use the metal-coated nanoparticle arrays as a stamp to transfer the metal coating onto a pliable polymer. Micro-fluidic devices could be imprinted in this manner for on-line SERS detection. Metal transfer also will permit the interrogation of the particle proximity by physical manipulation of the polymer film, as was done with our Ag-PDMS substrates. The early trials with this technique have

indicated that surface treatments will be necessary to facilitate the complete transfer of the metal from the resist to the elastomer.

References

References

(1) Vo Dinh, T.; Meier, M.; Wokaun, A. *Analytica Chimica Acta* **1986**, *181*, 139-148.
(2) Li, H.; Sun, J.; Cullum, B. M. *Proceedings of SPIE-The International Society for Optical Engineering* **2004**, *5588*, 19-30.
(3) Li, H.; Cullum, B. M. *Proceedings of SPIE-The International Society for Optical Engineering* **2004**, *5261*, 142-154.
(4) Yang, X. M.; Tryk, D. A.; Hasimoto, K.; Fujishima, A. *Applied Physics Letters* **1996**, *69*, 4020-4022.
(5) Rogers, J. A.; Jackman, R. J.; whitesides, G. M.; Wagener, J. L.; Vengsarkar, A. M. *Applied Physics Letters* **1997**, *70*, 7-9.
(6) Bechinger, C.; Muffler, H.; Schafle, C.; Sundberg, O.; Leiderer, P. *Thin Solid Films* **2000**, *366*, 135-138.
(7) Chen, Y.; Lebib, A.; Li, S.; Pepin, A.; Peyrade, D.; Natali, M.; Cambril, E. *European Physical Journal: Applied Physics* **2000**, *12*, 223-229.
(8) Musick, M. D.; Keating, C. D.; Lyon, L. A.; Botsko, S. L.; Pena, D. J.; Holliway, W. D.; McEvoy, T. M.; Richardson, J. N.; Natan, M. J. *Chemistry of Materials* **2000**, *12*, 2869-2881.
(9) Willing, G. A.; Han, C.; Noh, D. Y.; Wang, H. H. *Annual Meeting Archive - American Institute of Chemical Engineers, Indianapolis, IN, United States, Nov. 3-8, 2002* **2002**, 37-44.
(10) Shin, H. S.; Yang, H. J.; Jung, Y. M.; Kim, S. B. *Vibrational Spectroscopy* **2002**, *29*, 79-82.
(11) Huie, J. C. *Smart Materials and Structures* **2003**, *12*, 264-271.
(12) Choi, D.-G.; Jang, S. G.; Yu, H. K.; Yang, S.-M. *Chemistry of Materials* **2004**, *16*, 3410-3413.
(13) Tan, L.; Kong, Y. P.; Pang, S. W.; Yee, A. F. *Proceedings of SPIE-The International Society for Optical Engineering* **2004**, *5374*, 1017-1022.
(14) Tan, L.; Kong, Y. P.; Pang, S. W.; Yee, A. F. *Journal of Vacuum Science & Technology, B: Microelectronics and Nanometer Structures--Processing, Measurement, and Phenomena* **2004**, *22*, 2486-2492.
(15) Muir, B. V. O.; Luscombe, C. K.; Huck, W. T. S. *Encyclopedia of Nanoscience and Nanotechnology* **2004**, *3*, 497-510.
(16) Grabar, K. C.; Freeman, R. G.; Hommer, M. B.; Natan, M. J. *Analytical Chemistry* **1995**, *67*, 735-743.
(17) Grabar, K. C.; Allison, K. J.; Baker, B. E.; Bright, R. M.; Brown, K. R.; Freeman, R. G.; Fox, A. P.; Keating, C. D.; Musick, M. D.; Natan, M. J. *Langmuir* **1996**, *12*, 2353-2361.
(18) Baker, B. E.; Kline, N. J.; Treado, P. J.; Natan, M. J. *Journal of the American Chemical Society* **1996**, *118*, 8721-8722.
(19) Freeman, R. G.; Hommer, M. B.; Grabar, K. C.; Jackson, M. A.; Natan, M. J. *Journal of Physical Chemistry* **1996**, *100*, 718-724.
(20) Baker, B. E.; Natan, M. J.; Zhu, H.; Beebe, T. P., Jr. *Supramolecular Science* **1997**, *4*, 147-154.
(21) Bright, R. M.; Musick, M. D.; Natan, M. J. *Langmuir* **1998**, *14*, 5695-5701.

(22) Natan, M. J.; Keating, C.; (The Penn State Research Foundation, USA). Application: US
US, 2000, pp 56 pp.
(23) Hinde, R. J.; Sepaniak, M. J.; Compton, R. N.; Nordling, J.; Lavrik, N. *Chemical Physics Letters* **2001**, *339*, 167-173.
(24) Kerker, M.; Wang, D. S.; Chew, H. *Applied Optics* **1980**, *19*, 3373-3388.
(25) Moskovits, M.; Suh, J. S. *Journal of Physical Chemistry* **1984**, *88*, 5526-5530.
(26) Zeman, E. J.; Schatz, G. C. *Jerusalem Symposia on Quantum Chemistry and Biochemistry* **1984**, *17*, 413-424.
(27) Zou, S.; Janel, N.; Schatz, G. C. *Journal of Chemical Physics* **2004**, *120*, 10871-10875.
(28) Hao, E.; Schatz, G. C. *Journal of Chemical Physics* **2004**, *120*, 357-366.
(29) Vieu, C.; Carcenac, F.; Pepin, A.; Chen, Y.; Mejias, M.; Lebib, A.; Manin-Ferlazzo, L.; Couraud, L.; Launois, H. *Applied Surface Science* **2000**, *164*, 111-117.
(30) Broers, A. N.; Hoole, A. C. F.; Ryan, J. M. *Microelectronic Engineering* **1996**, *32*, 131-142.
(31) Gupta, R.; Dyer, M. J.; Weimer, W. A. *Journal of Applied Physics* **2002**, *92*, 5264-5271.
(32) Gupta, R.; Weimer, W. A. *Chemical Physics Letters* **2003**, *374*, 302-306.
(33) Chou, S. Y.; Krauss, P. R.; Renstrom, P. J. *Applied Physics Letters* **1995**, *67*, 3114-3116.
(34) Chou, S. Y.; Krauss, P. R.; Renstrom, P. J. *Journal of Vacuum Science & Technology, B: Microelectronics and Nanometer Structures* **1996**, *14*, 4129-4133.
(35) Chou, S. Y.; Krauss, P. R.; Renstrom, P. J. *Science (Washington, D. C.)* **1996**, *272*, 85-87.
(36) Chou, S. Y.; Krauss, P. R. *Microelectronic Engineering* **1997**, *35*, 237-240.
(37) Chou Stephen, Y.; Keimel, C.; Gu, J. *Nature* **2002**, *417*, 835-837.

Vita

Kathleen S. Giesfeldt was born in Oconomowoc, Wisconsin on June 8, 1964. She lived in Hartland, Wisconsin where she attended both grade school and high school. She graduated from Arrowhead High School in June of 1982. She entered the University of Wisconsin-Waukesha for her first year of college and moved to Dallas, Texas, where she apprenticed as a fine art conservator. She became a professional associate in the American Institute of Conservation and Preservation of Historic Works (AIC) in November of 1996 and was the Vice-Chair (1999) and Chair (2000) of the Conservators in Private Practice Subgroup of the AIC. In August of 1990, she entered the University of Texas at Dallas was subsequently awarded a Bachelor of Arts and Performance (emphasis in art history, fine arts, and literature) in January of 1993. She returned to the University of Texas at Dallas in August of 2000 to complete her Bachelor's degree in Chemistry. During a summer undergraduate research fellowship to complete her senior research requirements, at Oak Ridge National Laboratory under Dr. Panos Datskos, she met Dr. Michael J. Sepaniak and was recruited to the University of Tennessee, Knoxville in August of 2001 for her graduate studies. While at the University of Tennessee, Knoxville, she majored in analytical chemistry under Dr. Michael J. Sepaniak. Her graduate work involved the development and characterization of novel nanocomposite surface enhanced Raman scattering (SERS) substrates and began work on SERS substrates created by electron beam lithography. She officially received her doctoral degree in analytical chemistry in May, 2005.